Investigations of the Properties of Covalently Linked 2D Nano-sheets, ALD/CVD Grown Thin Films of Metal Chalcogenides, and C-doped Gallium Nitride

---

A Thesis Submitted for the Degree of

DOCTOR OF PHILOSOPHY

by

Reetendra Singh

JNCASR

New Chemistry Unit
Jawaharlal Nehru Centre for Advanced Scientific Research
(An Institution Deemed to be University)
Bangalore, India

March 2023

Dedicated to my teachers and parents

Declaration

*I hereby declare that the matter embodied in the thesis entitled "**Investigations of the Properties of Covalently Linked 2D Nano-sheets, ALD/CVD Grown Thin Films of Metal Chalcogenides, and C-doped Gallium Nitride**" is the result of investigations carried out by me at the New Chemistry Unit, Jawaharlal Nehru Centre for Advanced Scientific Research, Bengaluru, India under the supervision of Prof. C. N. R. Rao and that it has not been submitted elsewhere for the award of any degree or diploma.*

In keeping with the general practice in reporting scientific investigations, due acknowledgment has been made wherever the work described is based on the findings of other investigators. Any omission that might have occurred by oversight or error of judgment is regretted.

Singh

(Reetendra Singh)

Certificate

*I hereby declare that the matter embodied in the thesis entitled "**Investigations of the Properties of Covalently Linked 2D Nano-sheets, ALD/CVD Grown Thin Films of Metal Chalcogenides, and C-doped Gallium Nitride**" has been carried out by Mr. Reetendra Singh at the New Chemistry Unit, Jawaharlal Nehru Centre for Advanced Scientific Research, Bengaluru, India under my supervision and that it has not been submitted elsewhere for the award of any degree or diploma.*

(Prof. C. N. R. Rao)

(Research Supervisor)

Acknowledgements

First and foremost, I express my greatest gratitude to my research supervisor, **Prof. C. N. R. Rao, FRS**, for introducing me to the fascinating fields of "Two-dimensional nanomaterials and thin films". I consider myself privileged to have worked under his supervision. It was his passion that prompted in me the desire to pursue science and has continued to inspire me ever since. His innovative way of thinking and ability to handle any problem in the unique way have been the strength behind the completion of this work. It has been a fulfilling experience to work under his encouraging and full-spirited guidance. He has not only been influential in shaping my research, and my career but my entire personality, and my outlook toward life as a whole.

I express my sincere gratitude to Prof. Subi J George, Chairman of NCU, for his immense help and support in various aspects throughout my Ph.D.

My sincere thanks to my collaborator, Prof. Umesh. V. Waghmare, Dr. V. Sampath Kumar, Mr. Debendra Panda for their valuable contributions and discussions.

My work would have been incomplete without the help of my co-workers Dr. Uttam Gupta, Dr. M. M. Ayyub, Dr. Pramoda, Dr. K. Manjunath, Dr. Anand Roy, Dr. P. Chithaiah, Mr. N. K. Singh, and Mr. Amit, who worked with me on different projects.

I shall remain ever thankful to all my seniors for their valuable suggestions. It has been a wonderful experience working with all my past and present labmates Dr. Sreedhara, Dr. Anand Roy, Dr. K. Manjunath, Dr. P. Vishnoi, Dr. M. Chhetri, Dr. M. Kaur, Dr. M. M. Ayyub, Dr. Manasawee, Mr. N. K. Singh, Mr. Amit, Mr. Swaraj, Ms. Aditi, Mr. Rohit, Mr. Devesh, Mr. Sakil and I thank them all for their help in various occasions.

I thank the faculties namely Prof. H. Ila, Prof. S. Balasubramanian, Prof. A. Sundaresan, Prof. Eswaramoorthy, Prof. Sridhar Rajaram, Prof. Shobhana Narasimhan, Prof. T. K. Maji, Prof. S. J. George, Prof. R. Viswanatha, Prof. Jayanta Haldar, Prof. Kanishka Biswas, Prof. Sebastian C. Peter, Dr. S. Agasti, and Dr. Premkumar for all the illuminating courses and discussions.

I thank the timely help of the technical staff namely Ms. N. R. Selvi, Mrs. T. Usha, Mr. Vasu, Mr. Anil, Mr. Srinath, Mr. Mahesh, Dr. Ghatak, Mr. Kannan, Mr. Jagadish, Mr. Shivkumar and Ms. Minakshi.

I thank Mrs. Shashi, Mrs. Sudha, Mr. Gowda, and Mr. Victor for their help in various aspects.

I thank JNCASR and the Dept. of science and technology (India) for the research fellowship.

I extend my sincere thanks to the hostel, Admin, Academic, Library, Dining hall and Dhanvantari, and other departmental staff for all their help.

I take this opportunity to thank Mrs. Indumati Rao for all the affection and love I have received from her. Her enthusiasm age notwithstanding has been a source of inspiration for me. I consider myself blessed to have received all this care and more than everything the wise words of advice now and then.

I take this opportunity to thank Mr. Sanjay Rao for his hospitality.

Thanks to all my batchmates, Sudip, Abhishek, Dhimahi, Anjali, and Gurshid with whom I started my life at this centre, and whose cheerful company made these years of life so cherishable.

I thank my all friends from JNCASR specially, Dr. Rajendra, Dr. Shivram, Navneet, Momin, Shashank, Dr. Ashutosh, Bhupesh, Kamlesh, Debendra, Uttam, and Mayank.

I extend my lovely thanks to my friends specially Brajendra, Jagbhan, Neeraj, Preetam, Kishan, Jagdeep, and Shiva for the cheerful company made since childhood.

Last but not least, I thank my dearest parents, family members, and Roshni for their support, love, and care.

Preface

Over the decades there has been tremendous progress in thin layers with fundamentally new properties of materials. Two-dimensional thin nanosheets with atomic thickness and infinite planar lengths have gained tremendous importance due to their unique properties compared to other nanostructures and to their bulk counterparts. The thin films of materials also gained huge attraction in the field of device fabrication and catalysis. The present investigations mainly focus on the synthesis and characterization of 2D nanomaterials and thin films of metal chalcogenides, and their selected properties related to energy and sensor applications. The thesis is divided into three parts, wherein **Part I** deals with thin 2D materials, linked 2D nanosheets, their structures, properties, and their use in photochemical hydrogen evolution reaction (HER). **Part II** focused on the deposition of thin films of metal oxides and sulfide by chemical vapor deposition (CVD) and atomic layer deposition (ALD) and their detailed characterization, selected properties, and sensing applications. **Part III** deals with carbon-doped gallium nitride and related luminescence properties.

Part I is divided into four chapters of which **Chapter 1** gives a brief overview of the 2D nanomaterials, their unique properties, functionalization of 2D nanomaterials, heterostructures, nanocomposites, and the fundamentals of photocatalytic water splitting. **Chapter 2** discusses the facile synthesis and characterization of 1T phases of MoX_2 (X = S, Se) via solvothermal and hydrothermal methods. The stability of 1T phase obtained by these methods was found to be better than other methods and they show reasonable photochemical hydrogen production. **Chapter 3** describes the synthesis of covalently cross-linking of nanosheets of $MoSe_2$. These crosslinked nanosheets show better HER activity than their bulk (2H) phase or physical mixtures. **Chapter 4** deals with the role of interlayer separation of cross-linked nanosheets on the photochemical HER reactions. The nature of another layer in the cross-linked sheets also plays a crucial role, which describes in the later part of this chapter.

Part II is divided into three chapters with **Chapter 5** giving a brief overview of chemical vapor deposition (CVD) and atomic layer deposition (ALD) methods and their unique advantages over other techniques. **Chapter 6** discusses the growth and in detail characterization of V_2O_3 crystalline thin film obtained via ALD process followed by postdeposition annealing and its metal-insulator transition. **Chapter 7** describes the growth and characterization of NbO_2 thin films via CVD method. This chapter also describes the precursor modification for the required film. This precursor provides +4 oxidation state of Nb without further post-reduction of +5 oxidation state. **Chapter 8** describes the growth and characterization of the β-phase of nickel sulfide via ALD process and its application in enzyme-free electrochemical glucose sensors.

Part III contains **chapter 9** which describes the synthesis of carbon-doped gallium nitride via a solid-gas phase reaction route and detailed characterizations. An investigation of yellow luminescence caused by carbon doping and the origin of that is also discussed.

Table of Contents

Part I. 2D-layered Materials and Their Application in Hydrogen Production

Part II. Chemical Vapor Deposition (CVD) and Atomic Layer Deposition (ALD) of Thin Films of Metal Chalcogenides

Part III: Carbon-doped Gallium Nitride

Part I: 2D-layered Materials and Their Application in Hydrogen Production

Chapter 1

Two-dimensional Materials: A Bird's Eye View

Summary

The research in two-dimensional (2D) materials has increased promptly after the discovery of graphene in 2004. Ultrathin layers of 2D materials offer several properties and behave differently than their bulk counterparts. Among all the 2D materials, transition metal dichalcogenides (TMDs) have made great attention due to their metal to wide gap semiconducting nature. Non-metal based 2D materials also have been made great effort for catalysis such as hydrogen evolution.

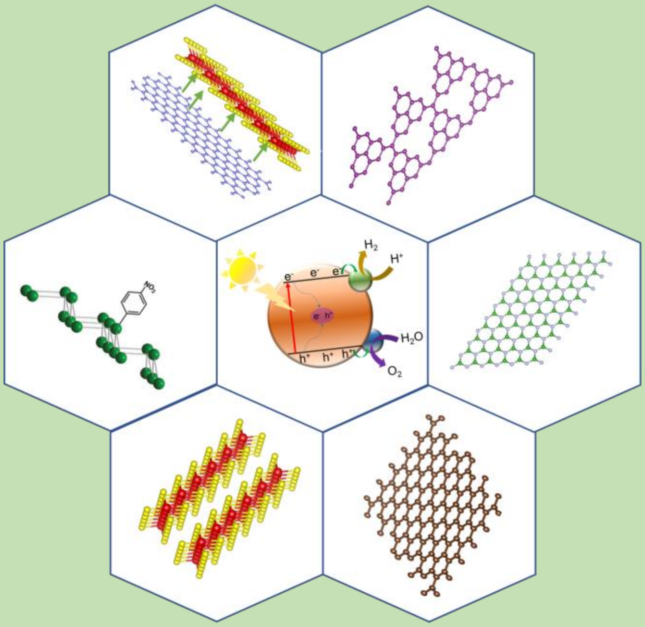

Surface functionalization of 2D materials alter the charateristics of materials and behave differently; also the useful for their stability and charge transfer channel. Non-covalently or covalently functionalization and cross-linking to form heterostructures and nano-composites are then considered which can be a interest of reaserch community.

1.1. Introduction

With the questions, “What could we do with layered structures with just the right layers?, What would happen if we could arrange the atoms one by one the way we want them?”, Richard P. Feynman encouraged the researchers to explore “the bottom” during a lecture “There’s Plenty of Room at the Bottom”[1]. These questions in his landmark 1959 lecture, with profound ideas about manipulating things on an atomic scale using quantum mechanics, motivated generations of scientists, to think about layered materials.

Atomic- and nano-range materials have undergone substantial research in the age of scientific invention to synthesize new materials that enhance the elemental output in several applications. Nanotechnology advancements are altering the world's perspective in several ways in the twenty-first century. The characteristics and behavior of a material are affected by its size. As a result, when the size is reduced to the nanoscale, the material's mechanical, chemical, electrical, and optical properties significantly improve. Therefore in technological advancement, nanomaterials can be in the range from zero dimensions (0D) to three dimensions (3D). Quantum dots are an example of a zero-dimensional material, while nanoribbons, nanotubes, and nanowires are examples of one-dimensional (1D) materials. Graphene, single-atom-thick carbon layer is a example of 2D materials whereas carbon’s other allotropes such as nanoballs and nanocones are examples of 3D materials[2].

Early in the 20th century, it was believed that two-dimensional layered materials were thermodynamically unstable and were only feasible in theory. But the isolation of graphene by Novoselov, Geim, and colleagues in 2004 from graphite defined the birth moment of 2D materials[3]. Due to a variety of changes in physical and chemical properties brought on by the quantum size effect arising from nanosized thickness, 2D materials have drawn a lot of attention. A huge number of applications of graphene including energy generation and storage[4], optical devices[5], high-speed electronics[6], and sensors[7] have been reported. Following these groundbreaking studies, 2D material research accelerated with researchers focusing on other 2D materials such as transition metal dichalcogenides (TMDs), transition metal oxides (TMOs), 2D salts, organics, metallic, and non-metallic 2D materials beyond graphene (**Figure 1**)[8].

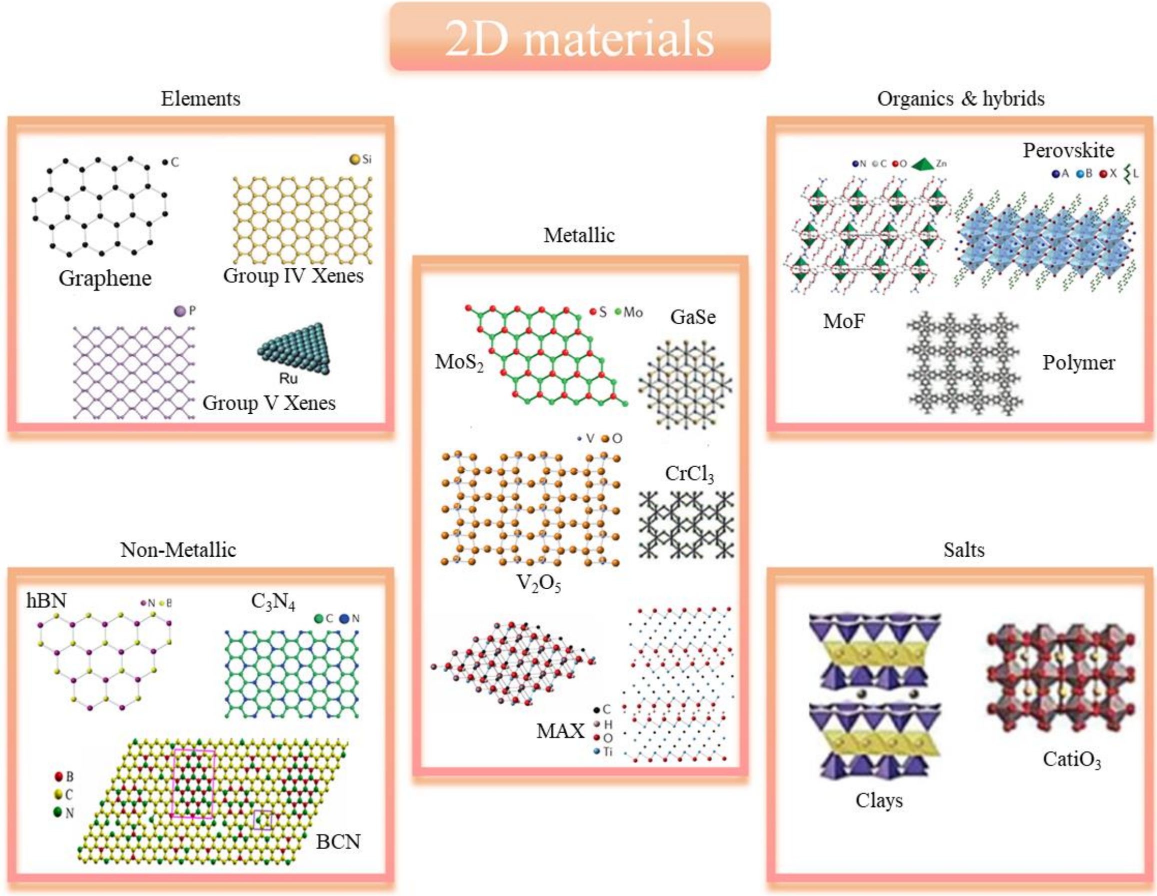

Figure 1: *Classification and structure of different two-dimensional layered materials. Reproduced with permission[8-10]. Copyright 2022, John Wiley & Sons; Copyright 2017, American Chemical Society; Copyright 2023, Springer Nature and Copyright 2017, CNKI.*

The 2D buckling nanosheets of group IV that resemble graphene-like structures have also newly attracted a lot of attention. The silicon- or germanium-based equivalents of graphene, silicene, and germanene, have quickly progressed from theoretical hypotheses to experimental proof[11,12]. It is discovered that they display graphene-like electronic properties and have the potential for device applications. With nitrogen and boron atoms in the site of carbon, hexagonal boron nitride (hBN)[13], boron carbon nitride (BCN)[14], and carbon nitride (C_3N_4)[15] resemble graphene in terms of crystallographic appearance and have also been studied extensively. In addition to topological insulators like Bi_2Se_3 and various clays, layered transition oxides like $CaTiO_3$ and La_2CuO_4 have also been studied[16]. These layered materials exhibit stacking structures, solid covalent bonds inside each sheet, and van der Waals interactions between neighbouring sheets in their bulk 3D crystals. These materials have intriguing features and span the entire spectrum of electronic properties, from insulators to metals. Mainly two methodologies, top-down and bottom-up approaches are used to categorize the synthesis of these 2D materials (**Figure 2**).

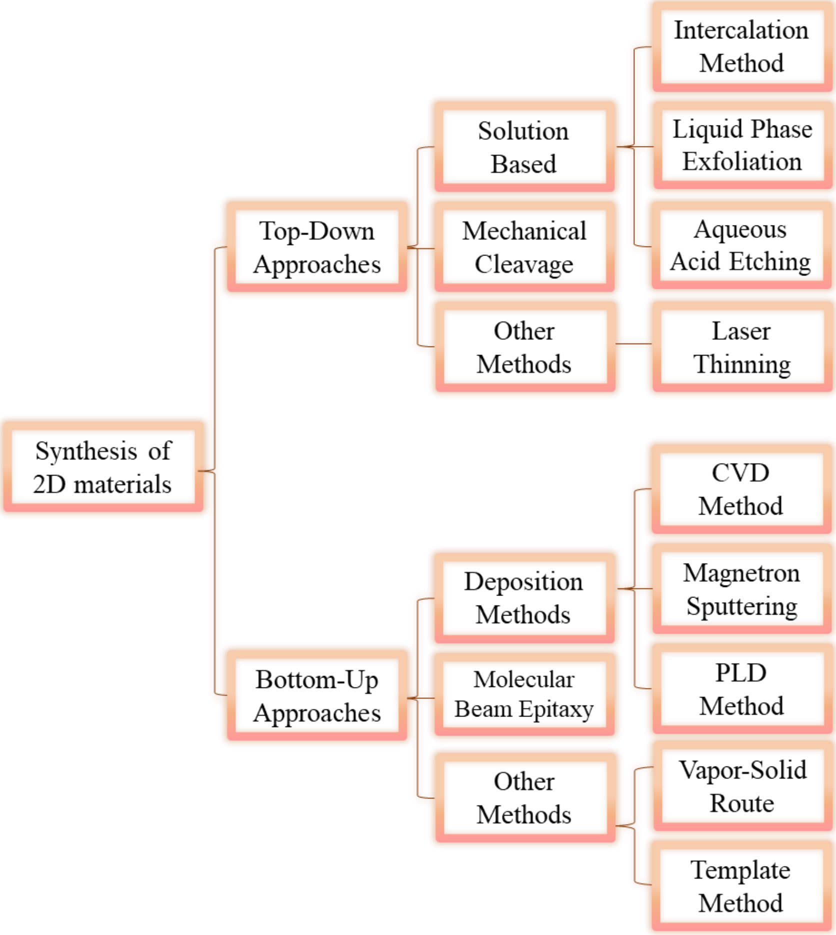

Figure 2: *The synthesis approaches of two-dimensional materials.*

In the top-down approach, 2D materials are synthesized by material removal followed by carving bulk or larger solid materials under regulated conditions, whereas, in the bottom-up approach, these 2D materials are sythesized from atomic or molecular reactants that can react each other to grow a 2D layered materials or self-assembe into a multifaceted 2D materials. Bottom-up approaches have been quite successful than top-down methods due to mass production. The Bottom-up approaches involve epitaxial growths such as molecular beam epitaxy (MBE), chemical vapor deposition (CVD), pulse laser deposition (PVD), microwave-assisted methods, and wet chemical methods whereas top-down involve mechanical exfoliation, liquid exfoliation followed by alkali metals intercalation, ultrasonic, ion-change, and electrochemical exfoliations as well as chemical reduction. A pictorial scheme of synthesis processes of 2D materials is shown in **Figure 3.**

The mechanical exfoliation can be used to separate layers of 2D materials from their counter bulk parts by weaking the van der Waals force. Two forces—lateral force and normal force—influence this layer separation. While the lateral force is applied between layers in a lateral direction, normal force is used to counteract the Van der Waals force during the peeling process. Weak Van der Waals forces hold mono-atomic layers of graphene together. The layers are separated by a distance of 3.34 Å and have a 2 eV nm^{-2} bonding energy.

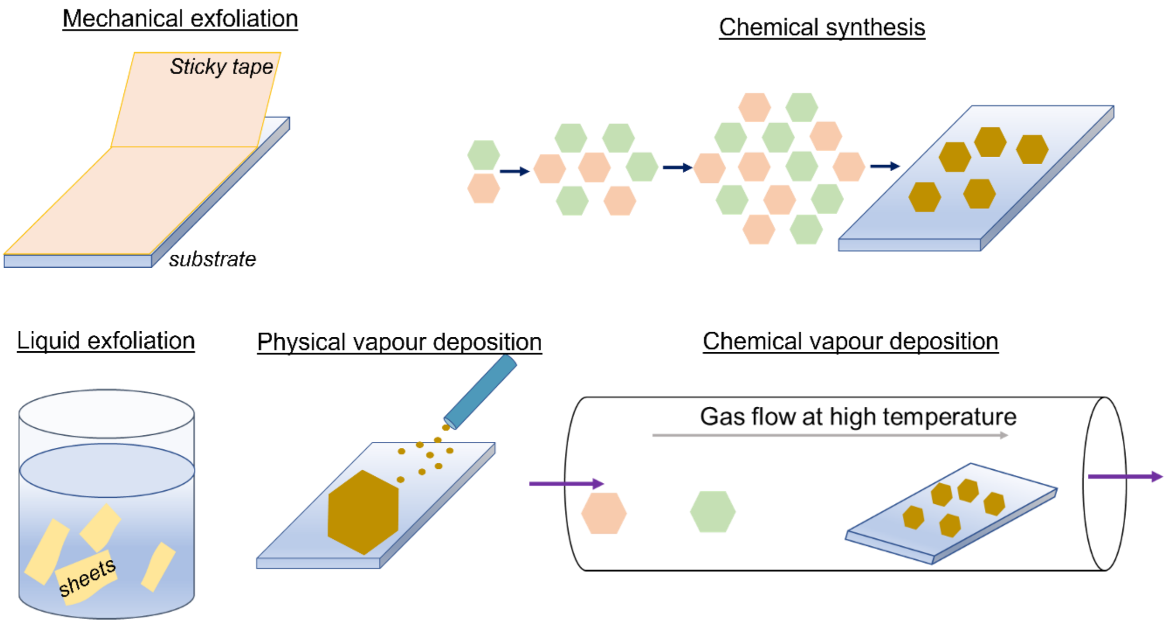

Figure 3: *The synthesis approaches of two-dimensional (2D) materials.*

A single layer needs to be separated during this exfoliation with an external force of 300 nN μm^{-2}. Novoselov and co-workers applied a scotch tape to peel out the graphite sheets repeatedly to obtain single- and few-layer graphene[3]. Yin *et al.* peeled a mono-layer MoS_2 from its bulk crystal[17], and Desalegne *et al.* exfoliated crystalline bismuth telluride (Bi_2Te_3) layes with a few atoms' worth of thickness[18]. Liu and co-workers reported tape-based exfoliation of single-layer black phosphorus of ≈0.85 nm step height[19]. In 2013, Li *et al.* reported mono-layer tungsten diselenide (WSe_2), tantalum disulfide (TaS_2), and $TaSe_2$ using tape-based mechanical exfoliation[20]. A successful exfoliation of MXenes using adhesive tape has been reported by Gkountaras *et al.* in 2020, in which the exfoliated MXenes sheets had found to be less defected[21]. Exfoliation of 2D layered materials has excellent integrity and minimal flaws, making this technique simple, quick, and inexpensive. Unfortunately, because it requires multiple peels to obtain a monolayer, the efficiency is very low. This method is therefore appropriate for laboratory-based scientific study, but it is challenging to use for mass production.

Chemical and liquid exfoliation procedures can overcome mechanical exfoliation's low yield and efficiency, however, the exfoliated materials obtained by these techniques are brief and of relatively poor quality and produces small sized sheets. However, deposition technologies (such as CVD and PVD) [22, 23] enable the production of thin films of 2D materials with decent sizes that are of great quality and efficiency. In CVD, any desired 2D material is deposited on the substrate in the reactor where the precursor‘s vapor is injected to obtain 2D sheets chemically at high temperatures. The crystallinity, morphology, and defect of the 2D sheets can be controlled by changing the CVD's control parameters for increased effectiveness and quality. The transfer process from deposited substrates to desired substrates for device fabrication and the polycrystalline nature of the substrates cause defects. Even though CVD processe produce a small sized sheets of 2D materials, it is still suitable for use in electronics and energy storage applications.

1.2. Graphene and other elemental materials

Graphene is a single layer, one atomic layer-thick sheet made of closely packed sp^2 carbon atoms in a honeycomb lattice. It can be wrapped into 0D fullerene, and 1D nanotubes, and can be restacked into 3D graphite, making graphene the mother of all graphitic forms[24]. The research community has paid close attention to graphene because of its special electrical characteristics, including high electron mobility (250,000 cm^2/Vs), enhanced thermal conductivity (5000 Wm/K), and extreme optical transparency (98%). Graphene also exhibits excellent mechanical strength with Young's modulus of 1 Tpa and specific surface area ($\approx$2630 m^2/g). Ambipolar electric field effect and anomalous quantum Hall effect[25] also make it fasinating. Graphene is a 2D semi-metal that has a very slight overlap between its valence and conduction bands. The properties of graphene also depend on its synthesis methods. The physical methods include mostly micromechanical exfoliation, CVD, and arc discharge methods. A large-scale production approach chemical reduction of graphene oxide (GO) to graphene is considered to be an effective method of low cost, but the quality of obtained graphene sheets from this process known to be slightly poor since it involves several chemical modifications.

Graphene lacks a bandgap, limiting its applications despite its remarkable qualities including transparency, flexibility, and high carrier mobility. Due to graphene's lack of a band gap, it is challenging that pristine graphene will be employed to fabricate logical circuits that can function at ambient temperature with low standby power dissipation. So, Graphene field-effect transistors have a low current on/off ratio as a result. Since the discovery of graphene, a significant deal of study has been done to find ways to make graphene have a bandgap. Some of these strategies include doping graphene, limiting graphene to nanoribbons, twisting graphene into a bilayer, and growing graphene on materials like h-BN. Finding graphene's semiconducting analogs rather than altering graphene was also of interest. In this circumstance, 2D monoelemental layered materials other than graphene have been synthesised and suggested as potentially viable substitutes.

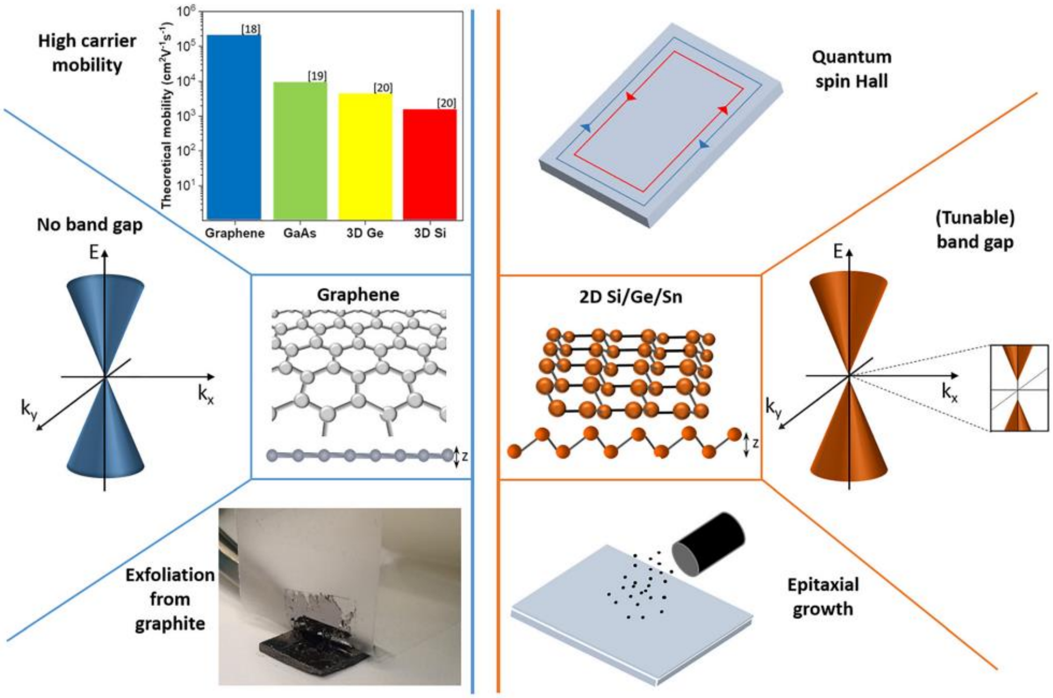

Figure 4: *Comparison of graphene (left side) with other 2D elemental layered materials (right side). Reproduced with permission[26] copyright 2019, AIP Publishing.*

These materials include borophene, silicene, germanene, phosphorene, and stanene etc. Mannix and co-workers reported thin layers of boron called as borophene on a silver substrate by molecular beam epitaxy (MBE)[27]. Silicene (Si) or germanene (Ge) cannot hybridize in a completely sp^2 manner like graphene because of the longer Si-Si or Ge-Ge link lengths **(Figure 4)**. As a result, Si or Ge exhibit mixed nature of sp^2-sp^3 hybridization in their single layers, which causes a minor buckling, or shift of present atoms in the direction of out-of-plane[28]. It's interesting to note that, buckling nature and the enhanced spin-orbit coupling of these elemental 2D layered make them topological insulators. The energy gaps for Se, Ge, and Sn sheets found to be approximately 1.5 meV, 23.9 meV, and 100 meV, respectively[26, 29, 30]. These topologically nontrivial electronic states enable quantum information to be preserved in the devices based on these 2D materials. However, these monolayers were found to be less stable in air than graphene. Fabrication of monolayers of these elemental materials also has been challenging due to less availability for their bulk counterpart and the selectivity of substrates.

Epitaxial thin film of silicene is grown on Ag(111) on in-situ Al_2O_3 capped mica substrate[31]. Germanene sheets in the shape of a honeycomb were successfully deposited by Dávila *et al.* on the surface of Au(111)[32]. On a metallic Bi_2Te_3(111) substrate, Zhu *et al.* (2015) deposited buckled monolayer sheet of stanene using MBE[33]. Atomically thin sheets of germanium are prepared using several metallic substrates such as Au(111), Pt(111), Cu(111), and Sb(111)[11]. Freestanding nanosheets of group V phosphorene[34, 35], arsenene[36], antimonene[36], and bismuthene[37, 38] were also synthesized (structural parameters and stacking mentioned in **Table 1**) from their multilayer allotropes in the thermodynamically stable monolayers.

Table 1. Overview of structures of group-V layered bulk materials and related allotropes [11].

Group V elements	Crystal system	Layered allotrope	Stacking pattern	Interlayer distance (Å)	Sheet thickness (Å)
phosphorus	Orthorhombic	α-BP	ABAB	3.20	2.20
arsenic	Rhombohedral	β -As	ABCABC	2.04	1.35
antimony	Rhombohedral	β -Sb	ABCABC	1.84	1.55
bismuth	Rhombohedral	β -Bi	ABCABC	2.35	1.55

Each phosphorus atom forms a puckered honeycomb structure by covalently bonding to three nearby atoms in a single layer. Contrary to graphene, in the site of the first Brillouin zone, the phosphorene is predicted to have a direct bandgap semiconductor with gap of 2 eV in monolayer[39] because the three bonds enclose all three of the valence electrons of phosphorus. Interlayer interactions for few-layer phosphorene cause the bandgap to shrink with each additional layer until it reaches 0.3 eV for bulk black phosphorus. Such a band structure offers a crucial gap for the field-effect transistor (FET) applications[40] shown in **Figure 5**. With a drain current modulation of $>10^5$ and a field-effect mobility of 984 $cm^2V^{-1}s^{-1}$ at ambient temperature, the device exhibits ambipolar behaviour.

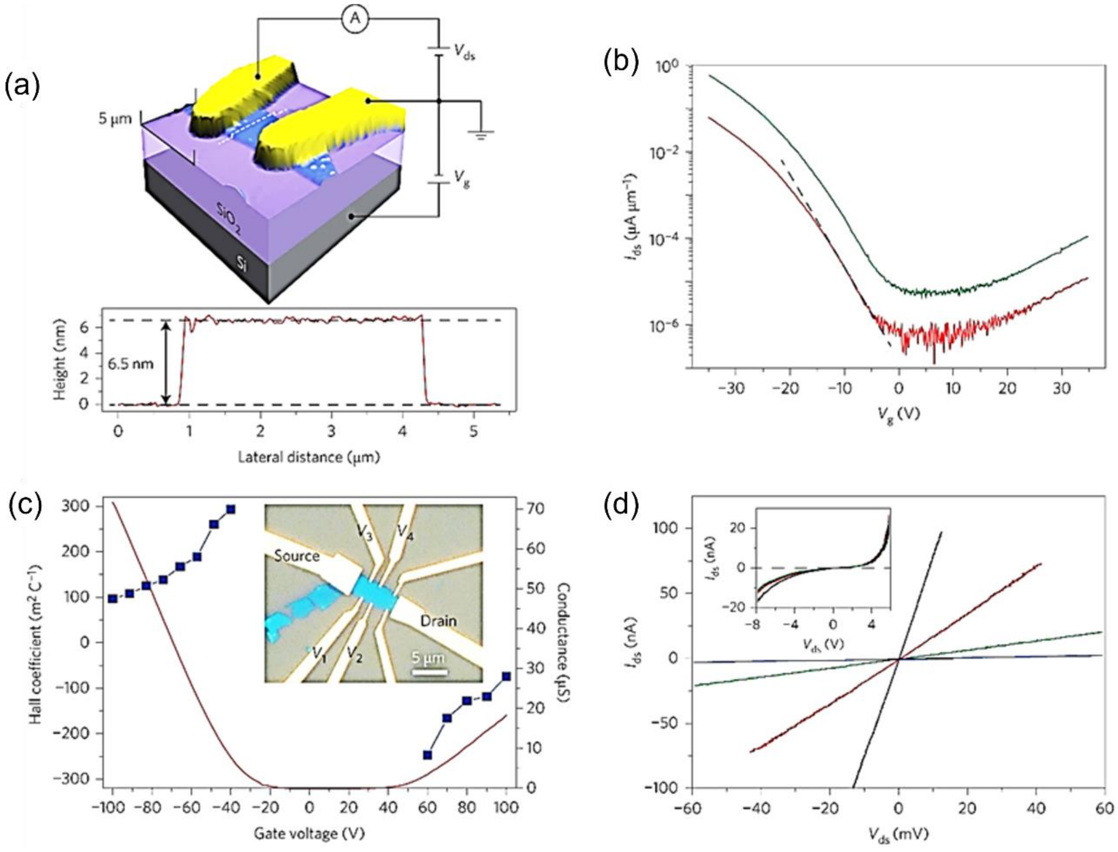

***Figure 5**: (a) Schematic of the FET fabricated from 6.5 nm thick, few-layer phosphorene. (b) Source-drain current obtained from a 5-nm thick device on a Si substrate as a function of gate voltage. (c) Conductance (red curve) and Hall coefficient (blue curve) as a function of gate voltage (d) I–V characteristics of the device. Reproduced with permission[40] copyright 2014, Springer Nature.*

1.3. Transition Metal Dichalcogenides (TMDs)

A class of 2D layered materials known as transition metal dichalcogenides have the generic formula MX_2, where M can be any transition metal atom (such as Ti, Zr, Hf, V, Nb, Ta, Mo, and W) and X can be any chalcogen (such as S, Se, and Te). There have been extensive attemps to investigate the structure, properties and potential applications of MoS_2 ever since Linus Pauling published his initial study on it in 1923[41]. The fabrication of a single-layer MoS_2 based transistor with mobility comparable to graphene nanoribbons[42] and photoluminescence (PL) in ultrathin layers of MoS_2[43] contributed to an increase in interest in this class of material. These TMDs crystallise in different polymorphs and stacking polytypes (1T, 2H, and 3R) shown in **Figure 6**.

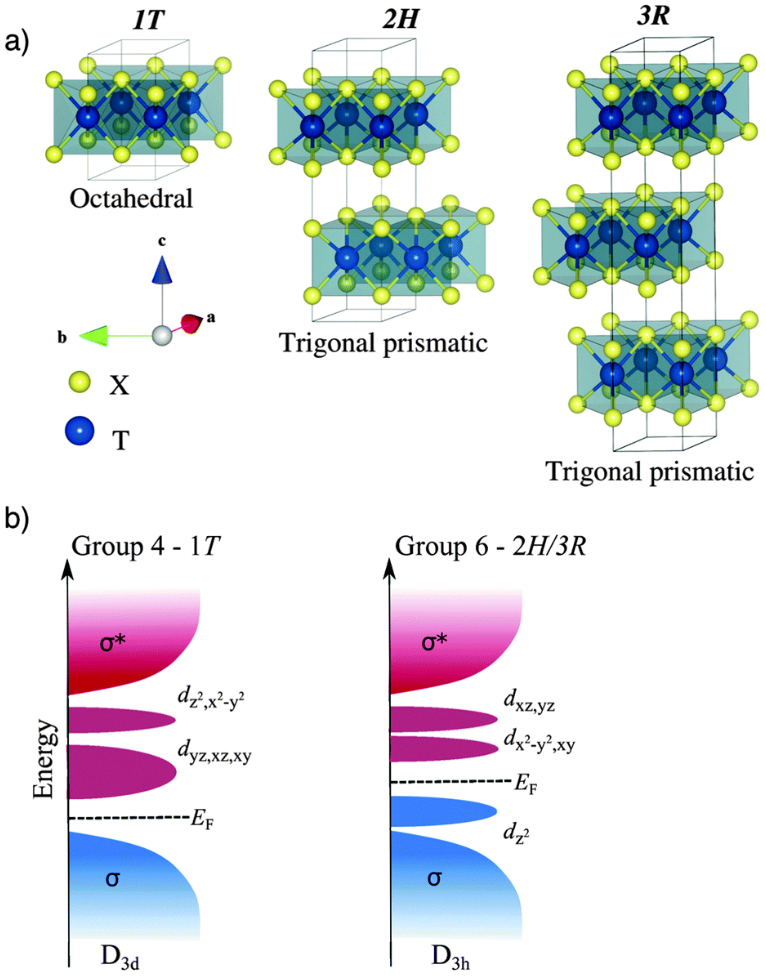

***Figure 6**: (a) Structural illustration of different polymorphs of MoS_2. The alphabets indicate symmetry in the system T: trigonal, H: hexagonal, and R: rhombohedral; and digits indicate the number of layers in the unit. (b) Depiction of the density of states of selected TMDs. Reproduced with permission[46] copyright 2015, Royal Society of Chemistry.*

Letters designate the type of symmetry; T stands for tetragonal (D_{3d} group), H stands for hexagonal (D_{3h} group), and R stands for rhombohedral (C_{3v}^{5} group) in the 1T, 2H, and 3R (**Figure 6a**). The digits represent the number of layers in the crystallographic unit cell. TMDs having monolayer can exhibit into two phases, namely, octahedral 1T and trigonal prismatic 2H and the electronic properties of these layers depend on filled electrons in the nonbonding *d* bands of metals (**Figure 6b**). 2H-$NbSe_2$ and 1T-ReS_2 show metallic nature because of partially filled orbital, whereas 1T-HfS_2, 2H-MoS_2, and 1T-PtS_2 show semiconducting due to fully occupied orbitals[47]. Thermodynamically stable phase of MoX_2 and WX_2 (X = S and Se) are 2H phase which show semiconducting properties[48-51] with an indirect bandgap in the bulk but convert to a direct bandgap semiconductor in the monolayers (**Figure 7**).

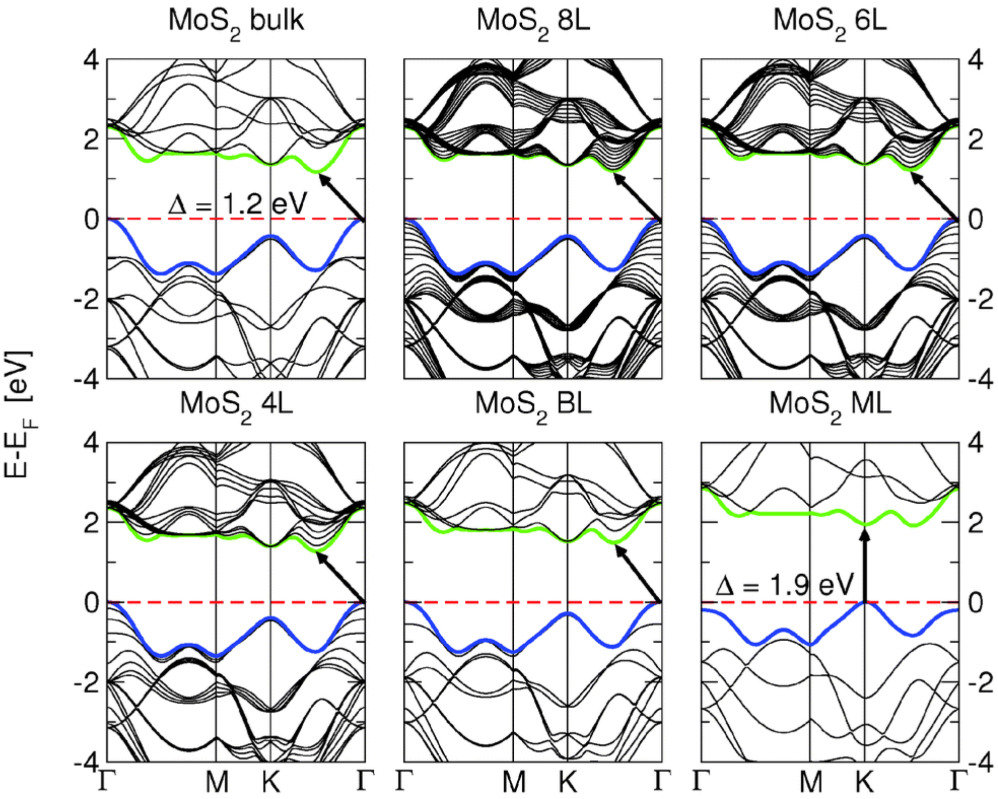

Figure 7*: Change in band structures of MoS_2 transforming from bulk to monolayer. Reproduced with the permission of [46] copyright 2015, Royal Society of Chemistry; and[52], copyright 2011, American Physical Society.*

The change in band structure leads by the quantum confinement which cause to a change in hybridization between d orbitals of metal and p_z orbitals chalcogen[50, 53]. As and example, bulk MoS_2 known to be a indirect bandgap semiconductor with the gap of 1 eV which transforms into a direct bandgap semicondcutor having gap of 1.9 eV in the monolayer (**Figure 7**). This transformation can be seen in PL of the monolayers of MoX_2[43,54] and WX_2[55].

The synthesis of TMDs has been studied for a long time; early research involved the conversion of MoS_2 from MoS_3 by hydrogen reduction[57] or high-temperature solution-based methods[58].

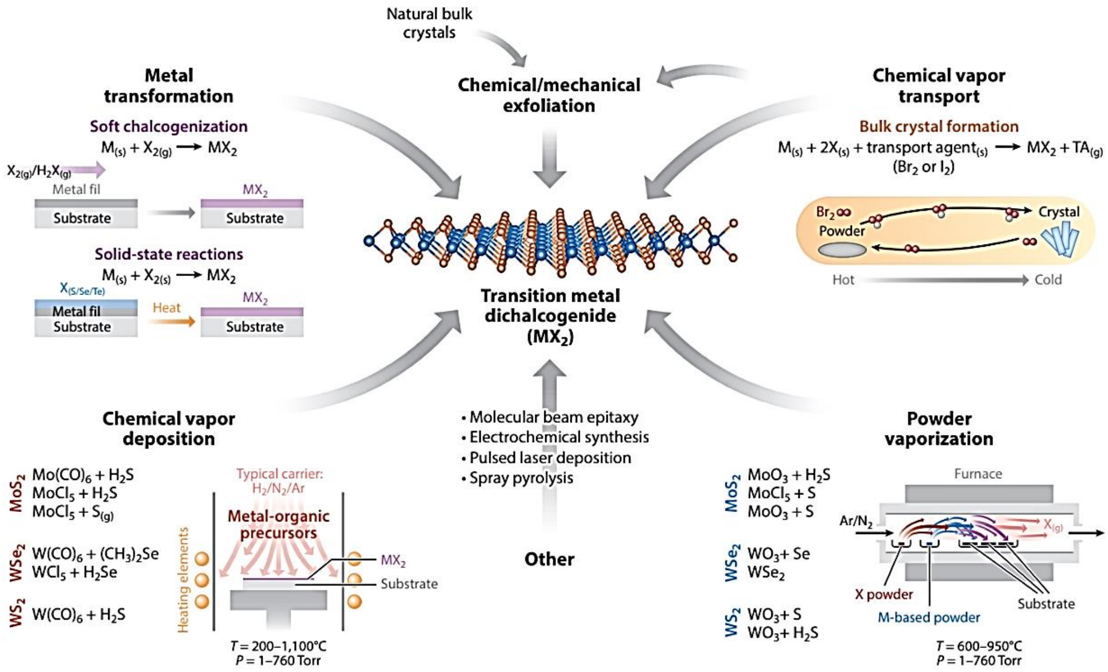

***Figure 8**: Summary of primary growth techniques for the synthesis TMDs. Reproduced with permission[56], Copyright 2015, Annual reviews.*

Although mechanical exfoliation[42] remains the best method, TMDs have been synthesized using several synthetic techniques, including liquid exfoliations[59, 60], powder vaporization[61], wet-chemical synthesis[62], metal transformation, and vapor-phase chemical processes (summarized in **Figure 8**). Due to their ability to control morphology and high scalability, vapor deposition techniques have been thoroughly studied. Chemical vapor transport (CVT) of TaS_2, $TaSe_2$, $MoTe_2$, and WTe_2 has been done using Br_2 or I_2 as transporting agents across a thermal gradient[63]. This process has been remarkably successful for the growth of bulk crystals for MoX_2 and WX_2 (X= S, Se, Te) with the use of stoichiometric vapors of metal and chalcogens[63, 64]. By the tarnishing reaction of appropriate chalcogen's vapor (S or Se) or H_2S, metals of Mo or W have been directly transformed in their TMDs[65, 66]. Vaporization of oxides such as MoO_3 and WO_3 can also produce MX_2 in presence of S/Se or H_2S at 600-950 °C as shown in **Figure 8**. Although the bulk form of TMDs obtained by above mentioned synthetic procedures provide ultrahigh and crystalline materials, processes are unable to fulfill the desires for electronics on the industrial levels. Therefore, numbers of growing processes for the synthesis of thin films of TMDs, including atomic layer deposition (ALD)[67], pulsed laser deposition (PLD)[68] of MoS_2, sputter deposition[69] of WS_x, spin deposition and dip coating[70], molecular beam epitaxy (MBE)[71] of $MoSe_2$, and chemical vapor deposition (CVD). CVD of TMDs has been extensively performed using a variety of precursors such as $MoCl_5$, $Mo(CO)_6$ as Mo sources, WCl_5, $WOCl_5$, $W(CO)_6$ as W sources combined with H_2S, $HS(CH_2)_2SH$, $HSC(CH_3)_3$, $Se(CH_3)_2$ as chalcogen sources as shown in **Figure 8**[72, 73]. Zhou *et al.*[74] reported a library of 2D transition-metal chalcogenides by the salt-assisted CVD method shown in **Figure 9**.

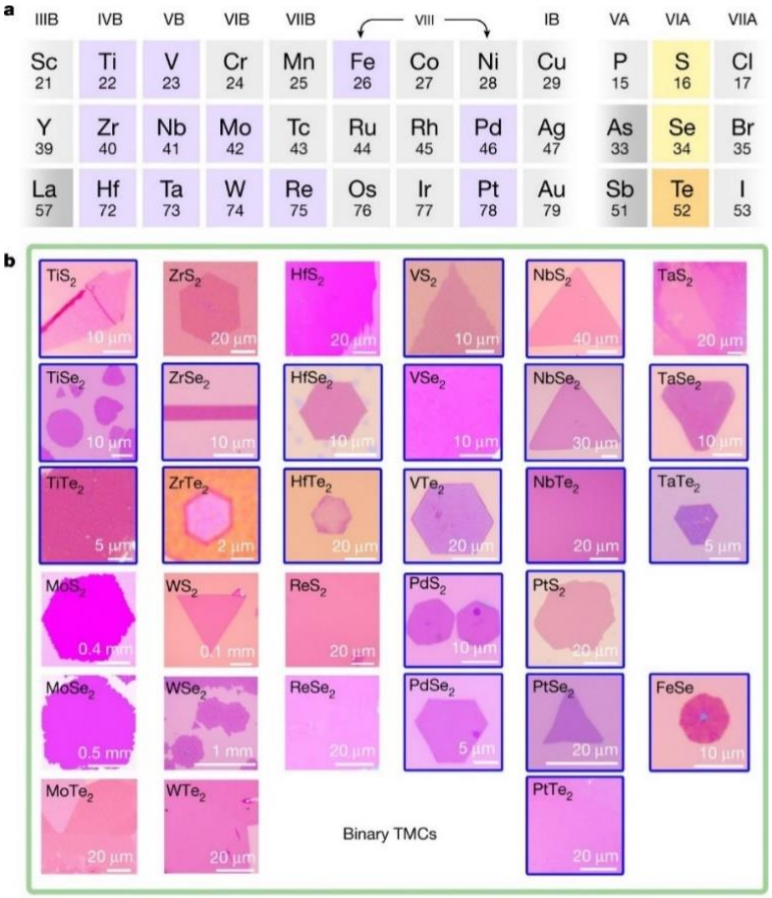

***Figure 9**: (a) Overview of metals and chalcogens those can be used to synthesize layered sulfides, selenides, and tellurides. (b) Optical images of synthesized TMCs. Reproduced with permission[74] copyright 2018, Springer Nature.*

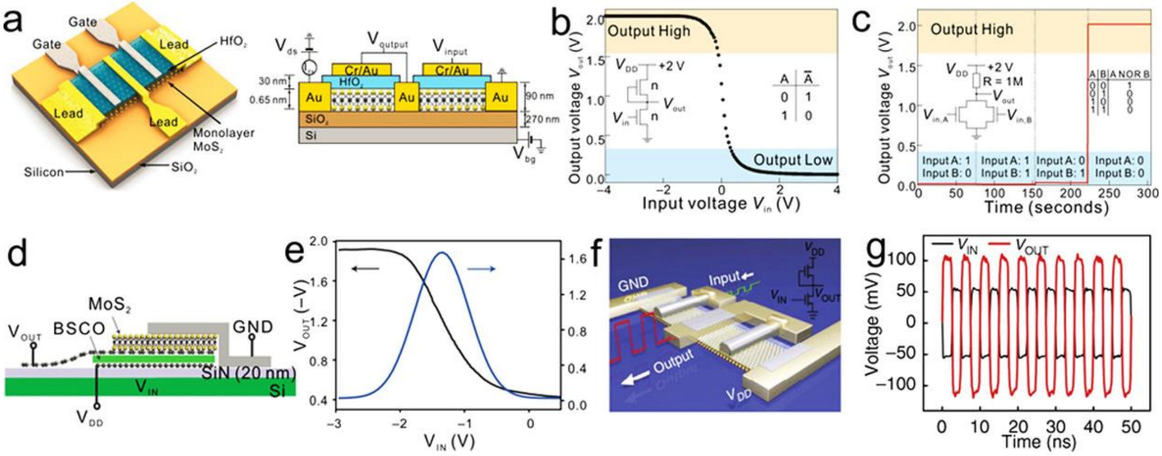

***Figure 10**: MoS$_2$-based electronic circuits such as logic gates and inverters. (a) presents the circuit on monolayer. (b) illustrates an inverter, (c) presents a NOR gate circuit, (d) presents of the vertical stacked inverter, (e) The features of the vertical stacked inverter, (f) shows a gigahertz signal inverter and, (g) show input and output signals of the inverter. Reproduced with permission[75-78], copyright 2011 & 2018, American Chemical Society; copyright 2012, Springer Nature.*

Over the years, researchers have been interested in the fabrication of MoS2-based electronics such as logic gates (**Figure 10a**) containing two or more components to design integrated circuits (ICs). Kis et al. reported n-channel metal-oxide-semiconductor (nMOS) transistors where MoS$_2$ layer has been used as an n-channel, that can work as NOT gates or inverters (**Figure 10b**). Transistors in parallel connections and a resistor of 1 MΩ is assisted as a load and can work as NOR gate (**Figure 10c**)[76]. Duan and co-worker proposed a vertical stacked FET (VFET) based on graphene and MoS$_2$ that could meet two crucial criteria for high current density and high on-to-off current ratio which, as a result of its NOT logic gate behaviour, could be employed as an inverter(**Figure 10d,e**)[77]. **Figure 10f** shows a dual-channel MoS$_2$ layer based FET fabricated which was used as an inverter. **Figure 10g** shows a 200 MHz square wave input signal can be inverted at a direct current bias of 5 V, and the inverted output signal with a relative voltage gain of 2 could be generated from the output electrode at the same operating frequency without any observable delay and that inverter can be used in RF amplifiers[78].

1.4. Non-metallic 2D materials

Carbon Nitrides

Berzelius and Liebig were the first to successfully synthesize carbon nitrides in 1834[79]. Then Franklin again reported a synthesis of carbon nitride in 1922[80]. Franklin proposed strategy to obtain carbon nitrides the de-ammonation of ammono-carbonic acids like melamine. The crystal structure of carbon nitrides studied by Pauling and Sturdivant[81] using X-ray and confirmed the presence of coplanar tri-s-triazine unit (**Figure 11**). Among all the allotropes of carbon nitrides graphitic carbon nitride (g-C_3N_4) is the most stable and widely explored.

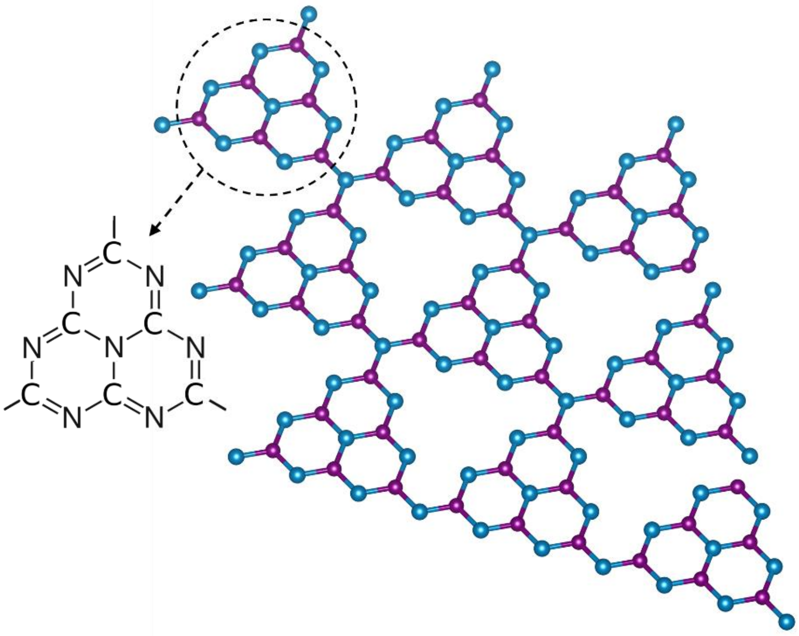

Figure 11: *Tri-s-triazine based 2D structure of g-C_3N_4.*

Most recently developed applications of C_3N_4 include photocatalytic water splitting, carbon dioxide activation, the destruction of contaminants and the disinfection of germs, organic synthesis, and electronic materials and devices. For benzene's Friedal-Crafts reaction, g-C_3N_4 reported as a heterogeneous catalyst by Goettmann *et al.*[83]. Wang *et al.* explored g-C_3N_4 for water splitting in 2009[84]. Theoretical calculation of electronic structure of carbon nitride suggests that water reduction as well as oxidation are energetically feasible. The position of conduction band found to be at −1.4 and valence band found to be at 1.3eV versus NHE (normal hydrogen electrode) at pH 7, respectively with an optical bandgap of 2.7eV. Carbon nitride nanosheets found to be a good condidate for insulating layer for a flexible, metal-free, and rewritable non-volatile memory device, which also includes graphene electrodes produced by direct laser writing[85]. Remarkable successful attempts have been made to use the C_3N_4 in the area of electrochemistry, including batteries such as lithium-ion which show a capacity of $494mAhg^{-1}$ [86], electrochemical hydrogen evolution reaction (HER) which shows a positive onset potential close to Pt, excellent current density of $0.43mAcm^{-2}$, and good cyclic performance with a durability of exceeding 5,000 cycles[87].

Boroncarbonitrides ($B_xC_yN_z$)

A novel class of 2D materials called borocarbonitrides, whose general formula is $B_xC_yN_z$, has a large range of compositional possibilities. These compositions are typically nanosheets made of graphene, BN domains, and potentially BCN rings. $B_xC_yN_z$ compositions include hexagonal networks of C-C, C-N, B-N, and C-B bonds but no N-N or B-B bonds[14] shown in **Figure 12**. If the ratio of BN to carbon is 1:1, the composition of $B_xC_yN_z$ would be BCN.

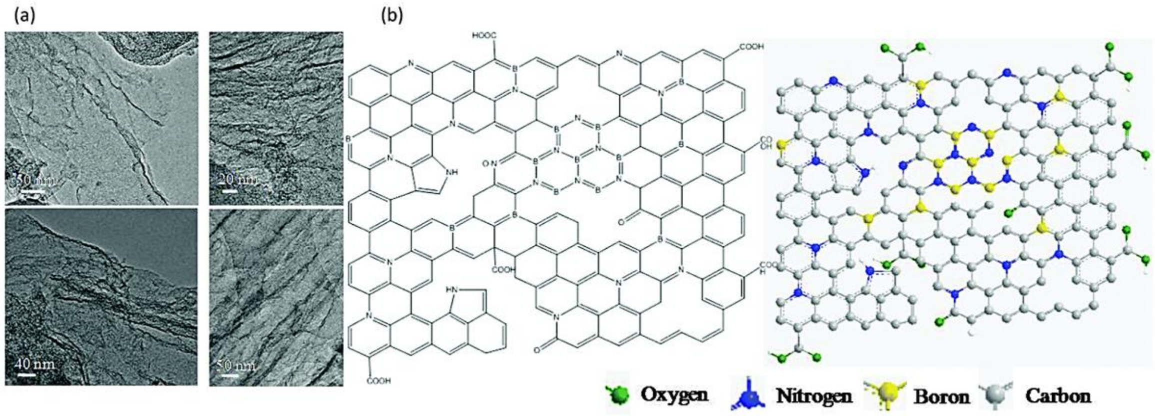

Figure 12: *(a) Transmission electron microscopy (TEM) images of BCN-1. (b) Representation of carbon-rich boroncarbonitride sheets showing the incorporation of boran and nitrogen into the carbon network. Reproduced with permission[88], copyright 2016, Royal Society of Chemistry.*

As the starting material, a close mixture of high surface-area activated charcoal (as C source), boric acid (as B source), and urea (as N source) has been used to synthesize borocarbonitrides, which may contain hexagonal $B_xC_yN_z$ networks with different compositions of graphene and BN domains [88, 89]. The composition of $B_{0.35}C_{0.30}N_{0.35}$ has been reported by Kaner *et al.* with the reaction of CH_4 with NH_3 and BCl_3 at 400–700 °C [90]. Other methods involve CVD to obtain graphene-BN heterojunctions on copper foil using ammonia-borane (NH_3–BH_3) and methane[91]. Boron-nitride-hybridized graphene (h-BNC) was grown on Cu by a thermal catalytic CVD method with CH_4 and ammonia borane as C and BN precursors, respectively[92].

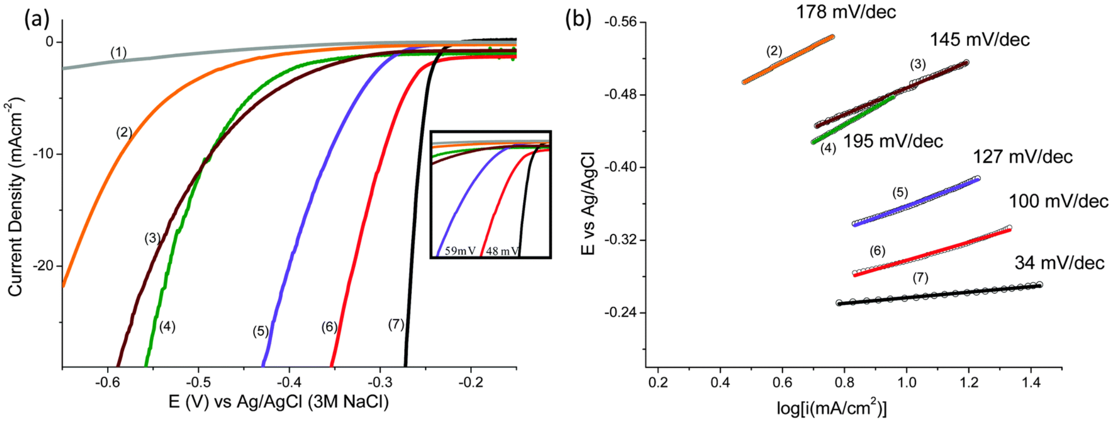

Figure 13: *(a) HER activity of BCN with different compositions. (a) Linear Sweep Voltammetry. (b) Tafel plots. (Numbers 1–6 indicates for BCNs and 7 for Pt/C as working electrodes). Reprinted with permission[88], copyright 2016, Royal Society of Chemistry.*

Chhetri *et al.*[88] reported a carbon-rich BCN as a metal-free catalyst for hydrogen generation with different chemical compositions where BC_7N_2 showed better activity with a positive onset potential of 56 mV vs. RHE and a significant 10 mA cm^{-2} current density at an overpotential of 70 mV, demonstrating BCN an excellent electrocatalytic active material based on compositions at par with Pt shown in **Figure 13**. Tunable B/N codoped BCN[93] and 3D BCN[94] show good oxygen reduction reaction (ORR) activity. BCNs have been reported with high surface areas and adsorption properties for CO_2 gas with 128 wt% at 195 K and 1 atm[89]. BCN is expected to show good supercapacitor properties[95] due to its conducting properties and high surface area. BCN based on urea has reported outstanding supercapacitor characteristics. In an ionic liquid, $BC_{4.5}N$ has a specific capacitance value of 240 F/g as opposed to 178 F/g in an aqueous electrolyte. BCN synthesized by graphene also shows excellent activity with the specific capacitance of 306 F/g [96]. Very recently, Ayyub *et al.* reported the electrochemical reduction of CO_2 on $B_xC_yN_z$ catalysts in an aqueous electrolyte medium[97]. $BC_{1.2}N_{0.8}$ was found to be good catalyst with a CO faradaic efficiency of 98% at -0.45 V and highly selective for CO.

1.5. Functionalization and heterostructures of 2D materials

Electrical modulation and good surface absorption in 2D materials are the results of their unique features such as atomic thinness, van der Waals gap, high crystallinity, and dangling bond surfaces. Although, these features provide many advantages over catalysis and other applications, also responsible to hinder by their limitations.

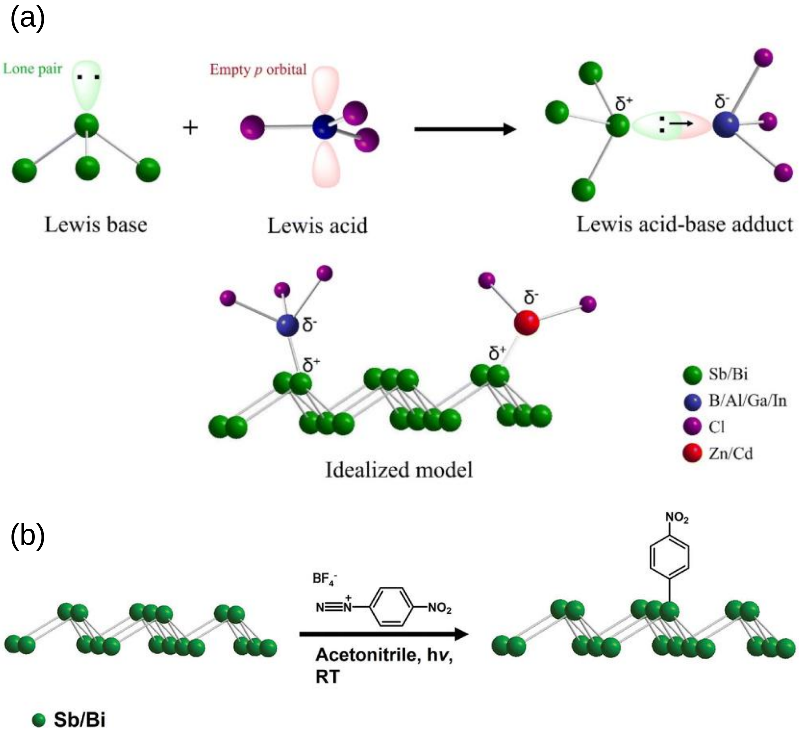

Figure 14: *(a) Representation of the interaction of pnictogens with Lewis acids to form Lewis acid-base adduct. Reprinted with permission[38], copyright 2022, Royal Society of Chemistry (b) Representation of covalent functionalization of pnictogens 2D layered materials with p-nitrobenzenediazonium tetrafluoroborate (p-NBD). Reprinted with permission[108], copyright 2022, John Wiley and Sons.*

For example, atomic-level thinness along with a large surface creates defects on the surface, and very thin layers are susceptible to ambient conditions and degrade by aging. Applications demand exfoliated 2D which involves those defects that reduce the activity or performance. Therefore, to make 2D materials versatile for a long time and efficient, proper treatment or modification of layer/surface is needed. A wide-ranging surface modification has been reported by traditional methods such as foreign elements doping[98], decoration of nanoparticles[99], wrinkling[100] or rolling of sheets[101], defects generations[102], chemical functionalization[103-105], and assembly of other 2D materials so-called heterostructures designs[106, 107]. Very recently, Ayyub *et al.* and Barua *et al.* reported Lewis acid-base adducts formation and covalent functionalization of antimonene and bismuthene sheets, suggesting the tunability of optical properties of the sheets and surface passivation[38, 108] (**Figure 14**).

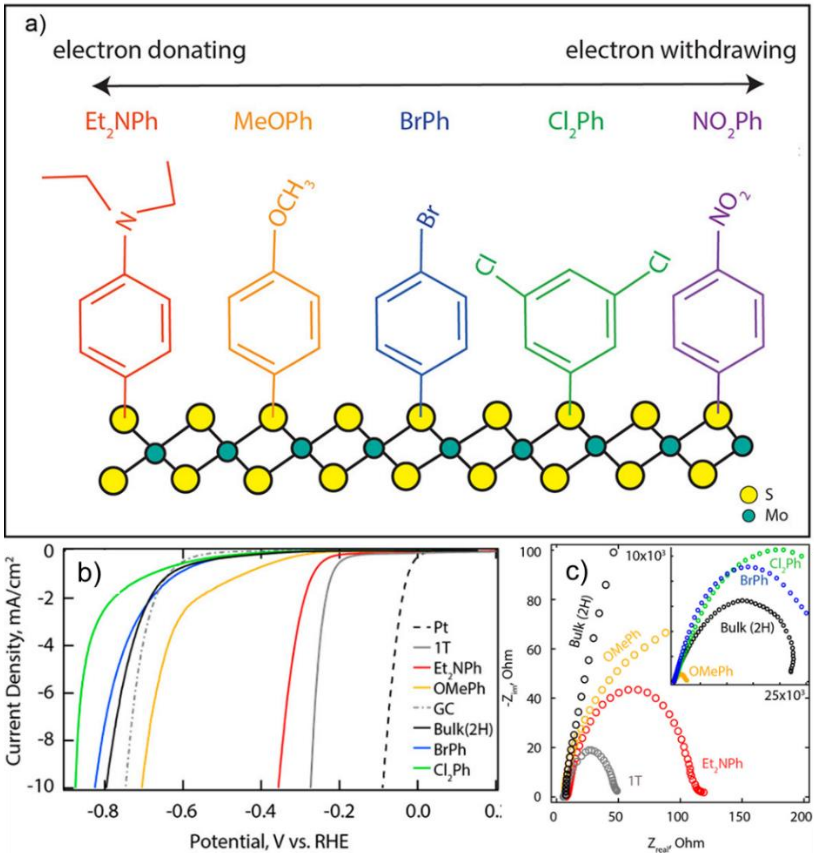

Figure 15: *(a) Representation of the numerous functional groups on 1T MoS_2. (b) Linear sweep voltammograms (LSVs) and (c) Nyquist plots for functionalized MoS_2 sheets. Reprinted with permission[109], copyright 2018, American Chemical Society.*

Antimonene and bismuthene nanosheets were functionalized covalently with diazonium salt and show tunability of the emission of antimonene from 2.23 to 2.18 eV and 2.33 to 2.27 eV for bismuthene sheets. Benson *et al.* reported functionalized 1T MoS_2 with different functional groups having electron-donating and withdrawing capabilities and studied electrochemical HER[109] (**Figure 15**). They observed a systematic shift in overpotential towards lower values (**Figure 15b**). Increase in HER activity was observed as the substituent on the phenyl ring attached to MoS_2 was replaced from the most electron-withdrawing group (which is Cl_2Ph) with the most electron-donating group (which is Et_2NPh). Electrochemical impedance spectra (Nyquist plots in **Figure 15c**) suggests the charge transfer resistance of the functionalized MoS_2 is larger than bulk 2H MoS_2 when the substituent becomes more electron-withdrawing. In addition to quenching of excess charge on MoS_2 layers on functionalization[110], electron-withdrawing groups elimate their electron density and change the electron transfer kinetics so the HER activity has reduced. Moreover the stability of the 1T phase which is its metallic state preserved for several weeks.

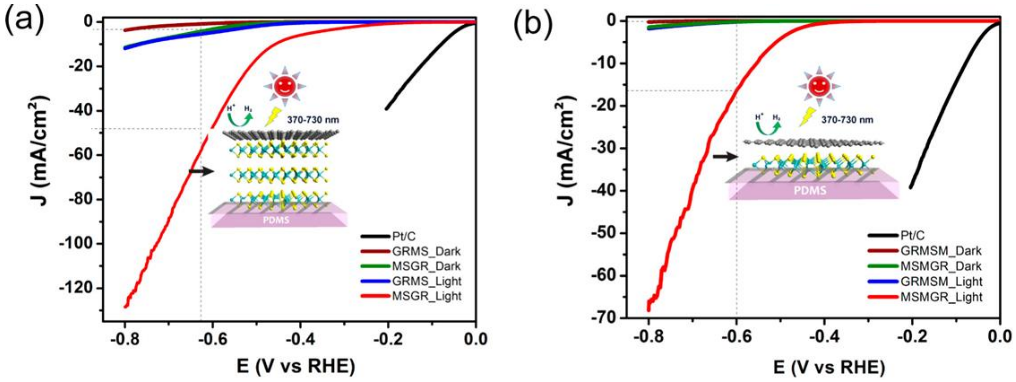

Figure 16: *Photoelectrochemical (PEC) HER activity of (a) heterostructure of graphene–few-layered MoS_2 and (b) heterostructure of graphene–monolayer MoS_2. (MSGR: graphene on top of few-layered MoS_2; GRMS: few-layered MoS_2 on top of graphene; MSMGR: graphene on top of MoS_2 monolayer; and GRMSM: MoS_2 monolayer on top of graphene). Reprinted with permission[111], copyright 2017, American Chemical Society.*

Researchers are discovering intriguing new physics and developing new ultrathin electronics by taking advantage of electrical modulation of the layers individually or by combining them such as zero band conductor graphene with an insulating BN layer to produce novel structures with atomically thin heterostructures[112]. Staking two or more 2D layers results in van ver Waal heterostructures that offer a variety of properties including interfacial quantum phenomena[113]. Heterostructures of different atomic layers are stacked on top of one another, can significantly alter the inherent electrocatalytic and photoelectrochemical activities of individual layers toward particular reactions and even activate a basal plane that would not normally be active in the bulk form[111, 114, 115], therefore shows higher activities than individual layers. **Figure 16** shows the HER activities of different heterostructures of MoS_2 with graphene and their PEC activities [111].

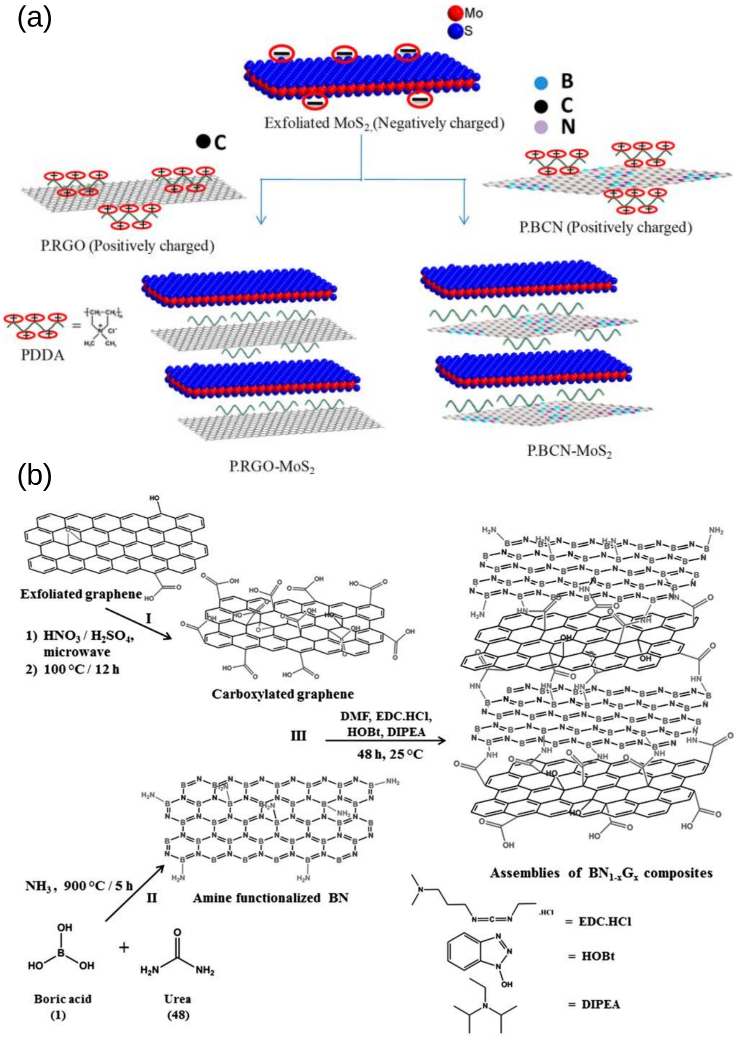

Figure 17: *Representation of the synthesis of nanocomposites (a) P.RGO-*MoS_2 *and P.BCN-*MoS_2*; Reprinted with permission[116], copyright 2020, American Chemical Society and (b) nanocomposites of BN and graphene synthesized by covalently cross-linking. Reprinted with permission[117], copyright 2015, John Wiley and Sons.*

The graphene on the top of MoS_2 (MSGR and MSMGR heterostructures) shows the highest photoresponse and hydrogen evolution activity in both the single- and multilayered MoS_2 samples, which suggests the importance of stacking sequence in heterostructures. Although van der Waals heterostructures show exceptional properties for electronics and catalysis, these need to fabricate complicated and sophisticated methods such as mechanical transfer stacking or CVD process.

Some facile synthesis is also reported, which offers heterostructures by solutions or dispersions and helps to form nanocomposites of functionalized 2D materials also (shown in **Figure 17**). Nanocomposites of boron nitride (BN) and carboxylated graphene ($BN_{1-x}G_x$) reported by Kumar *et al.* [117] using covalent cross-linking employing the carbodiimide reaction show decent performance for gas adsorption, super capacitance and electrocatalyst for oxygen reduction reaction as well. Nanocomposites formed by negatively charged MoS_2 with poly(diallyldimethylammonium chloride) functionalized reduced graphene oxide and boron carbonitride sheets show excellent photocatalytic HER by dye-sensitized method [116]. These reports of heterostructures or nanocomposites open wide scope for further studies in 2D photocatalysts candidates for hydrogen production.

1.6. Photochemical hydrogen production

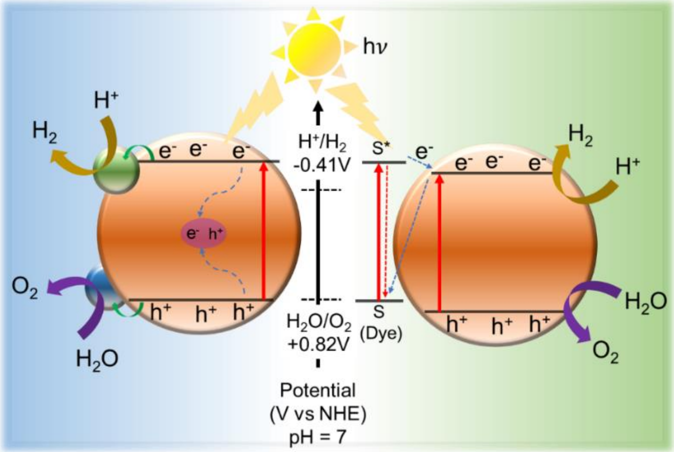

Figure 18: *Graphical representation of splitting of water photocatalytically using photocatalyst, kinetic illustration of electron transfer and recombinations.*

Water can be split in visible light photo catalytically to produes hydrogen gas and oxygen gas by following two redox reactions given below and illustrated in **Figure 18.** The difference between the potentials of the redox reaction of water splitting, H_2/H_2O and H_2O/O_2 half-cell reactions is only 1.23 V.

Reduction half :

$2H^+ + 2e^-$ --------> H_2 (g) $\Delta E° = -0.41V$

Oxidation half :

$2H_2O$ (l) --------> O_2 (g) + $4H^+ + 4e^-$ $\Delta E° = +0.82V$

Overall reaction :

H_2O (l) --------> H_2 (g) + $1/2O_2$ (g) $\Delta E° = 1.23V$, $\Delta G° = +237.2$ kJ/mol

TiO_2 photoelectrodes can split water under UV irradiation, as shown by Honda and Fujishima[118]. Solar illumination of a semiconductor in contact with water is also capable of causing water to undergo photolysis into hydrogen and oxygen. From a thermodynamic point of view, a semiconductor called photocatalyst or light-harvesting material such as photosenstizer (such as dye) absorbs the light radiation and then excitation energy transmitted to water molecule for reduction and oxidation. As shown in **Figure 18,** two approaches can be in a typical splitting process of water: 1) reduction and oxidation of water using only a single photocatalyst, and 2) based on artificial photosynthesis in which a photocatalyst with photosensitizer or two photocatalysts are used for the reduction and oxidation[119]. The potential level of the conduction band minimum (CBM) and valence band maximum (VBM) of the photocatalyst must match the reduction potentials and water oxidation, respectively. The CBM should be lower than the water reduction potential (0.41 V versus normal hydrogen electrode (NHE) at pH 7), whereas the VBM should be higher than the water oxidation potential (0.82 V versus NHE at pH 7). On the absorption of light by photocatalyst electrons excite and jump from the VB to the CB where the reduction of water occurs and holes present in the VB cause the oxidation of water. To ensure effective water splitting, the charge carriers must be separated. Hence, the process of splitting water may be roughly broken down into three steps: 1) light absorption, 2) charge carrier separation, and 3) redox reactions at the catalyst's surface. The thermodynamics and kinetics of the aforementioned processes determine the overall efficiency of photocatalytic water splitting. Catalysts with improved light absorption and effective charge carrier separation have been the subject of extensive investigation in the area of water splitting[119]. Because of tunable band structure, and facinating surface properties, 2D materials are preferred for water splitting. Due to their highly exposed catalytic sites, 2D materials are suited for this purpose since redox reactions at the surface depend on the number of catalytically active sites.

In dye-sensitized hydrogen generation, dye molecules can be excited by solar illustration for example in Eosin Y (EY) based dye sensitize water splitting (**Figure 18**) [120, 60]. On excitation, the dye absorbs visible light and converts into a singlet state (^{1}EY*), and transforms to a low-lying triplet state (^{3}EY*) via intersystem crossing (ISC). This ^{1}EY* species can take an electron from sacrificial agents such as triethanolamine (TEOA) to yield the radical anion of eosin (EY$^{\bullet-}$) and the oxidized form of donor (TEOA$^{\bullet+}$) (shown in **Figure 19**).

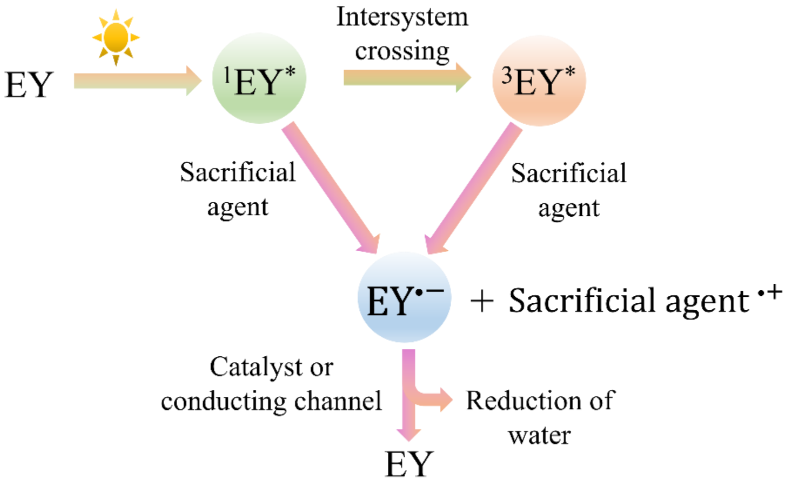

Figure 19: *Proposed electron pathways convoluted in the Eosin Y dye, sacrificial agent, and catalyst system for hydrogen generation in presence of light.*

These $EY^{\bullet-}$ species favorably transfer their electrons to the catalyst directly or via conducting channels (e.g. graphene oxide) to the catalyst due to their electron transport characteristics to reduce water [120, 60]. This kind of method could be beneficial for semiconductors having an indirect band gap or being able to make heterostructures with other conducting materials such as graphene or boron carbon nitrides[116].

1.7. Summary and outlook

The above discussion highlights the basics of two-dimensional materials, their optical, and electronic properties, synthesis methods, and potential applications in electronics, energy production, and storage. Phase selection, Surface modification, functionalization of 2D materials, heterostructures, and nanocomposites have been recently explored for altering the properties of individual layers. Interestingly, cross-linked nanocomposites have been shown well for adsorption and catalysis. In the recent challenges on green energy production, photocatalytic hydrogen production by photocatalysts is playing a crucial role. Therefore, a complete understanding of cross-linked layers of 2D photocatalysts can offer hidden advantages for the photocatalytic hydrogen production field. In the following chapters, the study deals with the synthesis of the active phase of photocatalysts, their covalently cross-linked layers, their photocatalytic hydrogen evolution reaction activities, the role of cross-linked interlayer spaces, and possible mechanisms.

1.8. References

[1] Feynman, R. P. Lecture, Caltech Engineering and Science, 23:5, **1959**, 22-36.

[2] Gupta, A.; Sakthivel, T.; Seal, S. *Prog. Mater. Sci.* **2015**, *73*, 44-126.

[3] Novoselov, K. S.; Geim, A. K.; Morozov, S. V.; Jiang, D.-e.; Zhang, Y.; Dubonos, S. V.; Grigorieva, I. V.; Firsov, A. A. *science* **2004**, *306* (5696), 666-669.

[4] Kim, K. S.; Zhao, Y.; Jang, H.; Lee, S. Y.; Kim, J. M.; Kim, K. S.; Ahn, J.-H.; Kim, P.; Choi, J.-Y.; Hong, B. H.. *nature* **2009**, *457* (7230), 706-710.

[5] Liu, M.; Yin, X.; Ulin-Avila, E.; Geng, B.; Zentgraf, T.; Ju, L.; Wang, F.; Zhang, X. *Nature* **2011**, *474* (7349), 64-67.

[6] Lin, Y. M.; Dimitrakopoulos, C.; Jenkins, K. A.; Farmer, D. B.; Chiu, H. Y.; Grill, A.; Avouris, P. *Science* **2010**, *327* (5966), 662-662.

[7] Deng, M.; Yang, X.; Silke, M.; Qiu, W.; Xu, M.; Borghs, G.; Chen, H. *Sens. Actuators B Chem.* **2011**, *158* (1), 176-184.

[8] Shanmugam, V.; Mensah, R. A.; Babu, K.; Gawusu, S.; Chanda, A.; Tu, Y.; Neisiany, R. E.; Försth, M.; Sas, G.; Das, O. *Part Part Syst Charact* . **2022**, 2200031.

[9] Rao, C. N. R.; Gopalakrishnan, K. *ACS Appl. Mater. Interfaces* **2017**, *9* (23), 19478-19494.

[10] Pinilla, S.; Coelho, J.; Li, K.; Liu, J.; Nicolosi, V. *Nat. Rev. Mater.* **2022**, 1-19.

[11] Vishnoi, P.; Pramoda, K.; Rao, C. N. R. *ChemNanoMat* **2019**, *5* (9), 1062-1091.

[12] Mannix, A. J.; Kiraly, B.; Hersam, M. C.; Guisinger, N. P. *Nat. Rev. Chem.* **2017**, *1* (2), 1-14.

[13] Zhang, K.; Feng, Y.; Wang, F.; Yang, Z.; Wang, J. *J. Mater. Chem. C* . **2017**, *5* (46), 11992-12022.

[14] Kumar, N.; Moses, K.; Pramoda, K.; Shirodkar, S. N.; Mishra, A. K.; Waghmare, U. V.; Sundaresan, A.; Rao, C. N. R. *J. Mater. Chem. A* **2013**, *1* (19), 5806-5821.

[15] Zhu, J.; Xiao, P.; Li, H.; Carabineiro, S. A. C. *ACS Appl. Mater. Interfaces* **2014**, *6* (19), 16449-16465.

[16] Zang, X.; Wang, T.; Han, Z.; Li, L.; Wu, X. *Nano* **2019**, *14* (02), 1930001.

[17] Yin, Z.; Li, H.; Li, H.; Jiang, L.; Shi, Y.; Sun, Y.; Lu, G.; Zhang, Q.; Chen, X.; Zhang, H. *ACS nano* **2012**, *6* (1), 74-80.

[18] Teweldebrhan, D.; Goyal, V.; Balandin, A. A. *Nano Lett.* **2010**, *10* (4), 1209-1218.

[19] Liu, H.; Neal, A. T.; Zhu, Z.; Luo, Z.; Xu, X.; Tománek, D.; Ye, P. D. *ACS nano* **2014**, *8* (4), 4033-4041.

[20] Li, H.; Lu, G.; Wang, Y.; Yin, Z.; Cong, C.; He, Q.; Wang, L.; Ding, F.; Yu, T.; Zhang, H. *small* **2013**, *9* (11), 1974-1981.

[21] Gkountaras, A.; Kim, Y.; Coraux, J.; Bouchiat, V.; Lisi, S.; Barsoum, M. W.; Ouisse, T. *Small* **2020**, *16* (4), 1905784.

[22] Xu, C.; Wang, L.; Liu, Z.; Chen, L.; Guo, J.; Kang, N.; Ma, X.-L.; Cheng, H.-M.; Ren, W. *Nat. Mater.* **2015**, *14* (11), 1135-1141.

[23] Xu, X.; Zhang, Z.; Qiu, L.; Zhuang, J.; Zhang, L.; Wang, H.; Liao, C.; Song, H.; Qiao, R.; Gao, P. *Nat. Nanotechnol.* **2016**, *11* (11), 930-935.

[24] Rao, C. N. R.; Sood, A. K.; Subrahmanyam, K. S.; Govindaraj, A. *Angew. Chem. Int. Ed.* **2009**, *48* (42), 7752-7777.

[25] Phiri, J.; Gane, P.; Maloney, T. C. *Mater. Sci. Eng. B.* **2017**, *215*, 9-28.

[26] Galbiati, M.; Motta, N.; De Crescenzi, M.; Camilli, L. *Appl. Phys. Rev.* **2019**, *6* (4), 041310.

[27] Mannix, A. J.; Zhou, X.-F.; Kiraly, B.; Wood, J. D.; Alducin, D.; Myers, B. D.; Liu, X.; Fisher, B. L.; Santiago, U.; Guest, J. R. *Science* **2015**, *350* (6267), 1513-1516.

[28] Molle, A.; Goldberger, J.; Houssa, M.; Xu, Y.; Zhang, S.-C.; Akinwande, D. *Nat. Mater.* **2017**, *16* (2), 163-169.

[29] Liu, C.-C.; Feng, W.; Yao, Y. *Phys. Rev. Lett.* **2011**, *107* (7), 076802.

[30] Van den Broek, B.; Houssa, M.; Scalise, E.; Pourtois, G.; Afanas'ev, V. V.; Stesmans, A. *2D Mater.* **2014**, *1* (2), 021004.

[31] Tao, L.; Cinquanta, E.; Chiappe, D.; Grazianetti, C.; Fanciulli, M.; Dubey, M.; Molle, A.; Akinwande, D. *Nat. Nanotechnol.* **2015**, *10* (3), 227-231.

[32] Dávila, M. E.; Xian, L.; Cahangirov, S.; Rubio, A.; Le Lay, G. *New J. Phys.* **2014**, *16* (9), 095002.

[33] Zhu, F.-f.; Chen, W.-j.; Xu, Y.; Gao, C.-l.; Guan, D.-d.; Liu, C.-h.; Qian, D.; Zhang, S.-C.; Jia, J.-f. *Nat. Mater.* **2015**, *14* (10), 1020-1025.

[34] Na, J.; Lee, Y. T.; Lim, J. A.; Hwang, D. K.; Kim, G.-T.; Choi, W. K.; Song, Y.-W. *ACS nano* **2014**, *8* (11), 11753-11762.

[35] Vishnoi, P.; Gupta, U.; Pandey, R.; Rao, C. N. R. *J. Mater. Chem. A* **2019**, *7* (12), 6631-6637.

[36] Zhang, S.; Yan, Z.; Li, Y.; Chen, Z.; Zeng, H. *Angew. Chem.* **2015**, *127* (10), 3155-3158.

[37] Hofmann, P. *Prog. Surf. Sci.* **2006**, *81* (5), 191-245.

[38] Barua, M.; Ayyub, M. M.; Acharya, S.; Rao, C. N. R. *Nanoscale* **2022**, *14* (37), 13834-13843.

[39] Takao, Y.; Morita, A. *Physica B+C* **1981**, *105* (1), 93-98.

[40] Li, L.; Yu, Y.; Ye, G. J.; Ge, Q.; Ou, X.; Wu, H.; Feng, D.; Chen, X. H.; Zhang, Y. *Nat. Nanotechnol.* **2014**, *9* (5), 372-377.

[41] Dickinson, R. G.; Pauling, L. *J. Am. Chem. Soc.* **1923**, *45* (6), 1466-1471.

[42] Radisavljevic, B.; Radenovic, A.; Brivio, J.; Giacometti, V.; Kis, A. *Nat. Nanotechnol.* **2011**, *6* (3), 147-150.

[43] Splendiani, A.; Sun, L.; Zhang, Y.; Li, T.; Kim, J.; Chim, C.-Y.; Galli, G.; Wang, F. *Nano letters* **2010**, *10* (4), 1271-1275.

[44] Chia, X.; Eng, A. Y. S.; Ambrosi, A.; Tan, S. M.; Pumera, M. *Chem. Rev.* **2015**, *115* (21), 11941-11966.

[45] Andoshe, D. M.; Jeon, J.-M.; Kim, S. Y.; Jang, H. W. *Electron. Mater. Lett.* **2015**, *11* (3), 323-335.

[46] Kuc, A.; Heine, T. *Chem Soc Rev* **2015**, *44* (9), 2603-2614.

[47] Chhowalla, M.; Shin, H. S.; Eda, G.; Li, L.-J.; Loh, K. P.; Zhang, H. *Nat. Chem.* **2013**, *5* (4), 263-275.

[48] Ataca, C.; Sahin, H.; Ciraci, S. *J. Phys. Chem. C* **2012**, *116* (16), 8983-8999.

[49] Ding, Y.; Wang, Y.; Ni, J.; Shi, L.; Shi, S.; Tang, W. *Phys. B: Condens. Matter.* **2011**, *406* (11), 2254-2260.

[50] Li, T.; Galli, G. *J. Phys. Chem. C* **2007**, *111* (44), 16192-16196.

[51] Kobayashi, K.; Yamauchi, J. *Phys. Rev. B.* **1995**, *51* (23), 17085.

[52] Kuc, A.; Zibouche, N.; Heine, T. *Phys. Rev. B.* **2011**, *83* (24), 245213.

[53] Mattheiss, L. F. *Phys. Rev. B.* **1973**, *8* (8), 3719.

[54] Tongay, S.; Zhou, J.; Ataca, C.; Lo, K.; Matthews, T. S.; Li, J.; Grossman, J. C.; Wu, J. *Nano letters* **2012**, *12* (11), 5576-5580.

[55] Zhao, W.; Ghorannevis, Z.; Chu, L.; Toh, M.; Kloc, C.; Tan, P.-H.; Eda, G. *ACS nano* **2013**, *7* (1), 791-797.

[56] Das, S.; Robinson, J. A.; Dubey, M.; Terrones, H.; Terrones, M. *Annu. Rev. Mater. Res.* **2015**, 1-27.

[57] Eggertsen, F. T.; Roberts, R. M. *J. Phys. Chem. A.* **1959**, *63* (11), 1981-1982.

[58] Arutyunyan, L. A.; Khurshud, E. K. *Geochem. Int.* **1966**, *3* (3), 479.

[59] Gupta, U.; Naidu, B. S.; Maitra, U.; Singh, A.; Shirodkar, S. N.; Waghmare, U. V.; Rao, C. N. R. *APL Mater.* **2014**, *2* (9), 092802.

[60] Maitra, U.; Gupta, U.; De, M.; Datta, R.; Govindaraj, A.; Rao, C. N. R. *Angew. Chem. Int. Ed.* **2013**, *52* (49), 13057-13061.

[61] Gutiérrez, H. R.; Perea-López, N.; Elías, A. L.; Berkdemir, A.; Wang, B.; Lv, R.; López-Urías, F.; Crespi, V. H.; Terrones, H.; Terrones, M. *Nano letters* **2013**, *13* (8), 3447-3454.

[62] Lv, R.; Robinson, J. A.; Schaak, R. E.; Sun, D.; Sun, Y.; Mallouk, T. E.; Terrones, M. *Acc. Chem. Res.* **2015**, *48* (1), 56-64.

[63] Al-Hilli, A. A.; Evans, B. L. *J. Cryst. Growth* **1972**, *15* (2), 93-101.

[64] Agarwal, M. K.; Reddy, K. N.; Patel, H. B. *J. Cryst. Growth* **1979**, *46* (1), 139-142.

[65] Hadouda, H.; Pouzet, J.; Bernede, J. C.; Barreau, A. *Mater. Chem. Phys.* **1995**, *42* (4), 291-297.

[66] Khelil, A.; Essaidi, H.; Bernede, J. C.; Bouacheria, A.; Pouzet, J. *J. Condens. Matter Phys.* **1994**, *6* (41), 8527.

[67] Sreedhara, M. B.; Gope, S.; Vishal, B.; Datta, R.; Bhattacharyya, A. J.; Rao, C. N. R. *J. Mater. Chem. A.* **2018**, *6* (5), 2302-2310.

[68] Donley, M. S.; Murray, P. T.; McDevitt, N. T. *MRS Online Proceedings Library (OPL)* **1988**, *140*.

[69] Regula, M.; Ballif, C.; Moser, J. H.; Lévy, F. *Thin Solid Films* **1996**, *280* (1-2), 67-75.

[70] Pütz, J.; Aegerter, M. A. *Thin Solid Films* **1999**, *351* (1-2), 119-124.

[71] Ohuchi, F. S.; Shimada, T.; Parkinson, B. A.; Ueno, K.; Koma, A. *J. Cryst. Growth* **1991**, *111* (1-4), 1033-1037.

[72] Hofmann, W. K. *J. Mater. Sci.* **1988**, *23* (11), 3981-3986.

[73] Boscher, N. D.; Carmalt, C. J.; Palgrave, R. G.; Gil-Tomas, J. J.; Parkin, I. P. *Chem. Vap. Depos.* **2006**, *12* (11), 692-698.

[74] Zhou, J.; Lin, J.; Huang, X.; Zhou, Y.; Chen, Y.; Xia, J.; Wang, H.; Xie, Y.; Yu, H.; Lei, J. *Nature* **2018**, *556* (7701), 355-359.

[75] Zeng, M.; Xiao, Y.; Liu, J.; Yang, K.; Fu, L. *Chem. Rev.* **2018**, *118* (13), 6236-6296.

[76] Radisavljevic, B.; Whitwick, M. B.; Kis, A. *ACS nano* **2011**, *5* (12), 9934-9938.

[77] Yu, W. J.; Li, Z.; Zhou, H.; Chen, Y.; Wang, Y.; Huang, Y.; Duan, X. *Nat. Mater.* **2013**, *12* (3), 246-252.

[78] Cheng, R.; Jiang, S.; Chen, Y.; Liu, Y.; Weiss, N.; Cheng, H.-C.; Wu, H.; Huang, Y.; Duan, X. *Nat. Commun.* **2014**, *5* (1), 1-9.

[79] Liebig, J. v. *Ann. Pharm* **1834**, *10* (10), 10.

[80] Franklin, E. C. *J. Am. Chem. Soc.* **1922**, *44* (3), 486-509.

[81] Pauling, L.; Sturdivant, J. H. *Proc. Natl. Acad. Sci.* **1937**, *23* (12), 615-620.

[82] Ayyub, M. M.; Singh, R.; Rao, C. N. R. *Sol. RRL* **2020**, *4* (8), 2000050.

[83] Goettmann, F.; Fischer, A.; Antonietti, M.; Thomas, A. *Chem. Commun.* **2006**, (43), 4530-4532.

[84] Wang, X.; Maeda, K.; Thomas, A.; Takanabe, K.; Xin, G.; Carlsson, J. M.; Domen, K.; Antonietti, M. *Nat. Mater.* **2009**, *8* (1), 76-80.

[85] Zhao, F.; Cheng, H.; Hu, Y.; Song, L.; Zhang, Z.; Jiang, L.; Qu, L. *Sci. Rep.* **2014**, *4* (1), 1-7.

[86] Li, X.; Liu, J.; Zhang, Y.; Li, Y.; Liu, H.; Meng, X.; Yang, J.; Geng, D.; Wang, D.; Li, R. *J. Power Sources.* **2012**, *197*, 238-245.

[87] Duan, J.; Chen, S.; Jaroniec, M.; Qiao, S. Z. *ACS nano* **2015**, *9* (1), 931-940.

[88] Chhetri, M.; Maitra, S.; Chakraborty, H.; Waghmare, U. V.; Rao, C. N. R. *Energy Environ. Sci.* **2016**, *9* (1), 95-101.

[89] Kumar, N.; Subrahmanyam, K. S.; Chaturbedy, P.; Raidongia, K.; Govindaraj, A.; Hembram, K. P. S. S.; Mishra, A. K.; Waghmare, U. V.; Rao, C. N. R. *ChemSusChem* **2011**, *4* (11), 1662-1670.

[90] Kaner, R. B.; Kouvetakis, J.; Warble, C. E.; Sattler, M. L.; Bartlett, N. *Mater. Res. Bull.* **1987**, *22* (3), 399-404.

[91] Levendorf, M. P.; Kim, C.-J.; Brown, L.; Huang, P. Y.; Havener, R. W.; Muller, D. A.; Park, J. *Nature* **2012**, *488* (7413), 627-632.

[92] Ci, L.; Song, L.; Jin, C.; Jariwala, D.; Wu, D.; Li, Y.; Srivastava, A.; Wang, Z. F.; Storr, K.; Balicas, L. *Nat. Mater.* **2010**, *9* (5), 430-435.

[93] Wang, S.; Zhang, L.; Xia, Z.; Roy, A.; Chang, D. W.; Baek, J. B.; Dai, L. *Angew. Chem. Int. Ed.* **2012**, *51* (17), 4209-4212.

[94] Xue, Y.; Yu, D.; Dai, L.; Wang, R.; Li, D.; Roy, A.; Lu, F.; Chen, H.; Liu, Y.; Qu, J. *Phys. Chem. Chem. Phys.* **2013**, *15* (29), 12220-12226.

[95] Gopalakrishnan, K.; Moses, K.; Govindaraj, A.; Rao, C. N. R. *Solid State Commun.* **2013**, *175*, 43-50.

[96] Sreedhara, M. B.; Gopalakrishnan, K.; Bharath, B.; Kumar, R.; Kulkarni, G. U.; Rao, C. N. R. *Chem. Phys. Lett.* **2016**, *657*, 124-130.

[97] Ayyub, M. M.; Rao, C. N. R. *Chem. Mater.* **2022**, *34* (14), 6626-6635.

[98] Loh, L.; Zhang, Z.; Bosman, M.; Eda, G. *Nano Res.* **2021**, *14* (6), 1668-1681.

[99] Wang, Z.; Ping, Y.; Fu, Q.; Pan, C. *MRS Adv.* **2018**, *3* (15-16), 849-854.

[100] Chen, W.; Gui, X.; Yang, L.; Zhu, H.; Tang, Z. *Nanoscale Horiz.* **2019**, *4* (2), 291-320.

[101] Deng, W.; You, C.; Chen, X.; Wang, Y.; Li, Y.; Feng, B.; Shi, K.; Chen, Y.; Sun, L.; Zhang, Y. *Small* **2019**, *15* (30), 1901544.

[102] Lin, Z.; Carvalho, B. R.; Kahn, E.; Lv, R.; Rao, R.; Terrones, H.; Pimenta, M. A.; Terrones, M. *2D Materials* **2016**, *3* (2), 022002.

[103] Bottari, G.; Herranz, M. Á.; Wibmer, L.; Volland, M.; Rodríguez-Pérez, L.; Guldi, D. M.; Hirsch, A.; Martín, N.; D'Souza, F.; Torres, T. *Chem Soc Rev* **2017**, *46* (15), 4464-4500.

[104] Jeong, J. H.; Kang, S.; Kim, N.; Joshi, R. K.; Lee, G.-H. *Phys. Chem. Chem. Phys.* **2022**.

[105] Brill, A. R.; Koren, E.; de Ruiter, G. *J. Mater. Chem. C* . **2021**, *9* (35), 11569-11587.

[106] Novoselov, K. S.; Mishchenko, o. A.; Carvalho, o. A.; Castro Neto, A. H. *Science* **2016**, *353* (6298), aac9439.

[107] Solís-Fernández, P.; Bissett, M.; Ago, H. *Chem Soc Rev* **2017**, *46* (15), 4572-4613.

[108] Ayyub, M. M.; Barua, M.; Acharya, S.; Rao, C. N. R. *Small* **2022**, *18* (38), 2203554.

[109] Benson, E. E.; Zhang, H.; Schuman, S. A.; Nanayakkara, S. U.; Bronstein, N. D.; Ferrere, S.; Blackburn, J. L.; Miller, E. M. *J. Am. Chem. Soc.* **2018**, *140* (1), 441-450.

[110] Knirsch, K. C.; Berner, N. C.; Nerl, H. C.; Cucinotta, C. S.; Gholamvand, Z.; McEvoy, N.; Wang, Z.; Abramovic, I.; Vecera, P.; Halik, M. *ACS nano* **2015**, *9* (6), 6018-6030.

[111] Biroju, R. K.; Das, D.; Sharma, R.; Pal, S.; Mawlong, L. P. L.; Bhorkar, K.; Giri, P. K.; Singh, A. K.; Narayanan, T. N. *ACS Energy Lett.* **2017**, *2* (6), 1355-1361.

[112] Geim, A. K.; Grigorieva, I. V. *Nature* **2013**, *499* (7459), 419-425.

[113] Dean, C. R.; Wang, L.; Maher, P.; Forsythe, C.; Ghahari, F.; Gao, Y.; Katoch, J.; Ishigami, M.; Moon, P.; Koshino, M. *Nature* **2013**, *497* (7451), 598-602.

[114] Yu, X.; Zhao, G.; Gong, S.; Liu, C.; Wu, C.; Lyu, P.; Maurin, G.; Zhang, N. *ACS Appl. Mater. Interfaces* **2020**, *12* (22), 24777-24785.

[115] Biroju, R. K.; Pal, S.; Sharma, R.; Giri, P. K.; Narayanan, T. N. *Nanotechnology* **2017**, *28* (8), 085101.

[116] Pramoda, K.; Servottam, S.; Kaur, M.; Rao, C. N. R. *ACS Appl. Nano Mater.* **2020**, *3* (2), 1792-1799.

[117] Kumar, R.; Gopalakrishnan, K.; Ahmad, I.; Rao, C. N. R. *Adv. Funct. Mater.* **2015**, *25* (37), 5910-5917.

[118] Fujishima, A.; Honda, K. *Nature* **1972**, *238* (5358), 37-38.

[119] Rao, C. N. R.; Lingampalli, S. R. *Small* **2016**, *12* (1), 16-23.

[120] Lewandowska-Andrałojć, A.; Larowska, D.; Gacka, E.; Pedzinski, T.; Marciniak, B. *J. Phys. Chem. C.* **2020**, *124* (5), 2747-2755.

Chapter 2

Synthesis of 1T Phase of MoX_2 (X = S, Se) by Solvo- and Hydro-thermal Methods for Photochemical Hydrogen Evolution Reaction

Summary

MoS_2 and $MoSe_2$ exhibit very low photocatalytic activity for the hydrogen evolution reaction (HER) in their stable semiconducting 2H phase. The metallic 1T forms of MoS_2 and $MoSe_2$ produced via lithium intercalation followed by exfoliation show comparable higher photocatalytic HER activity in contrast to the 2H forms. Unfortunately, this 1T phase prepared by lithium intercalation are unstable.

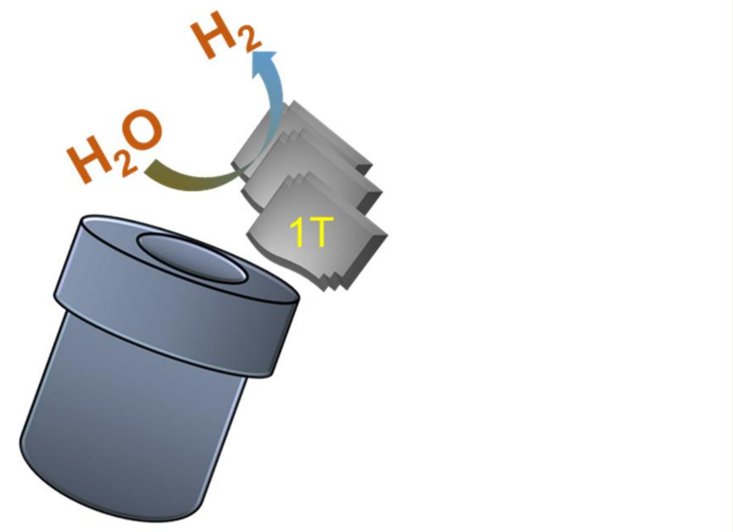

In order to overcome this stability issue, we prepared 1T forms of $MoSe_2$ and MoS_2 by solvothermal or hydrothermal methods. The prepared samples are quite stable and exhibit good photochemical activity for HER.

Paper based on this work has appeared in *J. Chem. Sci.* **2018**, 130, 131.

2.1. Introduction

After the discovery of graphene, a significant attraction has been observed in two-dimensional (2D) materials owing to their potential application in nano-electronics, catalysis, energy production, and energy storage[1-7]. Among all other 2D materials beyond graphene, MoS_2 and $MoSe_2$ have come up with excellent candidates for energy generation and are environment friendly because of their chemical properties and electrochemical properties[8-11]. The artificial photosynthesis process has been established as a promising method for water splitting and hydrogen or oxygen generation[12-15]. These transition metal dichalcogenides (MoS_2 and $MoSe_2$) are well-promising candidates for water splitting[16-19].

As discussed in chapter 1, based on atomic staking, it exists with than one polytypes-namely 1T, 2H, and 3R of MoS_2[20, 21]. The semiconducting 2H phase is in its most stable form and found in the nature as its mineral molybdenite whereas 1T-MoS_2 can be synthetically prepared by many methods[22]. The basal planes of the 2H phase are chemically inert so only edges are confirmed to be active[23]. But in 1T MoS_2 is found to be metastable but more active than the 2H phase due to the availability of active sites of both the edges and basal planes[9, 24]. The 1T phase of MoS_2 also shows very high properties such as chemical activity, and the enlarged interlayer distance compared to the semiconducting phase[25].

1T-MoS_2 can be synthesized by chemical exfoliation in water followed by intercalation with lithium[26, 27] and other alkali metals into the 2H phase, But this process is somewhat complicated and needs safety[28]. Even the metallic phase synthesized by this intercalation is not so stable and eventually converts back to the 2H phase again due to S-S van der Waals interaction which causes restacking of the sheets[29].

Similarly, 1T-$MoSe_2$ also have been explored as a good catalyst as well, even with higher activity than MoS_2[30]. Since $MoSe_2$ has high metallic character and know to have lower gibbs free energy for hydrogen adsorption, It allows the facial exchange of electrons compared to MoS_2 and and know to be batter photocatalyst that MoS_2. Over the years, many attempts have been made to synthesize the 1T phase and tried to stabilize from the top-down and bottom-up approaches as well[22, 28].

Top-down methos predominantly depend on the reversible transition of 2H phase to 1T phase in MoS_2. Many chemical methods have been explored to obtain 1T phase from MoS_2 bulk via n-butyl lithium and used for energy applications[31]. The electrochemical method[32], a physical method by electron beam[33], and strain engineering[34] also have been successfully implemented to achieve the 1T phase. Decent literature is also available on bottom-up synthetic methods via solvothermal[35, 36] and hydrothermal[37] processes. Although, a remarkable success to produce hydrogen by 1T MoS_2 has been reported via electrochemical[29, 38] and photo-electrochemical[39] methods. But to save electricity, a simple and low-cost method is still needed, so the photochemical process can be a good approach. Contrary to a 2H phase which is semiconducting and forms an electron-hole pair by light illumination, 1T-phase of MoS_2 is a metallic in nature so it can not be excited by light. Though, coupling this metallic phase with some other photo absorber can enhance the response of light and enhance the photoinduced hydrogen production, which can be endorsed to the increased number of electrons available for water reduction.

We must recall that 1T- $MoSe_2$ nanosheets are better than 1T-MoS_2 as catalysts in the production of hydrogen photochemically[30], so it will be of considerable interest to investigate HER activity of $MoSe_2$ and compare with 1T MoS_2 synthesized by simple routes.

2.2. Scope of present investigation

We have explored how the metallic 1T forms of MoS_2 and $MoSe_2$ were synthesized using easy hydrothermal and solvothermal methods. It should be emphasized that due to differences in surface characteristics, the 1T forms of Mo dichalcogenides prepared solvothermally or hydrothermally are not predicted to be the same as the 1T forms prepared via Li-intercalation and exfoliation. So the HER activities and stabilities of solvothermally or hydrothermally synthesized samples are found to be different.

2.3. Experimental

Materials

$MoCl_5$ (from Alfa Aesar, 99% purity), selenourea (Alfa Aesar, 99% purity), CH_3CSNH_2 (Loba Chemie, 99% purity), DMF (SD Fine chemicals, 99% purity), $NaMoO_4{\cdot}2H_2O$ (Merck, 99% purity), and $CS(NH_2)_2$ (SD Fine chemicals, 99% purity).

(i) Synthesis of stable 1T phases (Scheme 1):

Solvothermal synthesis of 1T-MoS_2 and 1T-$MoSe_2$

1 mmol of $MoCl_5$ as a Mo source and 10.1 mmol of thioacetamide (CH_3CSNH_2) as a sulfur source were dissolved in 30 mL of DMF. The solution was stirred for 30 min and then transferred to a Teflon-lined autoclave with the capacity of 25 mL. Then the autoclave was heated at 200 °C for 30 hours[40].

In the same way, 1T-$MoSe_2$ was also prepared in DMF solvent taking 0.1 mmol of $MoCl_5$, and 3 mmol of selenourea as a selenium source dissolved in 20 mL of DMF. This solution was also stirred for 30 min and transferred to a 25 mL Teflon-lined autoclave heated up to 200 °C for 48 hours. Then the autoclave was removed form oven and allowed to cool to room temperature, and the product was washed several times with water and ethanol and dried at 60 °C under vacuum.

Hydrothermal synthesis of 1T-MoS_2 and 1T-$MoSe_2$

1T-MoS_2 was synthesized hydrothermally by dissolving 1 mmol of $NaMoO_4{\cdot}2H_2O$ and 3 mmol of thiourea in a mixture of water and propionic acid (2:1). The solution was magnetically stirred for 30 min and transferred into Teflon-lined autoclave and then heated at 200 °C for 4 hours[37].

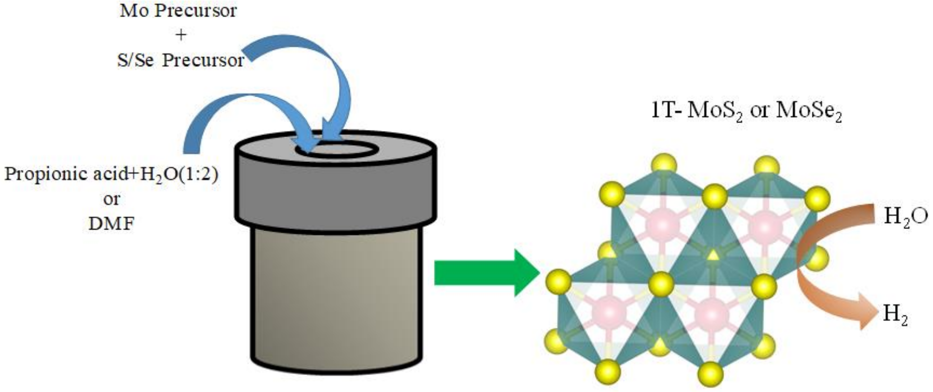

Scheme 1: *Synthesis of 1T phases of MoX_2 via solvo- or hydro-thermal method.*

To synthesize 1T-$MoSe_2$ selenourea was used as a se source. 1T-$MoSe_2$ was synthesized by dissolving 1 mmol of $NaMoO_4\cdot 2H_2O$ and 3 mmol of selenourea in a mixture of water and propionic acid in the ratio of 2:1. The solution was stirred for 30 min and then transferred into a Teflon-lined autoclave having capacity of 25 mL and heated at 200 °C for 4 h. On the completion of reaction, autoclave was removed and allowed to cool and the product was washed several times with water and alcohol and dried at 60 °C in a vacuum oven for 24 h.

(ii) Characterizations:

High-resolution TEM (HRTEM) was obtained with FEI Titan aberration-corrected electron microscopy. Raman spectra were collected with Jobin Yvon LabRam HR spectrometer using Ar-laser ($\lambda = 514.5$ nm).

(iii) Photocatalytic hydrogen evolution reaction (HER) study:

Scheme 2 demonstrates the principle of the HER method we used for hydrogen evolution studies. it suggests Eosin Y dye excites under light and converts to singlet state EY^{1*} and then goes to low-lying triplet state EY^{3*}. EY^{3*} becomes the highly reducing negatively charged state (EY^-) in the presence of triethanolamine (TEOA). The electron from the reducing species is transferred to the catalyst for hydrogen evolution reaction[27]. 2.5 mg of the catalyst was dispersed by sonication in an aqueous solution of triethanolamine (15% v/v, 48 mL) in a cylindrical glass vessel. 14 µmol Eosin Y dye was added as a sensitizer. This vessel was illuminated with a halogen lamp (100 W) under constant magnetically stirring. The evolved gas was manually collected and analyzed with a gas chromatograph PerkinElmer ARNL 580C equipped with a thermal conductivity detector.

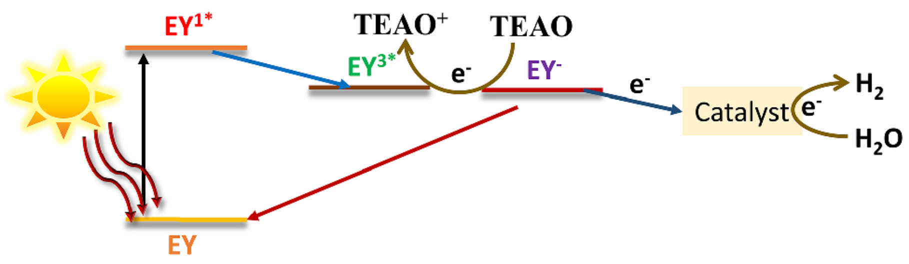

Scheme 2: *Simplified electronic state diagram of Eosin Y and plausible mechanism of H_2 reaction.*

2.4. Results and Discussion

The stable 1T-phase of MoS_2 and $MoSe_2$ were synthesized by solvothermal and hydrothermal routes. The synthetic procedures have been described in the experimental section. The as-synthesized samples were characterized by Raman spectroscopy. The Raman spectrum of 1T-MoS_2 synthesized via a solvothermal (DMF) route is shown in **Figure 1a**. The characteristic J_1, J_2, and J_3 bands of 1T-MoS_2 are at 147, 236, and 336 cm^{-1} respectively. The A_g^1 band characteristic of the 2H-phase has a very low intensity (**Figure 1a**) suggesting that the sample consists predominantly of the 1T phase. The intensity of the A_g^1 peak increases over long periods indicating slow conversion from 1T to 2H-phase (**Figures 1a and 2**). A_g^1, E_g^1, and E_{2g}^1 peaks appear due to S atom and Mo+S atoms vibrations in the direction of the *c*-axis and basal planes, respectively[41, 42]. These peaks also exist in the 2H phase. These additional J_1, J_2, and J_3 peaks are due to the results of superlattices which form in the basal planes of 1T MoS_2 and can be explained by the zone-folding mechanism[43].

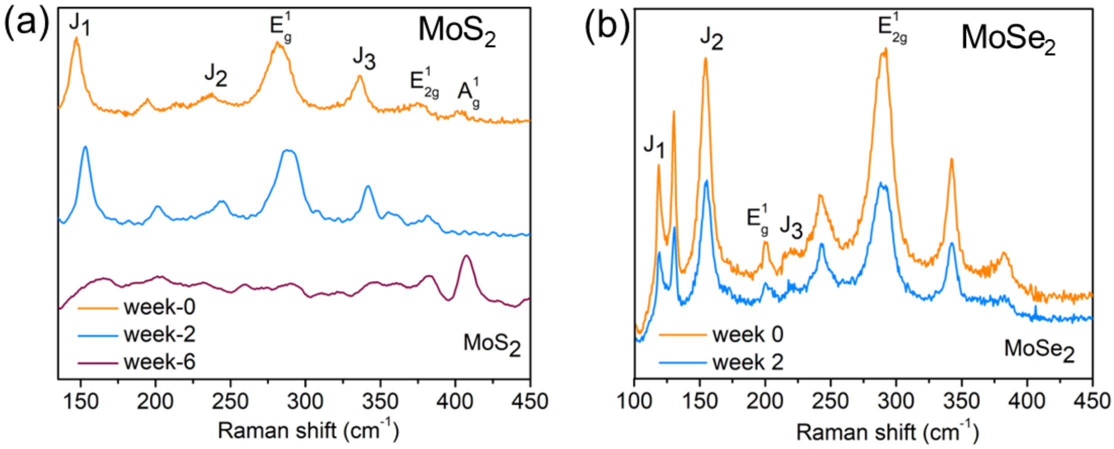

Figure 1: *Raman spectra of (a) 1T-MoS_2 and (b) 1T-$MoSe_2$ synthesized by solvothermal method (spectra with different periods to demonstrate the stability of the 1T-phase).*

The Raman spectrum of 1T-$MoSe_2$ exhibits the characteristic J_1, J_2, and J_3 bands appearing at 118, 154, and 221 cm^{-1}, respectively. The 1T-phase of $MoSe_2$ is stable for 2 weeks with no significant change in the relative Raman band intensities of J_1, J_2, and J_3 (**Figure 1b**).

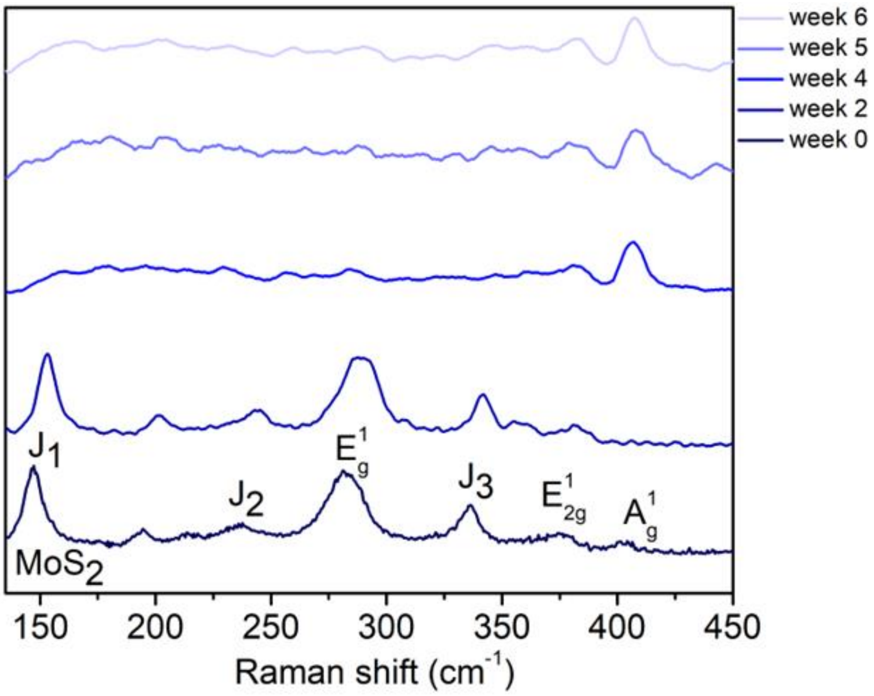

***Figure 2.** Raman spectra of 1T-MoS₂ was recorded for 6 weeks (the conversion from 1T phase to 2H phase appears after 4 weeks).*

There was a very weak appearance of the A_g^1 band of the 2H-form during this period. The 1T-phases of MoS₂ and MoSe₂ obtained via hydrothermal means also show the characteristic Raman bands. Thus, 1T-MoS₂ exhibits J_1, J_2, and J_3 bands at 154, 244, and 340 cm$^{-1,}$ and the intensity of the A_g^1 band due to the 2H phase are not significant. After 2 weeks also, we observed no change in the relative intensities of the bands indicating the stability of the 1T-phase (**Figure 3a**).

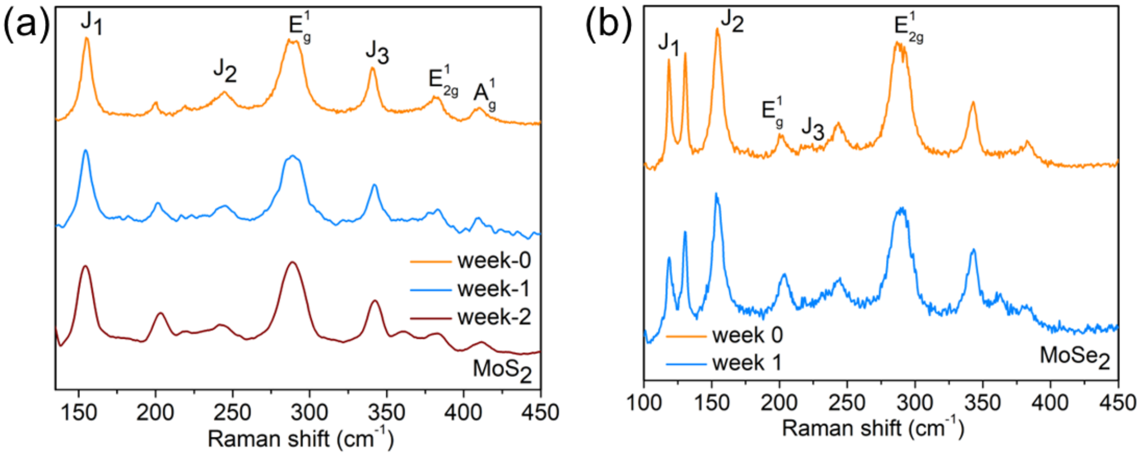

***Figure 3**. Raman spectra of (a) 1T-MoS₂ and (b) 1T-MoSe₂ synthesized by hydrothermal methods.*

J_1, J_2, and J_3 bands at 118, 154, and 222 cm^{-1}, respectively were observed in the Raman spectrum of the 1T-phase of $MoSe_2$ prepared by hydrothermal method. Similar to $MoSe_2$ synthesized via the solvothermal method, we observed a very weak A_g^1 band because of the 2H phase (**Figure 3b**). The relative peak intensities of the 1T phase do not change over a period of one week.

Figure 4 presents a typical high resolution TEM images of the 1T-phase synthesized via the hydrothermal or solvothermal route. The 1T phases of MoS_2 and $MoSe_2$ show the √3a×a arrangement that belongs to their electronic structure and the shift of the atoms from their equilibrium positions. This shift probably arises due to the Jahn-Teller instability, which results in chain clusterization of the metal atoms during the formation of a superlattice[30]. The Metal atoms in the 2T form have octahedral coordination whereas the 2H form has trigonal prismatic coordination as shown in TEM image in **Figure 4**.

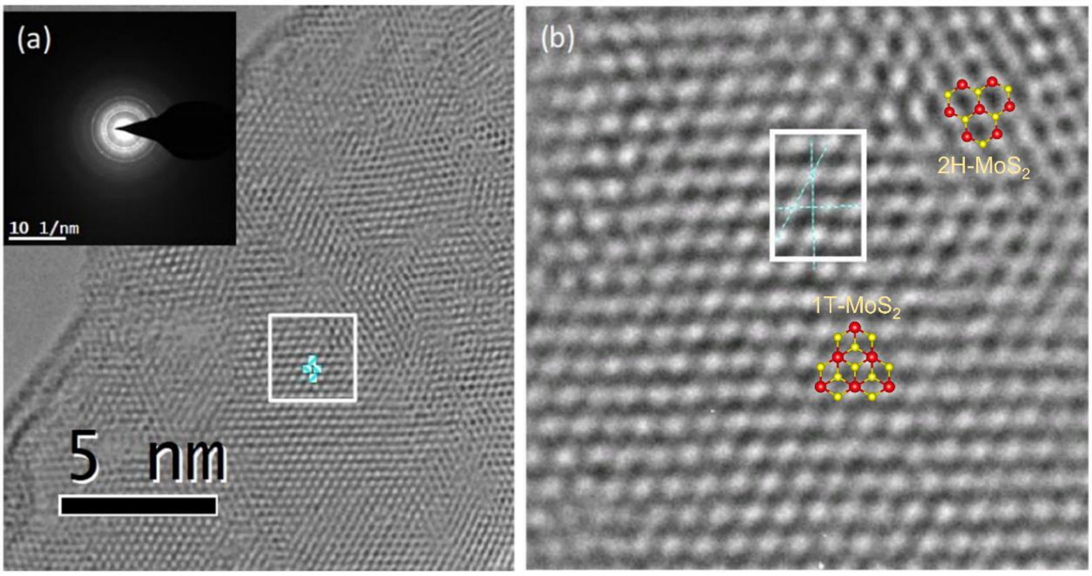

Figure 4: *Representative image of high resolution TEM of 1T-phase of MoS_2 .*

The 1T MoS_2 can reversibly convert into its 2H phase by charge rearrangement again (**Figure 5**). Phase conversion of 2H to 1T phase in monolayer was driven by atomic gliding (Lin *et al.*)[33] and change in the lattice structure, accompanied by electronic structure evolution, electron injection and rearrangement followed by charge loss[44].

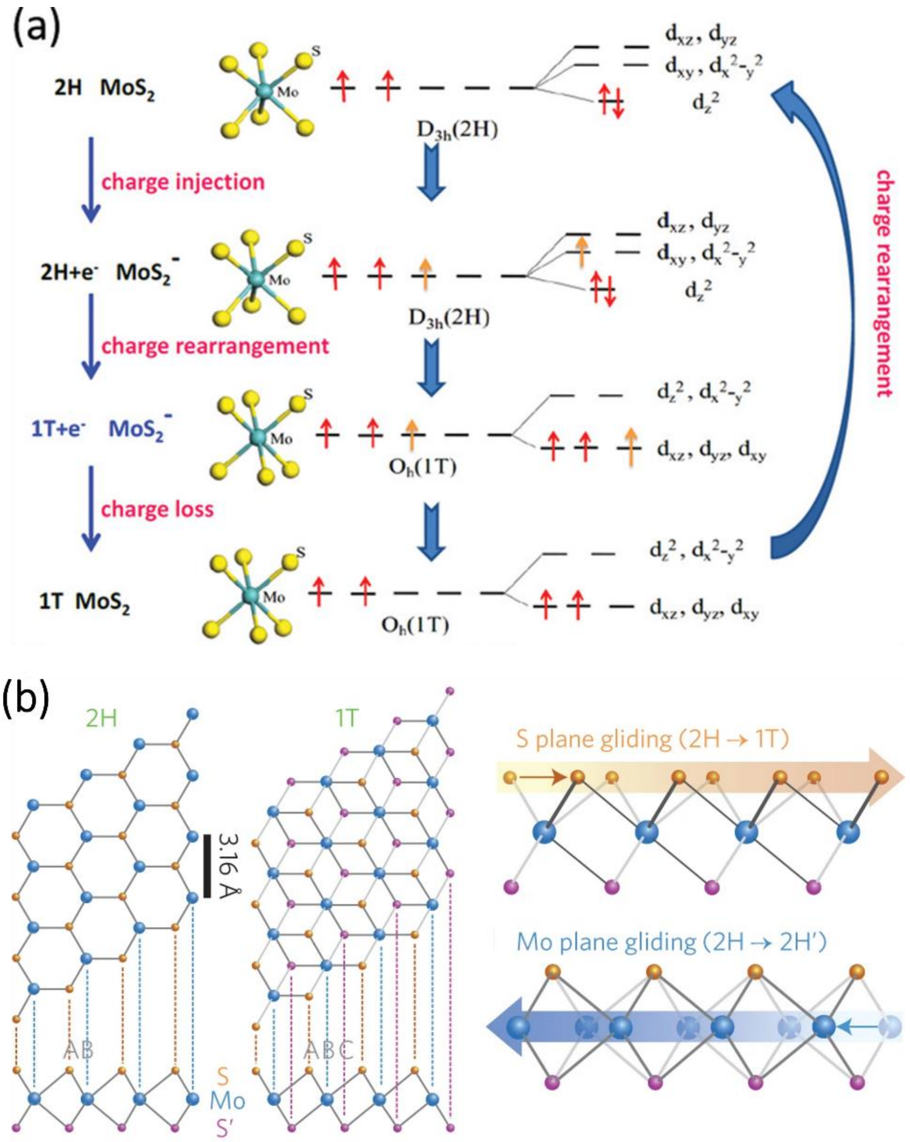

Figure 5: *(a) Based on crystal field theory, phase transformation mechanisms between the phases of 1T and 2H. Reproduced with permission[44], copyright 2019 John Wiley & Sons, and (b) basal plane view and cross-section view of 2H and 1T phases. Reproduced with permission[33], copyright 2014 Springer Nature.*

Liu *et al.*[45] synthesized stable 1T-MoS_2 phase intercalation of NH_4^+ in a in-situ manner. Protonated NH_4^+ were intercalated in situ which formed during the hydrothermal reaction of $(NH_4)_6Mo_7O_{24}·4H_2O$ with $CS(NH_2)_2$. NH_4^+ ions work as electron donors to stabilize the 1T phase. In our case Na^+ can generate in-site from precursor and stabilize 1T phase. Propionic acid also provides an sufficient acidic condition to increase the reducibility of thiourea for the formation of more and more Mo(IV) ions, so that oxidation (loss of electrons) can be inhibited in the 1T-MoS_2 and reduced the possibilites of transition to 2H-MoS_2[37, 46].

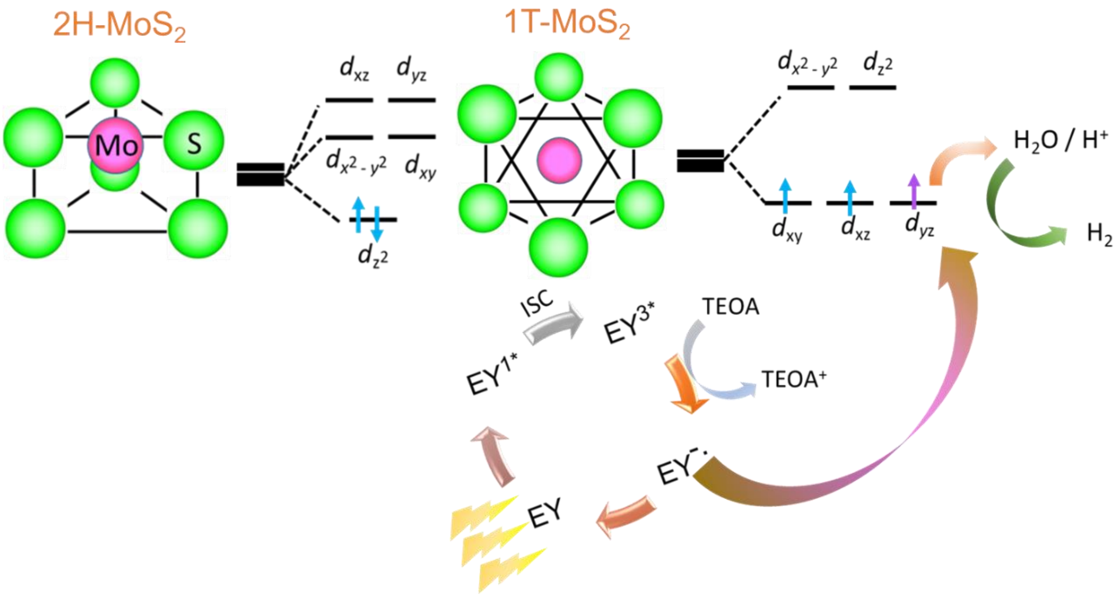

Figure 6: *Electronic configuration of 2H-MoS_2 and 1T-MoS_2 supported by crystal-field-splitting and proposed HER mechanism for water reduction by 1T-MoS_2.*

Figure 6 shows the possibility of electrons transfer from the photogenerated negatively charged species EY^- to H_2O through the partially filled $4d_{xy,xz,yz}$ in 1T-MoS_2[27]. This is not possible in the case of 2H phase where orbitals are completely occupied. So, we have studied the HER activity by dye-sensitized method of both 1T-MoS_2 and 1T-$MoSe_2$ synthesized by solvothermal and hydrothermal methods in the presence of photosensitizer eosin Y dye in aqueous solution triethanolamine (15% v/v). The activity of 1T-MoS_2 and 1T-$MoSe_2$ were found to be 31700 and 57500 μmol $g^{-1}h^{-1}$ (**Figure 7a**), the activity of $MoSe_2$ being higher than MoS_2 due to higher conductivity and low Gibbs free energy for hydrogen adsorption.

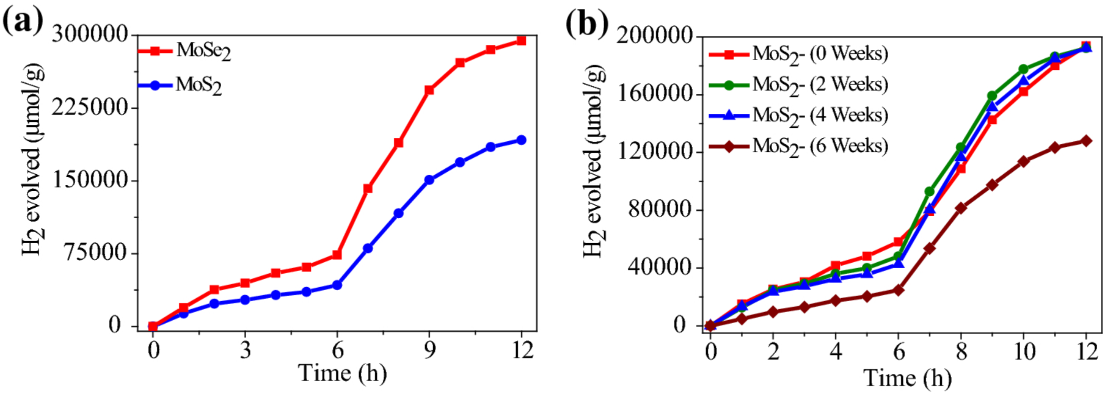

Figure 7: *HER activities of synthesized (a) 1T-MoS_2 and 1T-$MoSe_2$ via solvothermal method; (b) HER activity of MoS_2 over the period of 6 weeks.*

in contrast to MoS_2, both Mo and Se both sites can be active for hydrogen evolution in $MoSe_2$ because of similar hydrogen binding energy with Mo and Se, whereas only Mo atoms are the HER site in case of MoS_2[30]. The HER activity of the 1T-MoS_2 was observed over a period of 6 weeks. The activities were found to be 31700, 37700, 37000, and 28000 μmol $g^{-1}h^{-1}$ for 0, 2, 4, and 6 weeks, respectively (**Figure 7b** and **Table 1**).

Table 1: Photochemical hydrogen evolution activities of 1T-MoS_2 and $MoSe_2$ over the period of time. (The activities are shown before and after the addition of dye again after 6 hours-called as induction period).
(* First six hours, # next six hours on further addition of dye).

	Before Induction Period (μmoles g^{-1} h^{-1})*	**After Induction Period (μmoles g^{-1} h^{-1})#**
MoS_2 (Hydrothermal)		
0 Weeks	12600	31700
2 Weeks	12400	37700
4 Weeks	11700	37000
6 Weeks	4800	28000
$MoSe_2$ (Hydrothermal)	12700	57500
MoS_2 (Solvothermal)		
0 Weeks	5700	17000
2 Weeks	7300	14000
$MoSe_2$ (Solvothermal)	10000	35000

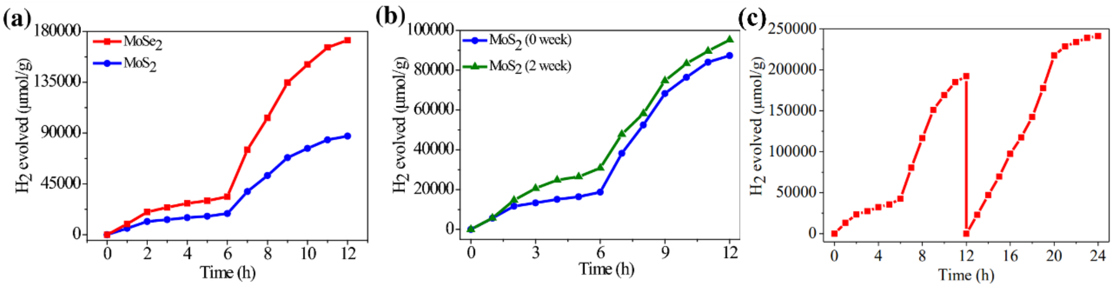

Figure 8: *HER performances of (a) 1T-MoS_2 and 1T-$MoSe_2$, synthesized via hydrothermal methods, (b) HER activity of 1T-MoS_2 over the period of 2 weeks, and (c) cycling studies of 1T-MoS_2.*

HER activity of the 1T-phases of MoS_2 and $MoSe_2$ synthesized via hydrothermal means was 17000 and 35000 μmol $g^{-1}h^{-1}$, respectively (**Figure 8**).

We observed a higher activity in the case of 1T-$MoSe_2$ synthesized in DMF also. The activity of 1T-MoS_2 was studied for two weeks and found to be 14000 µmol $g^{-1}h^{-1}$ (shown in the **Figure 8b** and **Table 1**). Photochemical performances of obtained samples by our solvothermal and hydrothermal methods have been compared with those synthesized from Li-intercalation and exfoliation in **Table 2.** The 1T phase from solvothermal and hydrothermal methods shows comparable photocatalytic activities and is found to be stable as well which indicates suitability for practical uses. Stable HER evolution over long periods is observed in cycling studies **(Figure 8c).** There is a decrease in the activity of the samples after 6 weeks which can be because of the slow conversion of the 1T to the 2H-phase as observed from Raman spectra (**Figure 2**).

Table 2: Comparison of photochemical HER activity of 1T-phases by different methods.

	Synthetic method	**Activity (µmoles g^{-1} h^{-1})**	**TOF (h^{-1})**
1T- MoS_2	(a) Li-intercalation and exfoliation[27]	30,000	4.8
	(b) $MoCl_5$+ Thioacetamide in DMF, 200 ^{0}C (Solvothermal)	37,000	6.0
	(c) $Na_2MoO_4 \cdot 2H_2O$ + Thiourea in water + propionic acid, 200 ^{0}C (Hydrothermal)	16,000	2.5
1T- $MoSe_2$	(a) Li-intercalation and exfoliation[30]	75,000	19.0
	(a) $MoCl_5$+ Selenourea in DMF, 200 ^{0}C (Solvothermal)	57,500	14.6
	(c) $Na_2MoO_4 \cdot 2H2O$ + Selenourea in water + propionic acid, 200 ^{0}C (Hydrothermal)	35,000	8.9

2.5. Conclusions and outlook

Stable 1T-MoS_2 and $MoSe_2$ have been synthesized by simple hydrothermal and solvothermal methods. Prepared samples were found to be stable (up to 2–4 weeks) unlike those obtained by lithium intercalation followed by exfoliation. Photochemical HER activities of 1T MoS_2 and 1T $MoSe_2$ were observed and found to be remarkable. With due remarkable HER activity, this strategy of the 1T phase of MoS_2 and $MoSe_2$ can be extended to other materials and may have wide applications beyond hydrogen production. This work also opens the thought toward the direction of stability and activity of 1T MoS_2 for other methods.

In the direction of stabiling the 1T phase of MoX_2, functionalization of TMDs can be a good approach to stabilize 1T phases as shown in **Figure 9**. The presence of characteristics J_1, J_2, and J_3 bands suggest that functionalization can preserve the stability of 1T phase **(Figure 10)**. Interestingly, functionalized nanosheets can be good candidates to prepare linked-2D nanosheets for potential applications which will be discussed in the next upcoming chapters.

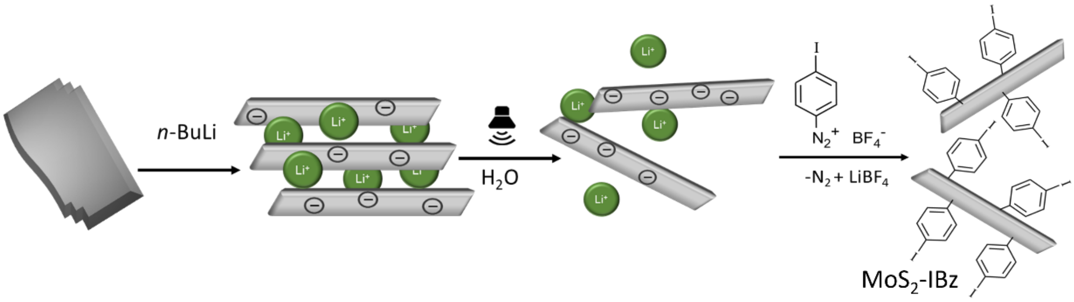

Figure 9: *Functionalization of exfoliated MoS_2 nanosheets.*

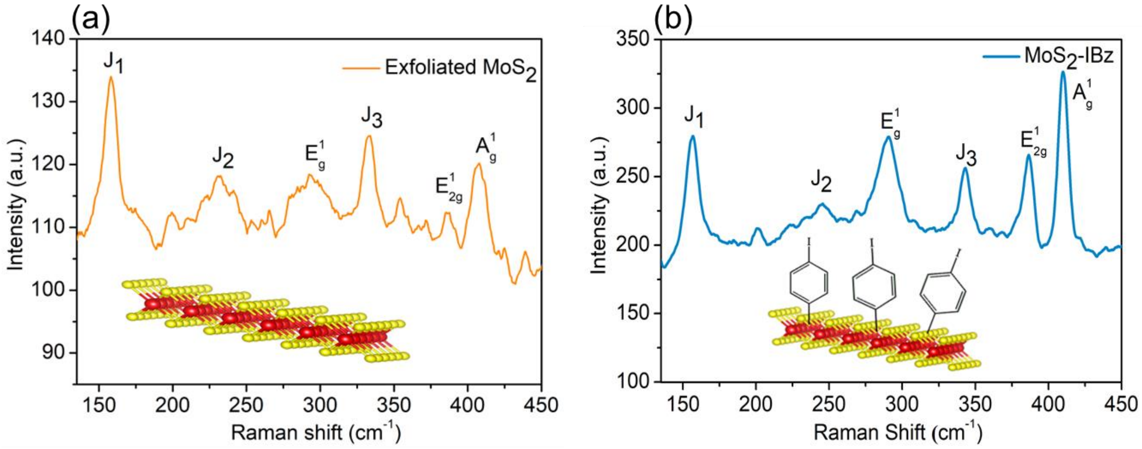

Figure 10: *Raman spectra of (a) exfoliated MoS_2 (b) iodobenzene functionalized MoS_2.*

2.6. References

[1] Zhang, X.; Hou, L.; Ciesielski, A.; Samorì, P. *Adv. Energy Mater.* **2016**, *6* (23), 1600671.

[2] Xu, J.; Zhang, J.; Zhang, W.; Lee, C. S. *Adv. Energy Mater.* **2017**, *7* (23), 1700571.

[3] Poorahong, S.; Izquierdo, R.; Siaj, M. *J. Mater. Chem. A* **2017**, *5* (39), 20993-21001.

[4] Pumera, M.; Sofer, Z.; Ambrosi, A. *J. Mater. Chem. A* **2014**, *2* (24), 8981-8987.

[5] Saravanakumar, B.; Kim, S.-J. *J. Phys. Chem. C.* **2014**, *118* (17), 8831-8836.

[6] Mak, K. F.; Shan, J. *Nat. Photon.* **2016**, *10* (4), 216-226.

[7] Xue, Y.; Zhang, Q.; Wang, W.; Cao, H.; Yang, Q.; Fu, L. *Adv. Energy Mater.* **2017**, *7* (19), 1602684.

[8] Li, Y.; Wang, H.; Xie, L.; Liang, Y.; Hong, G.; Dai, H. *J. Am. Chem. Soc.* **2011**, *133* (19), 7296-7299.

[9] Voiry, D.; Salehi, M.; Silva, R.; Fujita, T.; Chen, M.; Asefa, T.; Shenoy, V. B.; Eda, G.; Chhowalla, M. *Nano Lett.* **2013**, *13* (12), 6222-6227.

[10] Jiang, J.-W. *Front. Phys.* **2015**, *10* (3), 287-302.

[11] Das, S.; Swain, G.; Parida, K. *Mater. Chem. Front.* **2021**, *5* (5), 2143-2172.

[12] Millet, P.; Ngameni, R.; Grigoriev, S. A.; Mbemba, N.; Brisset, F.; Ranjbari, A.; Etiévant, C. *Int. J. Hydrog. Energy* **2010**, *35* (10), 5043-5052.

[13] Yu, J.; Qi, L.; Jaroniec, M. *J. Phys. Chem. C.* **2010**, *114* (30), 13118-13125.

[14] Wang, X.; Maeda, K.; Thomas, A.; Takanabe, K.; Xin, G.; Carlsson, J. M.; Domen, K.; Antonietti, M. *Nat. Mater.* **2009**, *8* (1), 76-80.

[15] Rao, C. N. R.; Lingampalli, S. R.; Dey, S.; Roy, A. *Philos. Trans. R. Soc. A* **2016**, *374* (2061), 20150088.

[16] Swain, G.; Sultana, S.; Naik, B.; Parida, K. *ACS Omega* **2017**, *2* (7), 3745-3753.

[17] Sharma, M. D.; Mahala, C.; Basu, M. *Inorg. Chem.* **2020**, *59* (7), 4377-4388.

[18] Wazir, M. B.; Daud, M.; Safeer, S.; Almarzooqi, F.; Qurashi, A. *ACS Omega* **2022**, *7* (20), 16856-16865.

[19] Sumesh, C. K.; Peter, S. C. *Dalton Trans.* **2019**, *48* (34), 12772-12802.

[20] He, Z.; Que, W. *Appl. Mater. Today* **2016**, *3*, 23-56.

[21] Voiry, D.; Mohite, A.; Chhowalla, M. *Chem Soc Rev* **2015**, *44* (9), 2702-2712.

[22] Lei, Z.; Zhan, J.; Tang, L.; Zhang, Y.; Wang, Y. *Adv. Energy Mater.* **2018**, *8* (19), 1703482.

[23] Jaramillo, T. F.; Jørgensen, K. P.; Bonde, J.; Nielsen, J. H.; Horch, S.; Chorkendorff, I. *Science* **2007**, *317* (5834), 100-102.

[24] Gan, X.; Lee, L. Y. S.; Wong, K.-y.; Lo, T. W.; Ho, K. H.; Lei, D. Y.; Zhao, H. *ACS Appl. Energy Mater.* **2018**, *1* (9), 4754-4765.

[25] Niu, H.; Zou, Z.; Wang, Q.; Zhu, K.; Ye, K.; Wang, G.; Cao, D.; Yan, J. *Chem. Eng. J.* **2020**, *399*, 125672.

[26] Eda, G.; Yamaguchi, H.; Voiry, D.; Fujita, T.; Chen, M.; Chhowalla, M. *Nano Lett.* **2011**, *11* (12), 5111-5116.

[27] Maitra, U.; Gupta, U.; De, M.; Datta, R.; Govindaraj, A.; Rao, C. N. R. *Angew. Chem. Int. Ed.* **2013**, 52 (49), 13057-13061.

[28] Jayabal, S.; Wu, J.; Chen, J.; Geng, D.; Meng, X. *Mater. Today Energy* **2018**, 10, 264-279.

[29] Wang, D.; Zhang, X.; Bao, S.; Zhang, Z.; Fei, H.; Wu, Z. *J. Mater. Chem. A* **2017**, 5 (6), 2681-2688.

[30] Gupta, U.; Naidu, B. S.; Maitra, U.; Singh, A.; Shirodkar, S. N.; Waghmare, U. V.; Rao, C. N. R. *APL Mater.* **2014**, 2 (9), 092802.

[31] Huang, H.; Cui, Y.; Li, Q.; Dun, C.; Zhou, W.; Huang, W.; Chen, L.; Hewitt, C. A.; Carroll, D. L. *Nano Energy* **2016**, 26, 172-179.

[32] Wang, X.; Shen, X.; Wang, Z.; Yu, R.; Chen, L. ACS Nano **2014**, 8 (11), 11394-11400.

[33] Lin, Y.-C.; Dumcenco, D. O.; Huang, Y.-S.; Suenaga, K. *Nat. Nanotechnol* **2014**, 9 (5), 391-396.

[34] Hwang, D. Y.; Choi, K. H.; Park, J. E.; Suh, D. H. *Nanoscale* **2017**, 9 (2), 503-508

[35] Wu, M.; Zhan, J.; Wu, K.; Li, Z.; Wang, L.; Geng, B.; Wang, L.; Pan, D. *J. Mater. Chem. A.* **2017**, 5 (27), 14061-14069.

[36] Yang, J.; Wang, K.; Zhu, J.; Zhang, C.; Liu, T. *ACS Appl. Mater. Interfaces* **2016**, 8 (46), 31702-31708.

[37] Liu, Z.; Gao, Z.; Liu, Y.; Xia, M.; Wang, R.; Li, N. *ACS Appl. Mater. Interfaces* **2017**, 9 (30), 25291-25297.

[38] He, H. Y. *Int. J. Hydrog. Energy.* **2017**, 42 (32), 20739-20748.

[39] Wang, D.; Su, B.; Jiang, Y.; Li, L.; Ng, B. K.; Wu, Z.; Liu, F. *Chem. Eng. J.* **2017**, 330, 102-108.

[40] Liu, Q.; Fang, Q.; Chu, W.; Wan, Y.; Li, X.; Xu, W.; Habib, M.; Tao, S.; Zhou, Y.; Liu, D.; et al. *Chem. Mater.* **2017**, 29 (11), 4738-4744.

[41] Wieting, T. J.; Verble, J. L. *Phys. Rev. B.* **1971**, 3 (12), 4286.

[42] Molina-Sanchez, A.; Wirtz, L. *Phys. Rev. B.* **2011**, 84 (15), 155413.

[43] Sandoval, S. J.; Yang, D.; Frindt, R. F.; Irwin, J. C. *Phys. Rev. B.* **1991**, 44 (8), 3955.

[44] Wu, C.; Zhang, J.; Tong, X.; Yu, P.; Xu, J.-Y.; Wu, J.; Wang, Z. M.; Lou, J.; Chueh, Y.-L. *Small* **2019**, 15 (35), 1900578.

[45] Liu, Q.; Li, X.; He, Q.; Khalil, A.; Liu, D.; Xiang, T.; Wu, X.; Song, L. *Small* **2015**, 11 (41), 5556-5564.

[46] Xin, D.; He, S.; Han, X.; Zhang, X.; Cheng, Z.; Xia, M. *J. Alloys Compd*. **2022**, 921, 166099.

Chapter 3

Covalently Cross-linked 2D-nanosheets of $MoSe_2$ for Photochemical Hydrogen Evolution Reaction

Summary

Among two-dimensional materials, molybdenum selenide ($MoSe_2$) is a potential candidate for photocatalytic hydrogen production. Although its metallic 1T phase, synthesized by chemical exfoliation found to be a very good photocatalyst but not stable for a long time and eventually converts to its semiconductor 2H phase. Covalent functionalization of exfoliated 1T sheets can preserve its stability. So recoupling these functionalized 2D sheets with itself or others 2D materials would be fascinating.

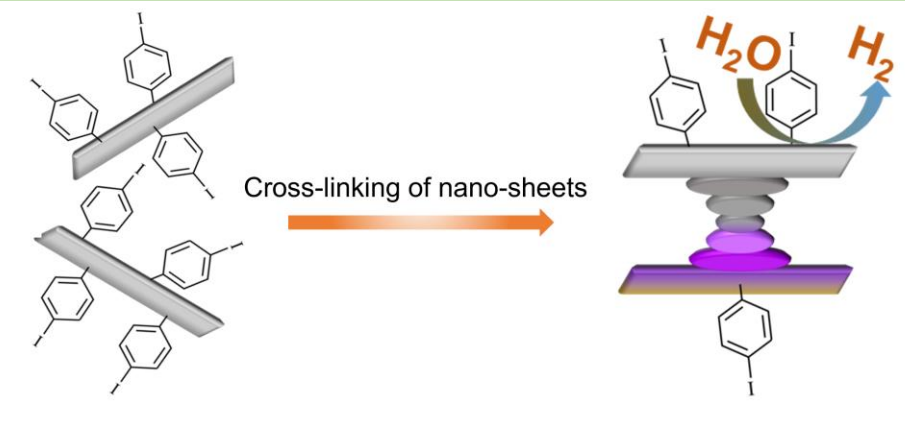

Interestingly, such cross-linked 2D-nanosheets, $MoSe_2$-$MoSe_2$ and $MoSe_2$-BCN show high photocatalytic hydrogen evolution reaction (HER) activity. The present study shows the important role played by covalent cross-linking of layered materials. covalently Cross-linked layer of $MoSe_2$ shows higher photochemical HER activity than that of bulk 2H-MoS_2.

Paper based on this work has appeared in *J. Chem. Sci.* **2018**, 130, 131.

3.1. Introduction

Following the exciting properties of graphene[1], other two-dimensional inorganic materials[2, 3] such as transition metal dichalcogenides (TMDs)[4, 5], carbon-nitride (C_3N_4)[6], boron-nitride(BN)[7, 8], and boron carbonitride (BCN)[9] have attracted tremendous attention due to their outstanding physical, chemical and electronic properties compared to their bulk counterparts. Among those, Molybdenum disulfide (MoS_2) and Molybdenum selenide ($MoSe_2$) are the most studied TMDs for hydrogen evolution reaction (HER) catalysis, making them useful models to understand the fundamental properties of TMDs, atomic structures, and mechanisms of catalysis. Especially for hydrogen production, $MoSe_2$ has been reported to show more active due to the following reasons (i) more metallic nature compared to MoS_2 because of the more metallic nature of Se, (ii) higher conductivity than MoS_2 due to unsaturated Se edges[10] (iii) a lower work function as compared to MoS_2[11], and (iv) due to lower Gibbs free energy of hydrogen adsorption onto $MoSe_2$ edges, which leads higher coverage of hydrogen on surface[12]. Even, though the metallic phase (1T) of $MoSe_2$ is more active than its 2H phase or any phase of MoS_2 but stabilization of the 1T phase is still challenging[11]. For $MoSe_2$ to be catalytically valuable, this metastable 1T metallic phase needs to be stabilized so that the stabilization process would also allow us for systematic control over the catalytic activity of HER reactions and other applications. Earlier attempts to stabilize 1T phases of MoS_2 by electron injection or charge a donation to TMDs have been quite successful[13]. The substrates such as graphene and single-wall nanotube that can increase the electron density of the layers have been good and stable catalysts for HER activity[14, 15].

Recently, covalent functionalization of metallic (1T phase) of MoS_2 has been reported, which helps to inhibit conversion to thermodynamically stable 2H phase and preserve its stability[16, 17]. To understand the mechanism of covalent functionalization, properties, and tuning of their electronic and catalytic properties, a wide literature has been reported[18-26]. Not only functionalization of surfaces can enhance the activity and performance of 2D materials, but the coupling of nanosheets with other materials (even with other dimensional materials) also shows outstanding properties. Such types of materials are called nano-composites and have been studied in recent years. Crosslinked graphene sheets using the Sonogashira coupling with organic linkers show excellent surface area, porosity, and remarkable storage capacity for CO_2 and H_2[27]. MoS_2 nanosheets chemically cross-linked through polymeric ligands with coordinated divalent metal ions show robust mechanical properties and are useful for thin film-based devices[28]. Crossed-linked MoS_2 with graphene[29], C_3N_4[30], and BCN[31] have been thoroughly explored for water splitting and show good HER activity in comparison to their individual component graphene or MoS_2. Therefore, a covalently crosslinking strategy for a good photocatalyst such as $MoSe_2$ layers would be interesting to observe the HER activity and stability of layers.

3.2. Scope of present investigation

In view of functionalization and nanocomposites, we have investigated nanosheets of $MoSe_2$ crosslinked with C_3N_4 and the carbon-rich borocarbonitride, BC_7N. a simple term BCN for BC_7N have been used throughout the study to designate this material. BCN–$MoSe_2$ cross-linked 2D-nanosheets were synthesized where BN domains of borocarbonitride cross-linked to $MoSe_2$ nanosheets as BN/BCN–$MoSe_2$ and the graphene domains of borocarbonitride cross-linked with $MoSe_2$ sheets as G/BCN–$MoSe_2$. In addition, linked-nanosheet of $MoSe_2$ layers with itself were also studied to compare the performance of these materials with those of a bulk $MoSe_2$ and cross-linked layers of MoS_2 reported in the literature.

3.3. Experimental

Materials

$MoSe_2$ (98%, Alpha aesar), 4-iodoaniline (98%, Sigma Aldrich), urea (98%, Sigma Aldrich), activated charcoal (98%, Sigma Aldrich), boric acid (98%, Sigma Aldrich), N-N-dimethylformamide (Spectrochem) and triethylamine (99%, Sigma Aldrich), CuI (98% Spectrochem) and $Pd(PPh_3)_4$ (Min. Assay of Pd About 9.5%, Spectrochem).

(i) Synthesis of cross-linked $MoSe_2$ nanosheets

Cross-linked $MoSe_2$ layers with other 2D layered nanomaterials were thoroughly prepared as follows. First the nanosheets of 1T-$MoSe_2$ were obtained by lithium intercalation of bulk 2H-$MoSe_2$, followed by exfoliation in deionized water[11]. These exfoliated $MoSe_2$ layers were reacted with 2- bromoacetic acid (with a 10-fold excess) to obtain functionalized $MoSe_2$ ($MoSe_2–CH_2COOH$) with the carboxyl groups attached with surface by the formation of the C–Se bond. The carboxyl groups present in the surface of $MoSe_2$ were utilized to cross-link with other 2D nanosheets. Similarly, 1T-$MoSe_2$ nanosheets were reacted with 4-iodoaniline (12-fold excess) to obtain the amine functionalized $MoSe_2$ ($MoSe_2–C_6H_4NH_2$) by forming the C–Se bonds[21].

Cross linked-nanosheet of $MoSe_2$ were prepared by the reaction of 1T-$MoSe_2$ with diazonium salt of 4-iodoaniline to obtain iodobenzene functionalized $MoSe_2$ ($MoSe_2–C_6H_4I$), followed by the addition of freshly prepared 1T-$MoSe_2$ again to form $MoSe_2$ linked-nanosheet by forming the C–Se bonds[21] ($MoSe_2–C_6H_4–MoSe_2$) (**Scheme 1**).

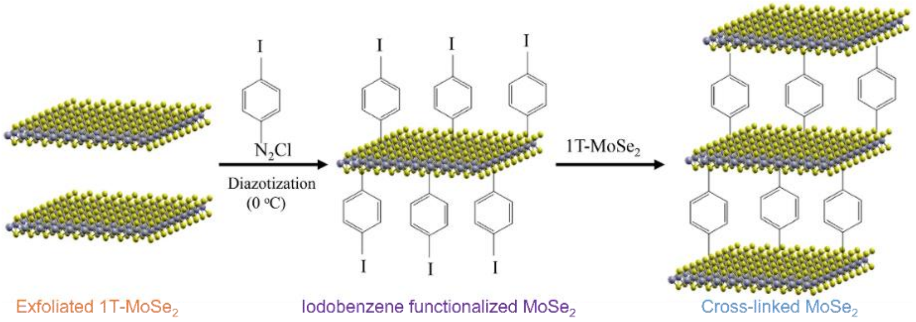

Scheme 1: *Presentation of strategy to obtain cross-linked $MoSe_2–MoSe_2$ nanosheets.*

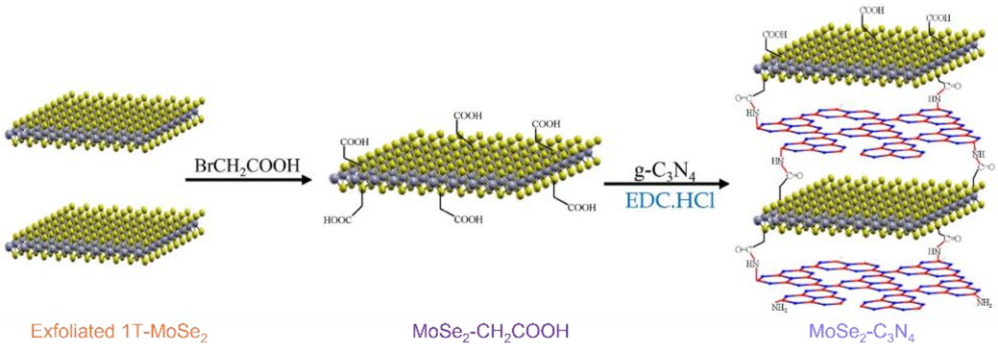

Scheme 2: *Presentation of strategy to obtain cross-linked $MoSe_2–C_3N_4$ nanosheets.*

To obtain cross-linked $MoSe_2$–C_3N_4, 30 mg $MoSe_2$–CH_2COOH and 30 mg C_3N_4 were dispersed in dry DMF in N_2 atmosphere. Equal amounts of 1- hydroxybenzotriazole (HOBt, 30 mg) and N-(3-(dimethylamino)propyl)-N-ethylcarbodiimidehydrochloride (EDC·HCl, 30 mg), were added in to mixture mentioned above along the addition of with N,N-diisopropyl ethylamine (DIPEA, 500 µL) and stirred at room temperature for 48 h in an inert atmosphere. The solid product was filtered and washed with DMF and dried at 60 ˚C under vacuum (**Scheme 2**).

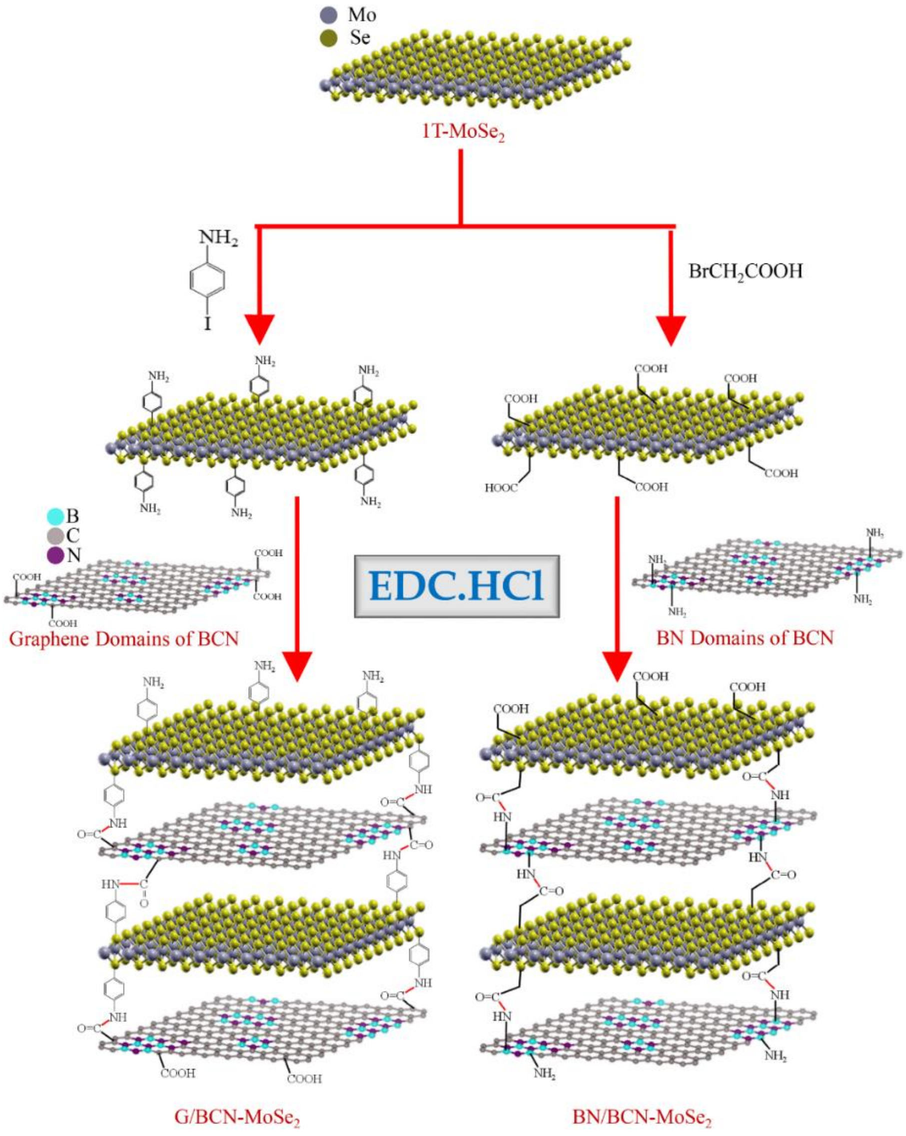

Scheme 3: *Presentation of strategy to obtain cross-linked G/BCN–$MoSe_2$ and BN/BCN–$MoSe_2$ nanosheets (EDC= 1-ethyl-3-(3 dimethylaminopropyl)carbodiimide).*

Borocarbonitride (BC_7N; denoted as BCN) nanosheets were obtained by using a protocol reported elsewhere [9, 32]. A mixture of urea (2.4 g), activated charcoal (500 mg), and boric acid (60 mg) was heated in a furnace at 900 ˚C in N_2 atmosphere for 10 hours. Then obtained black product was treated with NH_3 gas at 900 ˚C for 5 hours.

Since BCN have both the functional groups ($-NH_2$ in BN domain and -COOH in graphene domain), there are two possible ways of linking $MoSe_2$ nanosheets with BCN. Cross-linking to BN domains in BC_7N denoted to BN/BCN–$MoSe_2$ and by linking to graphene (G) domains in BC_7N denoted to G/BCN–$MoSe_2$ as shown in **Scheme 3**.

(ii) Characterizations:

The Infrared (IR) and Raman spectra were recorded using for the samples using Perkin Elmer ATR-FTIR and HORIBA LabRam HR800 spectrometers respectively. Transmission Electron Microscopy (TEM) was taken using JEOL, and scanning electron microscopy analysis of the sheets have been performed using Nova Nano SEM 600, FEI. PANanalytical Empyrean with Cu K-α radiation was used to obtain powder X-ray diffraction of the linked-nanosheets.

(iii) Photochemical HER study (Scheme 4):

HER study was done by dye-sensitized method as mentioned in chapter 1. 5 mg of the catalyst dispersed in an aqueous solution of triethanolamine (15% v/v, 48 mL) in a cylindrical glass vessel. To the reaction mixture, 14 µmol of eosin Y dye was added as a sensitizer and illuminated with visible light irradiation (400W Xenon lamp, with cut-off filter of >399 nm) under constant stirring. The evolved gas was analyzed with a gas chromatograph (PerkinElmer) equipped with a thermal conductivity detector.

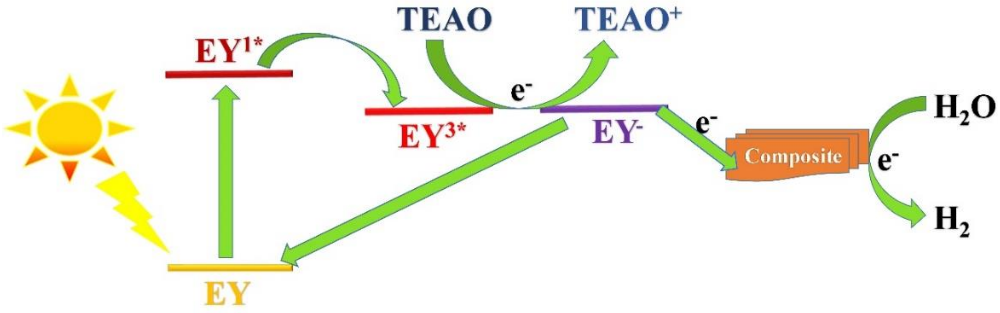

Scheme 4: *Representation of hydrogen evolution studied for the catalysts with Eosin Y.*

3.4. Results and Discussion

We were able to synthesize the covalent cross-linked 2D-nanosheets of $MoSe_2$ by cross-linking with other 2D materials such as C_3N_4, BC_7N, and with itself. $MoSe_2$ cross-linked to C_3N_4 and BC_7N and as well as the linked-nanosheets of $MoSe_2$ were characterized by X-ray diffraction, Fourier-transform infrared (FTIR) and Raman spectroscopy, and other techniques. The FTIR spectra of $MoSe_2$–CH_2COOH sheets shows strong bands at 1758 and 3210 cm^{-1} which correspond to C=O and –OH stretching vibrations, respectively of carboxylic groups along with a C-Se bond stretching at 736 cm^{-1} result from covalent functionalization shown in **Figure 1(a,b)**.

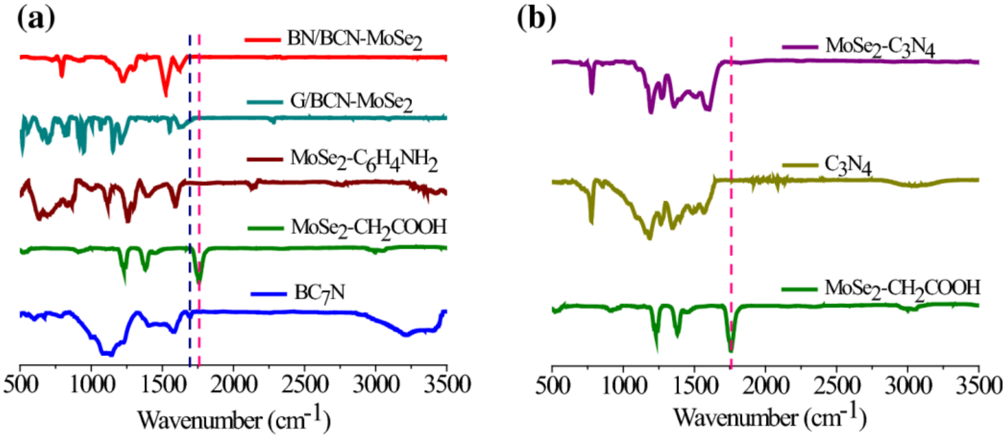

Figure 1: *FTIR spectra of cross-linked sheets of* $MoSe_2$ *with (a) BCN and (b)* C_3N_4*.*

BC_7N displays a band at 1591 cm^{-1} with strong intensity arising from C=C and a weak band around 1723 cm^{-1} arising C=O stretching vibrations along with a broad band in the 3065–3485 cm^{-1} region corresponding to the present amine and hydroxyl groups on the surface. A broad band around 950–1250 cm^{-1} is because of C–O stretching and O–H bending vibrations. The C=O stretching band in G/BCN–$MoSe_2$ sheets at 1638 cm^{-1} along with other characteristic bands from amino benzene moieties suggests the formation of amide linkages between carboxylic groups of graphene domains of BC_7N and amine-functionalized $MoSe_2$. Similarly, BN/BCN–$MoSe_2$ nanosheets shows a carbonyl stretching band at 1676 cm^{-1}, confirming cross-linking of the BC_7N and $MoSe_2$ layers by the amide bond shown in **Figure 1(a,b)**[33].

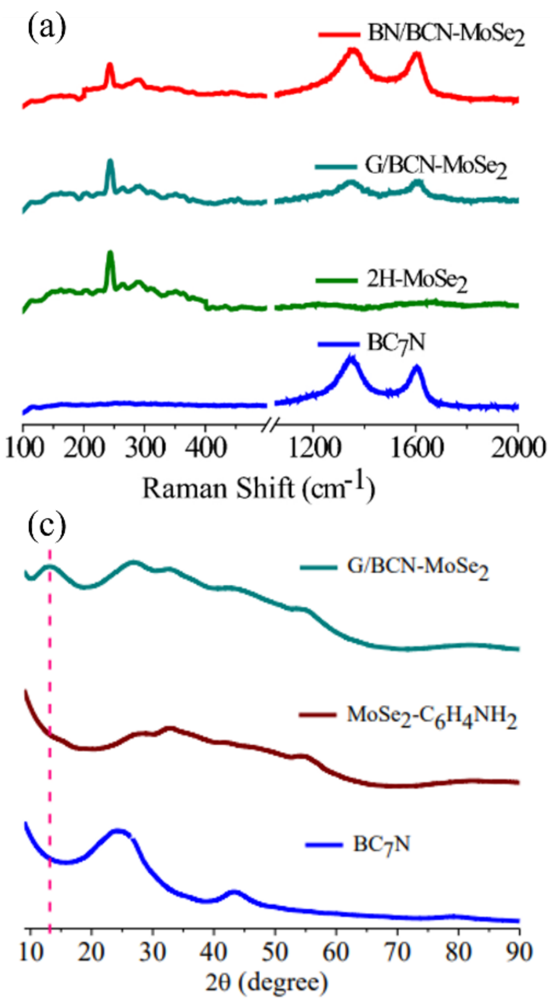

Figure 2: *(a) Raman spectra and (b-d) XRD patterns of $MoSe_2$ and its cross-linked nanosheets.*

Raman spectroscopy plays a crucial role in defining the stable form of $MoSe_2$ structure in cross-linked nanosheets. We show typical Raman spectra of BCN–$MoSe_2$ nanosheets are presented in **Figure 2(a)**. The spectra of the G/BCN–$MoSe_2$ and BN/BCN–$MoSe_2$ nanosheets show characteristic D and G bands of BC_7N at 1349 and 1606 cm^{-1}, respectively, along with the $A^1{}_g$ and $E^1{}_{2g}$ bands of $MoSe_2$ at 244 and 291 cm^{-1}, respectively[34]. The formation of covalently cross-linked sheets was also investigated using powder X-ray diffraction (PXRD) patterns of BN/BCN–$MoSe_2$, G/BCN–$MoSe_2$, and $MoSe_2$–C_3N_4 nanosheets which showed the appearance of new reflections at 2θ = 13.19° (d = 0.67 nm), 12.76° (d = 0.69 nm) and 13.09° (d = 0.68 nm) corresponding to the interlayer spacing between BC_7N–$MoSe_2$ and $MoSe_2$–C_3N_4 cross-linked nanosheets (**Figure 2b-d**).

Scanning electron microscope (SEM) and transmission electron microscope (TEM) images of the $MoSe_2$ linked-nanosheets, G/BC_7N–$MoSe_2$ and BN/BC_7N–$MoSe_2$ showed evidence for layer-by-layer assembly of sheet structure upon cross-linking of the constituent $MoSe_2$ and BC_7N layers (**Figure 3**).

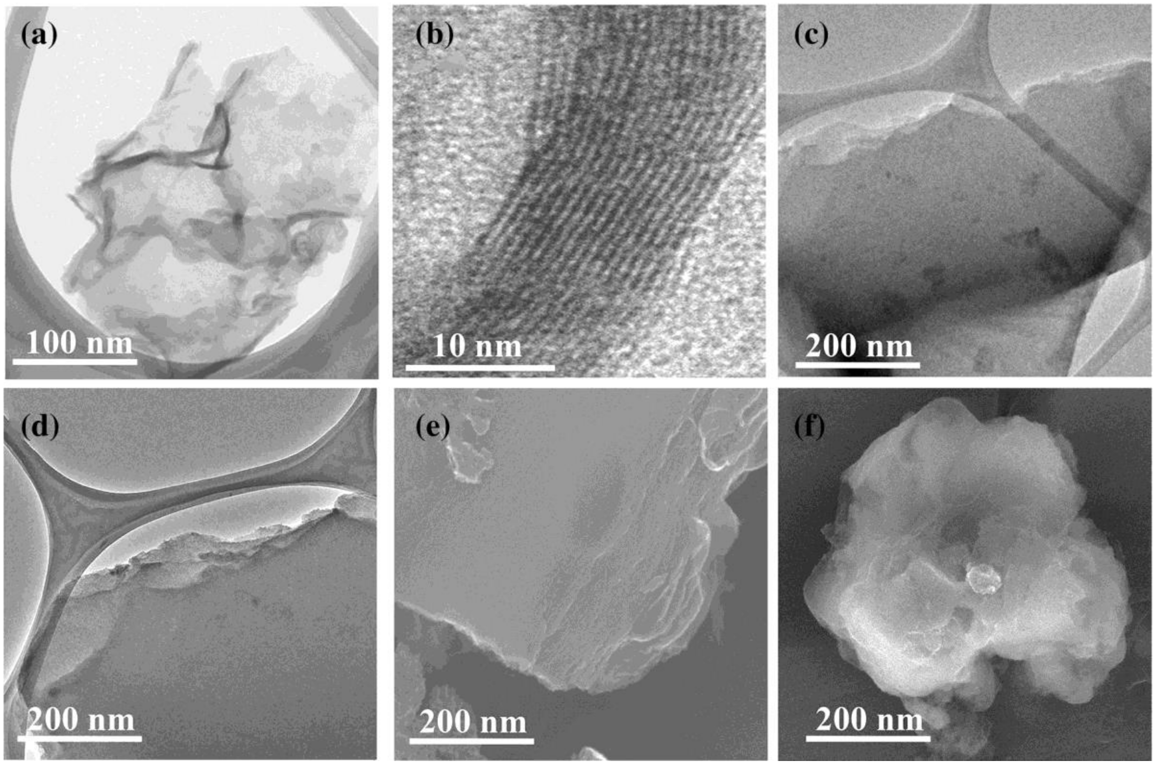

Figure 3: *(a, b) HRTEM image of $MoSe_2$ and cross-linked $MoSe_2$–$MoSe_2$, (c, d) TEM image of BCN with cross-linking of $MoSe_2$, BN/BCN–$MoSe_2$ and G/BCN–$MoSe_2$, (e, f) SEM image of cross-linked $MoSe_2$–$MoSe_2$ and $MoSe_2$–C_3N_4.*

Values of surface area obtained from BET N_2 adsorption-desorption isotherms (at 77 K) for BC_7N–$MoSe_2$, $MoSe_2$–$MoSe_2$, $MoSe_2$–C_3N_4 nanosheets and $MoSe_2$ done are 580, 312, 280 and 78 m^2/g respectively (**Figure 4**). We observe type-I characteristics in the low-pressure region along with a type-II hysteresis loop in the high-pressure region, as per the IUPAC nomenclature[35].

The photochemical hydrogen evolution was studied in the presence of Eosin Y (as a sensitizer) in an aqueous solution of triethanolamine (TEOA, sacrificial agent). The mechanism of hydrogen evolution with Eosin Y and triethanolamine is well-studied in the literature (**Scheme 4**)[11, 36].

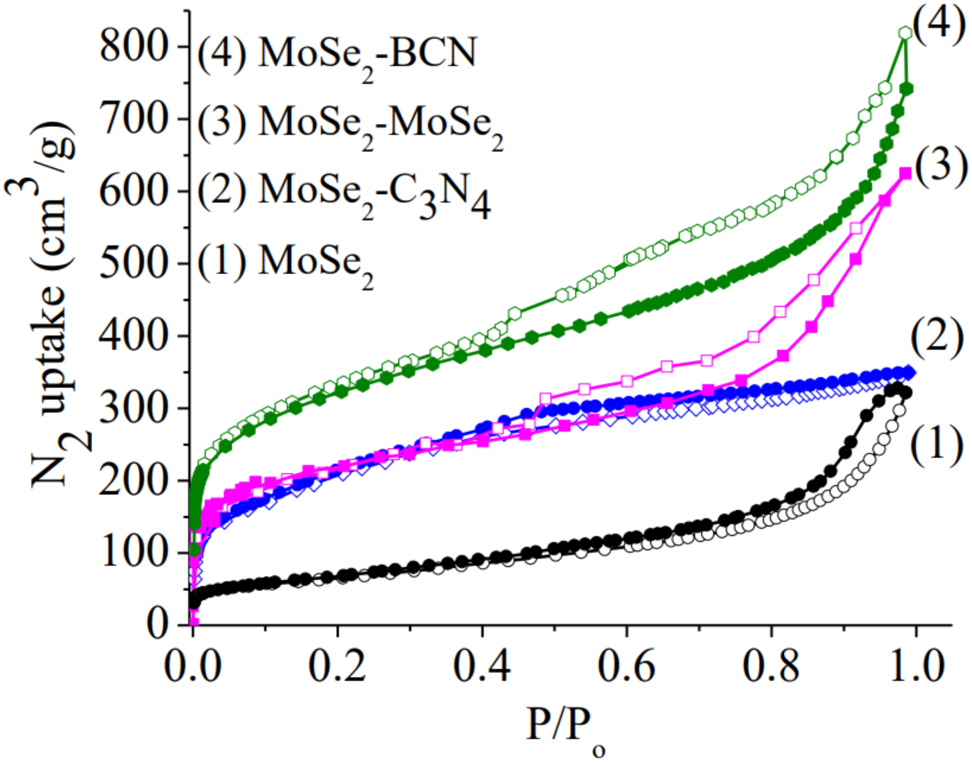

Figure 4: *Nitrogen sorption profiles of (1) $MoSe_2$, (2) $MoSe_2$-C_3N_4 , (3) $MoSe_2$-$MoSe_2$, and (4) $MoSe_2$-BCN cross-linked nanosheets.*

We compare the results of photochemical hydrogen yields of nanosheets of MoS_2 and $MoSe_2$. Pristine MoS_2 and $MoSe_2$ show a similar activity of 1663 and 1680 μmol $g^{-1}h^{-1}$, respectively[31]. Pristine BC_7N and pristine C_3N_4 show very low activities of 165 and 113 μmol $g^{-1}h^{-1}$, respectively (**Figure 5**). The self-assembly of $MoSe_2$, however, shows high activity reaching 8294 μmol $g^{-1}h^{-1}$. This is much higher than that of MoS_2 linked-nanosheets (1750 μmol $g^{-1}h^{-1}$) synthesized by the same method[29].

$MoSe_2$–C_3N_4 nanosheets exhibits a somewhat lower activity 2624 μmol $g^{-1}h^{-1}$ compared to MoS_2–C_3N_4. This is unlike BC_7N–$MoSe_2$ which exhibits a high activity of 10384 or 12584 μmol $g^{-1}h^{-1}$ compared to BC_7N–MoS_2 (6965 μmol $g^{-1}h^{-1}$) shown in

Figure 5 [30, 31, 37]. It is noteworthy that the photochemical activity and surface area vary in the same fashion. There is increase in HER activity in the crosslinked nanosheets with the enhancement of surface area as cross-linking opens up pores and slits where edges can act as HER sites. Moreover, cross-linking increases the planarity of the layer with increased overlap between the cross-linked layers, facilitating charge transfer across the network[30].

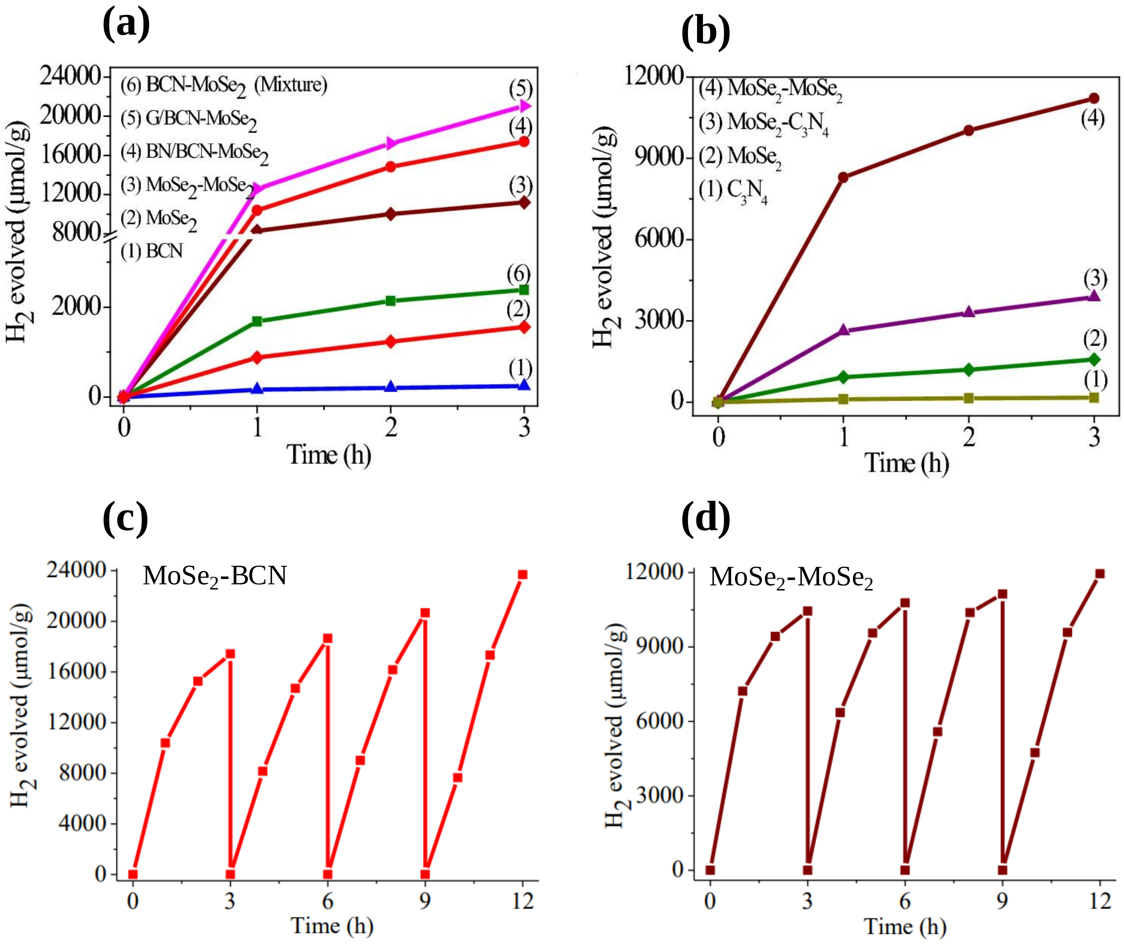

Figure 5: *(a,b) Comparison of the H_2 evolution activity of $MoSe_2$ and its cross-linked nanosheets and cycling studies of the H_2 evolution of (c) $MoSe_2$-BCN and (d) $MoSe_2$-$MoSe_2$.*

Moreover, HER activity with the physical mixture of BCN and $MoSe_2$ shows very small activity (878 μmol $g^{-1}h^{-1}$) which is much lower in compare to the cross-linked nano-sheets. This findings suggests that cross-linking has a role in enhancing the HER activity in **Table 1**. The activity of linked-nanosheets of BCN–$MoSe_2$ nanosheet is especially noteworthy. We can compare the performance of the $MoSe_2$ nanosheets with those of MoS_2. The performance of $MoSe_2$ nanosheets is generally higher than those of MoS_2 nanosheets, the only exception being the nanosheets with C_3N_4. We can significantly improve the photochemical HER activity of MoS_2 and $MoSe_2$ by covalent cross-linking with other 2D materials[29-31, 37].

Table 1: Photochemical HER activity of nanosheets of $MoSe_2$ cross-linked with other 2D layers

Materials	**Surface area (m^2/g)**	**Activity [μmol $g^{-1}h^{-1}$]**
2H-$MoSe_2$	78	1680
BCN	810	165
C_3N_4	29	113
$MoSe_2$–$MoSe_2$	312	8294
$MoSe_2$–C_3N_4	280	2624
BN/BCN–$MoSe_2$	580	10384
G/BCN–$MoSe_2$	576	12584
BCN–$MoSe_2$(mix)	–	878

The plausible explanations for the enhancement of HER are given by K. Pramoda *et al.*[30], (i) enhancement of surface area which increases the interfacial area, (ii) planarity between layers which increases the charge transfer, and (iii) minimum resistance immersed in the transport of charge within the catalyst. It is interesting to note that crosslinked MoS_2 (G/BCN–MoS_2 [31]) and $MoSe_2$ (G/BCN–$MoSe_2$) with graphene domains of BCN have higher activities than their respective BN domain-linked nanosheets.

3.5. Conclusions and outlook

The discussed findings show that it is possible to utilize the functionalized MoS_2 and $MoSe_2$ as photocatalysts for HER by forming covalently linked nanosheets with other 2D materials such as BC_7N or by it-self. The photochemical HER activity of covalently cross-linked nanosheets is sufficiently higher for possible practical use (though not as high as that of the 1T phases). The performance of MoS_2 and $MoSe_2$ nanosheets with a borocarbonitride such as BC_7N is noteworthy. It is interesting that by linking MoS_2 and $MoSe_2$ to another 2D material one can enhance the photochemical activity substantially. Cross-linking of 2H-MoS_2 and $MoSe_2$ with BC_7N and C_3N_4 is likely to involve charge transfer between the two hetero layers.

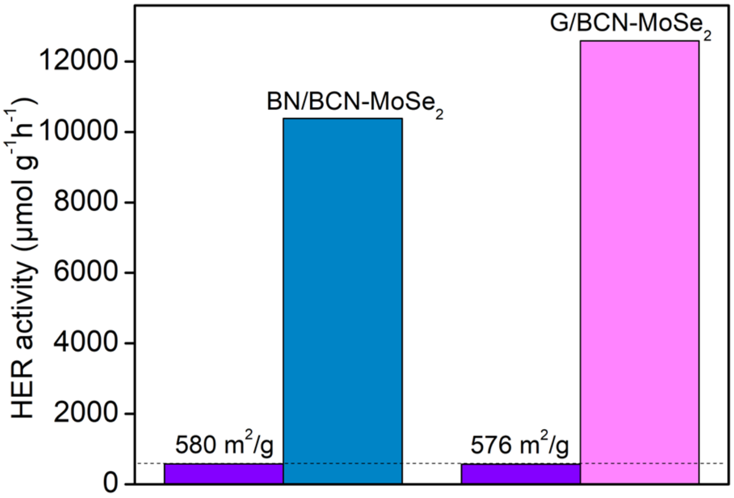

Figure 6: *Comparison of the HER performance of BN/BCN–$MoSe_2$ and G/BCN–$MoSe_2$.*

Although, the surface area of the nano-sheets of G/BCN–MoS_2[31] and G/BCN–$MoSe_2$ are similar (or a little less) of BN/BCN–MoS_2[31] and BN/BCN–$MoSe_2$ but HER activities are slightly higher (shown in **figure 6**). It means not only the surface area but bonding between the layers and the nature of linked sheets also plays a crucial role in HER activities. So, It is very necessary to study the role of interlayer space between the layers. Therefore a detailed study related to the role of interlayer separation and the nature of other linked layers will be discussed in the coming chapter 4.

3.6. References

[1] Novoselov, K. S.; Geim, A. K.; Morozov, S. V.; Jiang, D.; Zhang, Y.; Dubonos, S. V.; Grigorieva, I. V.; Firsov, A. A. *Science* **2004**, *306* (5696), 666-669.

[2] Nicolosi, V.; Chhowalla, M.; Kanatzidis, M. G.; Strano, M. S.; Coleman, J. N. *Science* **2013**, *340* (6139), 1226419.

[3] Rao, C. N. R.; Nag, A. *Eur. J. Inorg. Chem.* **2010**, *2010* (27), 4244-4250.

[4] Chhowalla, M.; Shin, H. S.; Eda, G.; Li, L.-J.; Loh, K. P.; Zhang, H. *Nat. Chem.* **2013**, *5* (4), 263-275.

[5] Ramakrishna Matte, H. S. S.; Gomathi, A.; Manna, A. K.; Late, D. J.; Datta, R.; Pati, S. K.; Rao, C. N. R. *Angew. Chem. Int. Ed.* **2010**, *49* (24), 4059-4062.

[6] Zhao, Z.; Sun, Y.; Dong, F. *Nanoscale* **2015**, *7* (1), 15-37.

[7] Raidongia, K.; Gomathi, A.; Rao, C. N. R. *Isr. J. Chem.* **2010**, *50* (4), 399-404.

[8] Deepak, F. L.; Vinod, C. P.; Mukhopadhyay, K.; Govindaraj, A.; Rao, C. N. R. *Chem. Phys. Lett.* **2002**, *353* (5), 345-352.

[9] Chhetri, M.; Maitra, S.; Chakraborty, H.; Waghmare, U. V.; Rao, C. N. R. *Energy Environ. Sci.* **2016**, *9* (1), 95-101.

[10] Xu, C.; Peng, S.; Tan, C.; Ang, H.; Tan, H.; Zhang, H.; Yan, Q. *J. Mater. Chem. A* **2014**, *2* (16), 5597-5601.

[11] Gupta, U.; Naidu, B. S.; Maitra, U.; Singh, A.; Shirodkar, S. N.; Waghmare, U. V.; Rao, C. N. R. *APL Mater.* **2014**, *2* (9), 092802.

[12] Tang, H.; Dou, K.; Kaun, C.-C.; Kuang, Q.; Yang, S. *J. Mater. Chem. A* **2014**, *2* (2), 360-364.

[13] Lei, Z.; Zhan, J.; Tang, L.; Zhang, Y.; Wang, Y. *Adv. Energy Mater.* **2018**, *8* (19), 1703482.

[14] Lei, Y.; Pakhira, S.; Fujisawa, K.; Wang, X.; Iyiola, O. O.; Perea López, N.; Laura Elías, A.; Pulickal Rajukumar, L.; Zhou, C.; Kabius, B.; *et al. ACS Nano* **2017**, *11* (5), 5103-5112.

[15] Liu, Q.; Fang, Q.; Chu, W.; Wan, Y.; Li, X.; Xu, W.; Habib, M.; Tao, S.; Zhou, Y.; Liu, D.; *et al. Chem. Mater.* **2017**, *29* (11), 4738-4744.

[16] Benson, E. E.; Zhang, H.; Schuman, S. A.; Nanayakkara, S. U.; Bronstein, N. D.; Ferrere, S.; Blackburn, J. L.; Miller, E. M. *J. Am. Chem. Soc.* **2018**, *140* (1), 441-450.

[17] Er, E.; Hou, H.-L.; Criado, A.; Langer, J.; Möller, M.; Erk, N.; Liz-Marzán, L. M.; Prato, M. *Chem. Mater.* **2019**, *31* (15), 5725-5734.

[18] Voiry, D.; Goswami, A.; Kappera, R.; Silva, C. d. C. C. e.; Kaplan, D.; Fujita, T.; Chen, M.; Asefa, T.; Chhowalla, M. *Nat. Chem.* **2015**, *7* (1), 45-49.

[19] Nguyen, E. P.; Carey, B. J.; Ou, J. Z.; van Embden, J.; Gaspera, E. D.; Chrimes, A. F.; Spencer, M. J. S.; Zhuiykov, S.; Kalantar-zadeh, K.; Daeneke, T. *Adv. Mater.* **2015**, *27* (40), 6225-6229.

[20] Presolski, S.; Pumera, M. *Mater. Today* **2016**, *19* (3), 140-145.

[21] Vishnoi, P.; Sampath, A.; Waghmare, U. V.; Rao, C. N. R. *Eur. J. Chem.* **2017**, *23* (4), 886-895.

[22] Zhou, L.; He, B.; Yang, Y.; He, Y. *RSC Adv.* **2014**, *4* (61), 32570-32578.

[23] García-Dalí, S.; Paredes, J. I.; Villar-Rodil, S.; Martínez-Jódar, A.; Martínez-Alonso, A.; Tascón, J. M. D. *ACS Appl. Mater. Interfaces* **2021**, *13* (28), 33157-33171.

[24] Knirsch, K. C.; Berner, N. C.; Nerl, H. C.; Cucinotta, C. S.; Gholamvand, Z.; McEvoy, N.; Wang, Z.; Abramovic, I.; Vecera, P.; Halik, M.; *et al. ACS Nano* **2015**, *9* (6), 6018-6030.

[25] Canton-Vitoria, R.; Sayed-Ahmad-Baraza, Y.; Pelaez-Fernandez, M.; Arenal, R.; Bittencourt, C.; Ewels, C. P.; Tagmatarchis, N. *npj 2D Mater. Appl.* **2017**, *1* (1), 13.

[26] Chen, X.; Denninger, P.; Stimpel-Lindner, T.; Spiecker, E.; Duesberg, G. S.; Backes, C.; Knirsch, K. C.; Hirsch, A. *Eur. J. Chem.* **2020**, *26* (29), 6535-6544.

[27] Kumar, R.; Suresh, V. M.; Maji, T. K.; Rao, C. N. R. *ChemComm* **2014**, *50* (16), 2015-2017.

[28] Liu, Y. T.; Tan, Z.; Xie, X. M.; Wang, Z. F.; Ye, X. Y. *Chem. Asian J.* **2013**, *8* (4), 817-823.

[29] Pramoda, K.; Gupta, U.; Ahmad, I.; Kumar, R.; Rao, C. N. R. *J. Mater. Chem. A* **2016**, *4* (23), 8989-8994.

[30] Pramoda, K.; Gupta, U.; Chhetri, M.; Bandyopadhyay, A.; Pati, S. K.; Rao, C. N. R. *ACS Appl. Mater. Interfaces* **2017**, *9* (12), 10664-10672.

[31] Pramoda, K.; Ayyub, M. M.; Singh, N. K.; Chhetri, M.; Gupta, U.; Soni, A.; Rao, C. N. R. *J. Phys. Chem. C .* **2017**, *122* (25), 13376-13384.

[32] Kumar, N.; Moses, K.; Pramoda, K.; Shirodkar, S. N.; Mishra, A. K.; Waghmare, U. V.; Sundaresan, A.; Rao, C. N. R. *J. Mater. Chem. A* **2013**, *1*, 5806-5821.

[33] Mayo, D. W.; Miller, F. A.; Hannah, R. W. *Course notes on the interpretation of infrared and Raman spectra*; John Wiley & Sons, 2004.

[34] Tonndorf, P.; Schmidt, R.; Böttger, P.; Zhang, X.; Börner, J.; Liebig, A.; Albrecht, M.; Kloc, C.; Gordan, O.; Zahn, D. R. T. *Opt. Express* **2013**, *21* (4), 4908-4916.

[35] Pramoda, K.; Kumar, R.; Rao, C. N. R. *Chem. Asian J.* **2015**, *10* (10), 2147-2152.

[36] Maitra, U.; Gupta, U.; De, M.; Datta, R.; Govindaraj, A.; Rao, C. N. R. *Angew. Chem. Int. Ed.* **2013**, *52* (49), 13057-13061.

[37] Singh, N. K.; Pramoda, K.; Gopalakrishnan, K.; Rao, C. N. R. *RSC Adv.* **2018**, *8* (31), 17237-17253.

Chapter 4

The Role of Interlayer Separation of Covalently Cross-linked 2D-Nanosheets on Photochemical Hydrogen Evolution Reaction

Summary

A new class of materials known as covalently cross-linked heterostructures of 2D materials exhibit electrochemical and photochemical hydrogen evolution capabilities. One can considerably increase the photochemical HER activity by linking the layers of the dichalcogenide with layers of other 2D materials, such as carbon-rich borocarbonitride (BCN). Investigating the influence of interlayer spacing on electrical structures and catalytic properties in nanosheets, involvement of MoS_2 and graphene or other sheets is of great interest.

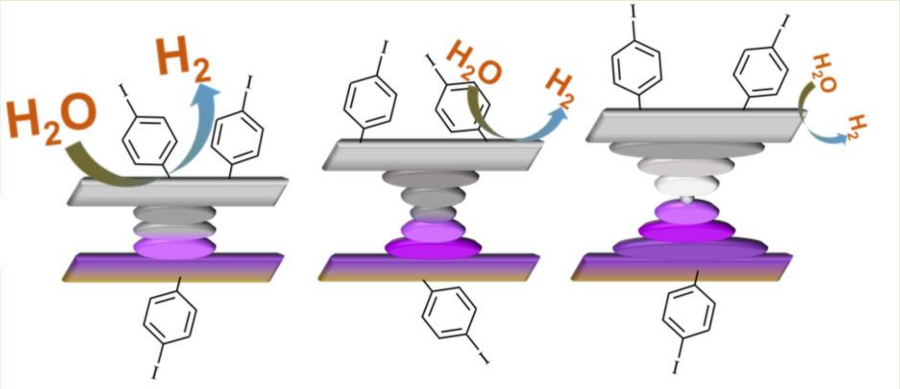

With a focus on these structures' factors pertaining to hydrogen evolution, we looked into this challenge through a combined experimental and theoretical analysis. By varying the linker, we linked different 2D materials with different interlayer spacing to MoS_2-based nanosheets and investigated their hydrogen evolution properties. We can attribute the decrease in hydrogen evolution activity for these sheets with longer linkers to a smaller charge transfer between the layers as interlayer distance increases. This new class of materials is quite intriguing since it offers possibilities to tailor the properties of cross-linked 2D materials by adjusting factors including the nature of the sheets, interlayer spacing, and linker properties.

Paper based on this work has appeared in *ChemPhysChem* **2019**, 20, 13, 1728-1737.

4.1. Introduction

Multi-layered three-dimensional (3D) heterostructures are known to have novel properties which can be synthesized by stacking appropriate two-dimensional (2D) atomic crystals on top of one another[1]. Van der Waal's heterostructures, which have atomically sharp interfaces between different materials and show a variety of phenomena with potential applications, have new interface-induced physical and chemical properties[1-4]. Also, the catalytic activity of these heterostructures has been investigated, and it was discovered that they outperformed individual layers[5]. The inherent electrocatalytic activities of the individual layers are significantly changed by the formation of these heterostructures, which have various atomic layers[6, 7]. The formation of these sandwich structures involving different 2D materials provides flexibility in controlling the chemical reactivity of the stacks.

Due to the fine porosity, considerable surface area, and network architectures, the assembly of 2D nanosheets into 3D frameworks opens up new possibilities for improving catalytic and other properties[8, 9]. Recently, covalently cross-linked layered structures have been reported by chemical means[10]. These materials establish an entirely new class of materials and exhibit novel, highly advantageous properties that are distinct from those of van der Waals heterostructures[11]. Covalently-linked heterostructures of MoS_2 linked with another layer of MoS_2 or with graphene[12], carbonitride (C_3N_4)[13] or a borocarbonitride (BCN)[14] have been reported. Some of the covalently cross-linked MoS_2 nanosheets exhibit good photochemical and electrochemical hydrogen evolution reaction (HER) activity as well[12-15]. To enhance the HER activity of MoS_2, theoretical and experimental studies have proposed anchoring of Co atoms and cobaloxime on the inert basal plane of MoS_2[16, 17], engineering in the defects sites[18, 19] and using metallic 1T-MoS_2[20]. Remarkable advances in heterostructure designs such as MoS_2/graphene superlattices[21], nanosized MoS_2/graphene hybrids[22], nonmetal plasmonic MoS_2/TiO_2 heterostructure[23], and MoS_2-WS_2 heterostructures by the physiochemical process have led to enhanced HER activity[24]. Some studies have also revealed enhanced HER activity by virtue of active sites[25-28].

As discussed in the previous chapter 3, although the surface area of the nanosheets of G/BCN–MoX_2[14, 15] (X=S or Se) are similar of BN/BCN–MoX_2[14, 15] but HER activities are slightly higher. So it is very necessary to study the role of interlayer space, the separation between the layers, and the nature of other linked nanosheets with MoS_2 on HER activity.

4.2. Scope of present investigation

Sheets of covalently cross-linked graphene have mainly been studied for their surface area and gas adsorption capabilities. Research revealed that the linker or interlayer separate affected the surface area and gas adsorption[10]. There isn't a clear account of how interlayer separation in graphene-graphene sheets is effective. There is reason to think that in the case of layers of the covalently cross-linked heterostructure, charge transfer across the layers is accountable for the network's efficient charge transport and the enhanced hydrogen evolution activity[13]. However, it is unclear how the layers interact with one another and how interlayer separation affects these interactions. Designing heterostructures with desirable physical qualities requires an understanding of how interlayer separation affects the characteristics of these novel sheets. Due to this, we have examined the properties of 2D layers of covalently linked materials with different linker lengths or interlayer spacing. We have synthesized covalently cross-linked MoS_2 nanosheets with MoS_2 itself or graphene layers with different lengths, namely using 1, 4 phenylene (L_1), 1,4-diethynylbenzene (L_2), and 4,4’-diethynylbiphenyl (L_3) by employing coupling reactions giving rise to varying the interlayer separation between the layers, MoS_2, and other 2D materials. We have also linked borocarbonitride (BCN) layers with the MoS_2 layer using carbodiimide coupling reaction. We have studied the effect of linker length or interlayer separation in the MoS_2-based 2D nanosheets on photochemical HER. To comprehend the impact of interlayer separation on the molecular and electronic structures of these MoS_2

nanosheets as well as those designed by other layers, we performed extensive first-principles calculations.

4.3. Experimental

Materials:

MoS_2 (98%, Alpha aesar), 4-iodoaniline (98%, Sigma Aldrich), urea (98%, Sigma Aldrich), boric acid (98%, Sigma Aldrich) and activated charcoal (98%, Sigma Aldrich), N-N-dimethylformamide (Spectrochem) and triethylamine (99%, Sigma Aldrich), $Pd(PPh_3)_4$ (Min.Assay of Pd About 9.5%, Spectrochem) and CuI (98% Spectrochem), 1,4-diethynylbenzene) 4,4'-diethynylbiphenyl (98%,TCI Chemicals).

(i) Synthesis of cross-linked 2D-nanosheets:

By synthesizing graphene oxide using a modified Hummer's technique, followed by reduction, reduced graphene oxide was obtained[29,30]. 1T-MoS_2 sheets were obtained by Li intercalation using n-butyl lithium of bulk MoS_2 followed by exfoliation in water. Iodobenzene functionalized MoS_2 (MoS_2-IBz) was prepared by the reaction of 1T-MoS_2 with a diazonium salt of 4-iodoaniline mentioned in reference[12] and shown in **Scheme 1**.

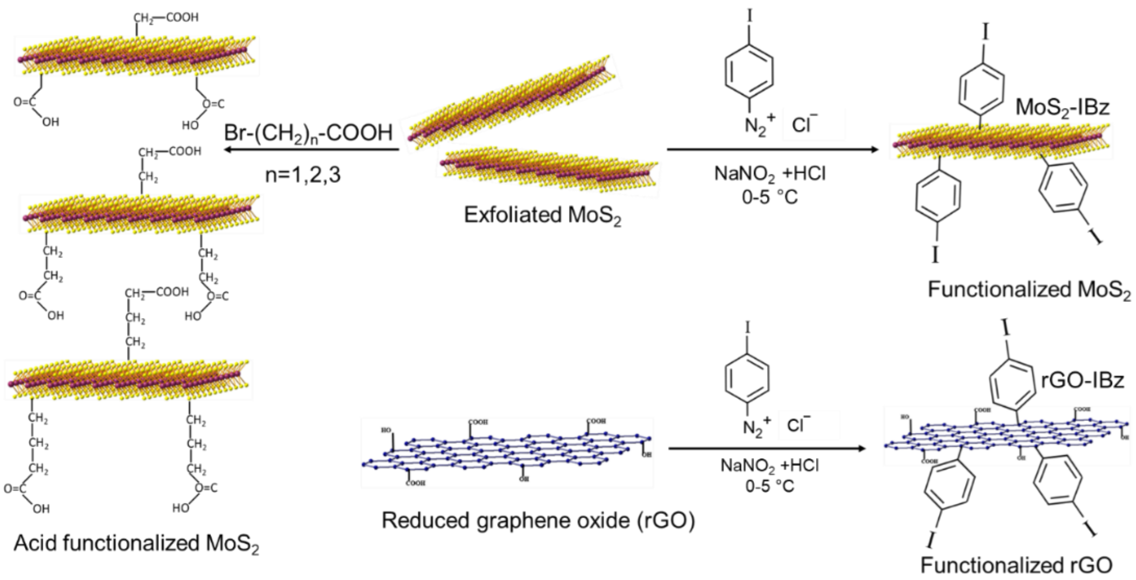

Scheme 1: *Functionalization of MoS_2 and rGO nanosheets (Mo, maroon and S, yellow).*

Similarly, iodobenzene functionalized reduced graphene oxide (rGO-IBz) was synthesized with graphene oxide followed by reduction and reaction with a diazonium salt of 4-iodoaniline[29] shown in **Scheme 1**. Both products MoS_2-IBz and rGO-IBz were washed with DMF, and ethanol and dried in a vacuum at 60°C. Borocarbonitride, BC_7N (denoted BCN) nanosheets were synthesized by a heating mixture of 2.4 g of urea, 60 mg of boric acid, and 500 mg of activated charcoal heated in a furnace at 900 °C under N_2 atmosphere for 10 h and subsequent heating in NH_3 at 900 °C for 5 h[31, 32]. MoS_2 cross-linked sheets with the layers of MoS_2 and other 2D materials were prepared by coupling the 2D sheets using suitable coupling reactions.

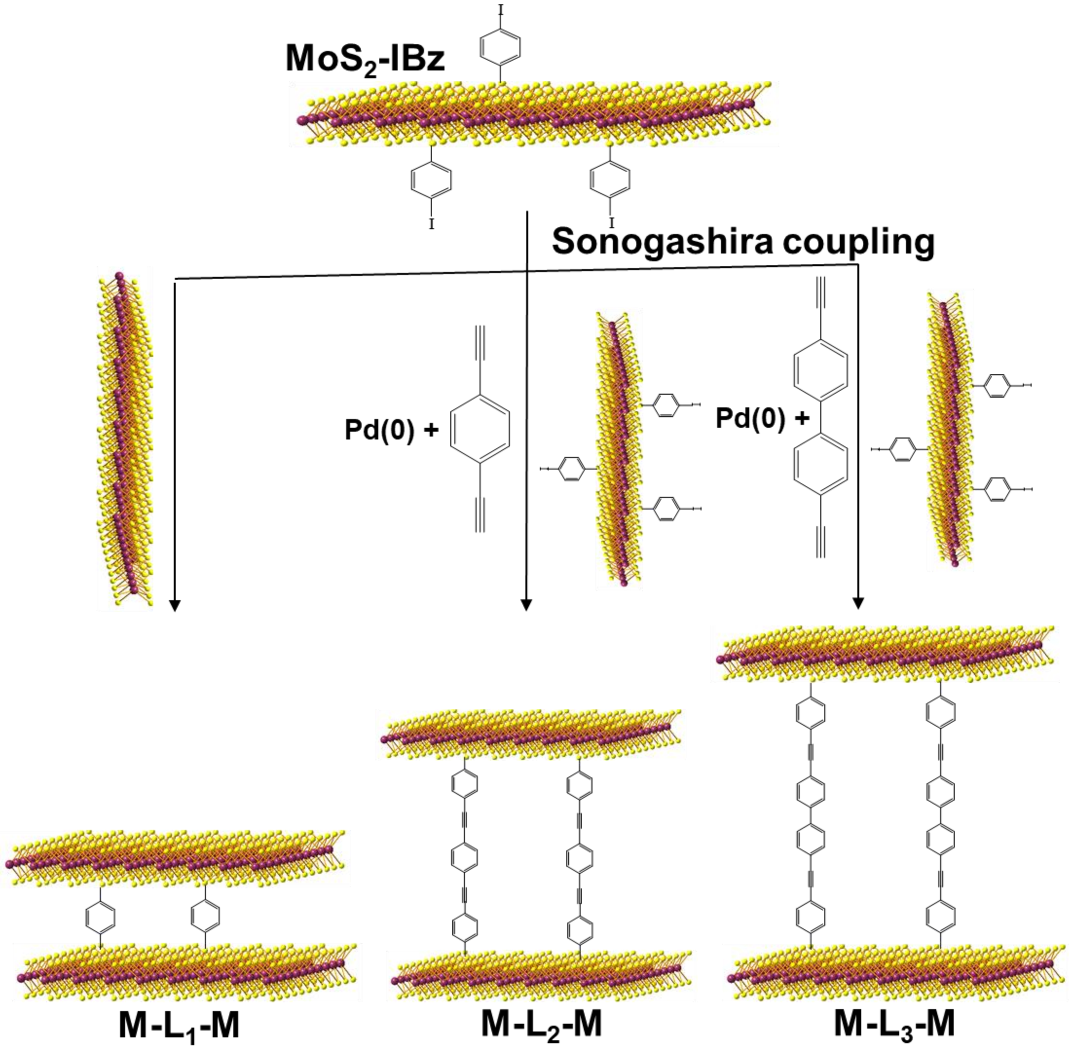

Scheme 2: *Schematic of synthesis of covalently cross-linked nanosheets of MoS_2 namely M-L_1-M, M-L_2-M, and M-L_3-M (Mo, maroon and S, yellow).*

Synthesis of MoS_2-MoS_2 linked-nanosheet (Scheme 2):

MoS_2-1,4-phenylene-MoS_2 (M-L_1-M) could be synthesized by the addition of 30mg of iodobenzene functionalized MoS_2 (MoS_2-IBz) in exfoliated 1T-MoS_2 dispersion and allowed to stirrer for three days[15]. For the synthesis of MoS_2-1,4-diethynylbenzene-MoS_2 (M-L_2-M), 30 mg of MoS_2-IBz was dispersed in N-N-dimethylformamide (DMF) (5 mL) and triethylamine (5 mL) by sonication in a Schlenk flask. In the reaction mixture $Pd(PPh_3)_4$ (5 mg) and CuI (3 mg) were added under stirring followed by raising the temperature to 80 °C and the solution of 50 mg of linker 1,4-diethynylbenzene dissolved in 1 mL DMF was added drop-wise to the mixture under Nitrogen atmosphere followed by raising the temperature to 140 °C and was allowed to stir for 12 h. A similar procedure was followed for the synthesis of MoS_2-4,4'-diethynylbiphenyl-MoS_2 (M-L_3-M) with 4,4'-diethynylbiphenyl (50 mg) as a linker.

Synthesis of MoS_2-rGO linked-nanosheet (Scheme 3):

MoS_2-1,4-phenylene-Graphene (M-L_1-G) was also synthesized by the similar procedure of M-L_1-M, the reaction of exfoliated 1T-MoS_2 nanosheets with iodobenzene functionalized rGO(rGO-IBz, 30 mg) in DMF[15]. To prepare MoS_2-1,4-diethynylbenzene-Graphene (M-L_2-G) and MoS_2-4,4'-diethynylbiphenyl-Graphene (M-L_3-G) sheets synthesized MoS_2-IBz (30 mg) and RGO-IBz (30 mg) were dispersed in DMF (5 ml) and TEA (5 ml) and above mentioned procedure for obtaining M-L_2-M and M-L_3-M were repeated using both the linkers 1,4-diethynylbenzene and 4, 4'-diethynylbiphenyl. Final products were washed with DMF, ethanol properly and dried in a vacuum at 60 °C.

Synthesis of MoS_2-BCN linked-nanosheet (Scheme 4):

Various acid-functionalized MoS_2 compounds acid were synthesized using the addition of 10 fold excess of 1-bromoacetic acid, 3-Bromo propionic acid, and 4-Bromo butyric acid as well in the dispersion of 1T-MoS_2 followed by stirring for three days. Obtained black products were washed with some amount of DMF and hexane and dried in a vacuum at 60 °C. MoS_2-BC_7N sheets MoS_2-CH_2-(CONH)-BC_7N (M-C_1-B), MoS_2-$(CH_2)_2$-(CONH)-BC_7N (M-C_2-B) and MoS_2-$(CH_2)_3$-(CONH)-BC_7N (M-C_1-B) were synthesized by reaction of those obtained functionalized MoS_2 with BC_7N.

30 mg of acid-functionalized MoS_2 and 30 mg of BC_7N were dispersed in dry DMF in N_2 atmosphere. To the above dispersion, 1-hydroxybenzotriazole (HOBt, 30mg) and N-(3-(dimethylamino) propyl)-N'-ethyl-carbodiimide-hydrochloride (EDC.HCl, 30 mg) were added along with N,N-diisopropylethylamine (DIPEA, 500 µL) and allowed to stir at room temperature for 48 h. Final products were washed with some amount of DMF, hexane and dried in a vacuum at 60 °C.

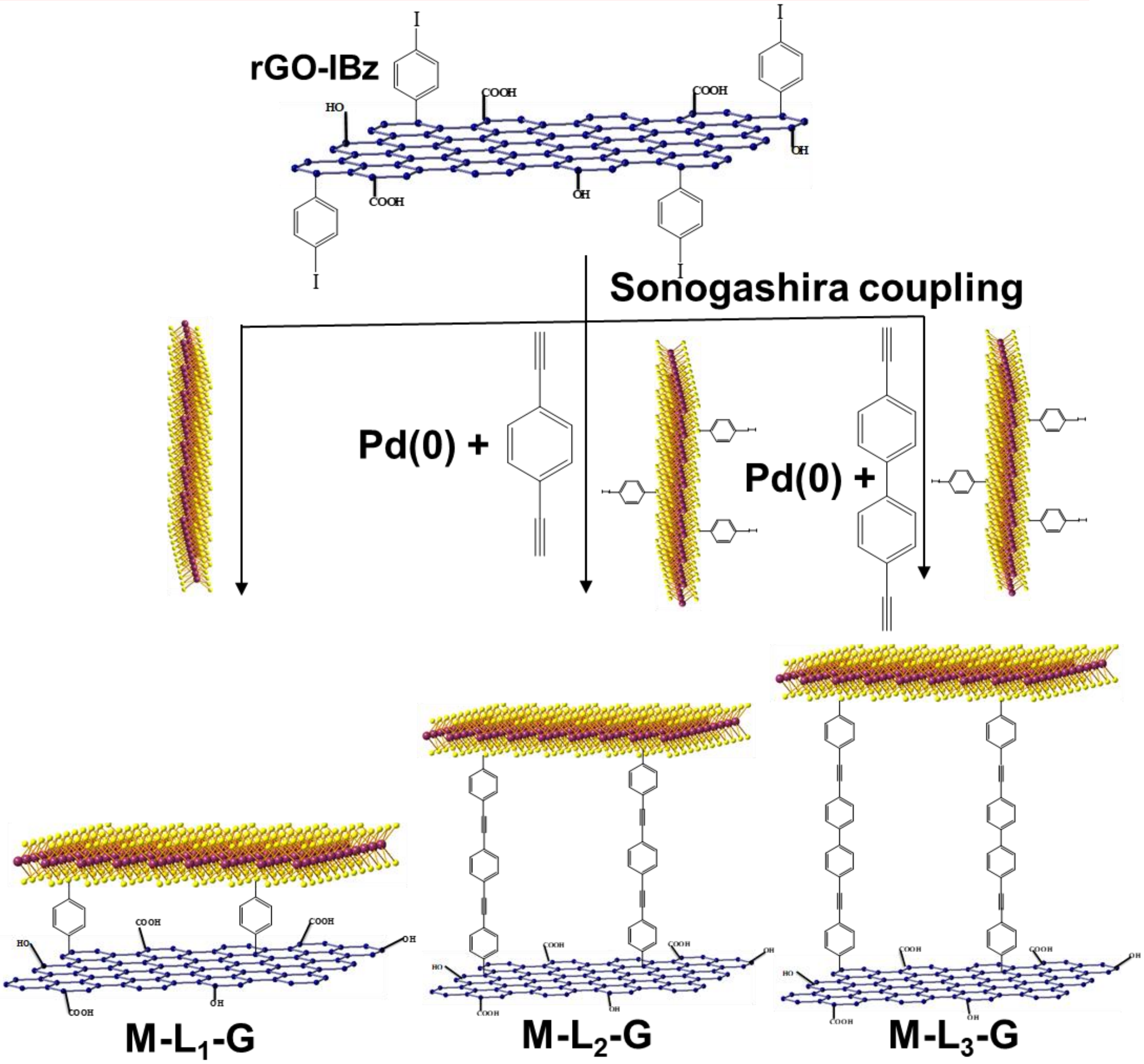

Scheme 3: *Schematic representation of the synthesis of covalently cross-linked nanosheets of* MoS_2 *namely* $M\text{-}L_1\text{-}G$*,* $M\text{-}L_2\text{-}G$*, and* $M\text{-}L_3\text{-}G$ *(C, blue; Mo, maroon and S, yellow).*

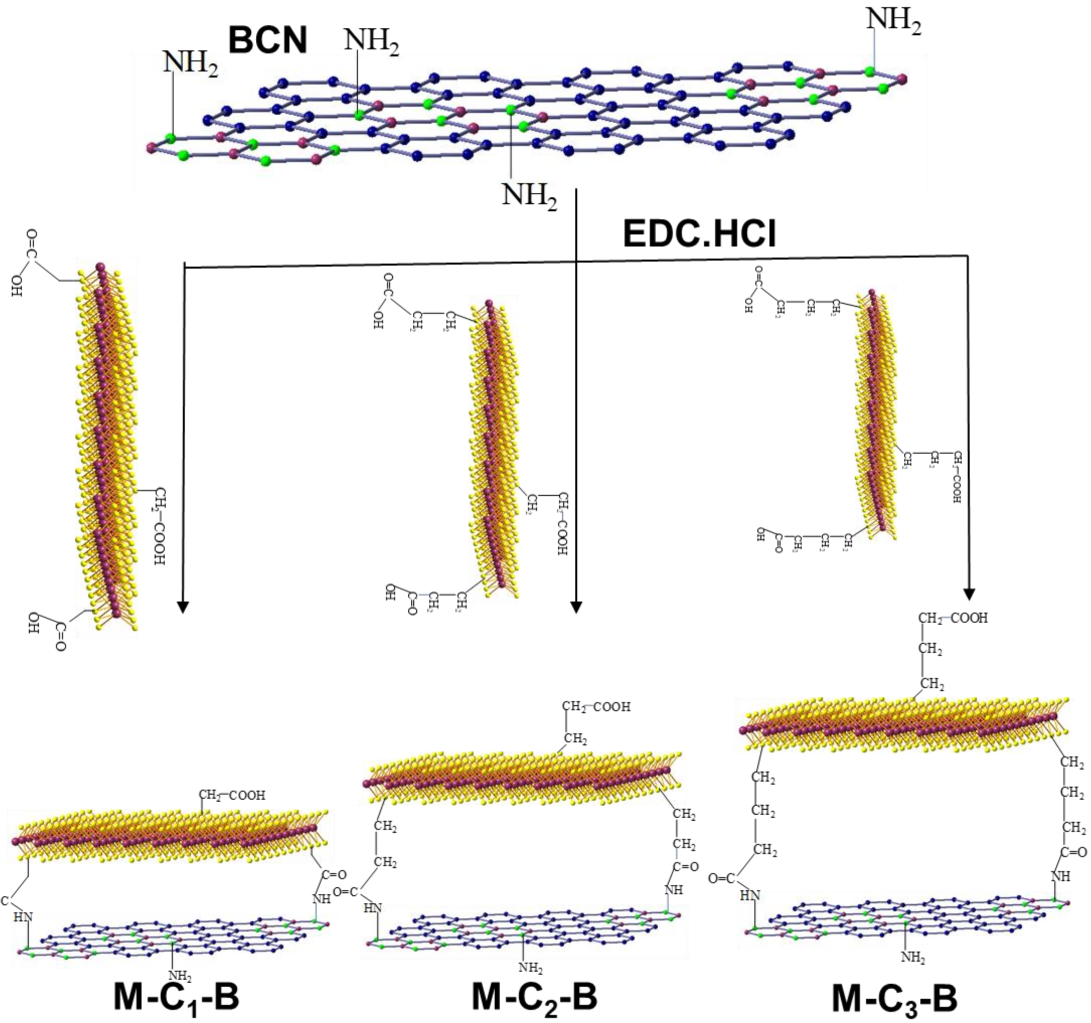

Scheme 4. *Schematic representation of synthesis of covalently cross-linked sheets of MoS_2 with BC_7N namely, M-C_1-B, M-C_2-B and M-C_3-B (C,blue; Mo,maroon; B(green); N,(Red) and S,yellow).*

(ii) Characterizations:

The Infrared (IR) and Raman spectra were recorded using for the samples using Perkin Elmer ATR-FTIR and HORIBA LabRam HR800 spectrometers respectively. Transmission Electron Microscopy (TEM) was taken using JEOL with an accelerating voltage of 80 kV, and scanning electron microscopy analysis of the materials have been performed using was used to do Morphological studies with Nova Nano SEM 600, FEI. PANanalytical Empyrean with Cu K-α radiation was used to obtain Powder X-ray diffraction of the linked-nanosheet.

(iii) Photochemical HER study (Scheme 5):

For the covalently linked sheets, dye-sensitized photocatalytic hydrogen evolution reaction was studied. A cylindrical glass vessel contained 5 mg of the catalyst dissolved in an aqueous solution of triethanolamine (15% v/v, 48 mL) was taken. As a sensitizer, 14 µmol of Eosin Y dye was added to the reaction mixture, which was then continuously stirred while being irradiated by a 400 W Xenon lamp. Using a gas chromatograph with a thermal conductivity detector (PerkinElmer ARNL 580C), the evolved gas was examined.

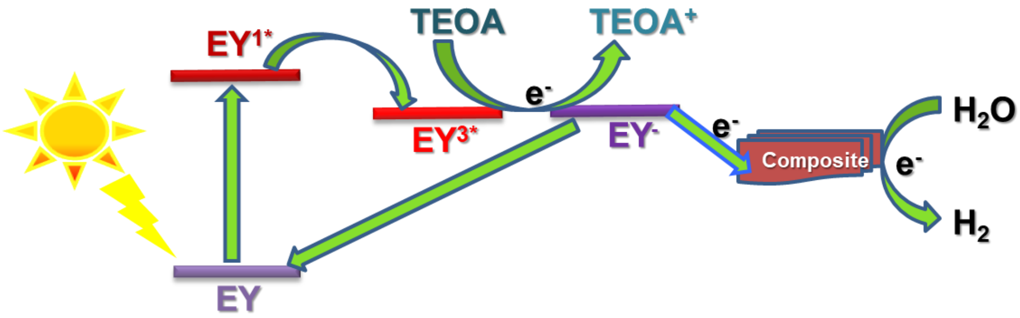

Scheme 5: *Simplified electronic state diagram of hydrogen evolution studied for the catalysts with Eosin Y.*

(iv) Methods of first-principle calculations:

First-principles calculations have been performed using plane-wave density functional theory (DFT) at the level of generalized gradient approximation (GGA) using Perdew-Burke-Ernzerhof (PBE) functional[33] as implemented in the Quantum Espresso package[34]. van der Waal`s interactions were included using the semi-empirical Grimme's-D2 method[35]. The Kohn-Sham wave functions were expanded using plane-wave basis sets with kinetic energy cutoffs for the wave functions 25 Ry (30) and charge density cutoffs 200 Ry (240) for geometry optimization and electronic structure calculations respectively. All the atomic positions were allowed to relax maximum force acting on each atom less than 10^{-3} Ry/Bohr and convergence of energy criteria is set to $1\text{x}10^{-6}$ Ry. The Brillouin zone is sampled using Γ-centered K-point mesh 3x3x1 for relaxation of geometric structures and 5x5x1 for total energy calculations. All the 2D nanosheets were modeled using the supercell method. For

Graphene-Graphene (MoS_2-MoS_2) sheets two graphene (MoS_2) single layers having 3x3 in-plane periodicity were used to connect with the different linker molecules to vary the interlayer separation. To make MoS_2-Graphene and MoS_2-BC_7N sheets 4x4 MoS2 and 5x5 graphene (BC_7N) single layers were connected with linker molecules. The in-plane lattice parameter of MoS_2-Graphene and MoS_2-BC_7N sheets is fixed to 4x4 MoS_2 lattice parameter which introduces a strain of around 1.9% in graphene and BC_7N sheets. A vacuum space of 20 Å or more normal to the composite was used.

4.4. Results and Discussion

(i) Experimental results:

Covalently cross-linked sheets of MoS_2 with itself namely M-L_1-M, M-L_2-M, and M-L_3-M and with graphene M-L_1-G, M-L_2-G, and M-L_3-G were prepared by 1,4-phenylene (L_1), 1,4-diethynylbenzene (L_2) and 4, 4'-diethynylbiphenyl (L_3) as linkers separating the two adjacent sheets.

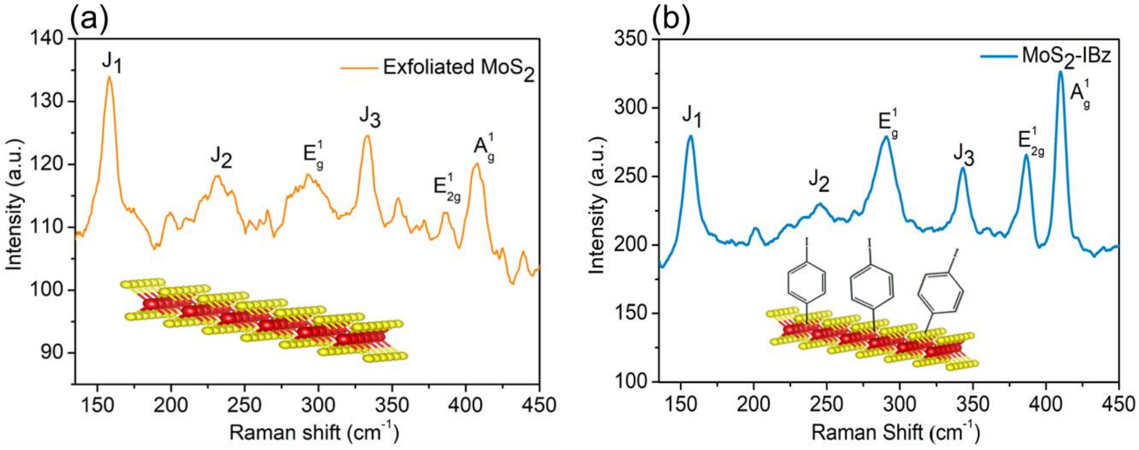

Figure 1: *Raman spectra of (a) Exfoliated MoS_2 (b) iodobenzene functionalized MoS_2.*

The samples were characterized by IR and Raman spectra. The chemically exfoliated MoS_2 had characteristic J_1, J_2, and J_3 Raman bands of the metallic 1T-phase at 158, 231, and 332 cm^{-1} along with E^1_{2g} and A^1_g bands at 383 and 407 cm^{-1} of the 2H-phase respectively shown in **Figure 1(a)**. Iodobenzene functionalized MoS_2 showed Raman spectra similar to exfoliated MoS_2 with enhancement in the intensity of E^1_{2g} and A^1_g indicating that the sample was primarily in the 2H phase shown in **Figure 1(b)**. MoS_2-MoS_2 linked-nanosheet show Raman bands E^1_{2g} and A_{1g} bands of MoS_2 at ≈387 cm^{-1} and ≈408 cm^{-1} respectively, and an additional band ≈1590 cm^{-1} because of C=C stretching bond of the linkers (**Figure 2a**). Raman spectra of covalently linked MoS_2-graphene linked-nanosheet, show the E^1_{2g} and A_{1g} bands of MoS_2 at ≈380 cm^{-1} and ≈406 cm^{-1}, D and G Raman bands of the reduced graphene oxide are observed in the range of 1336-1595 cm^{-1} (**Figure 2b**). A weak band due to C–S bond stretching in the iodobenzene functionalized MoS_2, is observed around 685 cm^{-1} in the infrared (IR) spectra of covalently cross-linked MoS_2-MoS_2 sheets and MoS_2-graphene in the range shown in **Figures 2(c,d)**.

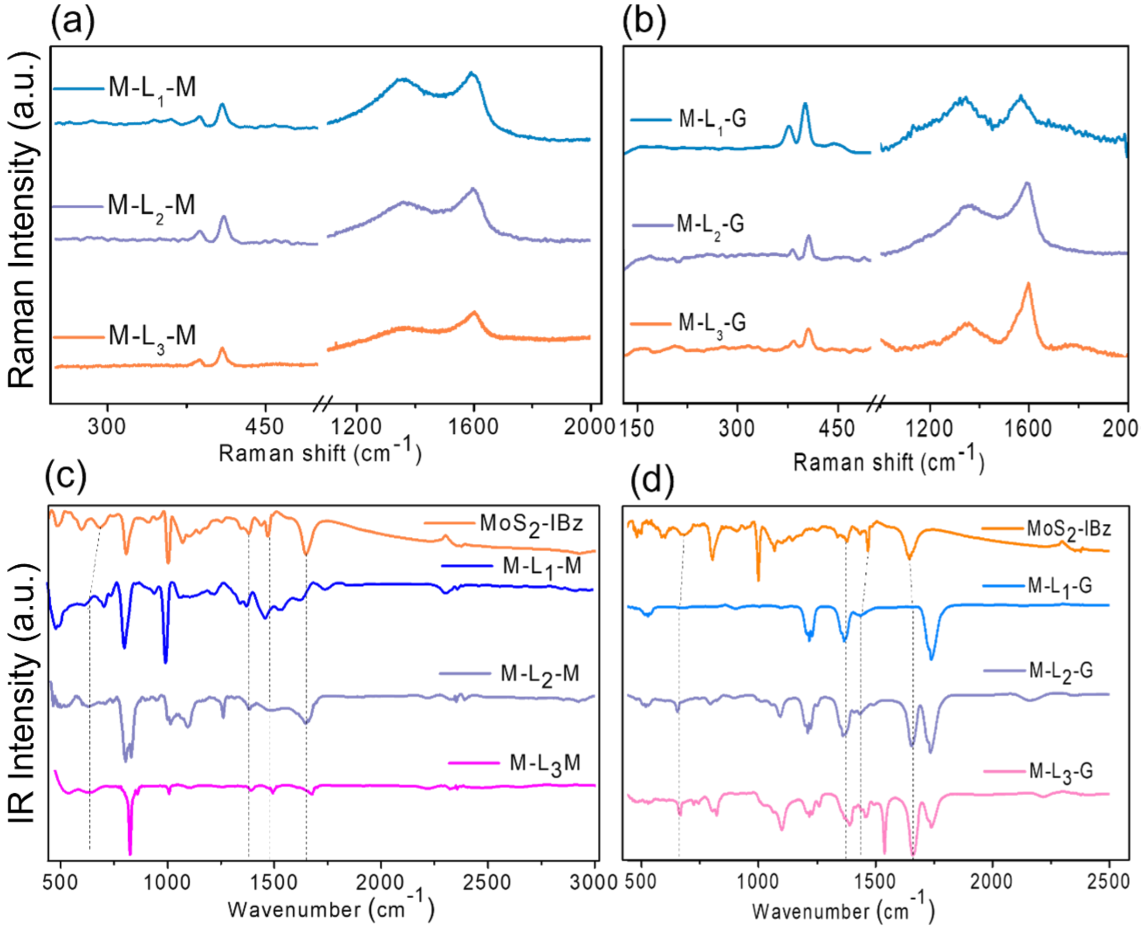

Figure 2: *Raman spectra of (a) covalently cross-linked MoS_2 with another MoS_2 layer and (b) with graphene layer and IR of (c) covalently cross-linked MoS_2 with another MoS_2 layer and (d) with graphene layer.*

The C=C stretching vibrational modes of the benzene rings of the linkers are seen in MoS_2-MoS_2 linked-nanosheet at 1650, 1468, and 1380 cm^{-1} (**Figure 2c**). In the same way, the bands are present at 1660, 1441, and 1380 cm^{-1} due to the C=C for MoS_2-graphene sheets (**Figure 2d**). An additional low-intensity IR band is observed at ≈2212 cm^{-1} in the case of the MoS_2-MoS_2 sheets and in the range of 2130-2220 cm^{-1} for MoS_2-graphene linked-nanosheet due to the C≡C stretching mode shown in **Figures 2(c,d)**. Large area field emission scanning electron microscope (FESEM) images (**Figure 3)** and elemental mapping images of cross-linked of MoS_2-MoS_2 and MoS_2-graphene sheets are shown in **Figure 4 and 5**.

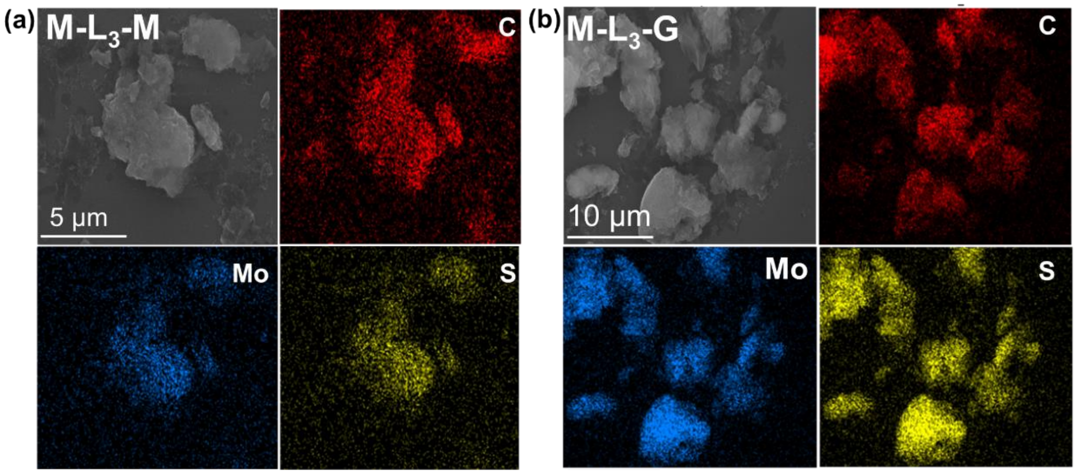

Figure 3: *FESEM image and Elemental mapping images of (a) M-L_3-M sheets and (b) M-L_3-G sheets (C, red; Mo, blue and S, yellow).*

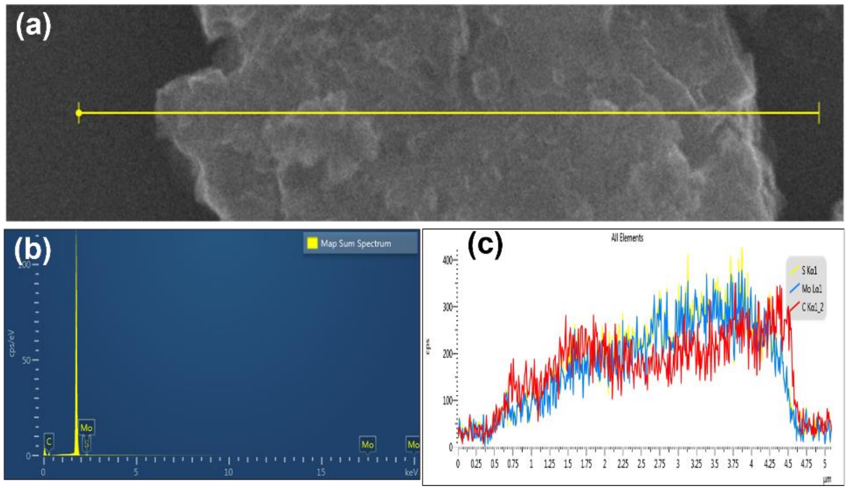

Figure 4: *(a) FESEM image (b) EDS pattern and (c) Line Scan of M-L_3-M sheets.*

The homogeneous distribution of C, Mo, and S in the cross-linked sheets of MoS_2-MoS_2 and MoS_2-Graphene sheets shows that the samples are uniformly formed. Energy Dispersive X-Ray Analysis (EDX), as well as line scanning of covalently cross-linked MoS_2 with itself and graphene, also attribute the homogeneous formation of sheets (**Figures 4 and 5**).

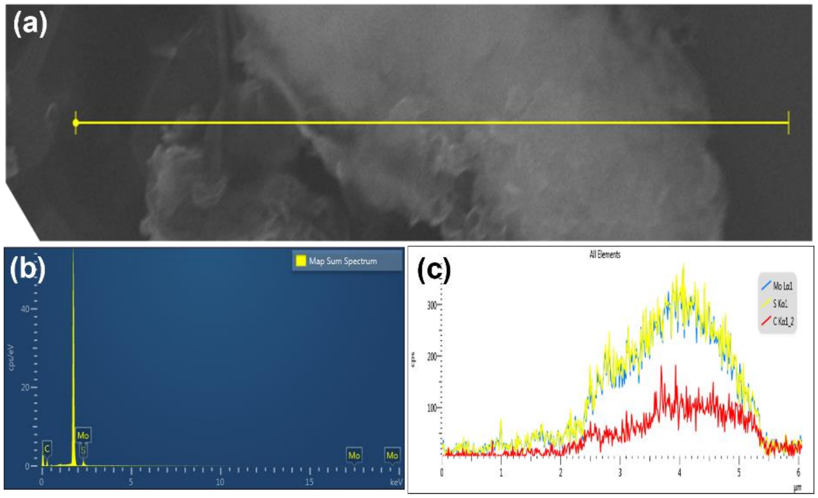

Figure 5: *(a) FESEM image (b) EDS pattern and (c) Line Scan of M-L_3-G sheets.*

Transmission electron microscope (TEM) images of the linked-nanosheet show the presence of layer-by-layer structure obtained due to cross-linking of MoS_2 with itself. HRTEM images of the cross-linked MoS_2 nanosheets show interlayer spacing of 1.68 nm confirming cross-linking of the layers by the linker which is larger than a few layer MoS_2 (0.67 nm) (shown in **Figure 6**).

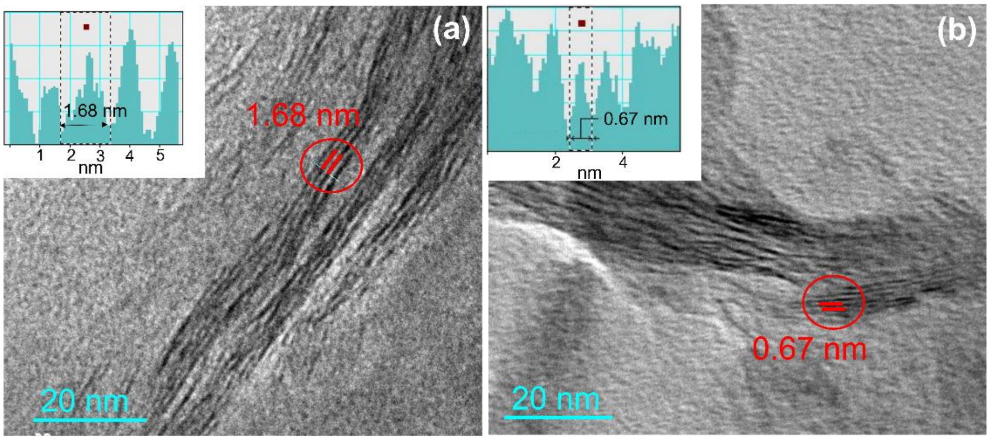

Figure 6: *HRTEM image of (a) M-L_3-M sheets and (b) few layer MoS_2.*

HRTEM images of the cross-linked MoS_2 with graphene show that the interlayer separation increases with increasing linker length which was also observed in X-ray diffraction (**Figure 7**).

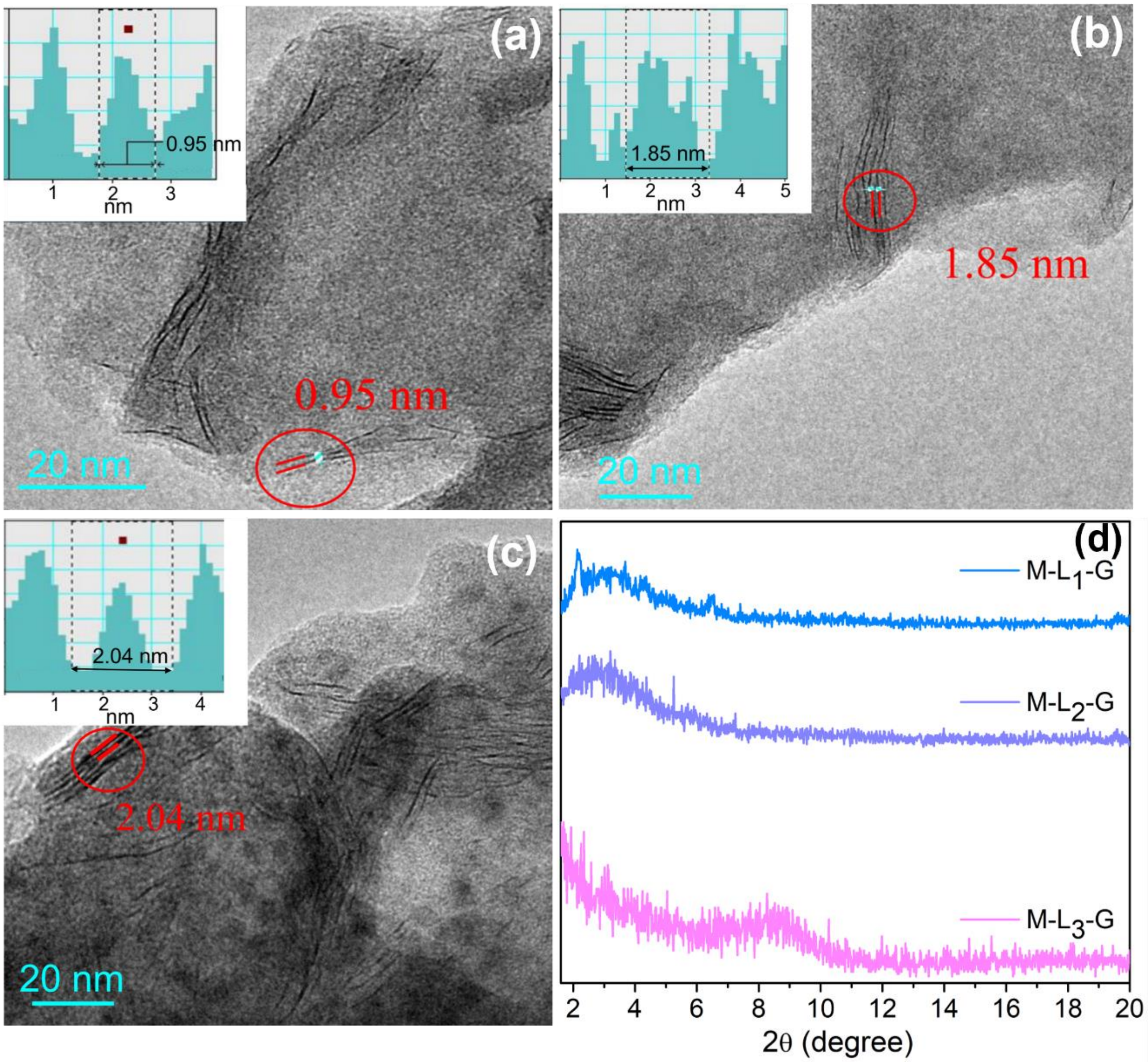

Figure 7: *Transmission Electron Microscope images of covalently cross-linked nanosheets of MoS_2 with graphene (a) M-L_1-G, (b) M-L_2-G, and (c) M-L_3-G. (d) X-ray diffraction of MoS_2-Graphene linked-nanosheets also show a shift to lower 2Θ values.*

Cross-linked MoS_2 nanosheets with graphene with the linkers 1,4-phenylene, 1,4-diethynylbenzene, and 4,4’-diethynylbiphenyl as linkers show a shift to lower 2Θ values in the XRD pattern due to the increase in the interlayer distance between the MoS_2 layers with the increase in linker length (**Figure 7d**).

Hydrogen evolution activity was studied by the dye-sensitized method using Eosin Y as the sensitizer. **Scheme 5** represents the catalytic model used for studying hydrogen evolution.

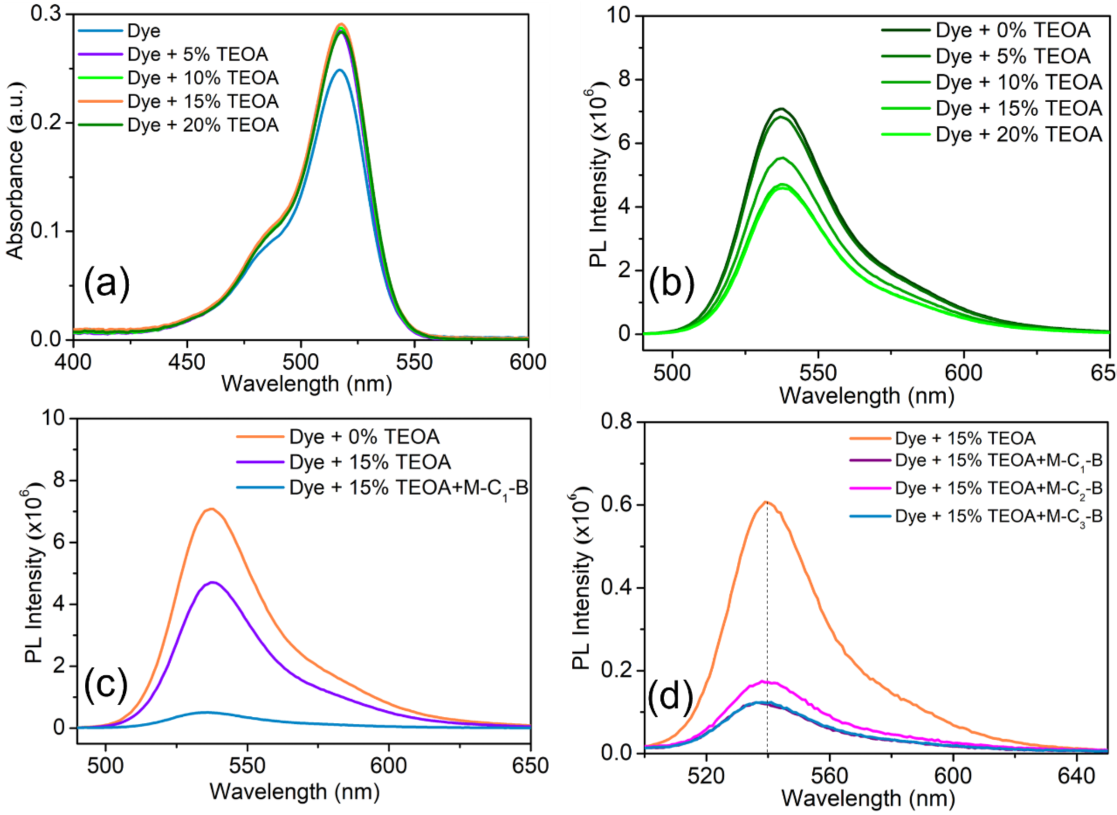

Figure 8: *(a) Ultraviolet-visible light absorption of Eosin Y with increasing concentration of TEAO. Photo-luminescence of (b) Eosin Y dye with increasing concentration of TEAO, (c) with catalyst M-C_1-B at 15% v/v, and (d) with different 2D-architecture.*

On illumination with light, the singlet ground-state as EY gets excited to singlet state EY^{1*} and goes to low-lying triplet state EY^{3*} via an intersystem crossing. The negatively charged state (EY^{-}) forms in the presence of triethanolamine (TEOA) from the EY^{3*}. The electron from the EY^{-} is transferred to the catalyst for the hydrogen evolution reaction[36,37]. We have performed ultra-violet visible light absorption and photoluminescence (PL) studies with an increase in the concentration of TEOA. We observe a systematic decrease in the PL intensity till 15 % V/V of TEOA which drastically decreases with the addition of the 2D architecture.

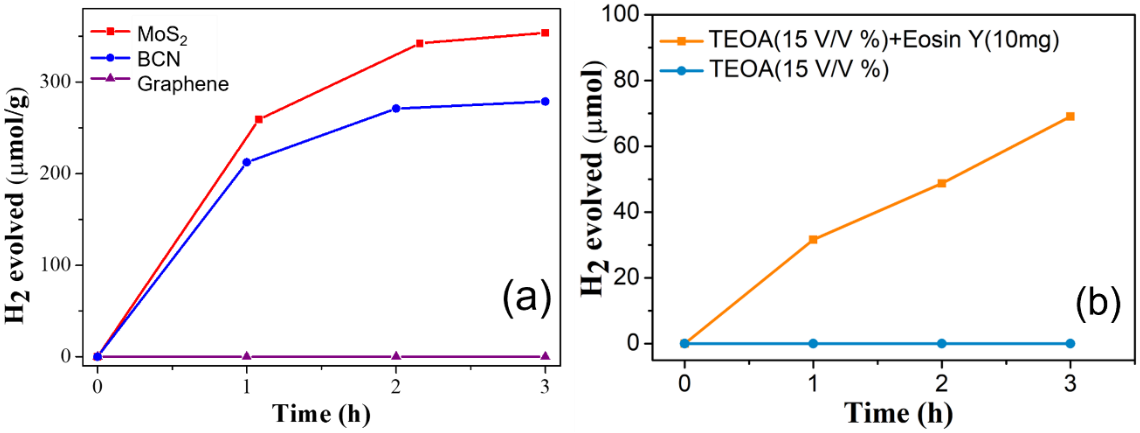

Figure 9: *(a) Hydrogen evolution reaction study of MoS_2, graphene, and BC_7N (b) TEOA (15 V/V %) in absence of Eosin y dye and in presence of 10mg Eosin y dye in 48 mL solution.*

The drastic decrease in the PL intensity suggests that charge transfer takes place from the dye to the catalyst (**Figure 8**). Control experiments show that MoS_2 has HER activity while graphene is HER inactive (**Figure 9a**). There is a negligible formation of hydrogen by TEOA oxidation (**Figure 9b**). This is in accordance with the literature. The nanosheets are more active than MoS_2 due to an increase in the surface area and the available sites for HER on either sheet of MoS_2. To understand the role of linker length on these sheets we studied their photochemical HER activity. The hydrogen evolution activity of MoS_2-MoS_2 sheets M-L_1-M, M-L_2-M, and M-L_3-M were 853, 365, and 255 µmol g^{-1} h^{-1} respectively (**Figure 10a**). The HER activity of the sheets decreases with increasing the linker length (**Figure 10c**). The efficiency of charge transfers decreases with an increase in the linker length. We have linked MoS_2 sheets to the more conducting graphene sheets to enhance the activity of the sheets. In the sheets of MoS_2 and graphene the electrons from the dye flow from graphene to MoS_2. Since graphene is inactive as shown in Figure 9, MoS_2 participates in photochemical HER. We observe that the HER activity of the MoS_2 and graphene sheets, M-L_1-G, M-L_2-G, and M-L_3-G exhibit HER activity of 3720, 1138, and 391 µmol g^{-1} h^{-1} respectively, the value decreases with increasing interlayer distance shown in **Figures 10(b,d)**.

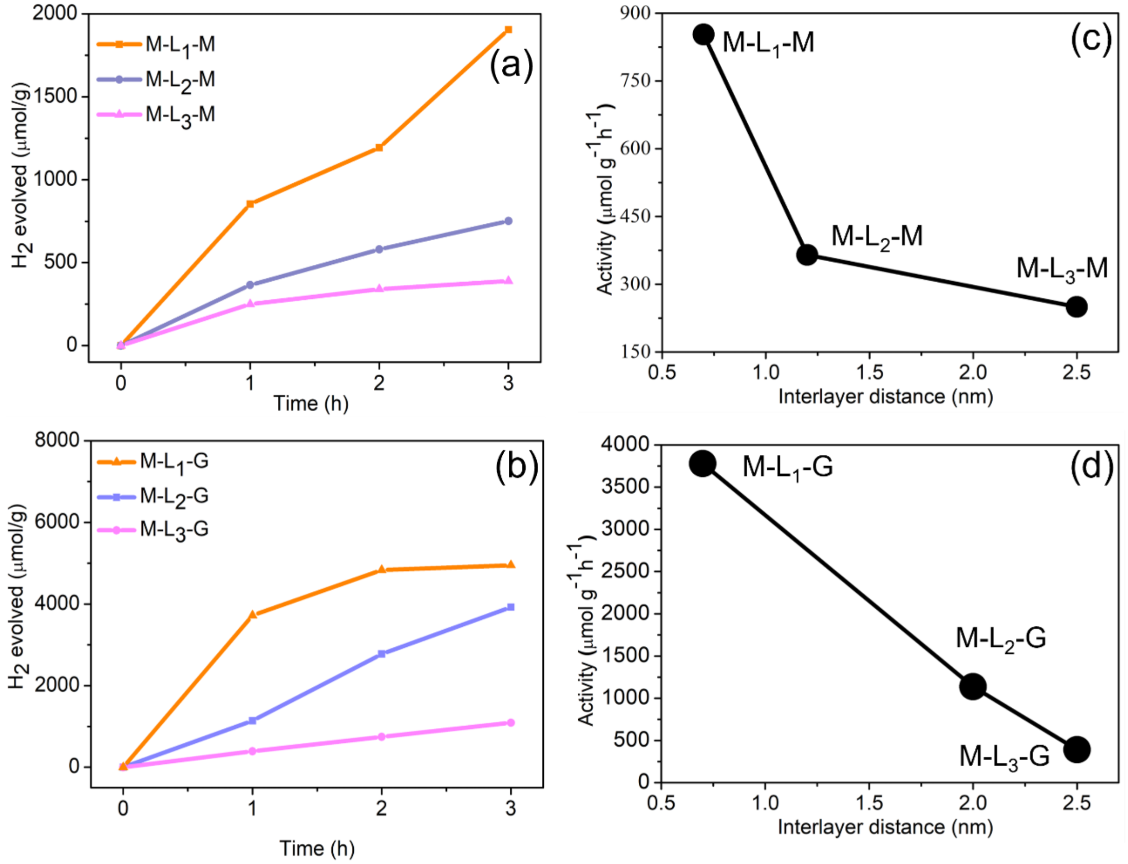

Figure 10: *Hydrogen evolution reaction (HER) study of (a) MoS_2 covalently linked sheets with itself and (b) MoS_2 and Graphene covalently-linked sheets and Comparison of the H_2 evolution activity with the interlayer separation of (c) MoS_2 covalently-linked sheets and (d) MoS_2 and Graphene covalently-linked sheets. The catalyst (5 mg) was sensitized with Eosin Y (4 X 10^{-4} M) dye in 48 ml aqueous solution of triethanolamine (15 % v/v) with visible light irradiation (400W Xenon lamp, with cut-off filter of >399 nm).*

The higher activity of MoS_2-graphene sheets is attributed to charge transfer from graphene to MoS_2 through the network. This is probably due to the built-in electric field at the graphene-MoS_2 interface which facilitates charge transfer across the interface[38]. Our control experiments show that graphene alone is not active under similar conditions studied for HER (**Figure 9a**). Thus, graphene in the nanosheet with MoS_2 acts as a charge transport layer between the MoS_2 layers. The charge transfer in MoS_2-graphene sheets decreases on increasing in the linker length(interlayer separation), therefore, decreasing the overall HER activity (**Table 1**).

Table 1. Photochemical hydrogen evolution activity of covalently cross-linked MoS_2 linked-nanosheet with MoS_2 itself and graphene linked by Sonogashira coupling.

Catalyst	Activity (μmol g^{-1} h^{-1})
MoS_2	259
Graphene	0
M-L_1-M	853
M-L_2-M	365
M-L_3-M	255
M-L_1-G	3720
M-L_2-G	1138
M-L_3-G	391

We have extended our study to BCN-MoS_2 sheets and studied the HER activity with a change in linker length. We have synthesized M-C_1-B, M-C_2-B, and M-C_3-B by varying the linker length by addition of -CH_2 group (**Figure 11**).

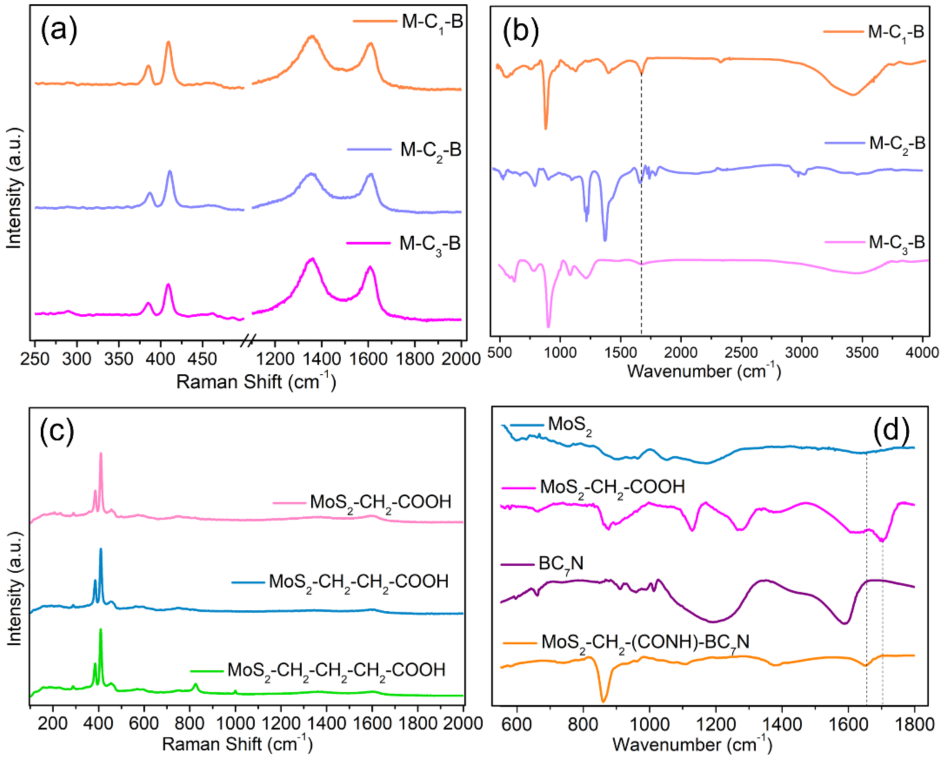

Figure 11: *(a). Raman spectra of the covalently cross-linked nanosheets of MoS_2 with BC_7N and (b) IR spectra of the covalently cross-linked nanosheets of MoS_2 with BC_7N (c) Raman spectra of Acid functionalized MoS_2 with 1-bromoacetic acid, 1-Bromo propionic acid and 1-Bromo butyric acid (b) IR spectra of M-L_1-B sheet.*

Raman spectra of cross-linked MoS_2 with BC_7N for varying interlayer spacing show the D and G Raman bands around ≈1355 and ≈1606 cm^{-1} respectively (**Figure 11a**) which are absent in the spectra of functionalized MoS_2 nanosheets (**Figure 11c**). The IR spectra of MoS_2-BC_7N sheets have a band of ≈1650 cm^{-1} resulting from EDC coupling (**Figure 11b**). The absence of an IR band ≈1705 cm^{-1} corresponds to the acid group present in acetic acid functionalized MoS_2 nanosheets (M-C_1-B) (**Figure 11d**), further confirming the formation of an amide bond.

FESEM images of cross-linked MoS_2-BCN sheets and elemental mapping images of sheets show the distribution of B, C, N, Mo, and S to be uniform (**Figure 12a**). Energy Dispersive Spectra (EDS), as well as line scanning of MoS_2-BC_7N sheets, indicate homogeneous composition (**Figure 12b**). HRTEM images of covalently cross-linked MoS_2 sheets with BC_7N show the spacing between the MoS_2 and BC_7N for M-C_3-B to be 1.01 nm confirming cross-linking (**Figure 12c**).

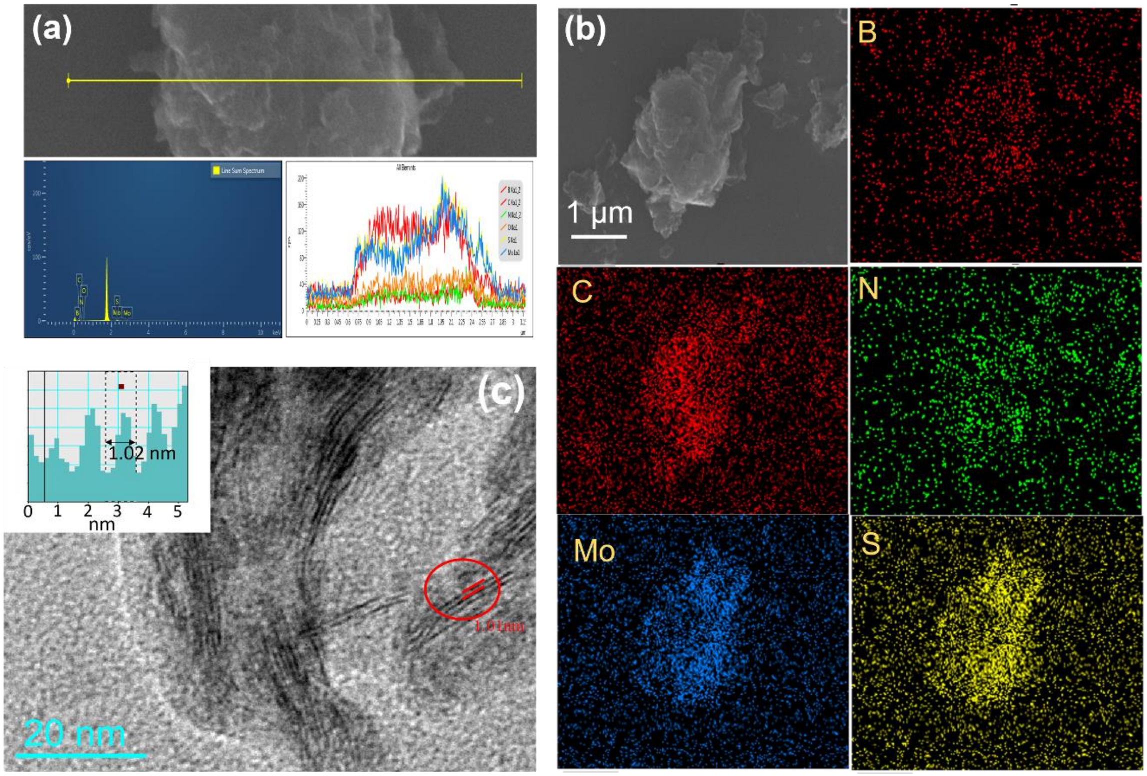

Figure 12: *(a) Line Scan and EDS pattern (b) FESEM image and Elemental mapping (B, dark red; C, red; N, green; Mo, blue; S, yellow) and (c) HRTEM images of M-C_3-B sheets.*

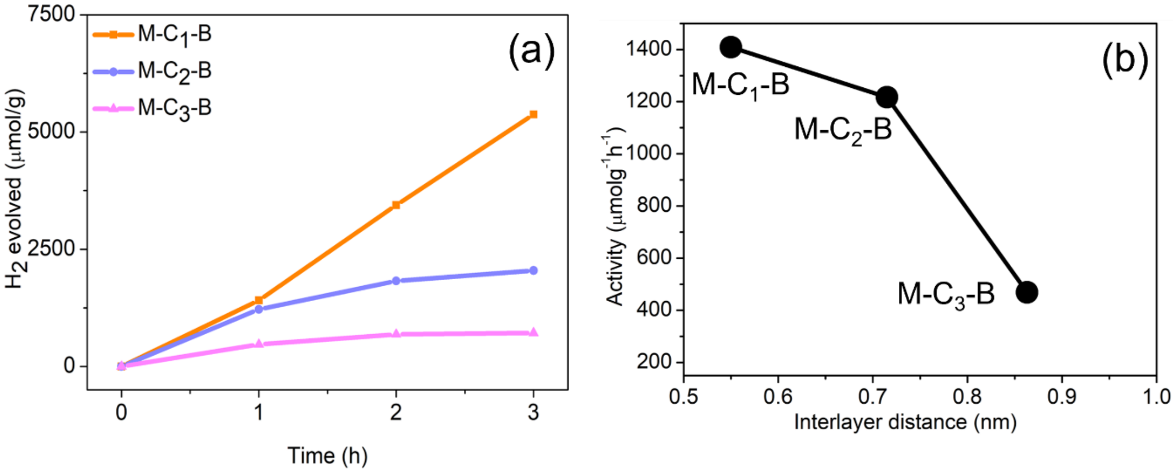

Figure 13: *(a) Hydrogen evolution reaction study of MoS_2 covalently linked with BC_7N and (b) and Comparison of the H_2 evolution activity with the interlayer separation of MoS_2 covalently-linked sheets with BC_7N.*

Both BCN and MoS_2 are active for HER, but MoS_2 is more active (**Figure 9**). M-C_1-B, M-C_2-B, and M-C_3-B exhibit HER activity of 1409, 1317, and 469 μmol $g^{-1}h^{-1}$ respectively (**Figure 13a**). The photochemical HER activity of the sheets clearly decreases with an increase in linker length (**Figure 13b**). The result suggests the role of charge transfer due to directional movements of electrons from BCN to MoS_2 across the layers in the covalently linked layers which is influenced by changing the linker length. Clearly, we see that by increasing the linker length; the HER activity decreases due to decreasing in the charge transfer across the layers (**Table 2**).

Table 2. Photochemical hydrogen evolution activity of covalently cross-linked sheets of MoS_2 and BCN by EDC.HCl Coupling.

Catalysts	Activity (μmol g^{-1} h^{-1})
MoS_2	259
BCN	212
M-C_1-B	1409
M-C_2-B	1217
M-C_3-B	469

(ii) Results of first-principle calculations:

To understand the mechanism behind the photocatalytic HER activity and other properties of covalently cross-linked 2D nanosheets as a function of the linker length, first-principle based DFT calculations have been performed. Graphene-Graphene, MoS_2-MoS_2, MoS_2-Graphene, and MoS_2-BC_7N sheets were studied with the variation in the linker length, for this purpose. The optimized structures of the graphene and MoS_2-based sheets with MoS_2, graphene, and BC_7N with varying linker length sheets with different linkers are shown in **Figure 14**.

The interaction energy (E_{int}) of the sheets is defined as[39]

$E_{int} = E_{LayerA\text{-}Linker\text{-}LayerB} - E_{LayerA} - E_{LayerB} - E_{Linker}$ ---(1)

Where $E_{LayerA\text{-}Linker\text{-}LayerB}$ is the total energy of the composite and $E_{Layer\ A}$, $E_{Layer\ B}$ and E_{Linker} are energies of layer A, layer B, and linker molecules calculated within the composite geometry.

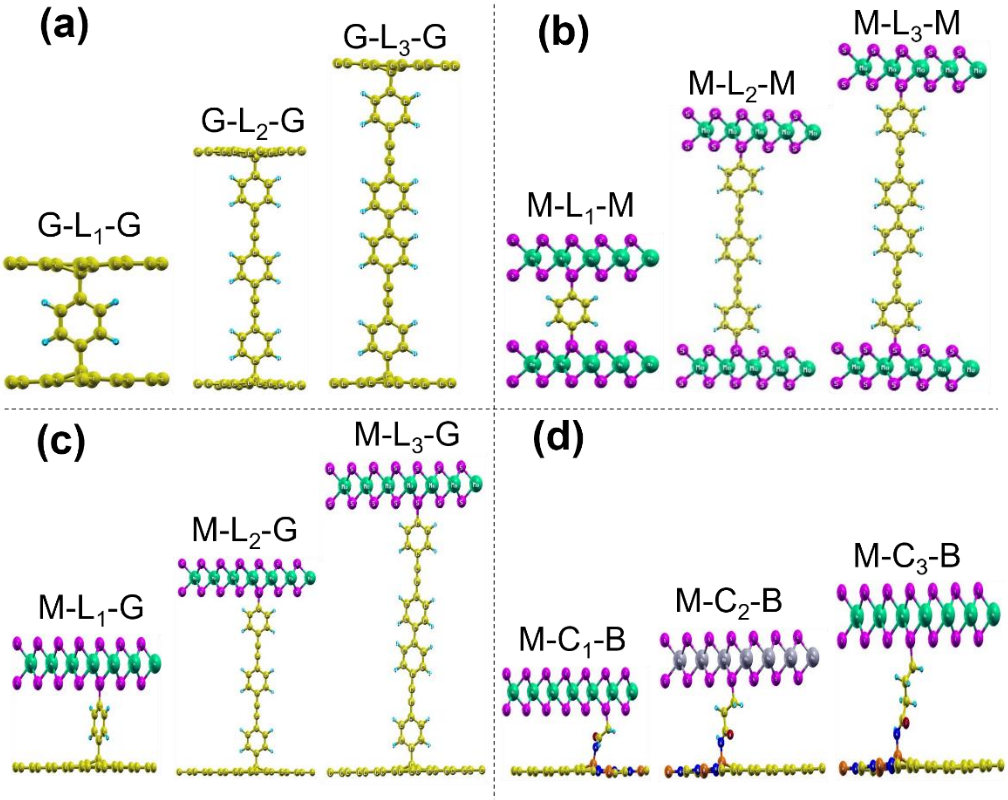

Figure 14: *The optimized structures of the (a) graphene and (b) MoS_2- MoS_2, (c) MoS_2-graphene, and (d) MoS_2-BC_7N with varying linker length (C, yellow; Mo, green; S, purple H, sky; N, blue; O, red; B, orange).*

With this definition, sheets with negative energies are stable. It is important to note that this definition includes deformation in the individual layers as well as in linker molecules due to linked-sheets formation. The calculated bond lengths, interaction energies, and interlayer separation for all the sheets are shown in **Table 3.** We first discuss the properties of graphene-graphene sheets namely Graphene-1,4-phenylene-Graphene (G-L_1-G), Graphene-1,4-diethynylbenzene-Graphene (G-L_2-G), and Graphene-4,4'-diethynylbiphenyl-Graphene (G-L_3-G) as a function of the linker length.

Table 3: Calculated interaction energies E_{int} (eV/linker), Bond lengths (Å), and interlayer separation d (Å) for three sheets.

Linked-sheet	***E_{int}*** **(eV/linker)**	**Bond lengths (Å) (C-C, C-S, B-N)**	**Interlayer separation *d* (Å)**
G-L_1-G	-5.00	1.58 (C-C)	7.0
G-L_2-G	-5.84	1.58 (C-C)	21.0
G-L_3-G	-5.75	1.58 (C-C)	25.0
M-L_1-M	-2.58	1.80 (C-S)	6.5
M-L_2-M	-2.84	1.81 (C-S)	20.3
M-L_3-M	-3.08	1.81 (C-S)	24.5
M-L_1-G	-3.96	1.57 (C-C), 1.80 (C-S)	7.0
M-L_2-G	-4.52	1.58 (C-C), 1.80 (C-S)	20.0
M-L_3-G	-4.53	1.58 (C-C), 1.81 (C-S)	25.0
M-C_1-B	-4.94	1.61 (B-N), 1.83(C-S)	5.5
M-C_2-B	-4.74	1.58 (B-N), 1.84 (C-S)	7.2
M-C_3-B	-4.68	1.58 (B-N), 1.85 (C-S)	8.6

As can be seen from **Table 3** that there is no significant change in the interaction energies of linked-sheets with linker variation. The calculated C-C bond length between linker molecules and graphene sheets is 1.58 Å for all three linked-sheets. The electronic structure such as density of states (DOS) and band structure for the three linked-sheets (**Figure 15**) show a peak in the DOS at the Fermi level E_F due to the covalent linking of graphene sheets with the linker molecules.

The covalent attachment of graphene with the linker molecules breaks the hexagonal symmetry of graphene at bonding sites leading to sp^2 to sp^3 rehybridization in graphene. This leads to the out of plane displacement of the graphene C atom at the bonding site can be seen from the optimized structures of linked-sheets shown in **Figure 14**.

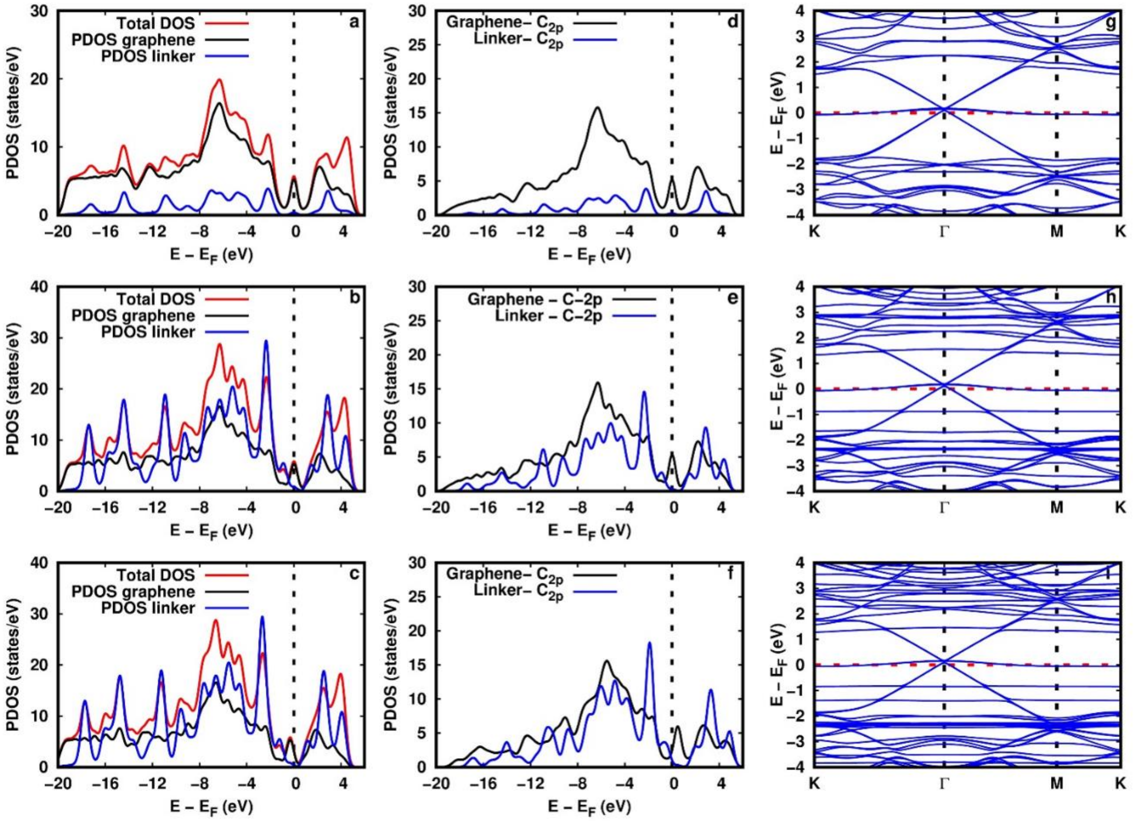

Figure 15: *Density of states (a),(d) G-L$_1$-G ;(b),(e) G-L$_2$-G ; (c),(f) G-L$_3$-G and Band structure (g), (h) (i) of linked-sheets.*

The orbital projected density of states depicts the partial overlap of C-2p orbitals of graphene and linker molecules suggesting covalent interaction between linker and graphene sheets. Band structure plots indicate a small gap opening in the linear dispersion of graphene at the Γ-point and a less dispersive band close to the Fermi level can be seen. This is mainly due to the local distortion in the graphene sheet due to covalent cross-linking with linker molecules. In order to gain insight into the nature of charge transfer, we have plotted the 3D charge density difference and its planar average along the z-direction for three linked-sheets.

The charge density difference is defined as

$$\Delta\rho=\rho_{\text{linked-sheet}}-\rho_{\text{Layer A}}-\rho_{\text{Layer B}}-\rho_{\text{Linker}} \quad \text{--(2)}$$

Here $\rho_{\text{linked-sheet}}$, $\rho_{\text{Layer A}}$, $\rho_{\text{Layer B}}$, and ρ_{Linker} are the charge densities of total composite, layer A, layer B, and linkers respectively. The calculated charge density difference and its plane average of graphene-graphene linked-sheets with the linker variation are shown in **Figure 16**.

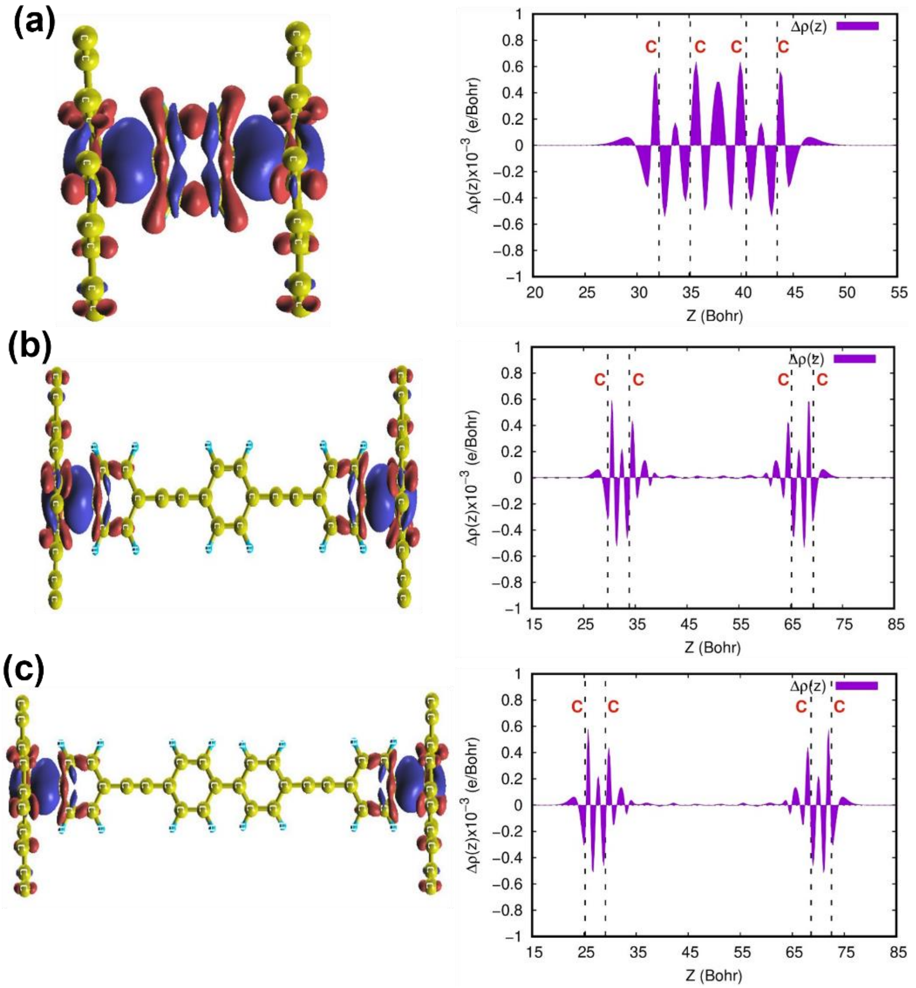

__Figure 16:__ Charge density difference and plane averaged charge density difference for (a) G-L_1-G (b) G-L_2-G (c) G-L_3-G linked-sheets. (C, yellow; H, sky; red, charge accumulation and blue, charge depletion).

The effect of linker length is in the charge density distribution. The charge redistribution is confined only up to one benzene ring of the linker molecule and decreases away from it. A similar trend in charge redistribution can also be seen in other 2D linked-nanosheets. Further, we discuss HER active MoS_2-based linked-sheets. The calculated interaction energies of linked-sheets of MoS_2 with different linker molecules are shown in **Table 3**. The interaction energy (E_{int}) decreases with increasing linker length for MoS_2-MoS_2 and MoS_2-graphene linked-sheets. Whereas for the MoS_2-BC_7N sheets, the variation in interlayer spacing with linker length was small and there was no significant change in interaction energies. From relaxed geometries of linked-sheet, the calculated lengths of C-C, C-S, and B-N bonds between 2D layers and the linker molecules at the contact sites were listed in Table.3. For MoS_2-MoS_2 and MoS_2-Graphene linked-sheets C-S (C-C) bond lengths were ≈1.8 Å (≈1.6 Å) close to typical C-S (C-C) bond lengths in carbon and sulfur compounds. The B-N bond length in the MoS_2-BC_7N linked-sheet is ≈1.6 Å.

The basal plane of layered MoS_2 shows poor HER activity due to its chemical inertness and poor electrical conductivity, which hinder the charge transfer kinetics[40]. It has been reported that chemical functionalization of the MoS_2 basal plane introduces HER active sites and significantly enhances the HER activity[41]. Chemical functionalization through covalent attachment of linker molecules displaces the atoms of the 2D layers at the contact region and breaks the symmetry of the layers leading to increased density of states at the Fermi level (E_F)[42]. It has also been reported that higher electron density at the MoS_2 sheet results in increased HER activity[43]. In the present study of 2D linked-sheets, the MoS_2 sheets provide the sites for HER activity.

The electronic structure of these linked-sheet are depicted in **Figure 17(a-i)**. From the total density of states (TDOS) and projected density of states (PDOS), it can be seen that the increased density of states at the E_F for all three linked-sheet. The significant contribution to increased density of states is from MoS_2 layers as compared to other 2D layers in the linked-sheets and less contribution from linker molecules.

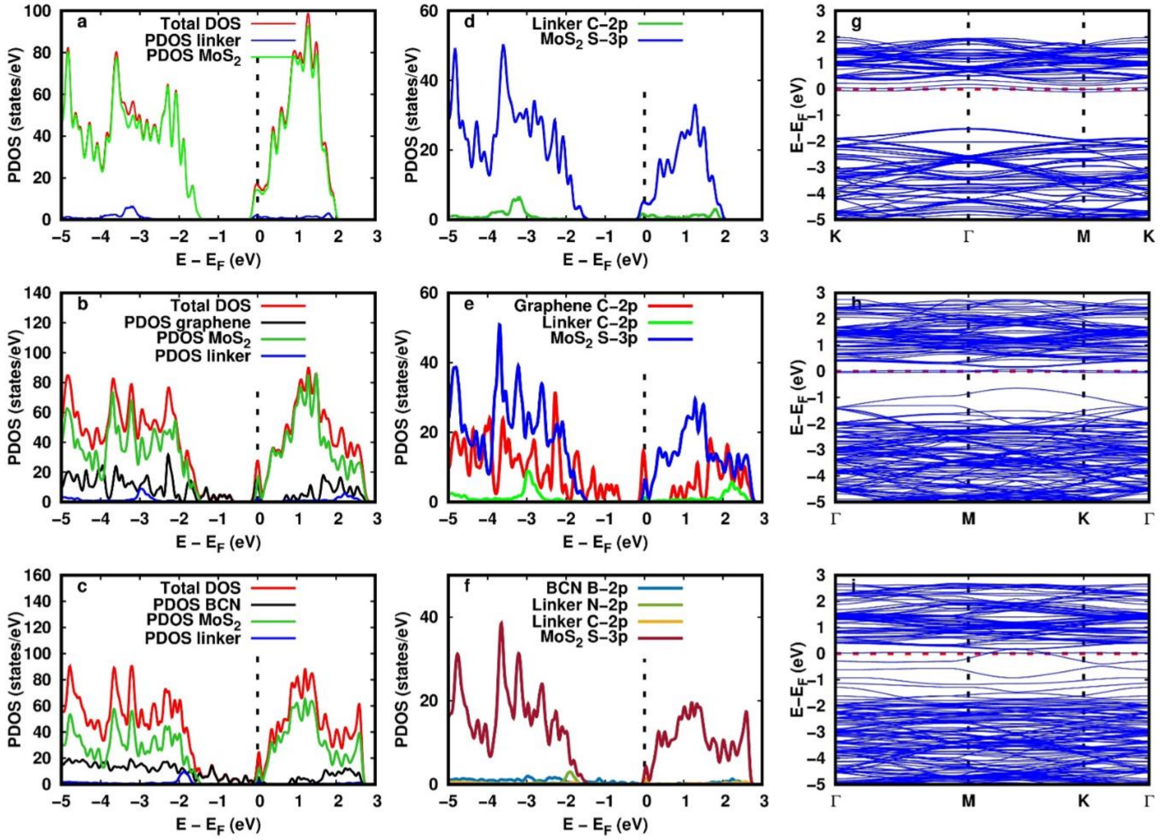

Figure 17: *Total, Projected density of states and band-structure for (a),(d),(g) M-L_1-M (b),(e),(h) M-L_1-G and (c),(f),(i) M-C_1-B linked-sheet.*

The bonding between the linker molecules and 2D layers can be understood from the orbital-projected DOS as shown in **Figures 17(d-f)**. For the MoS$_2$-MoS$_2$ linked-sheet, the energy levels of C and S atoms near the E$_F$ aligned at the same position, and significant overlap between C-2p orbitals of linker molecule and S-3p orbitals of MoS$_2$ indicates covalent interaction. From **Figure 17(e)** in the MoS$_2$-Graphene linked-sheets, graphene C-2p, MoS$_2$ S-2p orbitals overlap with the C-2p orbital of linker at the Fermi level suggests covalent interaction of layers with linker molecule by forming C-C and C-S bonds. MoS$_2$ and BC$_7$N sheets form C-S and B-N bonds with linker molecule which can be seen in **Figure 17(f)** form the overlap of corresponding atomic orbitals.

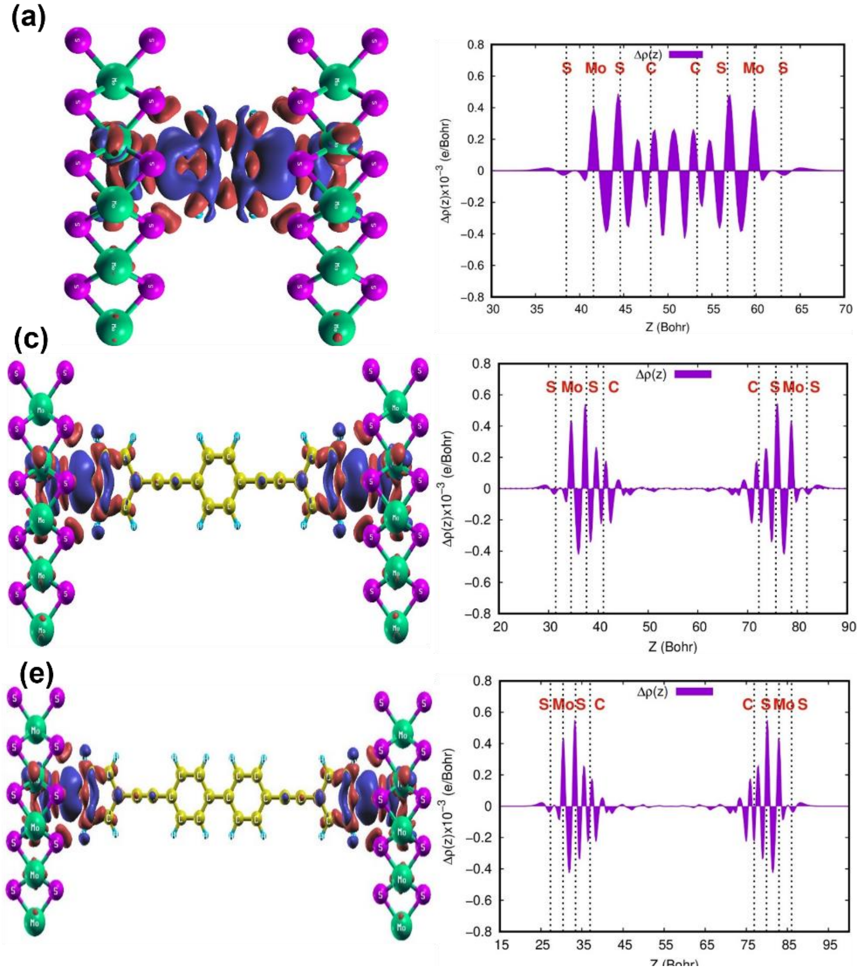

Figure 18: *Charge density difference and plane averaged charge density difference for (a) M-L$_1$-M (b) M-L$_2$-M (c) M-L$_3$-M linked-sheets. (C,yellow; Mo,green; S,purple; H,sky; red,charge accumulation and blue, charge depletion*

Charge density difference plots for MoS_2-MoS_2 linked-sheets with 1,4-phenylene, 1,4-diethynylbenzene, and 4,4'-diethynylbiphenyl linkers respectively are shown in **Figure 18(a-c)**. It can be seen from **Figure 18(a)** that upon covalent linking major charge redistributes at the contact region of 2D layers and linker molecules. Continuous charge accumulation and depletion throughout the linked-sheets via linker molecule serve as a charge transfer channel for photogenerated electrons thus enhancing the HER activity.

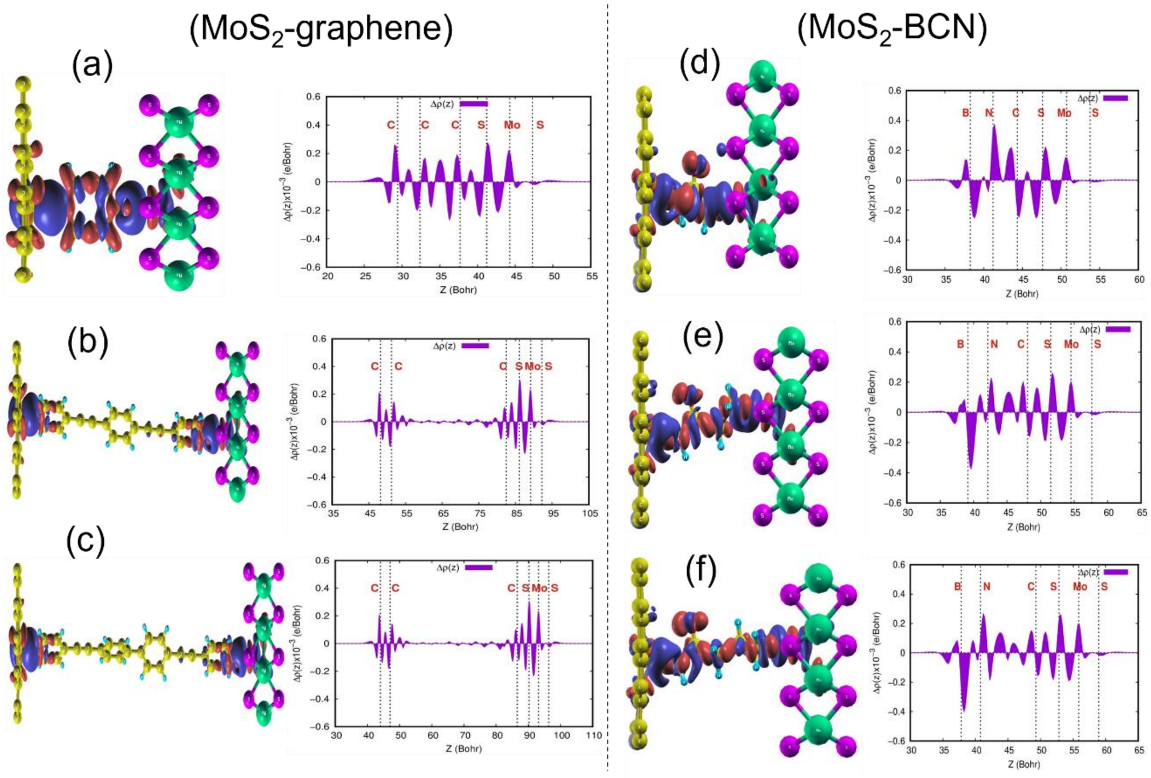

Figure 19: *Charge density difference and plane averaged charge density difference for (a) M-L_1-G (b) M-L_2-G (c) M-L_3-G; (d) M-C_1-B (e) M-C_2-B (f) M-C_3-B linked-sheets. (C, yellow; Mo, green; S, purple; H, sky; red, charge accumulation and blue, charge depletion).*

From the planar average of charge density, the charge accumulation and depletion represent the positive and negative values respectively. The sharp peak at the S layer connected to the linker molecule of both MoS_2 sheets can be seen, and there is no charge accumulation on opposite S layers. Besides, there is significant charge accumulation on the C sites of the linker molecule connected to the S layer. Based on the above data it seems that more charge carriers are located at the cross-linked S layers and these sites can be served as active sites for HER activity. As linker length increases, the charge redistribution confines close to the contact and reduces away from the interface. Due to charge confinement close to the interface in linked-sheets with longer linker length relatively lower HER activity is observed as compared to linked-sheets with short linkers. Because of charge confinement close to the interface, the charge flow between the layer decreases thus lowering the HER activity. The charge density difference for MoS_2-Graphene linked-sheets with 1,4-phenylene, 1,4-diethynylbenzene, and 4,4'-diethynylbiphenyl linkers is shown in **Figure 19(a-c)**. A similar trend in charge redistribution is observed for MoS_2-Graphene linked-sheets with a variation of linker length, the only difference being that one of the MoS_2 sheets is replaced by graphene.

In M-C_1-B, M-C_2-B, and M-C_3-B linked-sheets, continuous charge redistribution throughout the linked-sheets can be seen in **Figure 19(d-f)**. Compare to other linked-sheets the interlayer separation with linker length was small and charge redistribution away from the contact slightly decreases as a function of linker length. Furthermore, the direction of the flow of electrons can be understood from the work function of individual layers of the linked-sheets. The calculated work function of MoS_2, graphene, and BC_7N monolayers is 4.35 eV, 3.95 eV, and 3.57 eV respectively. Among these MoS_2 has the highest work function compared to other 2D layers which indicates that electrons can flow from graphene and BC_7N to the MoS_2 layer upon crosslinking with linker molecules which enhances HER activity. To investigate the mechanism behind the enhanced HER activity of 2D linked-nanosheet, the electronic structure (**Figure 17 (a-i)**), charge density difference (**Figures 18 and 19**), and work function were analyzed. Among the three linked-sheets with different linkers, the M-L_1-G linked-sheets shows the highest HER activity. This can be understood from theoretical investigations that higher electron density at the MoS_2 sheet due to covalent linking and increased charge transfer from graphene to MoS_2 via linker molecule enhances the photocatalytic HER activity.

4.5. Conclusions

MoS_2-based covalently cross-linked linked-sheets exhibit enhancement in hydrogen evolution reaction due to charge transfer across the network of the heterostructures. The enhancement in cross-linked linked-sheets with hetero-layer like graphene and BCN had higher activity than homo-layer MoS_2-MoS_2 linked-sheets. We further investigated the hydrogen evolution properties for these linked-sheets by varying the interlayer distance between the sheets by changing the linker. The decrease in the HER activity with an increase in linker length suggested that interlayer coupling definitely plays important role in influencing the HER activity. The charge transfer between the sheets decreases with increase in linker length resultantly decreases in the HER activity. The theoretical calculations also helped to explain the mechanism behind the enhanced photocatalytic HER activity in 2D linked-nanosheets as a function of linker length. Further, the formation of 2D linked-nanosheets by covalent cross-linking modifies the surface electronic structure of constituent 2D layers leading to the increased electron density on the sheets. Photogenerated electrons from dye efficiently transfer to MoS_2 sheets from other 2D sheets via charge transfer channels provided by linker molecules which were more prominent in linked-sheets with shorter linker length thus enhanced photocatalytic HER activity was observed in them. The interlayer spacing between 2D layers increases with linker length and the confinement of charge redistribution close to the interface region leads to decreased charge transfer between the MoS_2 and other 2D layers thus HER activity is relatively lower than the linked-sheets with short linker length. Charge redistribution is however limited to a short distance in the adjacent benzene ring in the linker. We have demonstrated a variety of properties of covalently cross-linked linked-sheets by varying the nature of 2D nanosheets linked as well as interlayer coupling by changing the linker. This study of opens the way to explore new properties of 2D materials in the cross-linked nanosheets.

4.6. References

[1] Geim, A. K.; Grigorieva, I. V. *Nature* **2013,** 499 (7459), 419-425.

[2] Novoselov, K.; Mishchenko, A.; Carvalho, A.; Neto, A. C. *Science* **2016,** 353, (6298), aac9439.

[3] Das, S.; Robinson, J. A.; Dubey, M.; Terrones, H.; Terrones, M. *Annu. Rev. Mater. Res.* **2015,** 45, 1-27.

[4] Li, M.-Y.; Chen, C.-H.; Shi, Y.; Li, L.-J. *Mater. Today* **2016,** 19, (6), 322-335.

[5] Deng, D.; Novoselov, K.; Fu, Q.; Zheng, N.; Tian, Z.; Bao, X. *Nat. Nanotechnol.* **2016,** 11, (3), 218.

[6] Biroju, R. K.; Das, D.; Sharma, R.; Pal, S.; Mawlong, L. P.; Bhorkar, K.; Giri, P.; Singh, A. K.; Narayanan, T. N. *Nano-technology* **2017,** 2, (6), 1355-1361.

[7] Shi, J.; Tong, R.; Zhou, X.; Gong, Y.; Zhang, Z.; Ji, Q.; Zhang, Y.; Fang, Q.; Gu, L.; Wang, X. *Adv. Mater.* **2016,** 28, (48), 10664-10672.

[8] Feng, S.; Song, J.; Fu, S.; Zhu, C.; Shi, Q.; Song, M.-K.; Du, D.; Lin, Y. J. *J. Mater. Chem. A* **2017,** 5, (45), 23737-23743.

[9] Kibsgaard, J.; Chen, Z.; Reinecke, B. N.; Jaramillo, T. F. *Nat. Mater.* **2012,** 11, (11), 963.

[10] Kumar, R.; Suresh, V. M.; Maji, T. K.; Rao, C. N. R. *Chem. Commun.* **2014,** 50, (16), 2015-2017.

[11] Rao, C. N. R.; Pramoda, K.; Kumar, R. *Chem. Commun.* **2017,** 53, (73), 10093-10107.

[12] Pramoda, K.; Gupta, U.; Ahmad, I.; Kumar, R.; Rao, C. N. R. *J. Mater. Chem. A* **2016,** 4, (23), 8989-8994.

[13] Pramoda, K.; Gupta, U.; Chhetri, M.; Bandyopadhyay, A.; Pati, S.; Rao, C. N. R. *ACS Appl. Mater. Interfaces* **2017,** 9, (12), 10664-10672.

[14] Pramoda, K.; Ayyub, M. M.; Singh, N. K.; Chhetri, M.; Gupta, U.; Soni, A.; Rao, C. N. R. *J. Phys. Chem. C* **2018,** 122, (25), 13376-13384.

[15] Singh, N. K.; Soni, A.; Singh, R.; Gupta, U.; Pramoda, K.; Rao, C. N. R. *J. Chem. Sci.* **2018,** 130, (10), 131.

[16] Park, S.; Park, J.; Abroshan, H.; Zhang, L.; Kim, J. K.; Zhang, J.; Guo, J.; Siahrostami, S.; Zheng, X. *ACS Energy Lett.* **2018,** 3, (11), 2685-2693.

[17] Cai, M.; Zhang, F.; Zhang, C.; Lu, C.; He, Y.; Qu, Y.; Tian, H.; Feng, X.; Zhuang, X. *J. Mater. Chem. A* **2018,** 6, (1), 138-144.

[18] Xie, J.; Zhang, H.; Li, S.; Wang, R.; Sun, X.; Zhou, M.; Zhou, J.; Lou, X. W.; Xie, Y. *Adv. Mater.* **2013,** 25, (40), 5807-5813.

[19] Ye, G.; Gong, Y.; Lin, J.; Li, B.; He, Y.; Pantelides, S. T.; Zhou, W.; Vajtai, R.; Ajayan, P. M. *Nano Lett.* **2016,** 16, (2), 1097-1103.

[20] Voiry, D.; Salehi, M.; Silva, R.; Fujita, T.; Chen, M.; Asefa, T.; Shenoy, V. B.; Eda, G.; Chhowalla, M. *Nano Lett* **2013,** 13, (12), 6222-6227.

[21] Xiong, P.; Ma, R.; Sakai, N.; Nurdiwijayanto, L.; Sasaki, T. *ACS Energy Lett.* **2018,** 3, (4), 997-1005.

[22] Chang, K.; Mei, Z.; Wang, T.; Kang, Q.; Ouyang, S.; Ye, J. *ACS Nano.* **2014,** 8, (7), 7078-7087.

[23] Guo, L.; Yang, Z.; Marcus, K.; Li, Z.; Luo, B.; Zhou, L.; Wang, X.; Du, Y.; Yang, Y. *Energy Environ. Sci.* **2018,** 11, (1), 106-114.

[24] Vikraman, D.; Hussain, S.; Akbar, K.; Truong, L.; Kathalingam, A.; Chun, S.; Jung, J.; Park, H.; Kim, H. *ACS Sustainable Chem. Eng.* **2018,** 6, 8400-8409.

[25] Li, G.; Zhang, D.; Qiao, Q.; Yu, Y.; Peterson, D.; Zafar, A.; Kumar, R.; Curtarolo, S.; Hunte, F.; Shannon, S. *J. Am. Chem. Soc.* **2016,** 138, (51), 16632-16638.

[26] Liu, P.; Zhu, J.; Zhang, J.; Xi, P.; Tao, K.; Gao, D.; Xue, D. *ACS Energy Lett.* **2017,** 2, (4), 745-752.

[27] Yan, Y.; Xia, B.; Ge, X.; Liu, Z.; Wang, J.-Y.; Wang, X. *ACS Appl. Mater. Interfaces* **2013,** 5, (24), 12794-12798.

[28] Zhang, J.; Wu, J.; Guo, H.; Chen, W.; Yuan, J.; Martinez, U.; Gupta, G.; Mohite, A.; Ajayan, P. M.; Lou, *Adv. Mater.* **2017,** 29, (42), 1701955.

[29] Jahan, M.; Bao, Q.; Yang, J.-X.; Loh, K. P. *J. Am. Chem. Soc.* **2010,** 132, (41), 14487-14495.

[30] Hummers Jr, W. S.; Offeman, R. E. *J. Am. Chem. Soc.* **1958,** 80, (6), 1339-1339.

[31] Moses, K.; Pramoda, K.; Shirodkar, S. N.; Mishra, A. K.; Waghmare, U. V.; Sundaresan, A.; Rao, C. N. R. *J. Mater. Chem. A* **2013,** 1, (19), 5806-5821.

[32] Chhetri, M.; Maitra, S.; Chakraborty, H.; Waghmare, U. V.; Rao, C. N. R. *Energy Environ. Sci.* **2016,** 9, (1), 95-101.

[33] Perdew, J. P.; Burke, K.; Ernzerhof, M. *Phys, Rev. Lett.* **1996,** 77, (18), 3865.

[34] Giannozzi, P.; Baroni, S.; Bonini, N.; Calandra, M.; Car, R.; Cavazzoni, C.; Ceresoli, D.; Chiarotti, G. L.; Cococcioni, M.; Dabo, I. *J. Phys. Condens. Matter* **2009,** 21, (39), 395502.

[35] Grimme, S. *J. Comput. Chem*. **2006,** 27, (15), 1787-1799.

[36] Gupta, U.; Naidu, B.; Maitra, U.; Singh, A.; Shirodkar, S. N.; Waghmare, U. V.; Rao, C. N. R. *APL Mater.* **2014,** 2, (9), 092802.[

[37] Maitra, U.; Gupta, U.; De, M.; Datta, R.; Govindaraj, A.; Rao, C. N. R. *Angew. Chem. Int. Ed.* **2013,** 52, (49), 13057-13061.

[38] Li, H.; Yu, K.; Li, C.; Tang, Z.; Guo, B.; Lei, X.; Fu, H.; Zhu, Z. *Sci. Rep*. **2015,** 5, 18730.

[39] Jha, S. K.; Roth, M.; Todde, G.; Buchanan, J. P.; Moser, R. D.; Shukla, M. K.; Subramanian, G. *J. Phys. Chem. C* **2018,** 122, (2), 1288-1298.

[40] Tang, Q.; Jiang, D.-e. *ACS Catal.* **2016,** 6, (8), 4953-4961.

[41] Tang, S.; Wu, W.; Zhang, S.; Ye, D.; Zhong, P.; Li, X.; Liu, L.; Li, Y.-F. *Phys. Chem. Chem. Phys.* **2018,** 20, (3), 1861-1871.

[42] Liao, T.; Sun, Z.; Sun, C.; Dou, S. X.; Searles, D. J. *Sci. Rep.* **2014,** 4, 6256.

[43] Benson, E. E.; Zhang, H.; Schuman, S. A.; Nanayakkara, S. U.; Bronstein, N. D.; Ferrere, S.; Blackburn, J. L.; Miller, E. M. *J. Am. Chem. Soc.* **2018,** 140, (1), 441-450.

Part II: Chemical Vapor Deposition (CVD) and Atomic Layer Deposition (ALD) of Thin Films of Metal Chalcogenides

Chapter 5

A Brief Overview of Chemical Vapor Deposition and Atomic Layer Deposition

Summary

Chemical vapor deposition (CVD) and atomic layer deposition (ALD) are chemical vapor phase techniques to deposit high quality thin films of materials with control over the thickness at an Ångstrom or monolayer level.

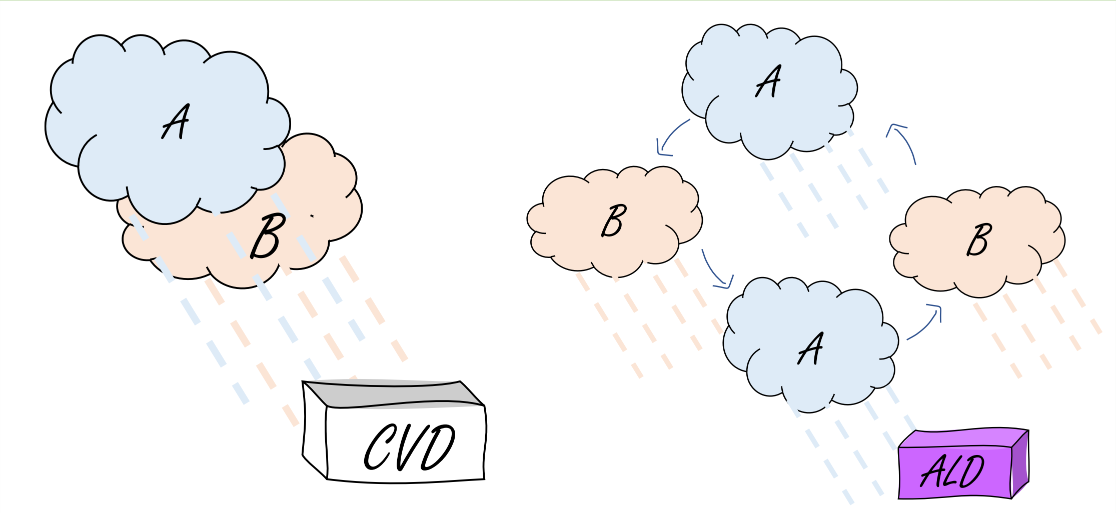

CVD reactions are semi-surface or source-controlled processes which can provide highly uniform films. However, ALD works on a sequential self-saturating reactions and a surface-controlled process, materials can be deposited in the 3D space with a high aspect ratio (highly conformal).

5.1. Introduction

A revolution in the advancement of electronic and photonic industries have occurred in the last decades based on quantum wall, low dimensional structures, and superlattices relying on thin films. Many fascinating discoveries and applications have been made possible by the quick advancements in electronics research and development, including organic light-emitting devices for display and illumination, photodetectors, solar cells, chemosensors, and logic gates. In the mentioned development areas, the deposition processes must be able to participate in the progress by producing multilayered thin films with layer thicknesses defined with subnanometer precision. They are also dictated by the requirements for device performance and fundamental material attributes.

There are several thin-film processing methods available using different kinds of precursors shown in **Figure 1**. For the most part, in order to fabricate devices by thin films, the physical vapor deposition (PVD) process has been explored extensively until recently in which the required material transforms from a condensed phase to a vapor phase and then back to a thin film again in the condensed phase. However, film deposition via chemical processes of the gaseous phase of reactants still has a scope to explore for potential applications.

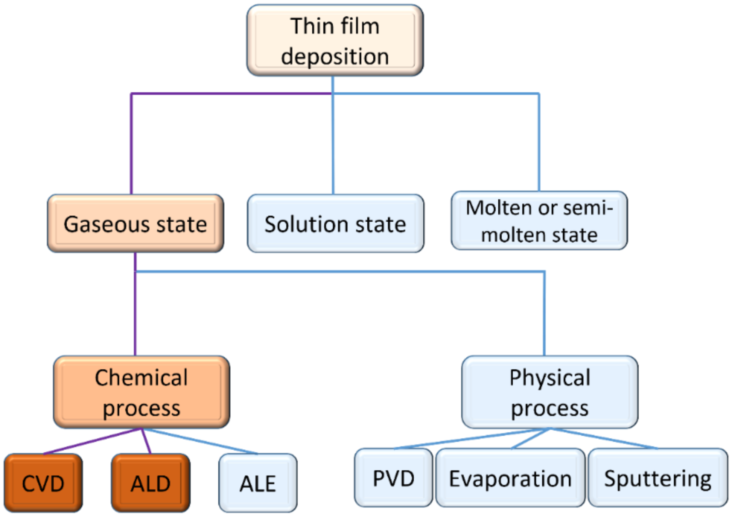

Figure 1*: Representation of thin films deposition methods based on precursors‘ state. (ALE: atomic layer etching).*

5.2. Chemical vapor deposition (CVD)

The CVD processes are being explored, and have the potential to solve many of the technological problems such as mass production and conformality. CVD offers a definite advantage over physical vapour deposition techniques like evaporation and sputtering since it relies on chemical processes that allow for adjustable deposition. In CVD processes, the precursor‘s vapors are first brought into the reactor. Following homogeneous reactions, these vapors may permeate straight through the boundary layer to the substrate to form desired films or can go via gas-phase interactions to produce intermediates and gaseous byproducts. In each instance, the intermediate reactants and the reactant gases disseminate on the heated substrate surface after adhering to it. Through the nucleation process, growth of film, and coalescence, as well as the production of byproducts after the reaction, the succeeding heterogeneous reactions at the gas-solid interface result in constant thin film deposition. Any byproducts in the form of gas and unreacted reactants then desorb from the substrate surface and are transported away from the reactor.

Depending on the advancement of CVD systems and their variants, the properties of products also can be tuned. There are various types of CVD systems available such as horizontal/vertical CVD, low/atmospheric pressure CVD, hot/cold wall CVD, plasma/laser/photo-assisted CVD, metal-organic CVD (MOCVD), atomic layer deposition (ALD) and molecular layer deposition (MLD)[1]. Recently, CVD technologies have been quite successful in the thin film deposition of graphene or carbon nanotubes or any low-dimensional carbon allotropes or transition metal chalcogenides (TMCs). Electrochemical applications need non-line-of-sight deposition on the three-dimensional substrates to obtain conformal coatings. Such types of dense, uniform, and conformal coatings can be easily obtained by ALD and CVD methods. Irrespective of variants in CVD processes, some elementary steps are similar for all the processes which are mentioned in **Figure 2**.

Initially, reactant molecules are injected into the CVD reactor. These reactants molecules can directly diffuse onto the substrate surface through the boundary layer and can be adsorbed and then proceed for the formation of the film through surface diffusion and heterogeneous reactions shown in **Figure 2**. These reactant molecules can form intermediates also via the gas-phase homogeneous reactions that can convert into by-products or start depositing onto the substrate by diffusion/adsorption. In the end, unreacted reactants and by-products are desorbed from the surfaces and forced out of the reactor.

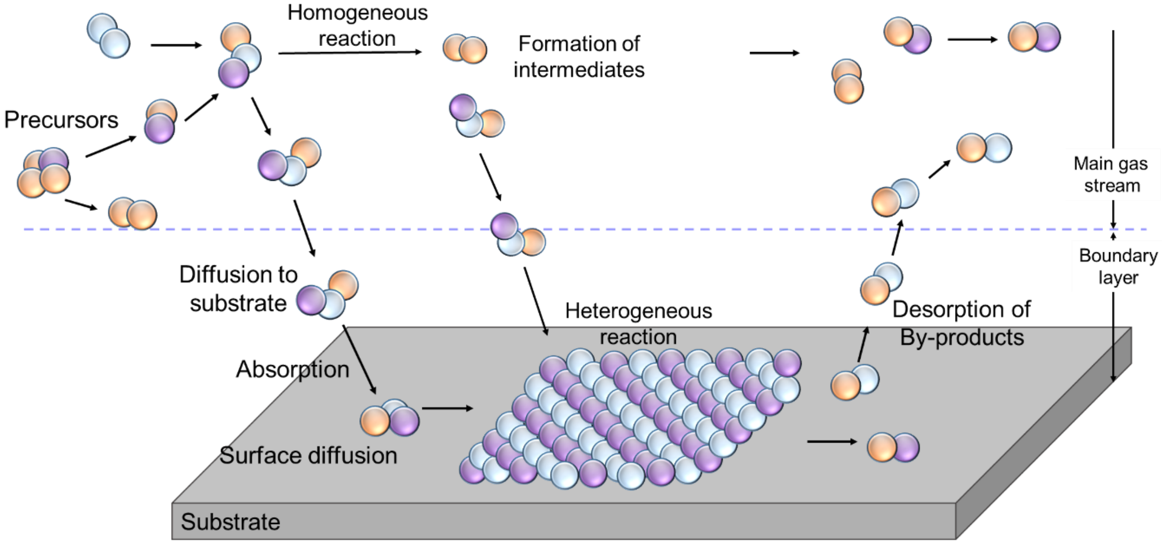

Figure 2*: Representation of general elementary steps involved in a typical chemical vapor deposition.*

CVD has been a better choice because it produced good quality films which are cost-effective and environmentally benign A molten-salt-assisted CVD has been applied to obtain many metal chalcogenides and their heterostructures using a variety of metal oxides as precursors[2]. 2D magnetic TMCs (Chromium chalcogenides : Cr_mX_n, X = S, Se, and Te) have been studied via the CVD method on mica and SiO_2/Si substrates using chloride and chalcogens as precursors[3].

Ta_2O_5[4] and Nb_2O_5[5] thin films for dielectric materials were achieved by using metal alkoxides such as $Ta(OEt)_5$ and $Nb(OEt)_5$. Although good-quality films can be grown using these alkoxides, these precursors have very low vapor pressures and therefore requires high temperature for evaporation. On the functionalization of a donor amine such as dimethyl aminoeth-oxide, $OCH_2CH_2NMe_2$(DMAE) with a metal center leads to a significant increase in vapor pressure[5]. Such donor functionalized precursor ($Nb(OEt)_4(dmae)$) has been explored for the growth of niobium oxide thin films[6]. A wafer size single-crystal Bi_2O_2Se film[7] (shown in **Figure 3**) can also be grown by the CVD process which shows good homogeneity, electron/hole/charge carrier mobilities of up to ~150 cm^{2}V^{-1}s^{-1}, and good switching behavior with large on/off ratio of >10^5.

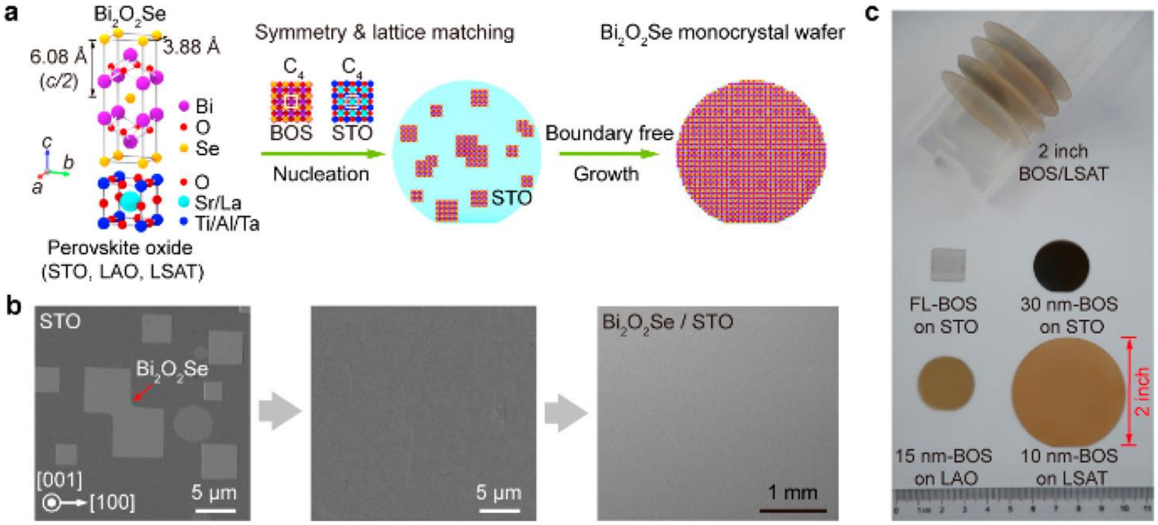

***Figure 3**: (a) Representation of epitaxial single-crystal 2D Bi_2O_2Se films grown by CVD on various substrates. (b) images by scanning electron microscopy (SEM) of Bi_2O_2Se crystals on the substrate of STO (001) grown by CVD. (c) Pictures of grown large-area and different thicknesses of Bi_2O_2Se films from a few layers (FL) thicknesses to 30 nm. Reprinted with permission[7], copyright 2019, American Chemical Society.*

Generally, the CVD growth process does not require any sophisticated instrumentation or high-vacuum environments, but a pressure-controlled mass transport and self-limiting absorption of precursor can enhance the quality of the films. Such a controlled and sequential pulsing of reactants causes the layer-by-layer deposition of thin films and called atomic layer deposition (ALD) or molecular layer deposition (MLD).

Prof. V.B. Aleskovskii made the initial discovery of the ALD method in the 1950s in the Soviet Union[8, 9]. ALD has been demonstrated with different names initially as atomic layer epitaxy (ALE) in Finland and as molecular layering (ML) in the Soviet Union. The concept of ALD was first described in a 1952 publication under the name molecular layering, but it took until the 1970s for research to make a substantial advancement. Prof. Tuomo Suntola and colleagues from Finland filed for the first ALD patent[10, 11].

5.3. Atomic layer deposition (ALD)

ALD has become a crucial process for the production of thin films for numerous applications. One of the primary motivations behind the recent development of ALD has been the processing of semiconductors. ALD is a CVD method for deposition of inorganic materials with the thickness of Ångstrom or monolayer level. The technique is based on the self-saturation of gas-solid reactions that occur on sequential pulsing of reactants[12, 13]. One ALD cycle consists of four repeating steps shown in **Figure 4**. These four repeating steps devided into two half cycles. First half cycle involves follwing steps: step (1) pulsing and self-saturation of reactant A, step (2) purging of reactant A to remove all the by-products.

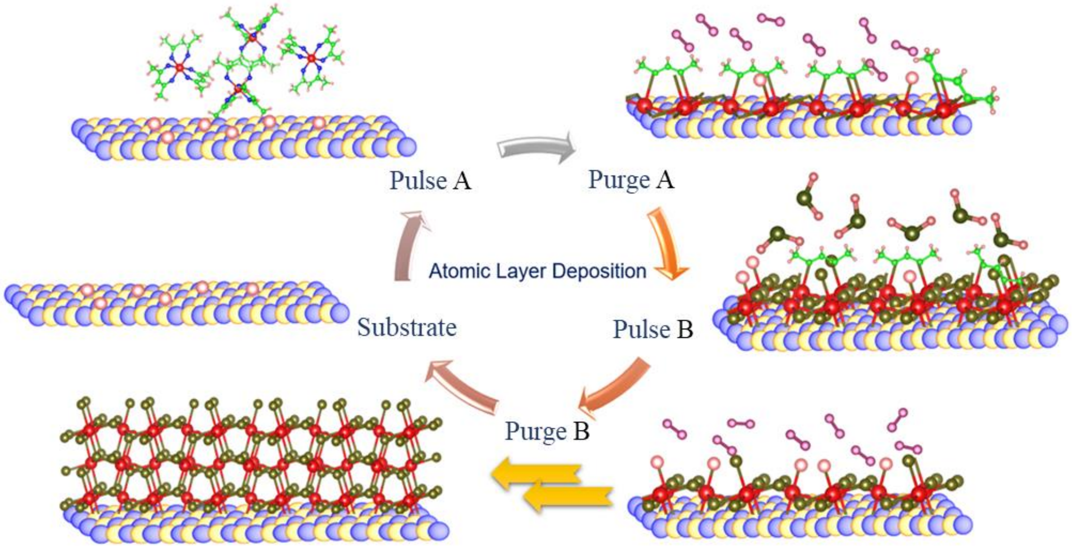

***Figure 4**: Schematic illustration of steps involved in the ALD process.*

Second half cycle further involves follwing steps: step (3) consists of pulsing of reactant B which can react with the functional group of reactant A, and finally step (4) evacuation of non-reacted reactant and by-products again. Self-saturating reactions demonstrate that ALD is a surface-controlled method, with little or no effect from process variables other than temperature, substrate, and reactants. ALD-based films are incredibly conformal and consistent in thickness due to the surface control phenomenon. Due to the self-saturation environment of the surface reactions in the ALD reactors, the reactant flux's randomness is no longer a significant component, which results in a nonstatistical deposition.

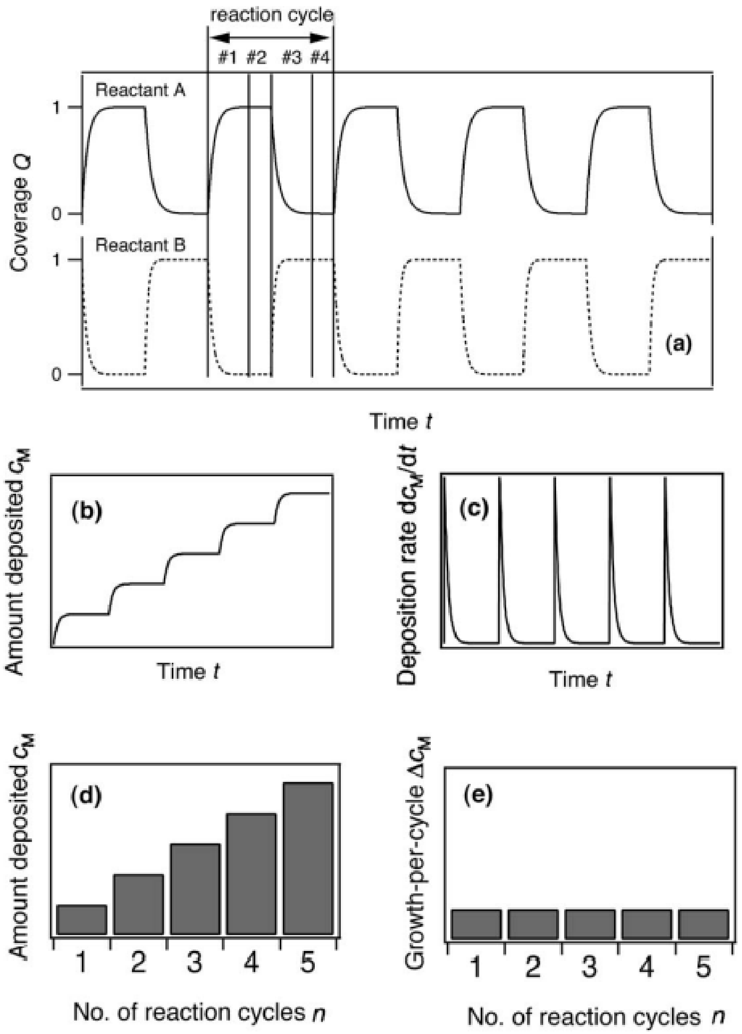

Figure 5: *Schematic illustration of cycles involved in the ALD process. Reprinted with permission[12], copyright 2005, AIP Publishing.*

The growth of thin films in ALD occurs based on chemisorption processes[12]. **Figure 5**(a) shows irreversible chemisorption with coverage (Q) as a function of deposition time. When reactant A enters the reactor coverage increases and gets saturated on termination of the reaction (step 1). coverage increases (step 3) due to the availability of another adsorbed species on the pulsing of reactant B, but coverage of adsorbed species from reactant A decrease up to zero. The coverages remain constant during the evacuation or purging of the precursors (step 2&4). **Figures 5(b) and 5(c)** present the amount of material deposited on the substrate and deposition rate respectively with respect to deposition time. It can be seen that time affects the chemisorption coverage in different ways and the process is in a transient state. **Figure 5(d)** suggests the amount of material deposited linearly as a function of reaction cycles or ALD cycles. In other way, the growth rate per cycle (GPC) has to be constant as shown in **Figure 5(e)** for an ideal ALD process.

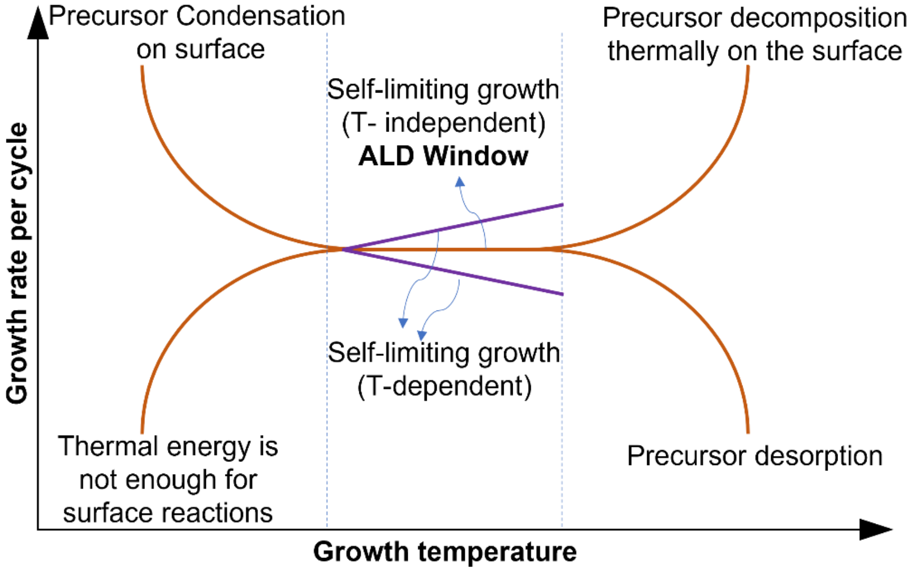

***Figure 6**: Schematic illustration of growth rate as a function of temperature and ALD window.*

Each ALD process has a unique set of chemical and physical requirements that result in a particular GPC and self-limiting growth. Each process is also thought to have a certain temperature range where ideal ALD growth can be observed. **Figure 6** presents growth rate as a function of growth temperature and a set of other reactions that can take place during growth. An ideal ALD process can be defined when the deposition temperature for films belongs within a precise range such that, the growth rate should be constant (independent of temperature). However, it is noticed that the rate can be higher when there is precursor condensation or decomposition on the substrate. A lower growth rate also can be seen when reactants do not have enough thermal energy to react to others or desorption takes place.

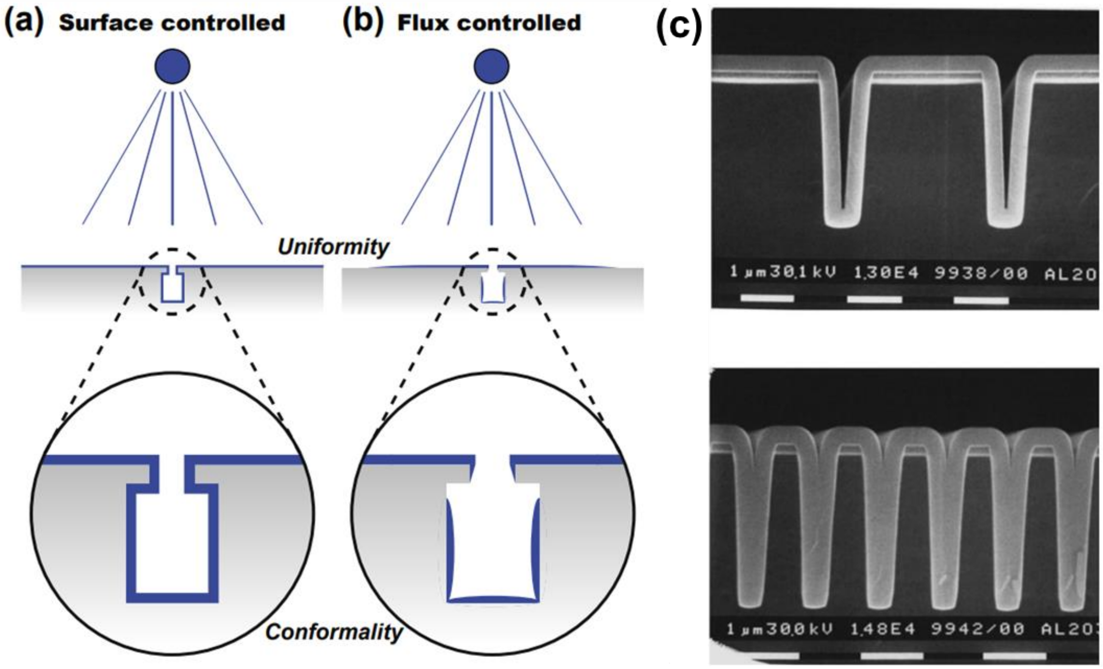

***Figure 7**: Illustration of uniformity and conformality for (a) surface-controlled deposition process and (b) flux-controlled deposition process; and (c) ALD-grown Al_2O_3 thin films. Reproduced with permission [14], copyright 2015, Elsevier, and with permission [15], copyright 1999, John Wiley and Sons.*

The coverage of material in the larger planer area called uniformity and coverage in the three-dimensional space called conformality are very important characteristics of thin films. Their parameters are highly dependent on the control of processes. **Figure 7(a,b)** shows features of uniformity and conformality depending on surface-controlled and flux/source-controlled processes. Since ALD works on a self-saturating nature and a surface-controlled process, materials can be deposited in the 3D space with a high aspect ratio. However other CVD reactions are semi-surface or source-controlled processes so we can expect fewer conformal films. **Figure 7c** shows cross-sectional scanning electron microscopy (SEM) images of 300 nm thick Al_2O_3 thin films on trenched Si wafers[15]. It can be seen Al_2O_3 has been deposited with 100% conformality and trenches are filled with materials and the film is grown continuously.

5.4. Instruments used for deposition of the thin films

A photograph shown in **Figure 8** is Beneq TFS-200 ALD system from Beneq (Finland) that has been installed in our lab. The TFS 200 setup is an example of cutting-edge technological innovation and design that permits the growth of exceptional quality coatings on a variety of substrate types and sizes. It features three separate modes for thin film deposition: thermal, remote plasma, and fluidized bed reactor (FBR). It also has an ozone generator so that it can use ozone as a co-reactant in place of any oxygen source. Six gas lines are connected with the system: two instrument lines for nitrogen, ammonia, hydrogen sulfide, and two plasma lines (nitrogen and oxygen). The TFS 200 system can coat planar objects including wafers, porous bulk materials, complex 3D objects with high aspect ratio features, and particles using FBR mode.

***Figure 8**: Photograph of Beneq TFS-200 ALD system.*

System is currently capable to use two liquid source precursors and one hot source up to 300 °C simultaneously. The installed system also has a crystal microbalance (QCM) and residual gas analyzer (RGA) to monitor the by-products and growth rate.

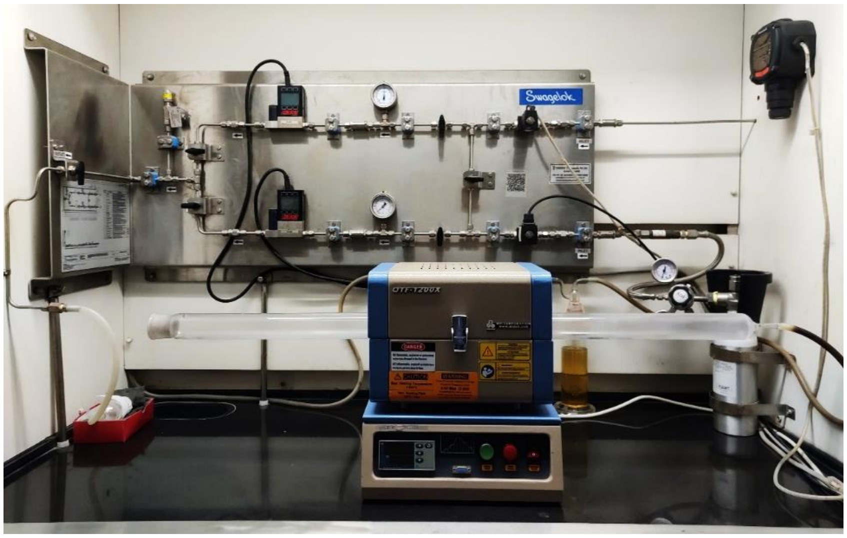

***Figure 9**: Custom builded furnace and gas controlling system for solid-state reaction and thin film deposition.*

A Furnace (OTF-1200X) from MTI corporation is installed for solid-state reaction and CVD processes (**Figure 9)**. A gas-controlling system has been assembled from the Swagelok. Two mass flow controllers were connected for controlled gas flow and mixing parallelly along with pressure gauges. A multi-gas sensor is also connected to the system to avoid gas leaks.

5.5. Summary

To demonstrate the significance of CVD and the advantage it can provide for contemporary industry, the current developments and difficulties of this technology in terms of mass production and controllability have also been addressed. Because of its sequential self-limiting processes, ALD is one of the most efficient ways to meet the demands of the device community for controlled and conformal films. The subsequent chapters deal with the CVD and ALD processes of metal chalcogenides V_2O_3, NbO_2, and NiS.

5.6. References

[1] Sun, L.; Yuan, G.; Gao, L.; Yang, J.; Chhowalla, M.; Gharahcheshmeh, M. H.; Gleason, K. K.; Choi, Y. S.; Hong, B. H.; Liu, Z. *Nat Rev Methods Primers* **2021**, *1* (1), 5.

[2] Zhou, J.; Lin, J.; Huang, X.; Zhou, Y.; Chen, Y.; Xia, J.; Wang, H.; Xie, Y.; Yu, H.; Lei, J. *Nature* **2018**, *556* (7701), 355-359.

[3] Tang, B.; Hu, D.; Zhao, X.; Wang, X.; Liu, Z. *ACS Appl. Electron. Mater.* **2022**, *4* (7), 3303-3324.

[4] Treichel, H.; Mitwalsky, A.; Tempel, G.; Zorn, G.; Kern, W.; Sandier, N.; Lane, A. P. *MRS Online Proceedings Library (OPL)* **1992**, *282*, 557.

[5] Jones, A. C. *Chem. Vap. Depos.* **1998**, *4* (5), 169-179.

[6] Dabirian, A.; Kuzminykh, Y.; Wagner, E.; Benvenuti, G.; Rushworth, S.; Hoffmann, P. *Thin solid films* **2014**, *571*, 94-101.

[7] Tan, C.; Tang, M.; Wu, J.; Liu, Y.; Li, T.; Liang, Y.; Deng, B.; Tan, Z.; Tu, T.; Zhang, Y. *Nano Lett.* **2019**, *19* (3), 2148-2153.

[8] Ahvenniemi, E.; Akbashev, A. R.; Ali, S.; Bechelany, M.; Berdova, M.; Boyadjiev, S.; Cameron, D. C.; Chen, R.; Chubarov, M.; Cremers, V. *J. Vac. Sci. Technol. A: Vac. Surf. Films* **2017**, *35* (1), 010801.

[9] Aleskovskii, V. B. *J. appl. chem. USSR .* **1974**, *47* (10), 2207-2217.

[10] Parsons, G. N.; Elam, J. W.; George, S. M.; Haukka, S.; Jeon, H.; Kessels, W. M. M.; Leskelä, M.; Poodt, P.; Ritala, M.; Rossnagel, S. M. *J. Vac. Sci. Technol. A: Vac. Surf. Films* **2013**, *31* (5), 050818.

[11] Suntola, T.; Antson, J. *US Patents*. **1977**.

[12] Puurunen, R. L. *J. Appl. Phys.* **2005**, *97* (12), 9.

[13] George, S. M. *Chem. Rev.* **2010**, *110* (1), 111-131.

[14] Knoops, H. C. M.; Potts, S. E.; Bol, A. A.; Kessels, W. M. M. In *Handbook of Crystal Growth*, Elsevier, 2015; pp 1101-1134.

[15] Ritala, M.; Leskelä, M.; Dekker, J. P.; Mutsaers, C.; Soininen, P. J.; Skarp, J. *Chem. Vap. Depos.* **1999**, *5* (1), 7-9.

Chapter 6

Metal-Insulator Transition (MIT) in V_2O_3 thin films: Atomic Layer Deposition and Postdeposition Annealing Studies

Summary

Vanadium oxides have gained substantial interest because of the variable oxidation states of vanadium and reversible metal-insulator transitions (MIT) in the particular phases, making them unique from the established semiconductors or insulators. V_2O_3 is deliberated a discrete transition metal oxide, showing first-order MIT from a high-temperature rhombohedral to a low-temperature monoclinic phase.

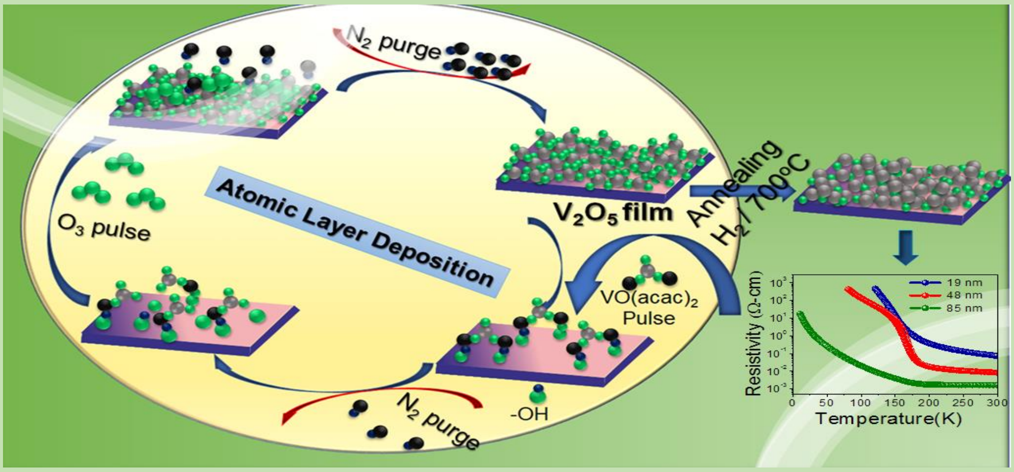

In this work, stable V_2O_3 thin films have been prepared by atomic layer deposition (ALD) using vanadyl acetylacetonate as the vanadium source and ozone as oxidant followed by post-treatment process on the *c*-Al_2O_3 substrate. The obtained V_2O_3 thin films were found to be crystalline, in single-phase and rhombohedral structure. The present ALD process is able to deposite film with a thickness of 48 nm by 1000 ALD cycles at the temperature of 200 °C. V_2O_3 films show a sharp metal-insulator transition (MIT) at a temperature of ≈165 K with jump of five orders of magnitude in the electrical resistivity.

Paper based on this work has appeared in *Phys. Status Solidi RRL* **2021**, 15, 2000565.

6.1. Introduction

Vanadium oxides (VOx) have attracted a lot of attention due to their different oxidation states and reversible metal-insulator transitions (MIT), which distinguish them apart from other insulators or semiconductors. When V_2O_3 transitions from a high-temperature rhombohedral phase to a low-temperature monoclinic phase, it exhibits first-order MIT, making it a unique transition metal oxide. Electrical resistivity drastically increases during this structural change, and this change is correlated with a $3d^1$ electronic configuration of vanadium oxide[1,2]. Using the molecular orbital theory, Goodenough proposed the electronic structure of V_2O_3[3] in which the octahedral crystal field splits the V*3d* orbitals into three-fold t_{2g} and two-fold e_g^σ orbitals. The t_{2g} orbitals further split into non-degenerate a_{1g} and two-fold eπg orbitals because of the small trigonal field. The e_g^π orbital is situated along the basal plane of V pairs and a_{1g} on the *c*-axis. Besides, the e_g^σ orbital is located parallel to the *c*-axis[4]. M-I transition temperature for bulk V_2O_3 is know to be at ≈155 K. Depending on the substrate, V_2O_3 films' electrical resistivity and transition temperature can change[5] and this transition temperature also depends on deposition conditions, a- and c-axes length ratios,[6-8] strain,[9-10] the lattice mismatch between substrate and film,[11] oxygen or vanadium vacancies,[12] and crystalline defects[13-14]. The transition temperature of MIT has been altered by modifying the bulk $V_{2-x}O_3$ stoichiometry and increasing the oxygen fraction, which lowers the transition temperature[15]. It was suggested that Cr raising excess oxygen in the films by preserving the metallic state was the cause of the suppression of MIT in Cr doped V_2O_3 thin films formed on sapphire (0001) substrates[16].

Because of versatile qualities in comparison to other conventional techniques like chemical vapour deposition (CVD) and physical vapour deposition (PVD), etc., atomic layer deposition (ALD) is considered as one of the unique thin film deposition techniques now as days[17-,21]. To date, many studies have reported VO_x films growth using ALD[22-25], but a phase pure V_2O_3 films has been not reported.

6.2. Scope of present investigation

V_2O_3 is a good candidate for device application, hence deposition of pure phase V_2O_3 films and investigating its electrical characteristics are actually recommended. In this work, V_2O_3 thin films were deposited by ALD on a crystalline *c*-Al_2O_3 (0001) substrate utilising successive pulses of VO(acac)$_2$ and ozone at 200 °C, followed by post-deposition annealing. MIT characteristics have been examined and films with various thickness have been used to examine MIT temperature.

6.3. Experimental

Materials:

Vanadyl acetylacetonate (VO(acac)$_2$, Sigma Adrich, 99.9%), Oxygen (Chemix, 99.9995%) and Nitrogen (Chemix, 99.9995%).

(i) ALD of V_2O_5 thin films (Scheme 1):

Using a flow-type ALD reactor (Beneq-TFS 200, Finland Oy), thin films of V_2O_5 were deposited on crystalline *c*-sapphire (0001) substrates by thermal ALD process. Vanadyl acetylacetonate (99.9%) and oxygen gas (Chemix, 99.9995 %) were used as the vanadium source and O_3 source and N_2 (Chemix 99.9995 %) as a purging gas during the deposition with the constant flow of 600 sccm. Vanadyl acetylacetonate was taken in the hot source bubbler HS-300 (Beneq) and heated slowly to 140 ˚C to produce sufficient vapour pressure. Reactor was heated up to 200 ˚C to set the deposition temperature. The temperature of the reactor and hot-source were keep in hot condition for 30 minutes to stabilize the temperature. Depositions of V_2O_5 films were carried out by the consecutive pulsing of VO(acac)$_2$ and ozone, respectively. A typical thermal ALD sequence used was VO(acac)$_2$ pulse/N_2 purge//O_3 pulse/N_2 purge for 3 s (t_1)/4 s (t_2)//2 s (t_3)/4 s (t_4), where t_1, t_3 are the pulsing times of VO(acac)$_2$ and O_3, respectively, and t_2, t_4 are the purging times of the precursors. The ALD depositions were carried out for 500, 1000 and 2000 cycles at 200 ˚C.

(ii) Synthesis of V_2O_3 thin films:

Reduction of V_2O_5 thin films was done at 700 ˚C for 8 h in the presence of hydrogen (chemix 99.9995%) to obtain V_2O_3 thin film where vanadium is present in +3 oxidation state via post-deposition annealing shown in **Scheme 1**.

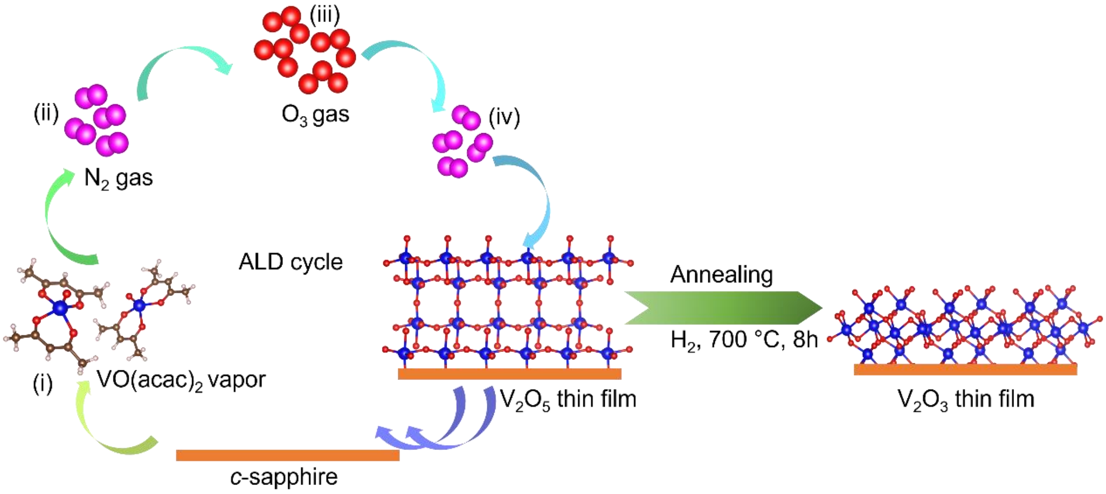

Scheme 1: *Presentation of growth of V_2O_5 film by ALD process and post reduction in presence of H_2 gas to obtain V_2O_3 thin films.*

(iii) Characterizations:

Using monochromatic Cu $K_{\alpha1}$ radiation (=1.540 Å), an Empyrean Panalytical diffractometer was used to produce the X-ray diffraction (XRD) patterns of ALD films. Field emission scanning electron microscopy (FESEM) was used to analyse the surface morphology and film thickness in cross-section mode using the Nova NanoSEM 600 FESEM. An Omicron spectrometer was used to measure the X-ray photoelectron spectra (XPS) using a Mg-K_α X-ray source. A 514 nm Ar laser was used to measure the Raman spectra using a Jobin-YvonLabRam HR spectrometer with backscattering geometry. Atomic force microscopy (AFM) was used to measure the surface roughness of thin films using a contact mode SNL-10 Bruker AFM probe with a 2 nm tip radius. Physical Property Measuring System (PPMS), Quantum Design, USA, was used to measure electrical resistivity.

6.4. Results and Discussion

X-ray diffraction patterns confirm the structure, crystallinity, and conformation of ALD grown V_2O_5 and annealed (V_2O_3) films (shown in **Figure 1**). The long 2θ scan (**Figure 1a**) of the as-deposited film (53 nm) confirms diffraction peak at 2θ ≈20.21° which suggests films exhibit orthorhombic phase of V_2O_5 (Pmmn space group, JCPDS card No. 00-009-0387) and grown preferentially oriented in the (001) direction along with (0006) planes of *c*-sapphire[26].

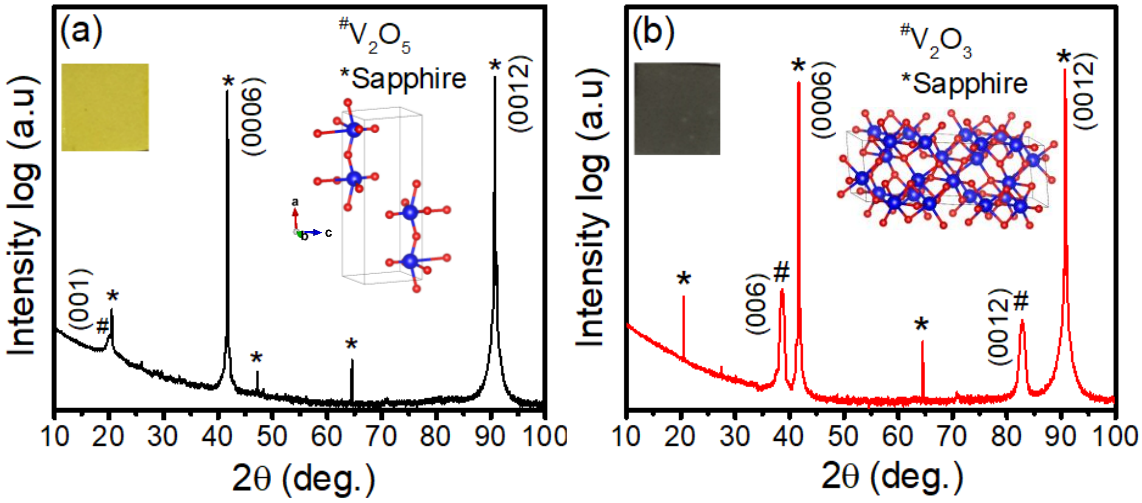

Figure 1: *XRD pattern of (a) V_2O_5 thin film (53 nm) and (b) V_2O_3 thin film (48 nm) grown on c-sapphire (0001) by ALD.*

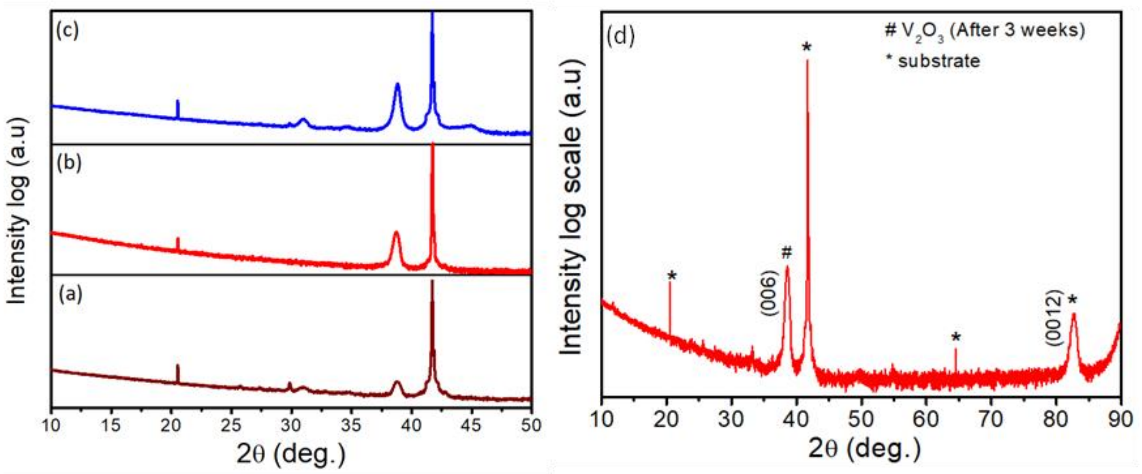

Figure 2: *XRD patterns of different thicknesses of V_2O_3 thin films (a) 19 nm (b) 48 nm and (c) 85 nm, and (d) 48 nm thick V_2O_3 thin film after 3 weeks.*

XRD pattern of the post-deposition annealed V_2O_5 film shown in Figure 1b confirms rhombohedral V_2O_3 phase having *R-3c* space group, (JCPDS card No. 00-026-0278) with preferred orientation of (006) plane at 2θ ≈38.64° and (0012) plane at 2θ ≈82.81° along with planes of *c*-sapphire[27]. As film thickness increases, the full-width half maximum (FWHM) of the (006) reflection of V_2O_3 films decreases due to an increase in crystallinity and long-range ordering in the preferred direction (**Figure 2a-c**). V_2O_3 thin film were found to be stable after 3 weeks also which is confirmed using XRD shown in **Figure 2d**.

We have studied the thicknesses of the V_2O_5 and V_2O_3 films using cross-sectional FESEM images. The average thicknesses of V_2O_5 films deposited by 500, 1000, and 2000 ALD cycles were found to be 22 nm, 53 nm and 89 nm, respectively. Whereas the thickness of V_2O_3 films of 500, 1000, and 2000 ALD cycles were found to be 19, 48 nm, and 85 nm, respectively (**Figure 3 and 4**). The thickness of the V_2O_5 thin films was reduced to a few nanometers after reduction at high temperatures in presence of hydrogen.

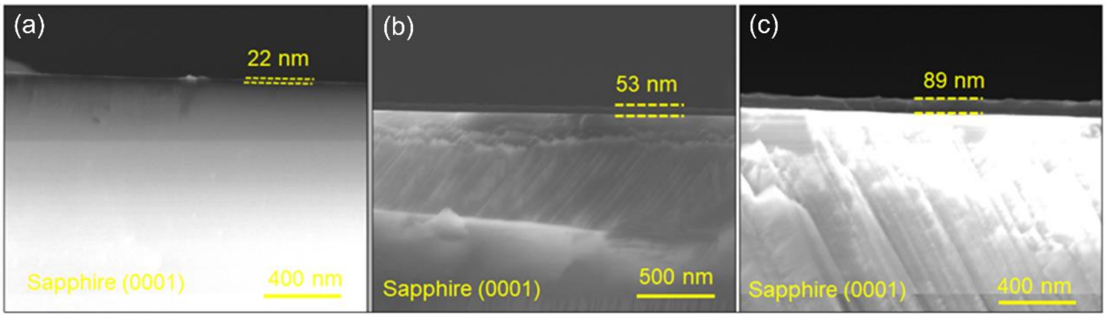

Figure 3: *Cross-section FESEM images of V_2O_5 thin films of (a) 22 nm (b) 53 nm and (c) 89 nm thickness.*

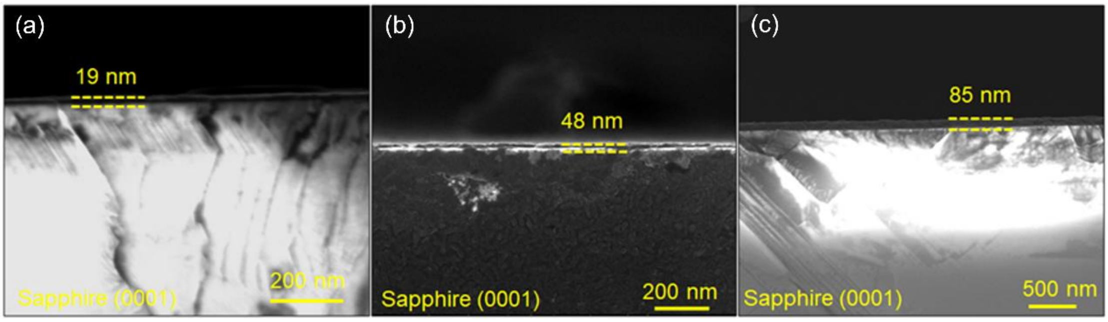

Figure 4: *Cross-section FESEM images of V_2O_3 thin films (a) 19 nm (b) 48 nm and (c) 85 nm thickness.*

Figure 5(a,b) shows the in-plane FESEM and AFM images of as grown 53 nm thick V_2O_5 film and 48 nm V_2O_3 thin film which indicates that both the films show same morphology of the grains. **Figures 6 and 7** show the FESEM images of films with varying thicknesses of V_2O_5 (22, 53, and 89 nm) and V_2O_3 (19, 48, and 85 nm), which illustrate the gradual enhancement in crystalline growth with an increase in film thickness.

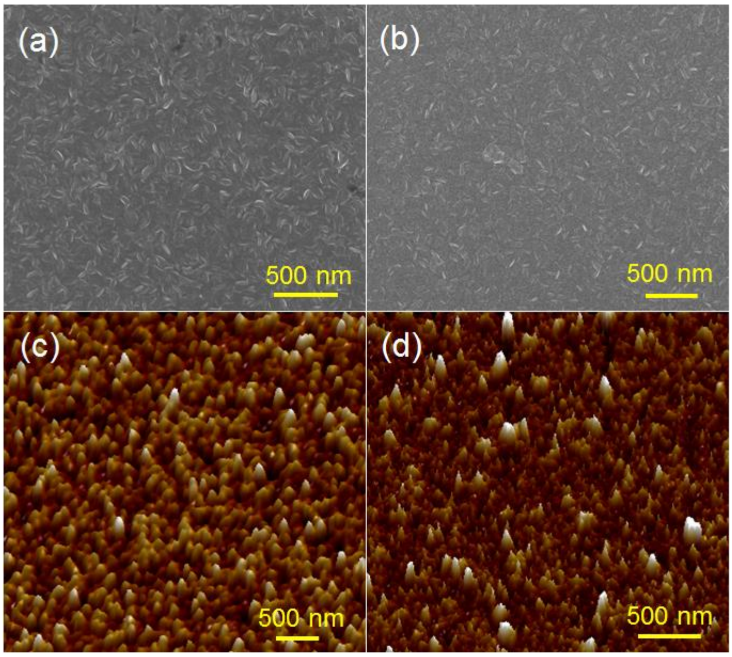

Figure 5: *(a, b) In-plane FESEM images, (c, d) AFM images, of* V_2O_5 *(53 nm) and* V_2O_3 *(48 nm) thin films grown on c-sapphire (0001) by ALD.*

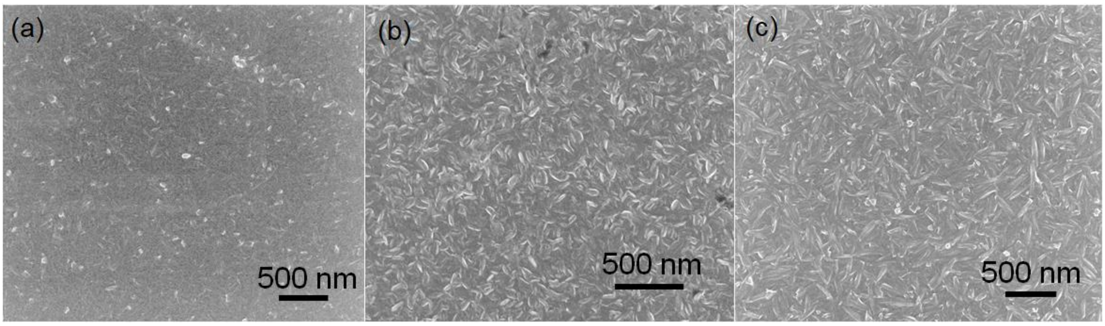

Figure 6: *In-plane FESEM images* V_2O_5 *thin films with different thickness (a) 22 nm, (b) 53 nm and (c) 89 nm grown on c-sapphire by ALD.*

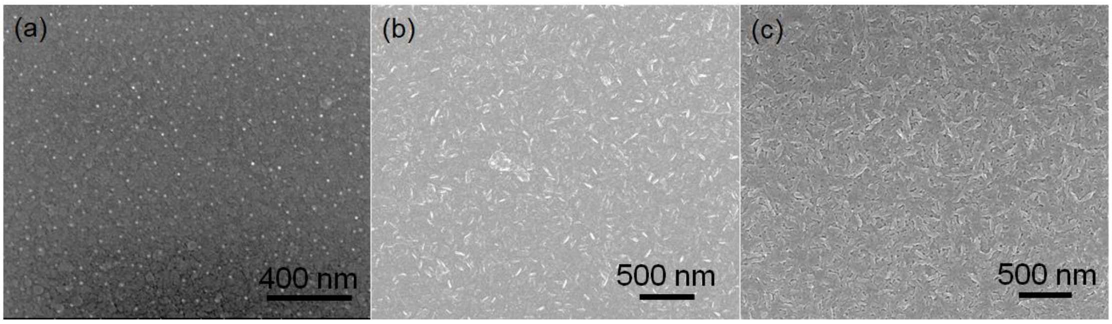

Figure 7: *In-plane FESEM images* V_2O_3 *thin films with different thickness (a) 19 nm, (b) 48 nm and (c) 85 nm grown on c-sapphire by ALD.*

Figure 5(c,d) shows the 3D-view of AFM images of V_2O_5 film (53 nm) and V_2O_3 film (48 nm) confirms the typical roughness of the surface. Root means square

(RMS) roughness of V_2O_3 and V_2O_5 films were found to be 2.9 and 3.7 nm, respectively. RMS roughness of V_2O_3 was found to be lower than V_2O_5, which indicated that V_2O_3 film might be etched up to a few nanometer thicknesses after reducing at elevated temperature (**Figure 5d**). So effect of annealing was observed by FESEM and AFM images of 48 nm thick V_2O_3 films (shown in **Figure 8**). A gradual change in surface morphology and grain formation was observed.

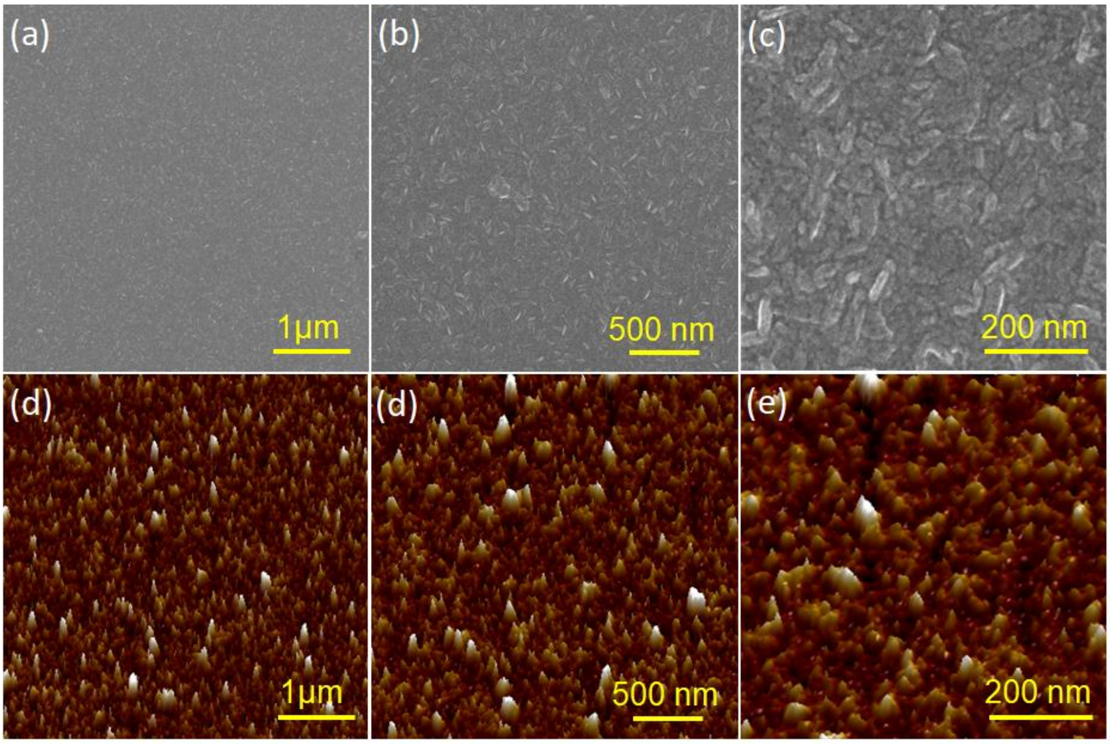

Figure 8: *Low, high resolution in-plane FESEM and AFM images 48 nm V_2O_3 thin films.*

Raman spectroscopy is useful for examining the phases and structures of the materials[26]. Raman spectra of as-deposited 53 nm thick film of V_2O_5 and 48 nm thick film of V_2O_3 films are shown between the range of 100-1000 cm^{-1}. **Figure 9a** shows the characteristic bands whose confirm the α-V_2O_5 phase of vanadium oxide. Raman spectrum of V_2O_3 film at room temperature explains the distinctive bands E_g, A_{1g}, E_g, and A_{1g} phonon modes at 210, 235, 291, and 506 cm^{-1}, respectively (shown in **Figure 9b**). Compared to the bulk[27,28], all the Raman bands of the V_2O_3 thin films were found to be slightly shifted towards the lower energy might be because of reduction of crystallite size and strain in the films. The displacement of vanadium atoms along the *c*-axis usually appears in the A_{1g} mode in Raman spectrum; therefore, a shift in lower wavenumber than the bulk V_2O_3, also confirms the strain in the thin film[27].

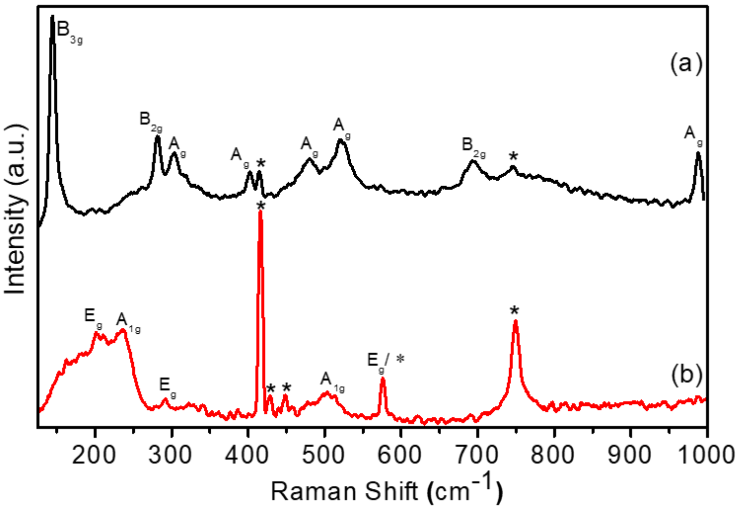

Figure 9: *Raman spectra of (a) V_2O_5 (53 nm) and (b) V_2O_3 (48 nm) thin films grown on c-sapphire (0001) by ALD. (* indicates the peaks corresponding to the substrate).*

The binding energy difference (Δ) between the O1s and the V2p$_{3/2}$ in X-ray photoelectron spectroscopy can be used to determine the vanadium oxidation state in the VO_x films[29]. Core-level spectra of vanadium and oxygen of the films of V_2O_5 and V_2O_3 are shown in **Figure 10**. Binding energies of V 2p$_{3/2}$ and O1s were found to be 517.30, and 530.32 eV, respectively and difference Δ was found to be 13.02 eV, which confirms +5 oxidation state of V in the V_2O_5 (**Figure 10a**)[29, 30].

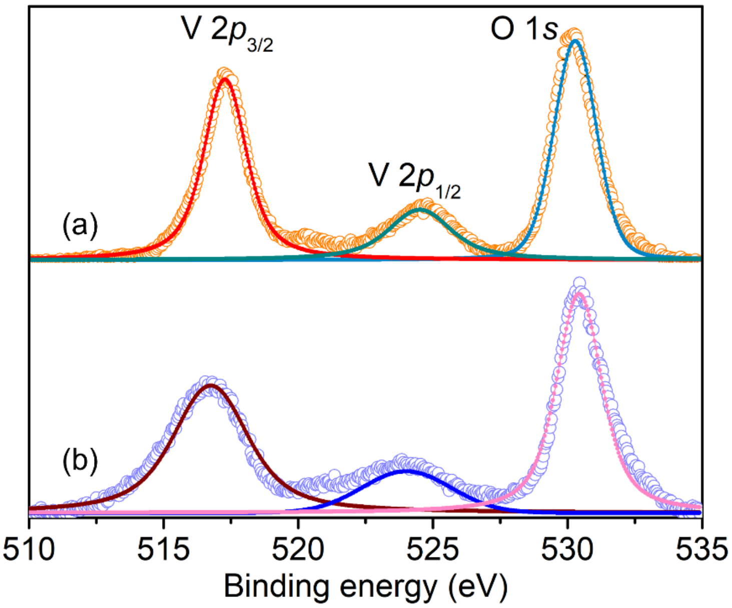

Figure 10: *XPS spectra of (a) V_2O_5 (53 nm) and (b) V_2O_3 (48 nm) thin films grown on c-sapphire (0001) by ALD.*

In the case of V_2O_3 films, the binding energy of V $2p_{3/2}$, $2p_{1/2}$ and O1s were found to be 515.88, 524.04 and 530.72 eV, respectively with the Δ (O1s and the V2$p_{3/2}$) of 14.84 eV which confirms the +3 oxidation state of vanadium (**Figure 10b**).

A rectangular piece of the film was placed on the resistivity puck for the electrical resistivity measurements, and four contacts were made with RS component silver paste. By applying 10 nA current and 0.5Hz frequency in the temperature range of 10-300 K, temperature-dependent resistance was measured using the traditional four-probe method in the Electrical transport option (ETO) mode of the physical property measuring system. **Figure 11a** demonstrates the temperature-dependent electrical resistivity with different thickness of V_2O_3 thin films. The Resistivity-Temperature curve of 48 nm thick V_2O_3 film shows a sharp metal-insulator transition at ≈165 K, with five orders of magnitude change in electrical resistivity and a 5 K thermal hysteresis between the heating and cooling branches.

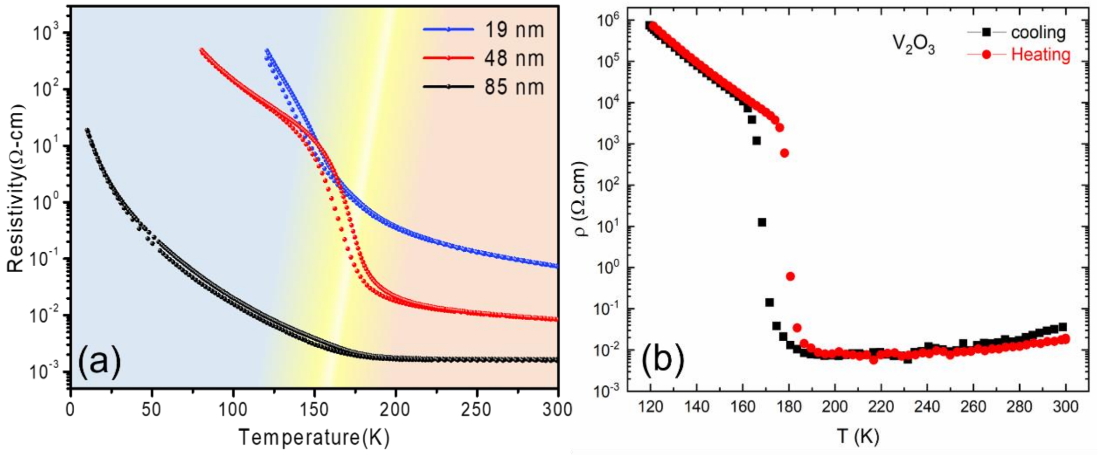

Figure 11: *Temperature-dependent resistivity measurements of different thicknesses of (a) V_2O_3 thin films grown by ALD (b) V_2O_3 bulk.*

The MIT nature of 48 nm thick V_2O_3 film is similar to bulk V_2O_3 (**Figure 11b**) prepared by reducing V_2O_5 bulk. A film with a thickness of 19 nm exhibits MIT with a jump of around three orders resistivity change.

To explore the behaviour of MIT in the V_2O_3 films with respect to thickness, lattice parameters, strain components, and lattice mismatch have been determined and are shown in **Table 1**. In-plane lattice parameter 'a' and out-of-plane parameter 'c' of V_2O_3 thin films were found smaller than that of bulk V_2O_3, which indicates that the films are having compressive strain all over the thickness range with the lattice mismatch of 2.5-2.6%.

Table 1. Calculated lattice parameters, strain components and crystallite size for 19 nm, 48 nm and 85 nm thick films of V_2O_3 (f = film , b= bulk, s = sapphire).

	a (Å)	*c* (Å)	*c/a*	Out-of-plane strain (%) $(c_f-c_b)/c_b$	a_s (Å)	in-plane strain (%) $(a_s-a_f)/a_s$	Mismatch (%) $(a_f-a_s)/a_f$	Crystallite size (nm)
19 nm	4.92676	13.9835	2.8382	-0.139	4.7991	-2.660	2.591	16.8
48 nm	4.92654	13.9870	2.8391	-0.114	4.7991	-2.656	2.587	20.7
85 nm	4.92602	13.9880	2.8396	-0.107	4.7991	-2.645	2.577	31.6
Bulk V_2O_3	4.9515	14.003	2.8280	-	-	-	-	-
Bulk Al_2O_3	4.758	12.991	-	-	-	-	-	-

Increasing the *c/a* ratio caused the M-I transition temperature to shift towards lower temperatures and the metallic phase region to expand into the insulating phase region at lower temperatures[31]. Although compressive strain in out-of-plane on V_2O_3 thin films by *c*-Al_2O_3 substrate causes the suppression of the MIT i.e., stabilization of the metallic phase[32] but there are several microstructural factors that may have a more profound impact on this suppression. Larger biaxial compressive strain in the (*ab*) plane compared to out-of-plane strain [33] or presence of minor impurities (shown in **Figure 2**) could be the reason of this MIT behaviour.

Low-temperature diffraction patterns of V_2O_3 films could help to confirm the structural phase transition in which only a single Bragg peak was observed either at higher temperature or lower temperature, whereas at the intermediate transition temperature, two peaks correspond to a mixture of rhombohedral and monoclinic phases were observed in the earlier reports[5].

6.5. Conclusions

Thermal ALD, using sequential exposure to $VO(acac)_2$ and ozone at 200 °C followed by post-deposition annealing in presence of hydrogen has been used to successfully growth of crystalline and stable V_2O_3 thin films on *c*-Al_2O_3 (0001) substrates. The V_2O_3 thin film's rhombohedral phase has been verified by XRD and Raman spectra at room temperature. A metal-insulator transition was observed at ≈165 K for the V_2O_3 thin films film with a five order jump in electrical resistivity.

Although, post-reduction method by hydrogen gas has been significantly reported including this work to obtain lower oxidation state of metals in oxides, but using hydrogen is quite unsafe to handle in normal laboratory conditions. Therefore, a precursor modification and a simple chemical vapor deposition (CVD) method will be discussed which helps to achieve lower oxidation state in the next chapter.

6.6. References

[1] McLeod, A. S.; Van Heumen, E.; Ramirez, J. G.; Wang, S.; Saerbeck, T.; S. Guenon,; Goldflam, M.; Anderegg, L.; Kelly, P.; Mueller, A.; Liu, M. K.; Schuller, I. K.; Basov, D. N. *Nat. Phys*. **2017**, 13, 80.

[2] Castellani, C.; Natoli, C.R.; Ranninger, J. Phys. Rev. B 1978, 18, 4945.

[3] Goodenough, J. B. in *Proc. Tenth Int. Conf. Phys. Semicond.* U.S. At. Energy Comm. Oak Ridge, **1970**, 304.

[4] Qazilbash, M. M.; Schafgans, A. A.; Burch, K. S.; Yun, S. J.; Chae, B. G.; Kim, B. J.; Kim, H. T.; Basov, D. N. *Phys. Rev. B*, **2008**, 77, 1.

[5] Kalcheim, Y.; Butakov, N.; Vargas, N. M.; Lee,M. H.; Valle, J. del.; Trastoy, J.; Salev, P.; Schuller, J.; Schuller, I. K. *Phys. Rev. Lett.* **2019**, 122, 057601.

[6] Sakai, J.; Limelette, P.; Funakubo, H. *Appl. Phys. Lett*. **2015**, 107, 1.

[7] Brockman, J.S.; Gao, L.; Hughes, B.; Rettner, C.T.; Samant, M.G.; Roche, K.P.; Parkin, S.S.P. *Nat. Nanotechnol*. **2014**, 9, 453.

[8] Valmianski, I.; Ramirez, J. G.; Urban, C.; Batlle, X.; Schuller, I. K. *Phys. Rev. B* **2017**, 95, 1.

[9] Salev, P.; Valle, J. D.; Kalcheim, Y.; Schuller, I. K. *Proc. Natl. Acad. Sci. USA* **2019**, 116 (18) 8798-8802.

[10] Kalcheim, Y.; Adda, C.; Salev, P.; Lee, M. H.; Ghazikhanian, N.; Vargas, N. M.; Valle, J. D.; Schuller, I. K. *Adv. Funct. Mater.* **2020**, 30, 2005939.

[11] Schuler, H.; Klimm, S.; Weissmann, G.; Renner, C.; Horn, S. *Thin Solid Films* **1997**, 299, 119.

[12] Brockman, J.; Aetukuri, N. P.; Topuria, T.; Samant, M. G.; Roche, K. P.; Parkin, S. S. P. *Appl. Phys. Lett.* **2011**, 98, 2.

[13] Brockman, J.; Samant, M. G.; Roche, K. P. *Appl. Phys. Lett.* **2012**, 101, 051606.

[14] Ramirez, J. G.; Saerbeck, T.; Wang, S.; Trastoy, J.; Malnou, M.; Lesueur, J.; Crocombette, J. P.; Villegas, J. E.; Schuller. I. K. *Phys. Rev. B* **2015**, 91, 205123

[15] Ueda, Y.; Kosuge, K.; Kachi, S. *J. Solid State Chem.* **1980**, 31, 171.

[16] Homm, P.; Dillemans, L.; Menghini, M.; Bilzen, B. Van; Bakalov, P.; Su, C. Y.; Lieten, R.; Houssa, M.; Esfahani, D. Nasr; Covaci, L.; Peeters, F. M.; Seo, J. W.; Locquet, J. P. *Appl. Phys. Lett.* **2015**, 107, 1.

[17] George, S. M. *Chem. Rev.* **2010**, 110, 111.

[18] Johnson, R.W.; Hultqvist, A.; Bent, S.F. *Mater. Today* **2014**, 17, 236.

[19] Banerjee, P.; Perez, I.; Henn-Lecordier, L.; Lee, S.B.; Rubloff, G.W. *Nat. Nanotechnol*, **2009**, 4, 292.

[20] Ritala, M.; Leskala, M. *Handbook of Thin Film Materials, Academic Press, San Diego*, CA, **2002**.

[21] Leskelä, M.; Ritala, M. *Angew. Chemie - Int. Ed.* **2003**, 42, 5548.

[22] Weimer, M. S.; Kim, I. S.; Guo, P.; Schaller, R. D.; Martinson, A. B. F.; Hock, A. S. *Chem. Mater.* **2017**, 29, 6238.

[23] Zhao, R.; Gao, Y.; Guo, Z.; Su, Y.; Wang, X. *ACS Appl. Mater. Interfaces* **2017**, 9, 1885−1890.

[24] Blanquart, T.; Niinisto, J.; Gavagnin, M.; Longo, V.; Heikkila, M.; Puukilainen, E.; Pallem, V. R.; Dussarrat, C.; Ritalaa, M.; Leskela, M. *RSC Adv.* **2013**, 3, 1179–1185.

[25] Santangelo, S.; Messina, G.; Faggio, G.; Willinger, M. G.; Pinna, N.; Donato, A.; Arena, A.; Donato, N.; Nerie, G. *Diamond & Related Materials* **2010**, 19, 590–594.

[26] Sreedhara, M. B.; Ghatak, J.; Bharath, B.; Rao, C. N. R. *ACS Appl. Mater. Interfaces,* **2017**, 9, 3178.

[27] Majid, S. S.; Shukla, D. K.; Rahman, F.; Gautam, K.; Choudhary, R. J.; Sathe, V. G.; Phase, D. M. *Appl. Phys. Lett.* **2017**, 110, 173101.

[28] Shvets, P.; Dikaya, O.; Maksimova, K.; Goikhman, A. *J. Raman Spectrosc.* **2019**, 50, 1226.

[29] Mendialdua, J.; Casanova, R.; Barbaux, Y. *J. Electron Spectros. Relat. Phenomena* **1995**, 71, 249.

[30] Hryha, E.; Rutqvist, E.; Nyborg, L. *Surf. Interface Anal.* **2012**, 44, 1022.

[31] Sakai, J.; Limelette, P.; Funakubo, H. *Appl. Phys. Lett.* **2015**, 107, 241901.

[32] Yonezawa, S.; Muraoka, Y.; Ueda, Y.; Hiroi, Z. *Solid State Commun.* **2004**, 129, 245.

[33] Grygiel, C.; Simon, Ch.; Mercey, B.; Prellier, W.; Frésard, R. *Appl. Phys. Lett.* **2007**, 91, 262103.

Chapter 7

Chemical Vapor Deposition of NbO_2: Precursor Modification and Thin Film Growth

Summary

The metal-insulator transition (Mott transition) is shown by niobium dioxide (NbO_2), which has the potential to be used in memristors and neuromorphic electronics. Traditionally, high-temperature reduction of Nb_2O_5 films using H_2 or sophisticated techniques like molecular beam epitaxy and pulsed laser deposition are required for the growth of NbO_2 thin films..

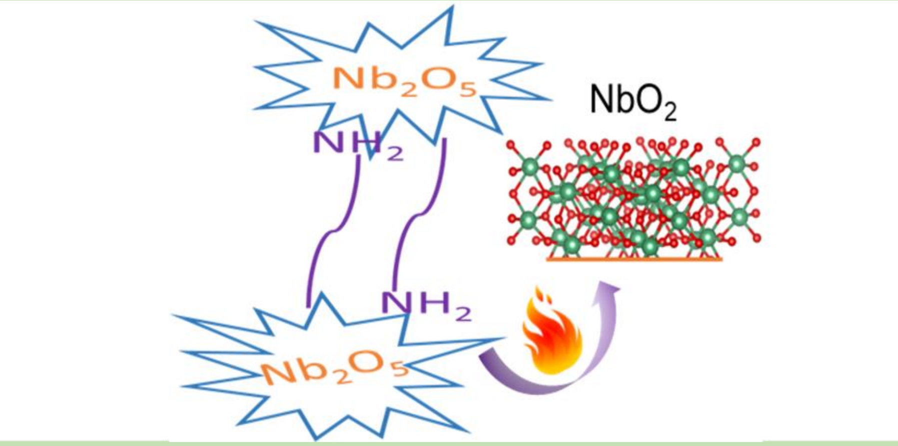

In this study, a modified niobium precursor Nb-hexadecylamine (Nb-HDA) complex is used to establish a straightforward chemical pathway for the direct growth of crystalline NbO_2 films via chemical vapour deposition (CVD). X-ray diffraction confirms that films exhibit in a distorted rutile body-centered-tetragonal (BCT) structure of NbO_2 with a highly preferred orientation on *c*-sapphire substrate. The +4 oxidation state is confirmed by X-ray photoelectron spectroscopy (XPS). The present study makes it simple to deposit NbO_2 films without further post-reduction processes of +5 oxidation state and making it an simple method for making NbO_2 based devices.

Paper based on this work has appeared in *Nanotechnology* **2023**, 34, 14, 145705.

7.1. Introduction

Transition metal oxides (TMOs) show a varied range of fascinating phenomena such as metal-to-insulator transitions (MIT), ferroic order, and interfacial two-dimensional electron gases[1-7]. Particularly, the MIT in oxides is an enticing subject of discussion due to its fast switching behavior and applications in neuromorphic devices[8, 9]. Among TMOs, Vanadium, and niobium based oxides are well-known for their sharp resistive switching across the MIT. Niobium forms various oxides such as NbO, NbO_2, and Nb_2O_5 in which Nb exists in +2, +4, and +5 oxidation states, respectively[10]. The electrical properties of Nb oxides' are highly sensitive to the oxidation state of Nb[10]. NbO_2 has a small band gap (between 0.5 and 1.2 eV)[10] and exhibits Mott-Peierls transition at ≈1081K [11, 12] like VO_2 [13, 14], whereas Nb_2O_5 is a semiconductor with wide band gap[15].

In spite of the significant interest in the switching behavior of NbO_2, the growth of NbO_2 thin films is scarce in the literature and most of the synthetic routes yield the stable Nb_2O_5 [16-20]. The growth of NbO_2 involves high temperature (> 900 ℃) reduction of Nb_2O_5 using hydrogen which is quite unsafe to handle in normal laboratory conditions[6]. High vacuum conditions and complex equipment are needed for some deposition techniques, including molecular beam epitaxy (MBE), pulsed laser deposition (PLD), chemical vapour transfer (CVT), and magnetron sputtering. In prior studies, polycrystalline and amorphous NbO_2 have been prepared by sputtering from Nb_2O_5 under a constant flow of dry H_2 [21, 22], melting stoichiometric quantities of Nb_2O_5 and Nb metal in an arc in argon[6]. Magnetron sputtering [23], ion beam deposition process [24], CVT [25], PLD [26], and MBE [27] were also used to obtain NbO_2 thin films. Despite the wide range of synthesis methods, industrial-scale synthesis is still difficult, and NbO_2 thin film deposition has to be made more accessible, straightforward, and ecologically friendly.

7.2. Scope of present investigation

In the present investigation, we have developed a modified precursor approach that enables direct CVD growth of NbO_2 thin films where Nb will be in +4 oxidation state without further high-temperature reduction of Nb_2O_5 (Nb in +5 state). A Nb-HDA complex was prepared for this purpose using wet chemistry and the complex was utilized under a nitrogen atmosphere to produce porous NbO_2 films.

7.3. Experimental

Materials:

Hydrogen peroxide (30% H_2O_2), Niobium (V) ethoxide, (99.95%, Sigma Aldrich), and 1-hexadecylamine ($C_{16}H_{33}NH_2$, HDA) were the starting materials.

(i) Synthesis of Niobium- hexadecylamine (Nb-HDA) complex:

Niobium (V) ethoxide, hydrogen peroxide, and 1-hexadecylamine ($C_{16}H_{33}NH_2$, HDA) were employed for the synthesis of Nb-HDA complex (see **Scheme 1**).

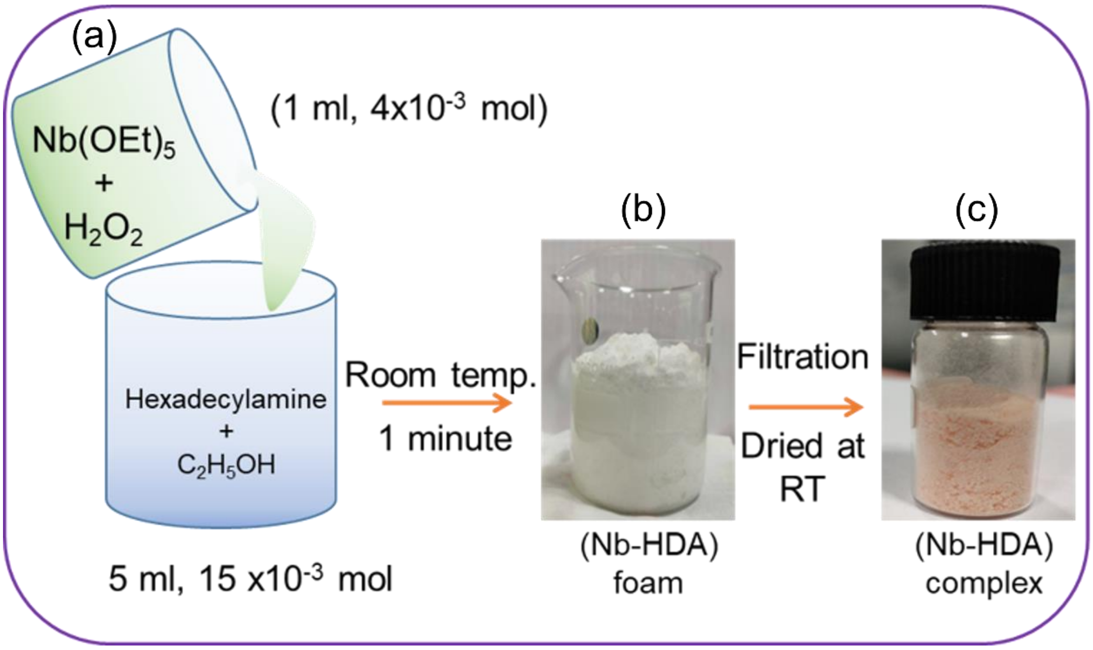

Scheme 1: *Synthesis of Nb-HDA complex using hydrogen peroxide and 1-hexadecylamine. (a) shows the mixing of dissolved niobium (V) ethoxide in* H_2O_2 *into Hexadecylaine (b) photograph of prepared foam after the compilation of reaction of* $Nb(OEt)_5$ *and HDA (c) photograph of precursor (Nb-HDA complex) after drying.*

Niobium (V) ethoxide (1 ml, $4x10^{-3}$ mol) was thoroughly dissolved in 30 ml of an H_2O_2 solution. Niobium (V) ethoxide solution was mixed with a 3.76 g HDA (15 x 10^{-3} mol) solution that had been prepared in 5ml ethanol at 70 °C. As a result Nb-HDA complex was formed as a foam. The resulting ultra-light foam was filter and cleaned with acetone and allowed to air dry. The compound was examined in detail and then used to grow NbO_2 films.

(ii) Deposition of NbO_2 thin films (Scheme 2):

For the deposition procedure, a horizontal flow furnace employing N_2 as a carrier gas was used (see **Scheme 2**). On a quartz boat, the substrates and Nb-HDA complex were assembled. The substrate (*c*-sapphire) was kept downstream and 10 mm apart from the complex. In a typical growth procedure, Nb-HDA complex and substrates were pushed into the preheated furnace (900 °C) with the help of a magnet while N_2 gas was continuously pumped in tube with the flow of 100 cm^3/min. An hour was allowed for the reaction to complete. The boat was then taken out of the hot zone after one hour, put in the cooler section of the CVD tube, and allowed to cool.

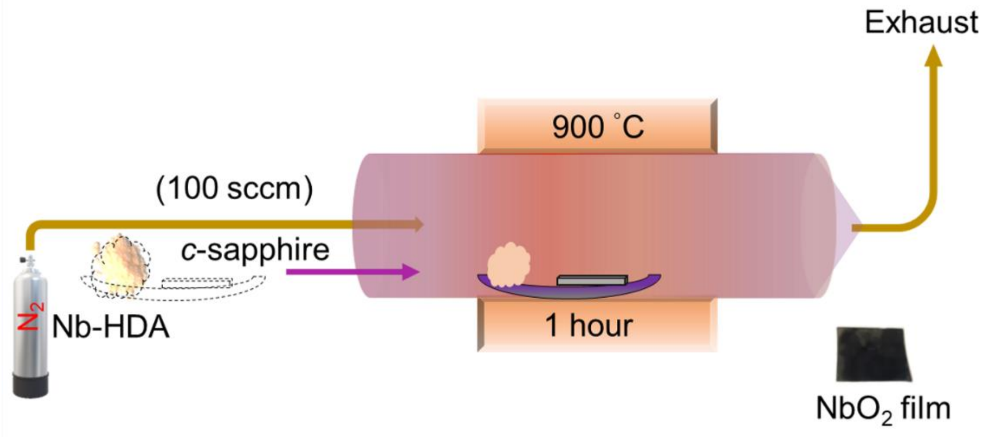

Scheme 2: *Graphical representation of the CVD setup for the synthesis of NbO2 thin films and a photograph of grown NbO_2 thin film on c-sapphire substrate.*

(iii) Characterizations:

Nb-HDA complex and NbO_2 films' X-ray diffraction (XRD) patterns were recorded using a Panalytical diffractometer (Empyrean) with monochromatic Cu $K_{\alpha1}$ radiation (λ = 1.5404 Å). An Apreo 2S field emission scanning electron microscope (FESEM) and a Bruker atomic force microscope were used to analyse the films' surface morphology (AFM). The Jobin Yvon LabRam HR spectrometer (630 nm Ar laser) recorded the Raman spectra of the NbO2 films in backscattering geometry. Thermofisher's X-ray photoelectron spectroscopy (XPS) tool was used to evaluate the chemical composition and oxidation state of the Nb.

7.4. Results and Discussion

By measuring the low-angle and wide-angle X-ray diffraction (**Figure 1**), we were able to determine the structure and arrangement of the HDA molecules in the Nb-HDA complex. **Figure 1a** shows the wide-angle XRD pattern in which diffraction peak at $2\theta \approx 21.56^\circ$ confirms the (100) planes of Nb_2O_5 (JCPDF No. 00-074-0312) [29]. It is anticipated that HDA molecules were intercalated between the smaller crystallite sizes of the Nb_2O_5 matrix indicated by the broad feature of XRD.

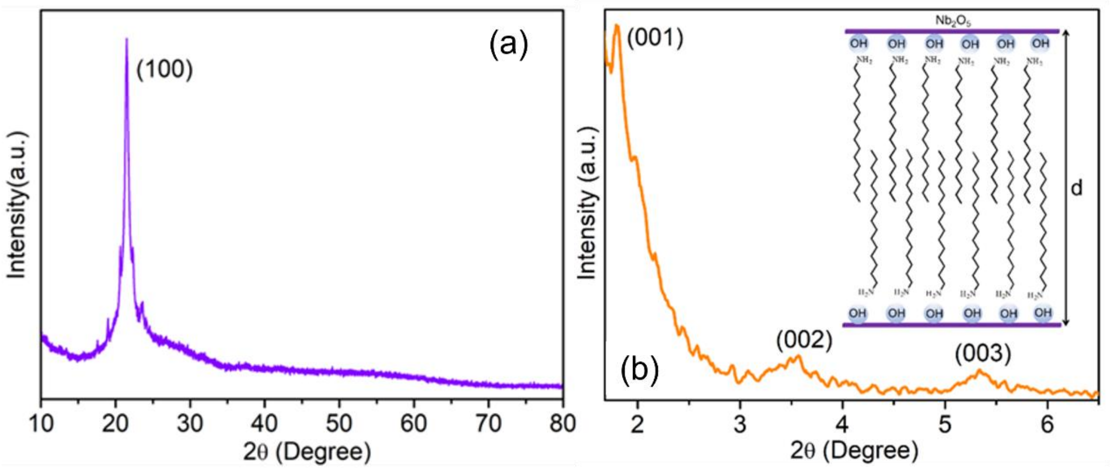

Figure 1: *(a) wide angle XRD shows (100) reflection of Nb_2O_5 and (b) Low angle X-ray diffraction pattern of Nb-HDA complex (inset shows a representation of intercalation of HDA in the Nb_2O_5 matrix.*

In the low-angle XRD pattern, diffraction peak at 1.8° indicates the interplanar distance (d=4.9 nm) between the Nb_2O_5 atomic chains intercalated with HDA molecules (**Figure 1b**). The d-spacing of 4.9 nm matches with twice the length of the HDA molecules which are bonded to Nb_2O_5 matrix in a regular fashion as shown in inset of **Figure 1b**, which resembles inorganic/organic hybrids of Nb-HDA lamellar mesostructures.

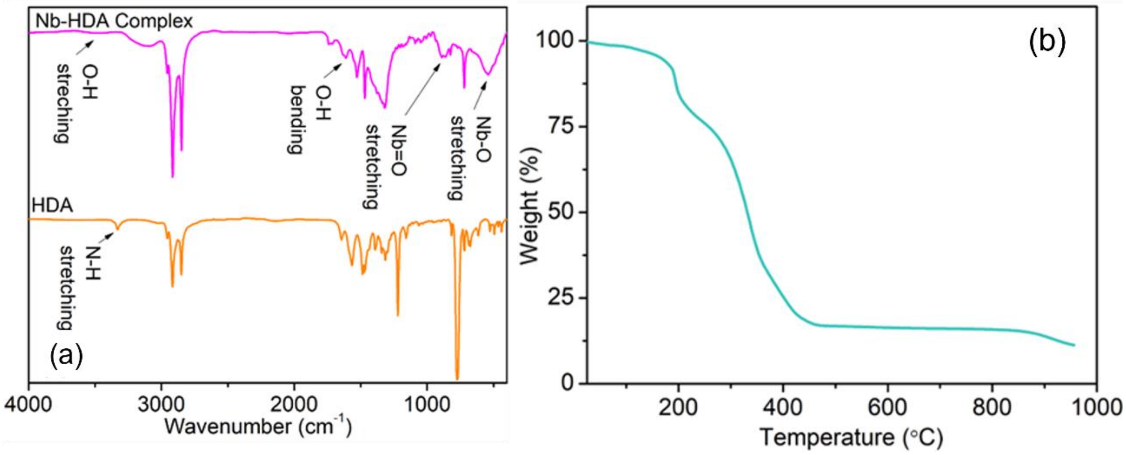

Figure 2: *Characterisation of Nb-HDA complex (a) IR spectra of HDA and Nb-HDA complex show the association of bonds of HDA molecules with* Nb_2O_5 *matrix (b) thermogravimetric analysis (TGA) of the Nb-HDA complex shows weight loss during the heating and decomposition.*

The self-assembly of two amine moieties between the Nb_2O_5 can be used as a representation of the lamellar structure of the Nb-HDA complex. The reported complexes of HDA with TiO_2 are compatible with the observed interplanar spacing[28]. The broader reflection at the angles 3.6 ° and 5.5 ° shown in **Figure 1b** are corresponding to a higher order reflection of (00*l*).

According to the complex's FTIR spectra (**Figure 2a**), the stretching band of the $-NH_2$ group broaden and shifts to lower wavenumbers at 3130 cm^{-1} rather than strong bands that correspond to free amines associated with HDA at 3331 cm^{-1}. This similar broadening and shifts were also observed for N-H bending ≈1605 cm^{-1} (due to $-NH_2$ deformation) [28]. These significant shifts are revealing an interaction between the head of the $-NH_2$ present in HDA molecule and the -OH bonds present in the inorganic Nb_2O_5 matrix. O-H band observed in IR confirms the presence of -OH bonds. The bands located at 550, and 900 cm^{-1} originated because of the stretching vibration of Nb-O and Nb=O, respectively. Long carbon chains present in intercalated HDA into the thin planar matrix of Nb_2O_5 to form a lamellar mesostructure are held together by hydrophobic interactions between the alkyl groups[28, 30]. The porous nanocrystalline TiO_2 foam has been reported by HDA intercalation exhibited a similar complicated structure[28].

Thermogravimetric analysis (TGA) was used to measure the Nb-HDA complex's volatility and thermal stability. TGA curve in **Figure 2b** shows the primary weight loss ≈10 wt% at 200 °C due to the evaporation of surface-adsorbed H_2O molecules or contamination. A huge weight loss up to ≈15 wt% around 300 °C can be ascribed to the decomposition of amine moieties intercalated in matrix. The remaining residual mass of around 15% corresponding to NbO_2 (vide infra). The Nb-HDA complex's thermogravimetric study shows that it is an appropriate precursor for the formation of NbO_2 by decomposing.

The Nb-HDA complex was decomposed to deposit the NbO_2 films on c-sapphire substrate, as indicated in **Scheme 2**. The films appeared to be black in colour which indicated that Nb is present in the lower oxidation state and it rules out the presence of Nb_2O_5 (Nb_2O_5 is white). The NbO_2 films on *c*-sapphire were found to be crystalline whereas on Si appear to be amorphous. We used NbO_2 grown film on *c*-sapphire for further investigation of the chemical state and the films were further analyzed by spectroscopy and microscopy to confirm the NbO_2 phase with +4 oxidation state and morphology, respectively (vide infra). XRD patterns (see **Figure 3a**) of NbO_2 films on *c*-sapphire show the growth of crystalline film with a low-temperature distorted rutile body-centered-tetragonal (BCT) structure of NbO_2.

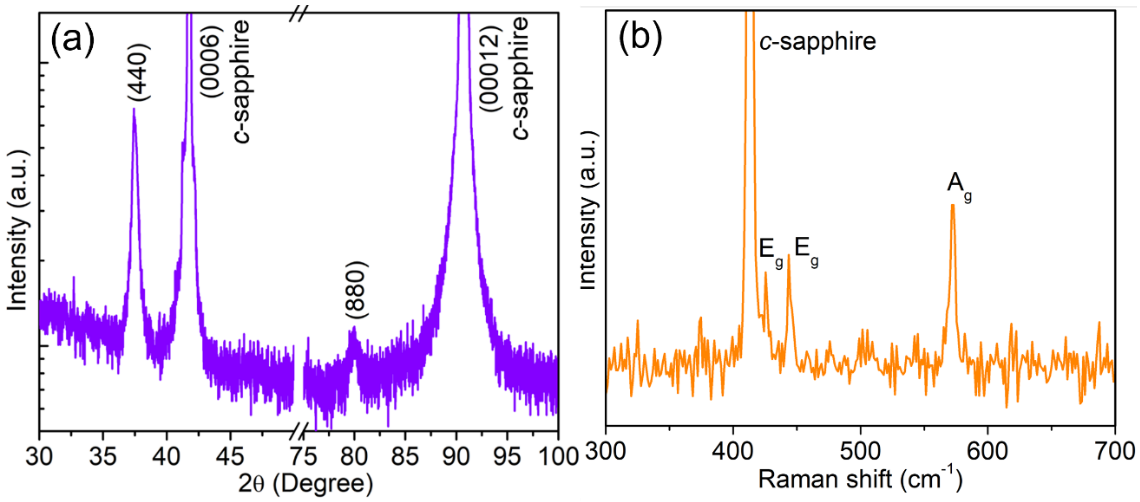

Figure 3: *(a) 2θ scan of NbO_2 thin film grown by the CVD method on c-sapphire substrate. (440) and (880) reflections correspond to the distorted rutile body-centered-tetragonal (BCT) structure of NbO_2 and (b) Raman spectrum at room temperature of NbO_2 thin film excited with a 630 nm laser.*

The diffraction peaks from the film at 37.48° and 80° correspond to the (440) and (880) Bragg planes of a distorted rutile body-centered-tetragonal (BCT) structure of NbO_2 [24, 31]. The peaks at 41.63° and 90.65° correspond to the underlying sapphire substrate. The appearance of only (hk0) reflection of the film with the (000*l*) peaks of the substrates indicated the highly preferred orientation of the film with the substrate. XRD results confirm the formation of single-phase NbO_2 films, the impurities such as Nb or Nb_2O_5 have not been observed.

NbO_2 films were analyzed by Raman spectroscopy. **Figure 3b** shows the Raman spectrum of NbO_2 thin film prepared on *c*-sapphire, which is in good agreement with reported NbO_2 nano-wires deposited by CVT [25], calculated phonon modes of BCT structure of NbO_2 [31] and NbO_2 film prepared by thermal oxidation [32]. Raman bands due to E_g phonons modes occur at 431 cm^{-1}, 445 cm^{-1}, and A_g phonon mode at 571 cm^{-1}, respectively (plausible phonon modes assigned based on a calculated vibrational mode by Wang Y *et al.* [31]). The observed Raman spectrum shows that Nb_2O_5 phonon modes were completely absent.

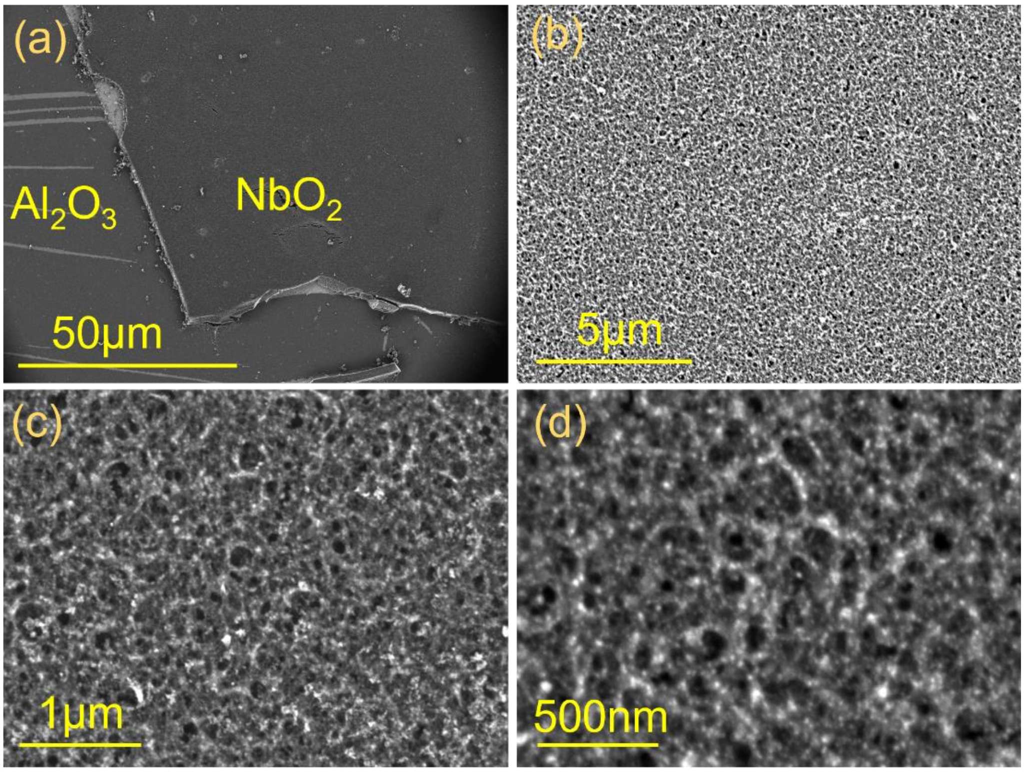

Figure 4: *Scanning electron microscope images of NbO_2 thin film at different magnification (a-d). (image in the first panel shows a masked and unmasked area of the substrate, the grown NbO_2 films is clearly seen as a step).*

The surface morphology of the NbO_2 films was investigated by scanning electron microscopy and atomic force microscopy. **Figure 4(a–d)** show a series of SEM images of NbO_2 film with different magnification. The high-resolution images reveal that the surface of the films appears to be network-type and porous in nature. The AFM images (**Figure 5**) of the films also reveal the rough surface of the film with the porous network.

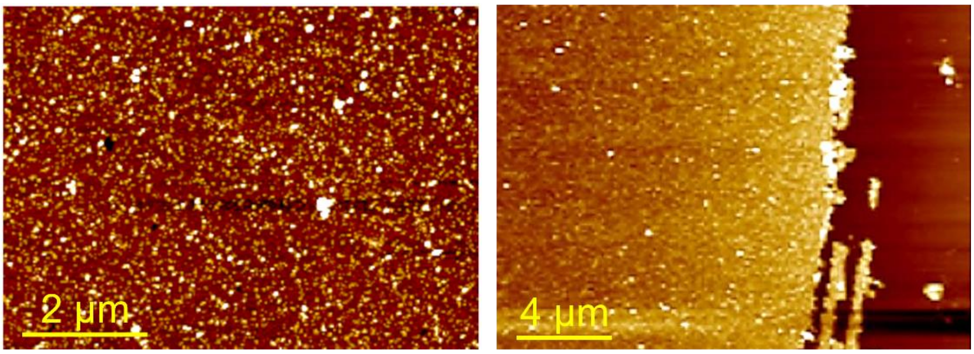

Figure 5: *Tapping-mode atomic force microscope images of NbO_2 thin film on a c-sapphire substrate grown by the CVD method show a porous network.*

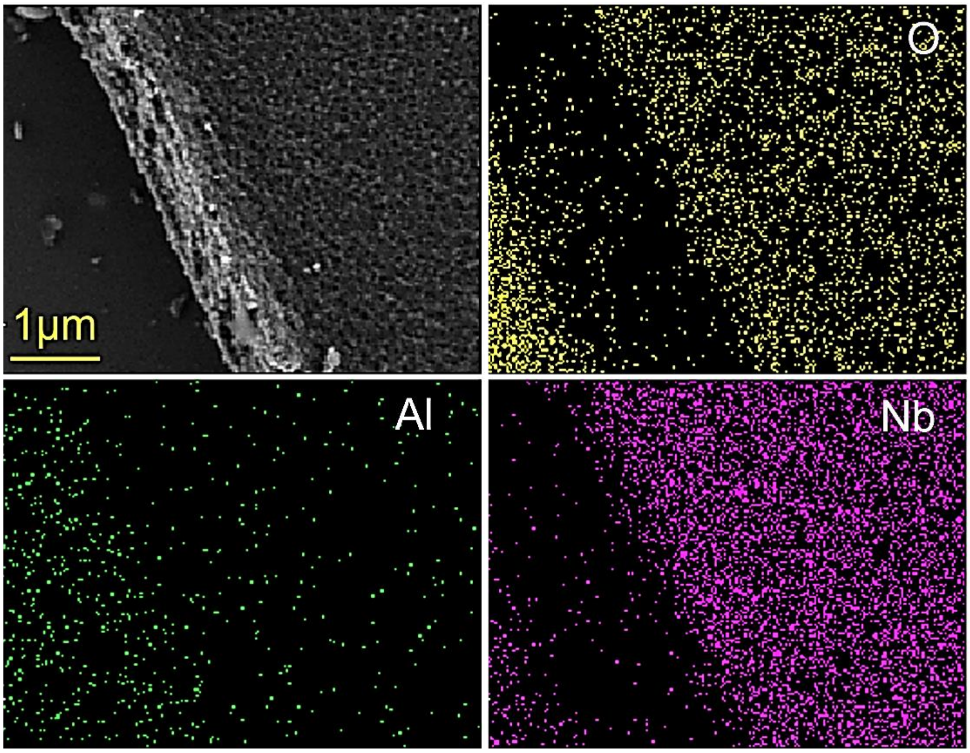

Figure 6: *Elemental mapping of thin films of NbO_2 deposited on c-sapphire by CVD, which shows Nb and O throughout the film and Al and O on the masked region.*

It can be understood the Nb-HDA complex is deposited on the substrate by evaporation and at a high temperature, the carbon of the aliphatic chain in the complex decomposes and escape along with snatching oxygen from Nb_2O_5. During the evaporation process, the intercalated molecules create porosity in the film hence films appear to have a rough surface with network morphology. The elemental mapping of Nb and O in the film shows the uniform distribution of Nb and O throughout the film (**Figure 6**). The masked region of the film shows only the presence of Al and O from the substrate.

We thoroughly analysed the films using X-ray photoelectron spectroscopy in order to further study the exact oxidation state of Nb and composition in them (**Figure 7**). The films were analyzed step by step by sputtering the film surface in order to understand the surface and the bulk composition of the film. The XPS spectrum of the as-prepared NbO_2 films (without sputtering) shows the characteristic feature of Nb core level of $3d_{5/2}$ and $3d_{3/2}$ appearing at 207.5 and 210.5 eV respectively, which represents the Nb in +5 oxidation state corresponding to the Nb_2O_5 (**Figure 7a**).

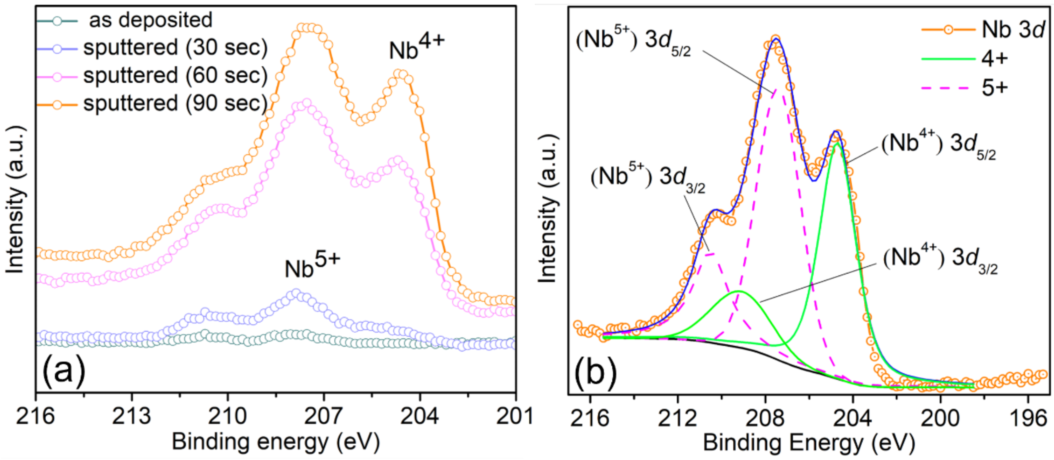

Figure 7: *(a) Core level Nb 3d spectra of thin film grown on c-sapphire and cleaned with different sputtering times by 2 KeV Ar+ ion beam (b) deconvoluted core-level XP spectra of Nb 3d of thin film grown on c-sapphire and sputtered for 90 s.*

Deconvoluted spectra in **Figure 7b** shows that The strong signal and shift in the Nb core level appear at 205.0 and 208.8 eV following 60 seconds of sputtering with Ar^+ ions, confirming the Nb in +4 oxidation state, and it can be recognized to NbO_2 [24,33].

The sputtered films (60 and 90 s) reveal the contribution from both Nb (+5) and Nb(+4) oxidation states, indicates the surface of the film is very sensitive to oxidation. The peak area for +4 oxidation state is found to be 45.2% of the overall integrated intensities, which suggests a significant presence of +5 oxidation state in the films after sputtering.

It is generally known that NbO_2 is a strong reducing agent and that, even at high vacuum, it quickly oxidises to Nb_2O_5 [24,33]. Therefore, despite the film's surface having sputtered before to measurement in high vacuum conditions, a large fraction of NbO_2 on the surface immediately oxidises into Nb2O5 by reacting with oxygen, moisture, or CO_2 present in the XPS chamber. The XPS study reveals that method produces NbO_2 films, which continuously oxidise due to their strong reducing nature and make it challenging to describe the fresh surface with pure Nb (+4) state. Yet, Nb (+4) state's distinctive properties continue to be more pronounced after sputtering, and Nb (+4) state's contribution increases from 60 to 90 seconds of sputtering, further demonstrating that the prepared films are in fact NbO_2 phase and Nb in the (+4) oxidation state.

XRD and Raman spectroscopy were used to characterise the leftover residual powder after the decomposition of the precursor shown in **Figure 8**. XRD of residual part matches with bulk NbO_2 (JCPDS No. 00-071-0020) [22] and all the modes present in the Raman spectrum also confirm BCT structure of NbO_2.

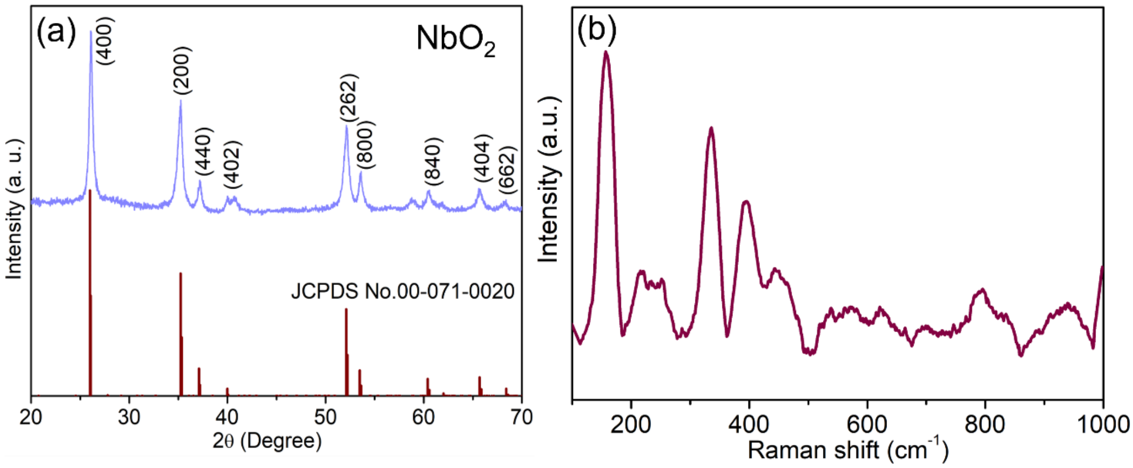

Figure 8: *(a) XRD pattern and (b) Raman spectrum of leftover residual powder after the decomposition of the precursor, confirms distorted rutile body-centered-tetragonal (BCT) phase of* NbO_2.

7.5. Conclusions

In conclusion, a new precursor method has been proposed for the growth of NbO_2 thin films. The NbO_2 films were grown by decomposition of the Nb-HDA organic-inorganic hybrid complex at high temperatures. The method provides highly crystalline distorted rutile body-centered-tetragonal (BCT) phase of NbO_2 films with the preferred orientation on *c*-sapphire, which is an important parameter to investigate fundamental properties as well as switching applications in the films. The findings of the chemical investigation showed that Nb is in the +4 oxidation state. The straightforward chemical method described here would facilitate for the large-scale CVD deposition of NbO_2 thin films, which could be useful for electrical devices.

7.6. References

[1] Alonso, J. A.; Martínez-Lope, M. J.; Casais, M. T.; García-Muñoz, J. L.; Fernández-Díaz, M. T. *Phys. Rev. B.* **2000**, 61 (3), 1756-1763.

[2] Sellier, C.; Boucher, F.; Janod, E. *Solid State Sci.* **2003** 5 (4), 591-599.

[3] Marley, P. M.; Stabile, A. A.; Kwan, C. P.; Singh, S.; Zhang, P.; Sambandamurthy, G.; Banerjee, S. *Adv. Funct. Mater.* **2013**, 23 (2), 153-160.

[4] Greenblatt, M. *Chem. Rev*, **1988**, 88 (1), 31-53.

[5] Fogle, W.; Perlstein, J. H. *Phys. Rev. B.* **1972**, 6 (4), 1402-1412.

[6] Rao, C. N. R.; Rao, G. R.; Rao, G. V. S. *Solid State Chem.* **1973**, 6 (3), 340-343.

[7] Manjunath, K.; Singh, R.; Panda, D. P.; Rao, C. N. R. *Phys. Status Solidi Rapid Res. Lett.* **2021**, 15 (6), 2000565.

[8] Zhang, S.; Vo, H.; Galli, G.; *Chem. Mater.* **2021**, 33, 3187–3195.

[9] Schofield, P.; Bradicich, A.; Gurrola, R. M.; Zhang, Y.; Brown, T. D.; Pharr, M.; Shamberger, P. J.; Banerjee, S. *Adv. Mater.* **2022**, 2205294.

[10] Nico, C.; Monteiro, T.; Graça, M. P. F. *Prog. Mater. Sci.* **2016**, 80, 1-37.

[11] Wahila, M. J.; Paez, G.; Singh, C. N.; Regoutz, A.; Sallis, S.; Zuba, M. J.; Rana, J.; Tellekamp, M. B.; Boschker, J. E.; Markurt, T.; Swallow, J. E. *Phys. Rev. Mater.* **2019**, 3(7), 074602.

[12] Kulmus, K.; Gemming, S.; Schreiber, M.; Pashov, D.; Acharya, S. *Phys. Rev. B.* **2021**, 104(3), 035128.

[13] Cavalleri, A.; Dekorsy, T.; Chong, H. H. W.; Kieffer, J. C.; Schoenlein, R. W. *Phys. Rev. B.* **2004**, 70 (16), 161102.

[14] Biermann, S.; Poteryaev, A.; Lichtenstein, A. I.; Georges, A. *Phys. Rev. Lett.* **2005**, 94 (2), 026404.

[15] Weibin, Z.; Weidong, W.; Xueming, W.; Xinlu, C.; Dawei, Y.; Changle, S.; Liping, P.; Yuying, W.; Li, B. *Surf. Interface Anal.* **2013**, 45(8), 1206-1210.

[16] Sim, H.; Choi, D.; Lee, D.; Hasan, M.; Samantaray, C. B.; Hwang, H. *Microelectron. Eng.* **2005**, 80, 317.

[17] Blanquart, T.; Niinistö, J.; Heikkilä, M.; Sajavaara, T.; Kukli, K.; Puukilainen, E.; Xu, C.; Hunks, W.; Ritala, M.; Leskelä, M. *Chem. Mater.* **2012**, 24 (6), 975– 980.

[18] Wylezich, H. Mähne, H.; Rensberg, J.; Ronning, C.; Zahn, P., Slesazeck, S.; Mikolajick, T. *ACS Appl. Mater. Interfaces* **2014**, 6 (20), 17474– 17480.

[19] O'Neill, S. A.; Parkin, I. P.; Clark, R. J. H.; Mills, A.; Elliott, N. *J. Mater. Chem.* **2003**, 13 (12), 2952– 2956.

[20] Rahtu, A.; Kukli, K.; Ritala, M. *Chem. Mater.* **2001**, 13(3), 817-823.

[21] Gallego, J. M.; Thomas, C. B. *Thin Solid Films* **1982**, 98 (1), 11-22.

[22] Cheetham, A. K.; Rao, C. N. R. *Acta. Crystallogr. B. Struct.* **1976**, 32 (5), 1579-1580.

[23] Liu, X.; Sadaf, S. M.; Kim, S.; Biju, K. P.; Cao, X.; Son, M.; Choudhury, S. H.; Jung, G. Y.; Hwang, H. *ECS Solid State Lett.* **2012**, 1(5), Q35.

[24] Wang, Y.; Comes, R. B.; Kittiwatanakul, S.; Wolf, S. A.; Lu, J. *J. Vac. Sci. Technol. A* **2015**, 33 (2), 021516.

[25] Lee, S. H.; Yoon, H. N.; Yoon, I. S.; Kim, B. S.; *Bull Korean Chem Soc.* **2012**, 33(3), 839-842.

[26] Joshi, T.; Senty, T. R.; Borisov, P.; Bristow, A. D.; Lederman, D.; *J. Phys. D: Appl. Phys.* **2015**, 48(33), 335308.

[27] Wong, F. J.; Ramanathan, S. *J. Mater. Res.* **2013**, 28(18), 2555-2563.

[28] Arabatzis, I. M.; Falaras, P. *Nano Lett.* **2003**, 3 (2), 249-251.

[29] Gruehn, R. *J. less-common met.* **1966**, 11(2), 119-126.

[30] Dasgupta, S.; Agarwal, M.; Datta, A. *J. Mater. Chem,* **2002**, 12, 162-164.

[31] Wang, Y.; Nie, Z.; Shi, Y.; Wang, Y.; Wang, F. *Phys. Rev. Mater.* **2022**, 6(3), 035005.

[32] Zhao, Y.; Zhang, Z.; Lin, Y. *J. Phys. D: Appl. Phys.* **2004**, 37(24), 3392.

[33] Wong, F. J.; Hong, N.; Ramanathan, S. *Phys. Rev. B.* **2014**, 90(11), 115135

Chapter 8

Atomic Layer Deposition of β-NiS for Thin Film Based Electrochemical Glucose Sensors

Summary

Nickel sulphide is known for good electrode material and metal to insulator transition in hexagonal phase but its phase pure deposition by ALD or CVD still challenging. By sequential pulsing of nickel acetylacetonate [Ni(acac)$_2$] as the nickel precursor and H_2S gas as the sulphur precursor, rhombohedral nickel sulphide (β-NiS) thin films were grown on a *c*-sapphire substrate using the ALD process.

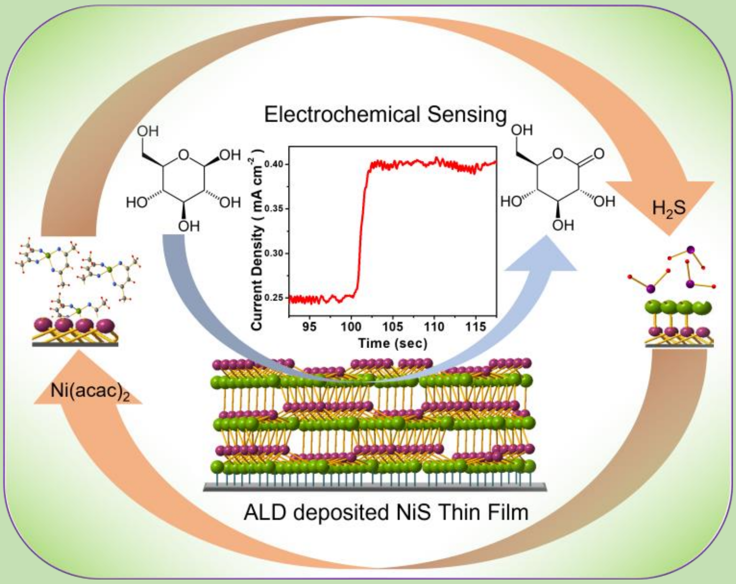

The self-limiting nature of the ALD process was found to be in the temperature range of 200-240 °C, which provides crystalline NiS thin films without further annealing. At 200 °C, a growth rate of ≈0.2 Å/cycle was observed. For non-enzymatic electrochemical glucose sensing, as-deposited thin films were investigated. The sensor has an outstanding sensitivity of 5.78 μA mM^{-1} cm^{-2}, a low detection limit of 0.052 μM, and a very quick response time of ≈2 s.

Paper based on this work has appeared in *ACS Appl. Electron. Mater.* **2021**, 3, 1912–1919.

8.1. Introduction

As discussed in chapter 5, atomic layer deposition (ALD) has developed as a highly useful tool that is capable of depositing thin films of a broad range of materials, including transition-metal sulfides and oxides, with nanometer precision[1-3]. In the past, numerous metal sulphide ALD methods have been investigated, including GaS_x [4], Bi_2S_3 [5], MoS_2 [6,7], Co_9S_8 [8], MnS [9], AlS_x [10], FeS_x [11], VS_4 [12], ReS_2 [13], GeS [14], SnS [14], metal pyrites [15,16], HfS_2, and ZrS_2 [17], with their potential applications in energy production, storage, and catalysis. For the production of sensors, solar cells, solar selective coatings, photodiode arrays, and photoconductors with a variety of applications in (opto)electronics, thin films of metal sulphides produced by ALD are particularly impressive[18]. NiS has received a lot of interest among sulphides because of its metal-insulator transition in the hexagonal phase[19] and is a promising candidate for several vital applications in solar cells, supercapacitors, catalysis, and batteries[20,21]. To date, few attempts have been made to grow godlevskite-structured and polycrystalline nickel sulfide via ALD using bis(2,2,6,6-tetramethylheptane 3,5-dionate) nickel(II) and bis(N, N '-ditertbutylacetamidinato)nickel(II) as the nickel precursors and H_2S gas as the sulfur precursor on glass or SiO_2/Si substrates[20-23]. However, NiS has not been fully investigated by the ALD method in terms of phase selectivity, crystallinity, and cheap cost of the precursors on a variety of substrates and applications; specially in clinical diagnosis field.

Effective glucose detection is crucial in many different disciplines due to its promising applications in clinical diagnosis, pharmacological analysis, the treatment of diabetes mellitus, the food industry, and environmental monitoring [24–27]. Due to the extensive use of enzymes, which are sensitive to various environmental variables, commercially available glucose sensors are less useful (for instance, humidity, pH, solvent, and temperature)[28–30]. Due to a difficult technique for anchoring the enzymes, the production of enzyme-based sensors raises additional issues[26]. Due to the advantage of direct electrochemical oxidation of glucose to gluconolactone by noble metal (Pt and Au) catalysts, non-enzymatic detection has recently attracted a lot of attention[31,32]. Many transition-metal oxides or sulfides[33-36] also have been used as the electrode materials. Transition-metal-based sensors are far more desirable than noble metal-based sensors from an ecological and financial standpoint. Numerous Ni-based glucose sensors have been developed to date using oxide and sulfide materials using a variety of morphological modifications and processing methods, including electrochemical deposition and a few ALD-deposited films[37–42]. $Ni(OH)_x$ on glassy carbon and carbon cloth, synthesized by an electrochemical oxidation process of ALD-deposited NiS_x, also has been used for glucose detection[43]. Due to the high conductivity of transition-metal sulfides in the sensing sector, understanding the detection of glucose by a selective phase of NiS developed by the ALD technique will be of great interest.

8.2. Scope of present investigation

In the present study, we investigate an innovative layer-by-layer ALD approach to fabricating crystalline nickel sulfide thin films on *c*-sapphire substrates by sequentially exposing nickel acetylacetonate[$Ni(acac)_2$] to the substrate as nickel and H_2S as sulfur precursors, respectively, over the 200-240 °C temperature range with the growth rate of ~0.2 Å/cycle. Further, we have explored the ALD-deposited films NiS thin films for non-enzymatic electrochemical glucose sensing. glucose sensors exhibit an excellent sensitivity of 5.78 $\mu A\ mM^{-1}\ cm^{-2}$ and a low detection limit of 0.052 µM with fast response (< 2 s).

8.3. Experimental

Materials:

Nickel acetylacetonate ($Ni(acac)_2$, Sigma Adrich, 99.9%), H_2S (Bhuruka gases, 97.5%) and Nitrogen (Chemix, 99.9995%).

(i) Growth of NiS thin films:

Beneq, Finland-designed ALD apparatus (TFS 200) was used to deposit nickel sulfide thin films onto single crystalline *c*-sapphire (0001) substrates. Prior to film deposition, sapphire substrates were prepared by cutting them into roughly ca. 2 × 1 cm^2 rectangles, cleaning them completely with a 1:4 solution of H_2O_2 and H_2SO_4, ultrasonically cleaning them in isopropanol (IPA), acetone, and other solvents, and then properly drying them in the chamber under N_2 atmosphere.

Nitrogen gas (Spec. Gases, 99.9995%) was used as a purging and carrier gas during the depositions at a flow rate of 600 sccm. To stabilize the temperature, the instrument's reaction chamber was heated to 200 °C and maintained there for 15 minutes. The HS-300 bubbler that served as the hot source was filled with nickel acetylacetonate, which was gradually heated to 160 °C to produce enough vapor. Before pulsing to the reactor, the bubbler was boosted for one second with highly pure N_2 to achieve sufficient $Ni(acac)_2$ vapor pressure. Sequential pulsing of $Ni(acac)_2$ and H_2S was applied for the deposition of the films. The ALD sequence (t_1 / t_2 // t_3 / t_4) for deposition was kept as 3/3//3/3 s, where t_1 and t_2 are the optimized pulsing times for $Ni(acac)_2$ and H_2S gas, respectively, and t_3, t_4 are the purging times for both the precursors (**Scheme 1**). The chamber pressure remained essentially steady throughout the whole deposition while the reactor pressure was maintained between 1 and 3 mbar. Films were deposited at various substrate temperatures in order to determine the temperature window. Additionally, the NiS films' thickness-dependent growth was observed when the ALD process was repeated for 500, 1000, 1500, and 2000 cycles at 200 °C. To examine the self-terminating characteristics, films were grown with the variation of substrate temperatures (180-280 °C) and pulse times of both the precursors at 200 °C. The desiccator was used to preserve all reposited films obtained without additional post-annealing. To perform electrochemical glucose sensing on the conducting substrate, thin NiS films were deposited on fluorine-doped tin oxide (FTO) using the same conditions for 2000 cycles.

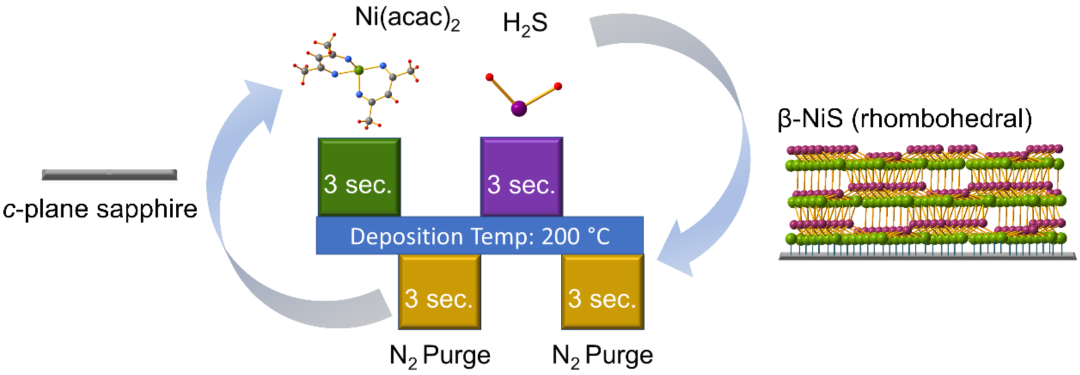

Scheme 1: *Representation of the thermal ALD process representing complete ALD cycles, including pulsing of* $Ni(acac)_2$ *and* H_2S *followed by purging of* N_2 *leading to the growth of rhombohedral β-NiS films on c-plane sapphire.*

(ii) Characterizations:

A Nova Nano SEM 600 field emission scanning electron microscope (FESEM) with energy-dispersive X-ray (EDX) offered by FEI Corporation was used to measure the thickness and surface morphology of the films. Using Mg K_α as the X-ray source, X-ray photoelectron spectra (XPS) were collected using an Omicron nanotechnology spectrometer. The X-ray diffraction (XRD) patterns of the films were recorded using the Panalytical diffractometer (Empyrean) instrument with monochromatic Cu $K_{\alpha 1}$ radiation (λ = 1.5404Å). The Raman spectra of NiS in backscattering geometry were obtained using a Jobin Yvon LabRam HR spectrometer and a 514 nm Ar laser. The surface roughness of the films was examined using an SNL-10 Bruker atomic force microscopy (AFM) device with high resolution. By applying 0.1 μA current and 0.5 Hz frequency in the temperature range of 50–450 K, the electrical transport operation (ETO) option of the Quantum Design system was used to measure temperature-dependent resistance.

(iii) Electrochemical study:

The CHI 760E electrochemical workstation was used to conduct the electrochemical studies. A typical three-electrode method was used, consisting of a saturated calomel electrode (SCE) as the reference electrode, a platinum coil as the counter electrode, and NiS/FTO films as the working electrode in an aqueous 0.1 M NaOH alkaline solution. All the potentials mentioned in the manuscript are with respect to SCE.

8.4. Results and Discussion

Ultrathin crystalline films of NiS were deposited on *c*-sapphire substrate by self-limiting surface reactions of $Ni(acac)_2$ as Ni source and H_2S as S source. **Scheme 1** represents sequential pulsing of $Ni(acac)_2$ and H_2S followed by a purging step after each precursor pulse shows a typical thermal ALD cycle of NiS showing. The NiS films were deposited by considering the thermal stability of $Ni(acac)_2$ during heating. The growth mechanism of NiS films can be like to those proposed in prior reports valid for other Ni precursors [20-23].

$$Ni(acac)_2 + H_2S \longrightarrow NiS + 2H(acac) \qquad (1)$$

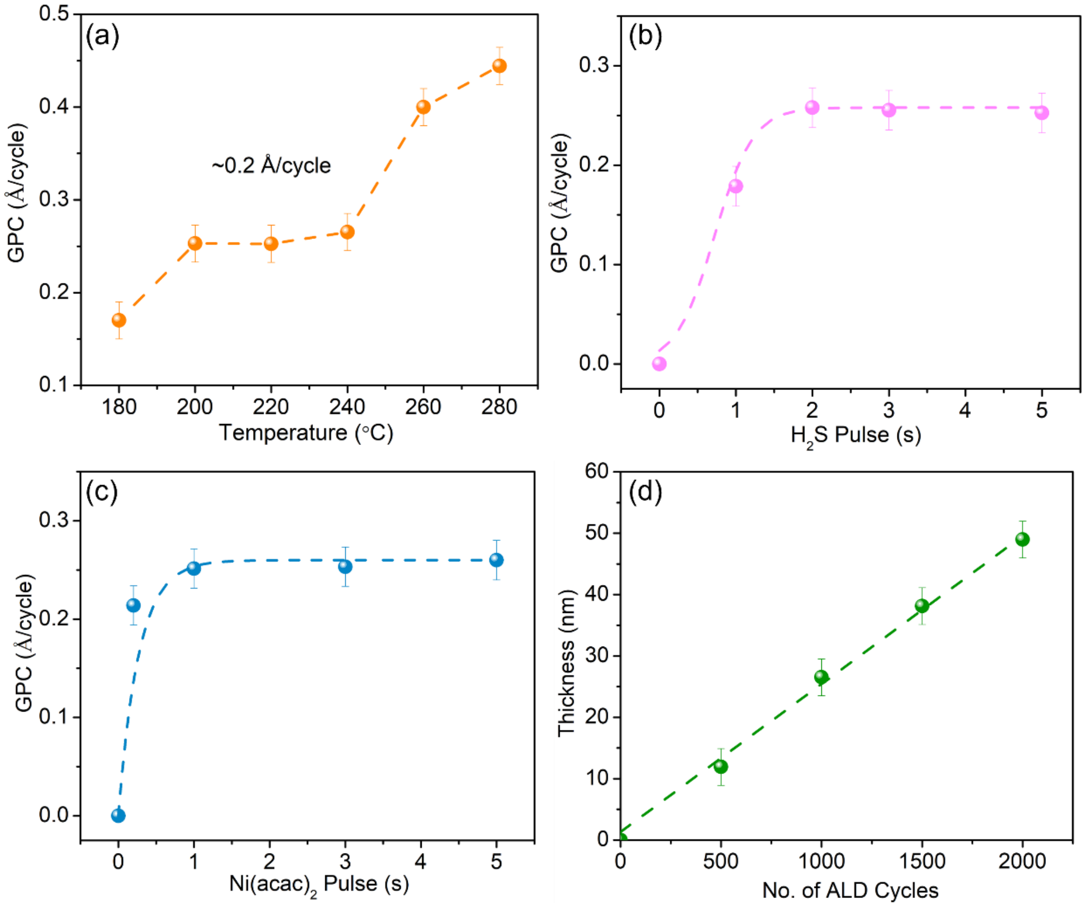

Figure 1: *(a) shows growth rate per cycle (GPC) as a function of the deposition temperature of NiS on c-sapphire, (b,c) show saturation behavior with Ni(acac)*$_2$ *and* H_2S *pulse time, respectively, (d) thickness of the NiS film as a function of the ALD cycles.*

Figure 1 shows the thickness of the as-deposited films by 1000 ALD cycles to measure the growth rate per cycle (GPC) using a cross-sectional FESEM for the determination of the saturation of the Ni and S precursors, reacting in a self-limiting manner with the surface. The growth rate was explored from 180 to 280 °C (**Figure 1a**). A steady growth rate was found to be ~0.2 ± 0.02 Å/cycle between the temperature range of 200-240 °C, indicating an ideal saturated and self-limiting thermal ALD process for NiS films (the cross-sectional FESEM images are shown in **Figure 2**). However, below 200 °C a lower GPC was observed, which indicates that the temperature is not sufficient for the precursors to react due to insufficient activation energy, while above 250 °C the substrate temperature results in the partial decomposition of the precursors to give a higher growth rate. **Figure 1b,c** shows the variation of pulse time for Ni(acac)$_2$ and H_2S gas to examine the self-saturating growth of the film.

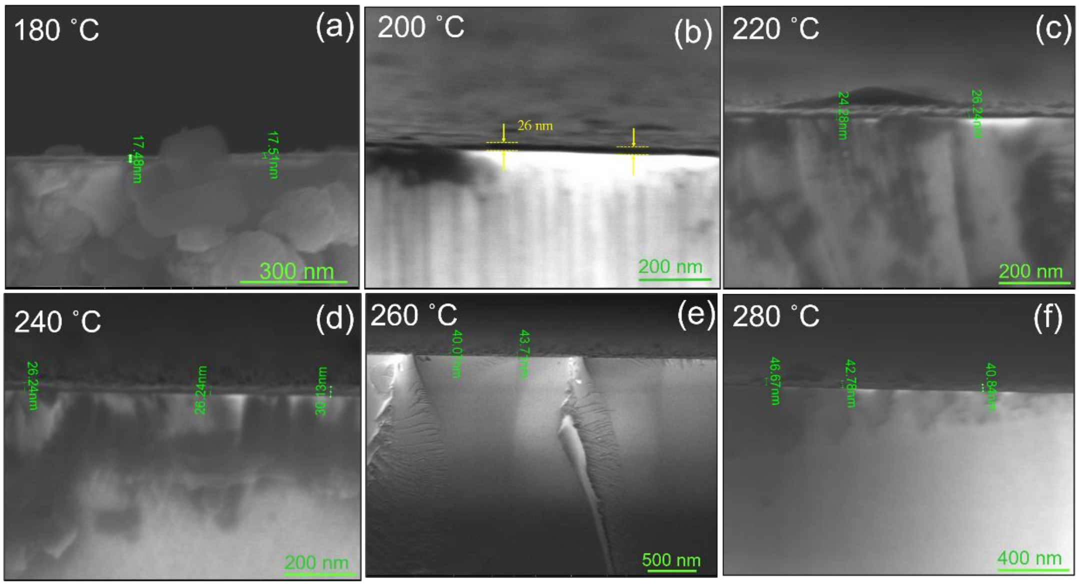

Figure 2: *Cross-section FESEM images of NiS film deposited on c-sapphire substrate by 1000 ALD cycles at (a) 180 ˚C, (b) 220 ˚C, (c) 240 ˚C, (d) 260 ˚C, and (e) 280 ˚C, respectively.*

To achieve saturation ALD growth of NiS, a long pulse time and a purge time of 3s were provided for both precursors. The thickness of the NiS as a function of the ALD cycles indicates a linear behavior with the cycles shown in **Figure 1d** (cross-sectional FESEM images are shown in **Figure 3**) which indicates a typical ALD process where the growth rate should remain independent of the ALD cycles. Because to the films' layer-by-layer deposition, the slope of the curve (GPC) is also constant during the period of the ALD cycles. The fitted line to the thicknesses is not passing through the origin. This phenomenon might be due to the slightly fast nucleation in the initially or agglomeration of the Ni species to form clusters of NiS on the substrate[22]. This trend observed in the earlier report also[20].

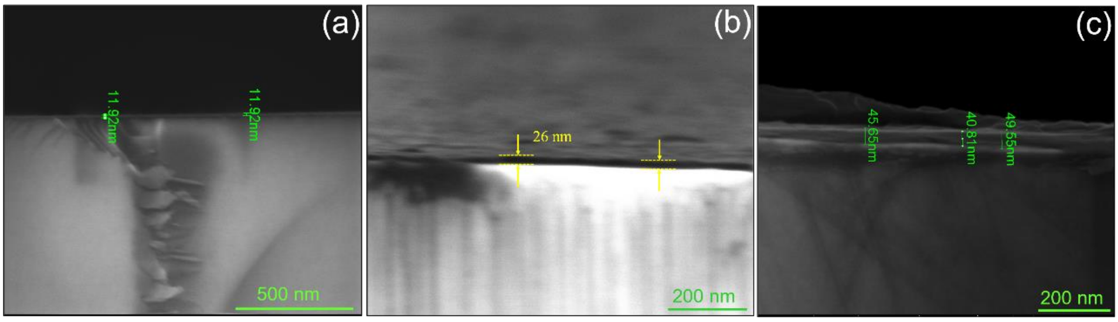

Figure 3: *Cross-section FESEM images of NiS film deposited at 200 ˚C on c-sapphire by (a) 500, (b) 1000, and (c) 2000 ALD cycles, respectively.*

By using XRD, the crystalline nature of the NiS films deposited by ALD was thoroughly investigated. **Figure 4a** shows the XRD pattern of the NiS film deposited on crystalline *c*-sapphire (0001) substrates. The diffraction peaks confirms the formation of crystalline rhombohedral NiS (β-phase) having the *R*3*m* space group (JCPDS card No. 00-075-0612) with a preferred orientation (300) plane (shown in **Figure 4**) [44,45].

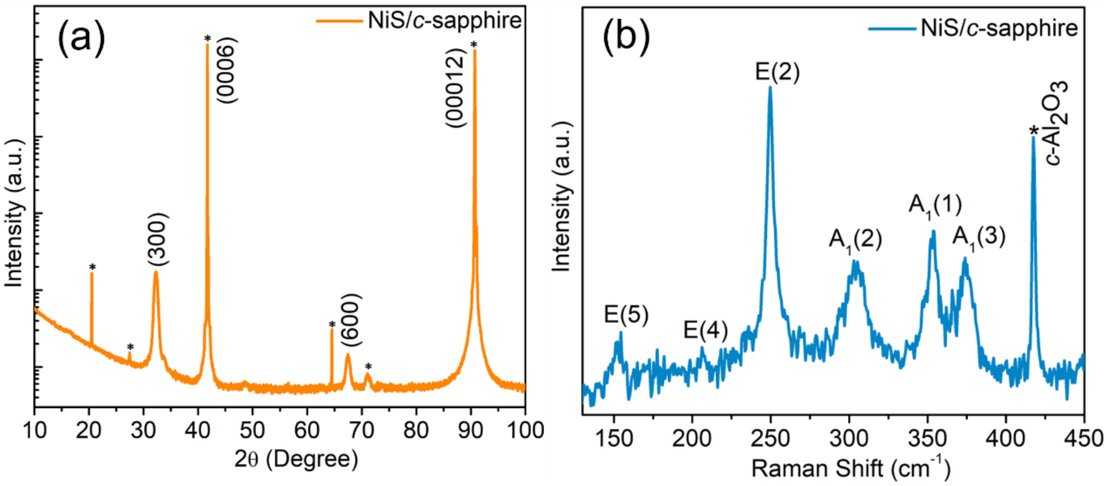

Figure 4: *(a) XRD pattern and (b) room-temperature Raman spectra of the β-NiS film grown at 200 °C on c- sapphire by 1000 ALD cycles (* denotes the substrate/holder peaks).*

The XRD pattern of the NiS films as a function of the substrate temperature also be used to confirm the ALD temperature window of NiS (**Figure 5a**), where the peak corresponding to the (300) plane was only observed in the temperature range of 200-240 °C. In the investigation of the thickness-dependent XRD pattern, the crystallinity of the films was observed. After 2000 cycles, peaks with a very low intensity corresponding to the (110), (101), and (021) planes were also observed **(Figure 5b)**. The decrease in full width at half-maximum (FWHM) of the (003) peak of NiS shows the improvement of crystallinity with increasing ALD cycles (film thickness) due to long-range ordering in the preferred direction.

The crystal structure (phase) and electronic structure of the deposited NiS films were determined using Raman spectroscopy. **Figure 4b** shows the Raman spectra of the NiS films deposited by ALD on *c*-sapphire substrates. The spectra confirms good agreement with the previously reported computational results, and the peaks due to $A_1(3)$, $A_1(1)$, $A_1(2)$, E(2), E(4), and E(5) phonon modes are observed at 374, 351, 301, 248, 203, and 150 cm^{-1}, respectively[46,47]. Notably, the peaks observed at 301 and 374 cm^{-1} confirm the formation of the β-phase of NiS. **Figure 5c** shows the Raman spectra as a function of the substrate temperature, in which the peaks corresponding to the β-phase of NiS are only visible in the range of 200-240 °C. The ALD temperature window, suitable for NiS phase-selective deposition, is correlated with the XRD patterns and Raman spectroscopy results.

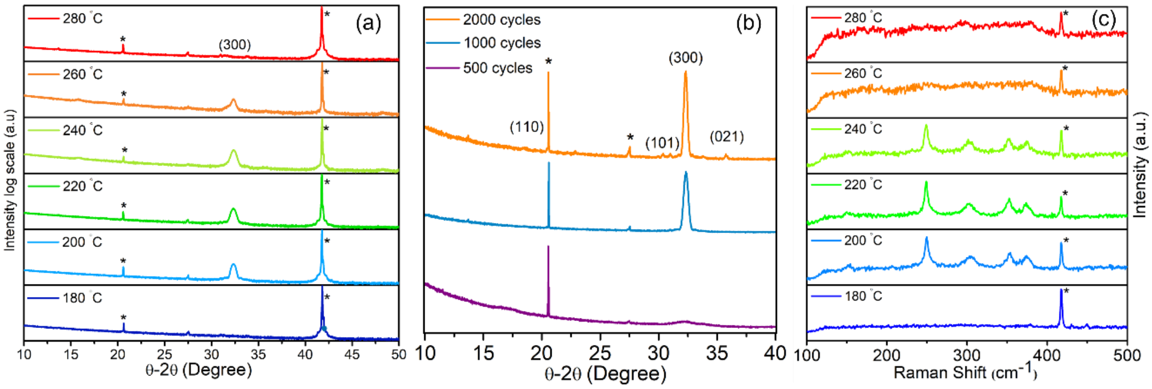

Figure 5: *(a) XRD pattern vs substrate temperature (b)XRD pattern vs ALD cycles (c) room temperature Raman spectra deposited on c-plane sapphire by 1000 ALD cycles as a function of deposition temperature (* denotes the substrate peaks).*

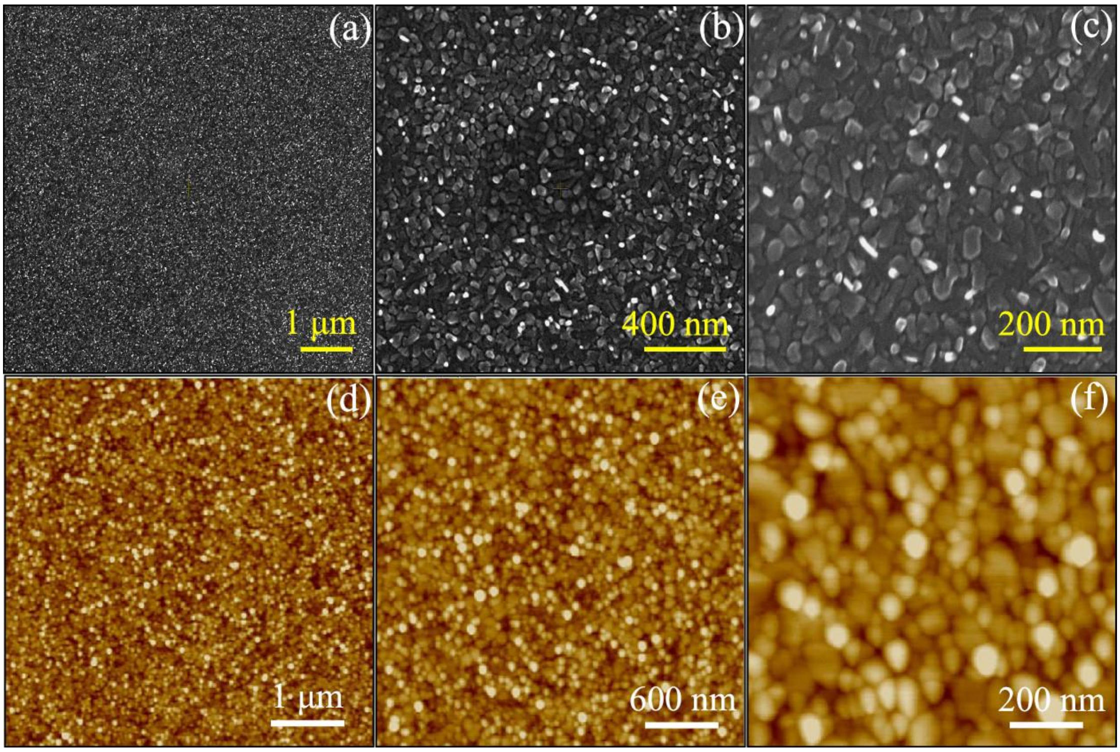

Figure 6: *(a–c) plane view of FESEM images. (d–f) tapping-mode AFM images of crystalline NiS thin films deposited at 200 °C by 1000 ALD cycles grown on c-sapphire showing a granular structure at different magnifications.*

Topographic atomic force microscopy (AFM) images and FESEM images were used to evaluate the morphology of the NiS films. **Figure 6a-c** shows the plane-view FESEM images of the ~26 nm thick film deposited on *c*-sapphire by 1000 ALD cycles, which shows the uniform granular morphology of the film. The roughness (R_{RMS}) of the film extracted from the AFM images shown in **Figure 6d-f** was found to be 2.60 nm for an ~26 nm film.

X-ray photoelectron spectroscopy (XPS) of the NiS films deposited on c-sapphire at 200 °C by 1000 ALD cycles was done to confirm the chemical environment of Ni and the composition of the films **(Figure 7)**. The XP survey-scan spectrum of the NiS films (**Figure 8a**) collected in the range of 1100−0 eV shows the presence of all the characteristic elements corresponding to NiS. **Figure 7a** shows the deconvoluted core-level XP spectra of Ni 2p showing the peaks of Ni $2p_{3/2}$ and Ni $2p_{1/2}$ at 853.3 and 870.5 eV, respectively. The peak positions of the Ni $2p_{3/2}$ and Ni $2p_{1/2}$ of NiS thin films are attributed to the Ni^{2+} oxidation state of nickel with sulfur, validating the formation of the NiS phase only[44]. The peaks at 860.4 and 873.3 eV correspond to the shake-up satellite (sat.) peaks of Ni $2p_{3/2}$ and Ni $2p_{1/2}$, respectively. The peak shouldered at 855.6 eV is due to the satellite peak of NiS as reported elsewhere [22].

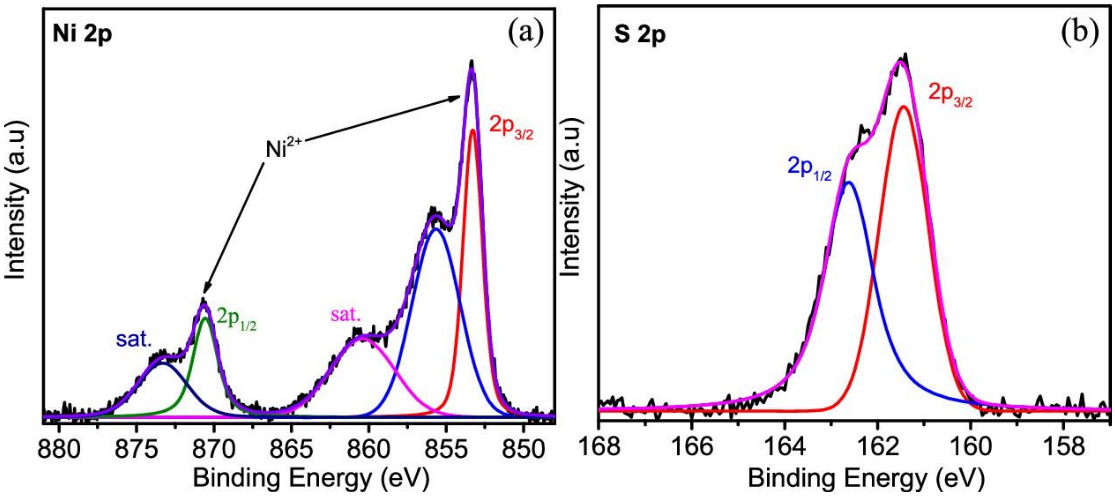

Figure 7: *High-resolution core-level XP spectra of (a) Ni 2p and (b) S 2p of NiS thin films grown on c-sapphire at 200 °C by 1000 ALD cycles.*

The asymmetrically broadened peak of S 2p shown in **Figure 7b** can be deconvoluted into two peaks, S $2p_{3/2}$ and S $2p_{1/2}$, at 161.4 and 162.5 eV, respectively. **Figure 8b,c** shows the core-level spectra of C 1s and O 1s, respectively.

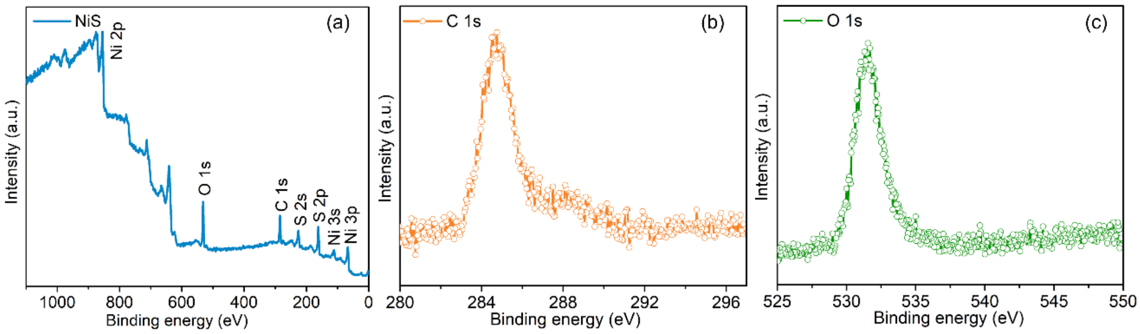

Figure 8: *(a) Long range survey-scan showing all the elements present (b) High resolution core level XPS of C 1s and (c) O 1s of NiS film deposited on c-sapphire at 200 ˚C by 1000 ALD cycles.*

C 1s spectra show an asymmetric nature due to the many types of carbon impurities that are deposited due to the very small decomposition of $Ni(acac)_2$ near the ALD window (~230 to 250 °C) as shown in thermogravimetric analysis (TGA) measurement (**Figure 9**). The chemical composition of the NiS films calculated by XP spectra was found to be $Ni_{1.1}S$, which can be considered as almost stoichiometric, considering experimental errors or instrument calibration. The chemical composition calculated using XPS is in good agreement with the energy-dispersive X-ray (EDX) spectroscopy results (**Figure 10**).

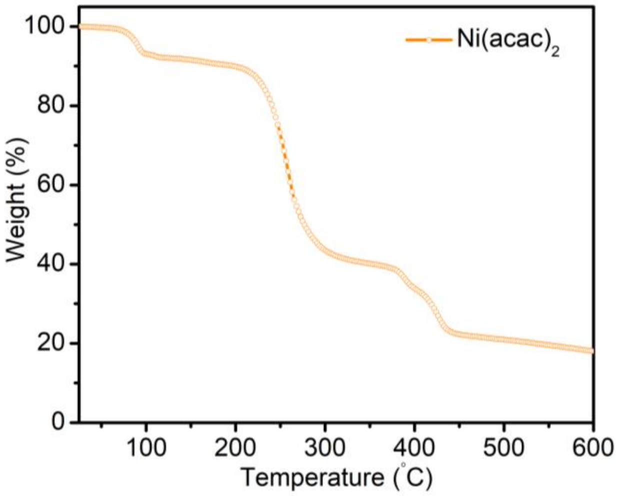

Figure 9: *(a) TGA of nickel acetylacetonate in presence of nitrogen gas.*

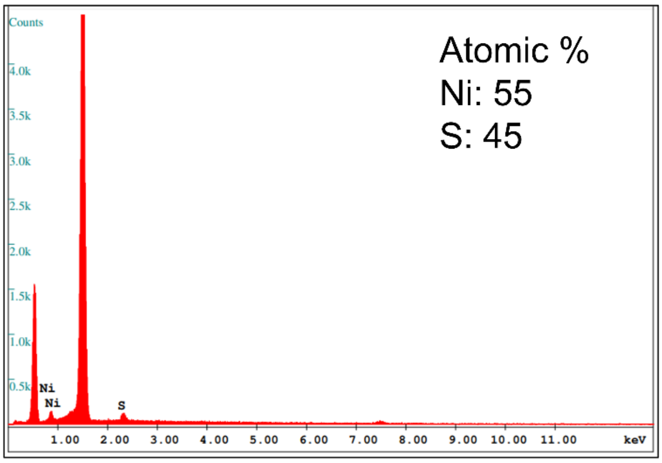

Figure 10: *EDX spectrum of the NiS film grown at 200 ˚C reactor temperature on c-plane sapphire by 1000 thermal ALD cycles.*

In order to determine the electrical properties of the NiS films deposited on *c*-sapphire, resistivity with respect to temperature was measured by the four-probes van der Pauw method. A thin film of ≈26 nm thickness shows a resistivity of 1.65×10^{-4} Ω·cm at room temperature and a quasilinear increase was found with the temperature (shown in **Figure 11)**.

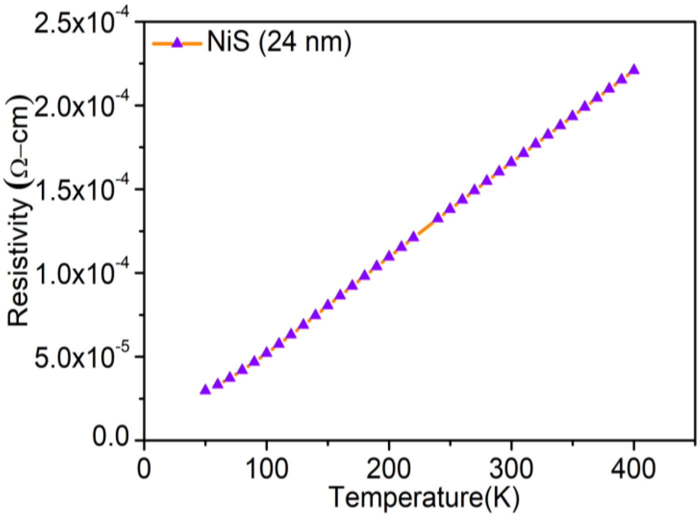

Figure 11: *Electrical properties of NiS film on c-sapphire as a function of temperature for electrical resistivity.*

To explore the NiS thin films as electrode material for electrochemical glucose sensing, ≈50 nm films were grown on conducting fluorine-doped tin oxide (FTO) substrate by 2000 ALD cycles with the same parameters of temperature and pulsing times. The phase of NiS was confirmed by Raman spectrum, as shown in **Figure 12**.

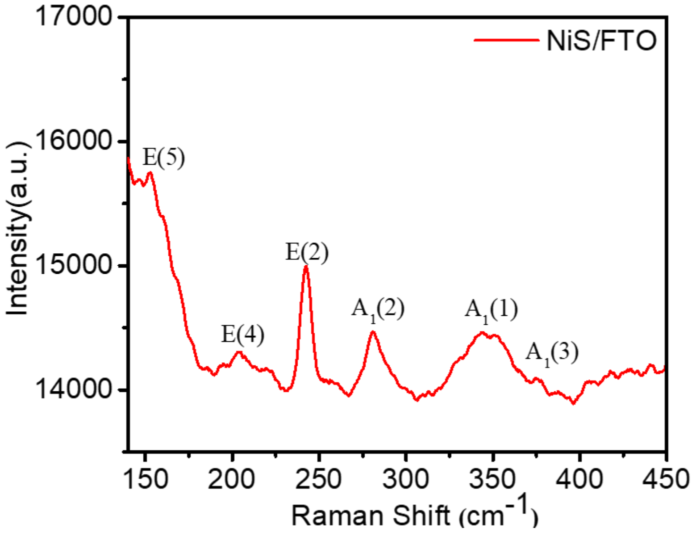

Figure 12: *(a) Raman spectrum of NiS thin film on FTO grown by 2000 ALD Cycles.*

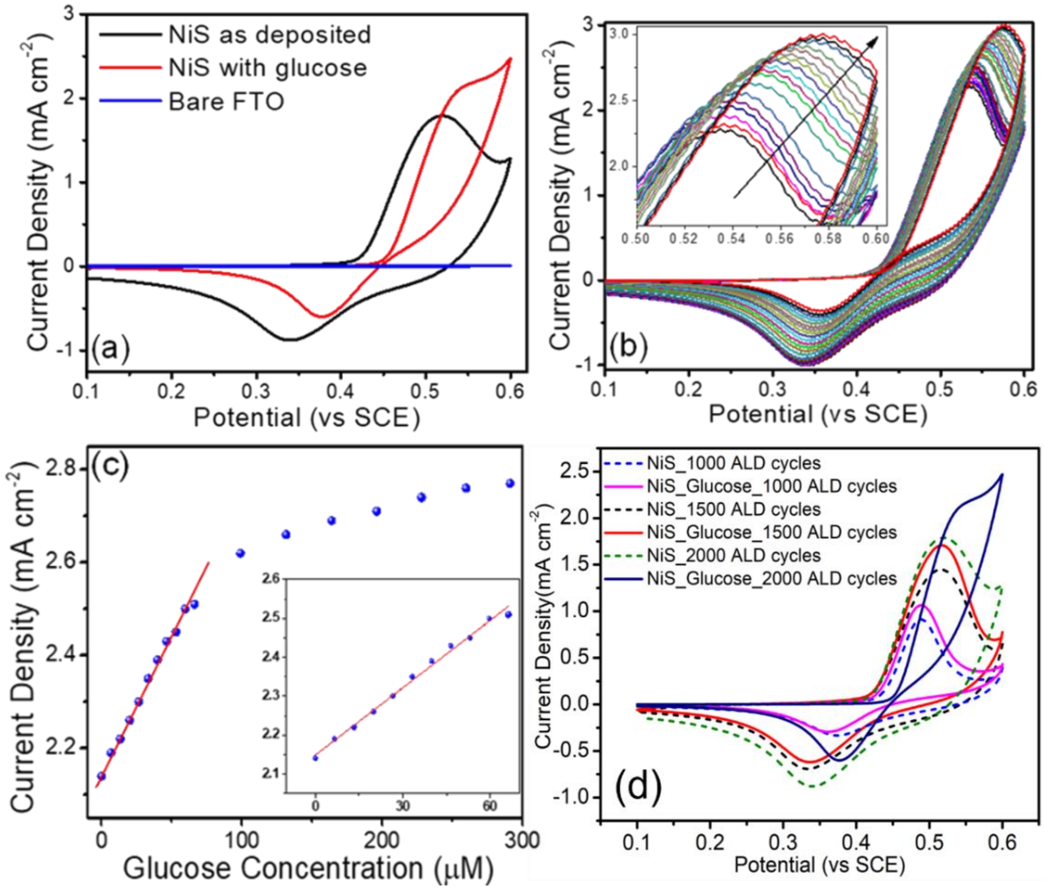

Figure 13: *(a) Cyclic voltammogram (CV) of NiS/FTO thin film in 0.1M NaOH at a scan-rate of 50 mVs-1 (b) with increasing concentration (0 to 500 µM) of glucose, inset: expanded view of the anodic current density in the potential range of 0.5–0.6 V (c) the corresponding calibration plot for successive additions of 0 to 300 µM glucose at the potential of 0.55 V, inset: linear fitting of the calibration curve in the lower detection range of 0-60 µM (d) Cyclic voltammogram of NiS/FTO thin film in 0.1M NaOH at a scan-rate of 50 mVs^{-1} with different thickness without and with presence of 130 µM concentrated glucose solution.*

Cyclic voltammetry and amperometry studies were carried out in 0.1 M NaOH (**Figure 13**). The valuable parameters of a viable glucose sensor, such as selectivity, sensitivity, stability, and response time, were thoroughly studied. Figure 5a demonstrates the CV curves of bare FTO and as-deposited NiS/FTO along with NiS/FTO in the presence of glucose. Oxidation and reduction peaks were not observed for the bare FTO in the potential range of 0−0.6 V. However, the NiS films exhibited reversible redox peaks in the same potential range, which is due to the reversible redox reaction of NiS in an alkaline medium[39]. Upon addition of glucose to the electrolyte, a clear increase in the current density of the anodic peak and a decrease in the cathodic peak were observed, which suggests catalytic oxidation of glucose (**Figure 13a,b**). The catalytic oxidation of glucose was found to be dependent on the film thickness, as the 2000-ALD-cycles NiS exhibited the highest current density (**Figure 13d**).

The increment in anodic current density with increasing concentration of glucose further confirms the catalytic nature of NiS films for the oxidation of glucose[43]. Kannan *et al.* nicely explained the mechanism of reversible redox reaction and its glucose sensing in an alkaline medium for the thin-film NiS[39]. Likewise, **Figure 13c** shows the calibration plot of the current density with respect to the concentration of glucose in the range of 0-300 μM, which shows a decent linear relation ($R^2 = 0.993$) described by

$$I\,[\mathrm{mA}] = 0.0057\,[\mathrm{glucose}]\mu\mathrm{M} + 2.1482 \quad \text{--}(2)$$

The limit of detection ($LOD = 3S_b/m$), limit of quantification ($LOQ = 10S_b/m$), and sensitivity of the sensor were calculated using the standard deviation (S_b) acquired from five blank measurements (0.0001 mA), and the slope value (m) obtained from the calibration plot[48]. The sensor shows excellent sensitivity, LOQ, and LOD with values of 5.78 μA mM^{-1} cm^{-2} , 0.173 μM, and 0.052 μM, respectively, with a response time of < 2 s. Moreover, stability and selectivity are the foremost concerns in biosensors; therefore, chronoamperometric studies were done to evaluate the stability and selectivity of the NiS/FTOALD-based glucose sensor. **Figure 14a** shows the current density plotted against time at 0.55 V for a chronoamperometric response with the addition of the testing solution (TS), which was a mixture of glucose (4.5 mM) and possible electroactive, fouling interferents such as ascorbic acid (0.05 mM), uric acid (0.3 mM), L-cystine (0.01 mM), dopamine (0.05 mM), and sucrose (0.05 mM) present in the human blood in accordance with their respective concentrations[49]. The current density continuously increases as the concentration of glucose is increased stepwise, and steady-state currents are achieved within less than 2 s. A gradual increment in the current density was observed on the addition of 20 µM glucose in the testing solution containing a high concentration (375 µM) of glucose, which shows the good detection feature of the sensor. The selectivity of the sensor was estimated by observing the current density response on the addition of ascorbic acid, uric acid, Na^+ ion, sucrose, L-cystine, and dopamine as the interferents into the glucose solution as shown in **Figure 14b**.

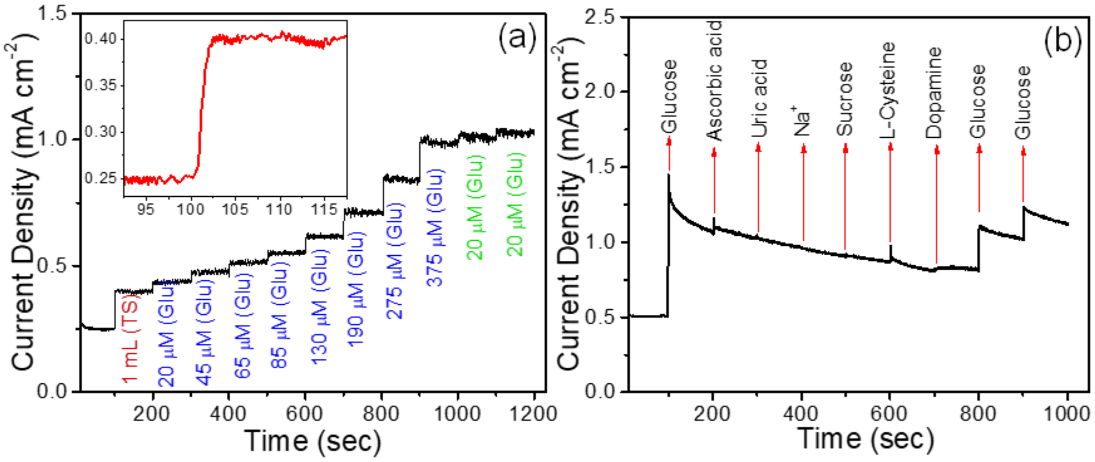

Figure 14: *Chronoamperometric response of NiS/FTO in 0.1M NaOH at 0.55 V (a) with consecutive addition of glucose with con-centrations range of 0 to 425 µM (Insets: response time) (b) in the presence of interferents. (TS: Testing Solution, Glu: Glucose).*

A negligible increase in the current density on the addition of 0.05 mM of each interferent in comparison to 1 mM concentration of glucose shows the excellent selectivity of the sensor. The stability of the NiS/FTO-based electrode was further evaluated by CV and chronoamperometric studies after 1 week of the sensing as shown in **Figure 15a,b**.

Very small changes were observed in the current density, CV, and chronoamperometric characteristics of the films, which indicates the good stability of the NiS/FTO-based electrode and no effect of interferents on the film.

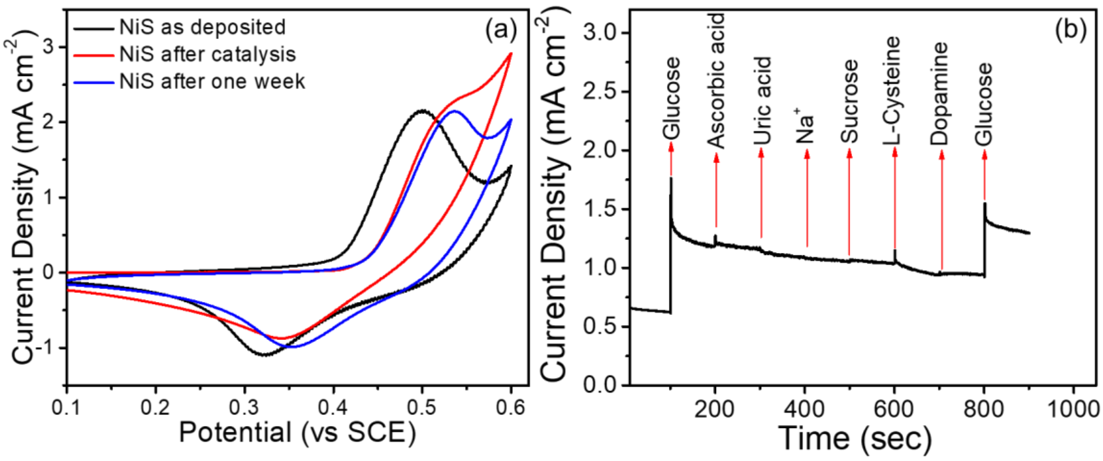

Figure 15: *Stability of NiS/FTO electrode by (a) cyclic voltammogram and (b) chronoamperometric response in the presence of interferents after one week of glucose sensing with NiS/ FTO electrode in 0.1M NaOH at a scan-rate of 50 mVs^{-1}.*

The surface morphology and chemical composition of the NiS/FTO films were investigated after 10 cycles of glucose sensing with 130 µM glucose concentration. The line scan spectra of the present elements, Ni, S, O, and C, show that the intensity of oxygen increases and that of sulfur decreases after the sensing (**Figure 16**), confirming partial hydroxide formation on the NiS films in alkaline medium[50,51].

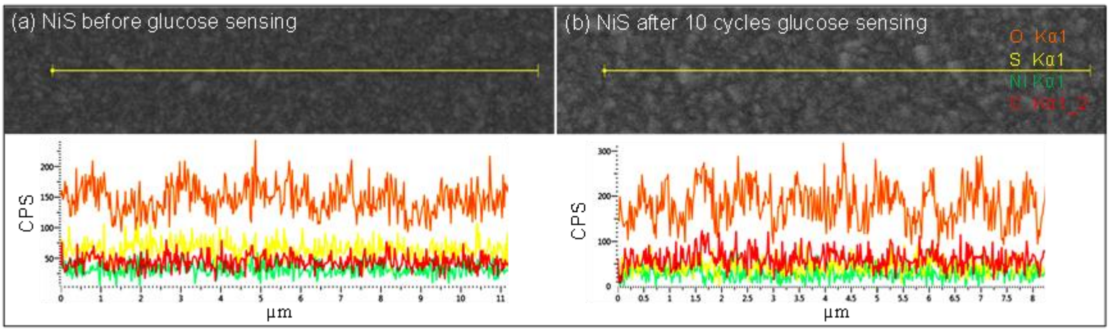

Figure 16: *Line scan spectra of NiS/FTO films (a) before and (b) after the glucose sensing.*

As-deposited films were found to be smooth, whereas after sensing the films became slightly rough (**Figure 17**). The presence of sulfur after 10 cycles of detection of glucose was also observed in the EDX and elemental mapping of the present elements in the films (**Figures 17** and **18**).

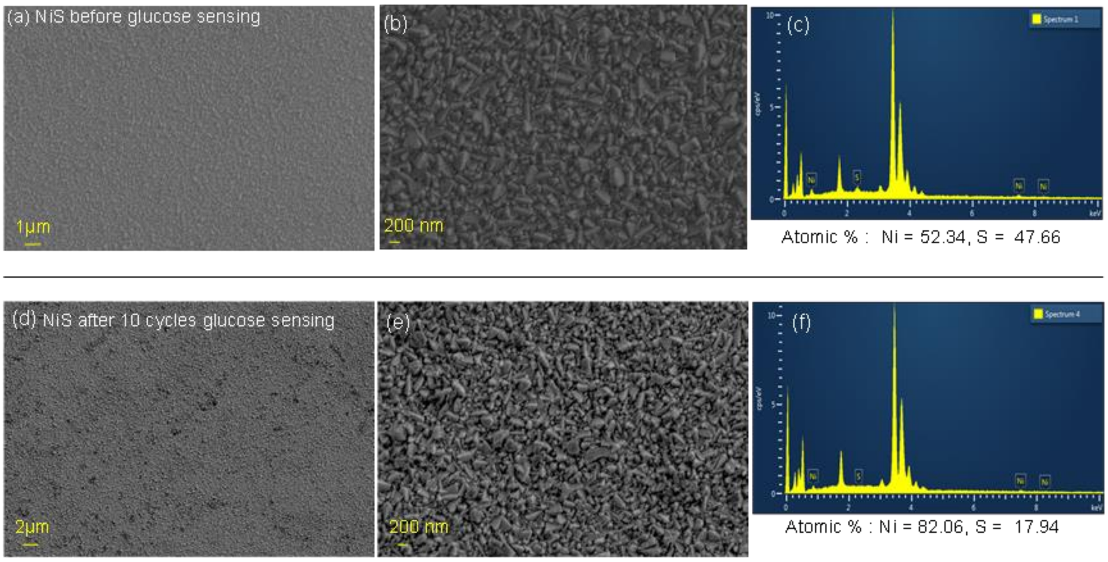

Figure 17: *(a,b) FESEM and (c) EDX spectra of NiS/FTO film of before glucose detection (as deposited) and (d,e) FESEM and (f) EDX spectra of films after 10 cycles glucose detection.*

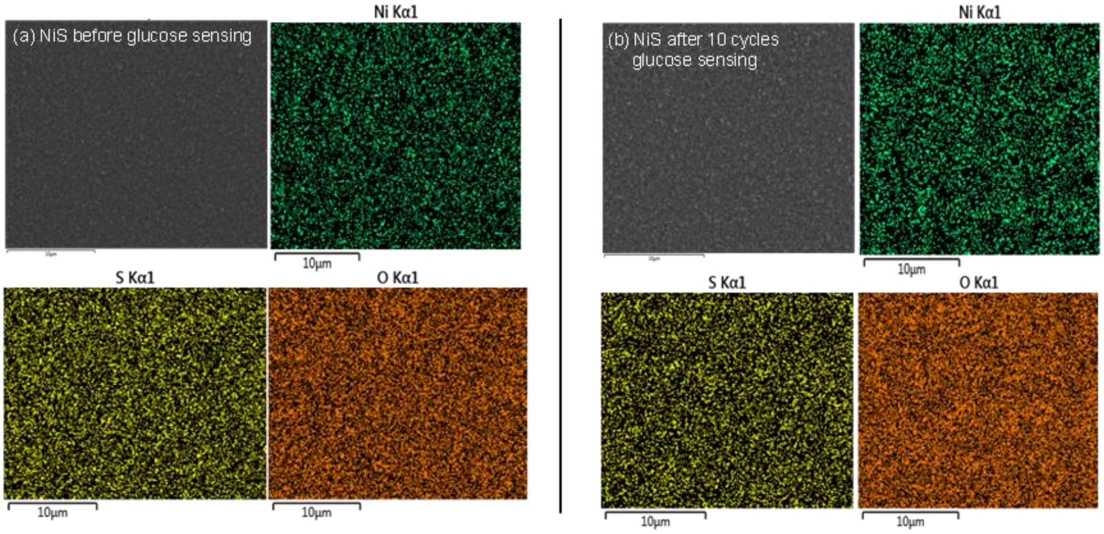

Figure 18: *Elemental mapping of the present elements in the NiS/FTO film of before (a) glucose detection (as deposited) and (b) after 10 cycles glucose detection.*

The performance of the present NiS/FTO-based sensor was compared with that of various enzymatic, metal chalcogenides, and Ni-based glucose sensors. The NiS thin film proves to be a good electrode material in terms of sensitivity, LOD, and response time compared to other materials synthesized by different routes, including the ALD process, as shown in **Table 1**.

Table 1. Comparison of the various glucose sensors based on metal chalcogenides and Nickel materials with the present work.

Electrode material	Sensitivity ($\mu AmM^{-1}cm^{-2}$)	LOD [µM]	Response time [s]	Methods	Ref.
CuS	7.842	-	10	Solvothermal	34
MoS_2-Cu	1055	-	-	Chemical reduction	35
GOD-CS/PB/Bi_2S_3	24.55	3.8	3	Electrodeposition	36
Ni_3S_2/CNT	3345	1.0	-	Hydrothermal	37
NiS/S-g-C_3N_4	80	1.5	5	Pyrolysis	38
NiS	7.43	0.32	< 8	Electrodeposition	39
CNT-Ni	1384.1	2	3	ALD	40
NiO/SCCNTS	1252.3	0.1	< 2	ALD	41
NiO/SiC	2037	0.32	-	ALD	42
$Ni(OH)_x$/CC	19470	0.47	-	ALD	43
NiS	**5.78**	**0.052**	**< 2**	**ALD**	**This work**

8.5. Conclusions

In conclusion, employing successive pulsing of [$Ni(acac)_2$] as the Ni precursor and H_2S as the S precursor, we have standardised an ALD process to grow thin films of rhombohedral NiS on *c*-plane sapphire. The process achieves crystalline NiS on a substrate at 200 °C without further annealing which could be beneficial for a variety of applications in the electronics. Using nickel sulphide grown by ALD, we fabricated the electrochemical non-enzymatic glucose sensor. The thin-film NiS/FTO-based glucose sensor exhibits superior sensing from the point of view of sensitivity and LOD, with values of 5.78 $\mu A\ mM^{-1}\ cm^{-2}$ and 0.052 µM, respectively, with a fast response time of < 2 s.

The NiS/FTO electrode has acceptable selectivity and stability, making them a top choice for sensing applications. The investigations mentioned in this study explored the deposition of crystalline NiS films and their usage in thin-film-based biosensors, which have promise for use in electrocatalysis, the food industry, biosensing, and other areas.

8.6. References

[1] Lim, B. S.; Rahtu, A.; Gordon, R. G. *Nat. Mater.* **2003**, 2, 749−754.

[2] Miikkulainen, V.; Leskelä, M.; Ritala, M.; Puurunen, R. L. *J. Appl. Phys.* **2013**, 113, 021301.

[3] George, S. M. *Chem. Rev.* **2010**, 110, 111−131.

[4] Meng, X.; He, K.; Su, D.; Zhang, X.; Sun, C.; Ren, Y.; Wang, H. H.; Weng, W.; Trahey, L.; Canlas, C. P.; Elam, J. W. *Adv. Funct. Mater.* **2014**, 24, 5435−5442.

[5] Mahuli, N.; Saha, D.; Sarkar, S. K. *J. Phys. Chem. C* **2017**, 121, 8136−8144.

[6] Sreedhara, M.; Gope, S.; Vishal, B.; Datta, R.; Bhattacharyya, A. J.; Rao, C. N. R. *J. Mater. Chem. A* **2018**, 6, 2302−2310.

[7] Tan, L. K.; Liu, B.; Teng, J. H.; Guo, S.; Low, H. Y.; Loh, K. P. *Nanoscale* **2014**, 6, 10584−10588.

[8] Li, H.; Gao, Y.; Shao, Y.; Su, Y.; Wang, X. J. *Nano Lett.* **2015**, 15, 6689−6695.

[9] Riha, S. C.; Koegel, A. A.; Meng, X.; Kim, I. S.; Cao, Y.; Pellin, M. J.; Elam, J. W.; Martinson, A. B. F. *ACS Appl. Mater. Interfaces* **2016**, 8, 2774−2780.

[10] Meng, X.; Cao, Y.; Libera, J. A.; Elam, J. W. *Chem. Mater.* **2017**, 29, 9043−9052.

[11] Shao, Y.; Guo, Z.; Li, H.; Su, Y.; Wang, X. *Angew. Chem.* **2017**, 129, 3274−3279.

[12] Weimer, M. S.; McCarthy, R. F.; Emery, J. D.; Bedzyk, M. J.; Sen, F. G.; Kinaci, A.; Chan, M. K.; Hock, A. S.; Martinson, A. B. F. *Chem. Mater.* **2017**, 29, 2864−2873.

[13] Hämäläinen, J.; Mattinen, M.; Mizohata, K.; Meinander, K.; Vehkamäki, M.; Räisänen, J.; Ritala, M.; Leskelä, M. *Adv. Mater.* **2018**, 30, No. 1703622.

[14] Kim, S. B.; Sinsermsuksakul, P.; Pike, R. D.; Gordon, R. G.; *et al. Chem. Mater.* **2014**, 26, 3065−3073.

[15] Guo, Z.; Wang, X. *Angew. Chem., Int. Ed.* **2018**, 57, 5898−5902.

[16] Wang, J.; Guo, Z.; Xiong, W.; Wang, X. *Chem. - Eur. J.* **2018**, 24, 18568−18574.

[17] Mattinen, M.; Popov, G.; Vehkamäki, M.; King, P. J.; Mizohata, K.; Jalkanen, P.; Räisänen, J.; Leskelä, M.; Ritala, M. *Chem. Mater.* **2019**, 31, 5713−5724.

[18] Dasgupta, N. P.; Meng, X.; Elam, J. W.; Martinson, A. B. F. *Acc. Chem. Res.* **2015**, 48, 341−348.

[19] Mattheiss, L. F. *Phys. Rev. B* **1974**, 10, 995.

[20] Çimen, Y.; Peters, A. W.; Avila, J. R.; Hoffeditz, W. L.; Goswami, S.; Farha, O. K.; Hupp, J. T. J. *Langmuir* **2016**, 32, 12005−12012.

[21] Mahuli, N.; Sarkar, S. K. *J. Vac. Sci. Technol., A* **2016**, 34, 01A142.

[22] Zhao, R.; Wang, X. *Chem. Mater.* **2019**, 31, 445− 453.

[23] Li, H.; Shao, Y.; Su, Y.; Gao, Y.; Wang, X. *Chem. Mater.* **2016**, 28, 1155−1164.

[24] Witkowska Nery, E.; Kundys, M.; Jelen, P. S.; Jönsson-́ Niedziółka, M. *Anal. Chem.* **2016**, 88, 11271−11282.

[25] Hwang, D.-W.; Lee, S.; Seo, M.; Chung, T. D. *Anal. Chim. Acta* **2018**, 1033, 1−34.

[26] Bruen, D.; Delaney, C.; Florea, L.; Diamond, D. *Sensors* **2017**, 17, 1866.

[27] Nan, C.; Zhang, Y.; Zhang, G.; Dong, C.; Shuang, S.; Choi, M. M. F. *Enzyme Microb. Technol.* **2009**, 44, 249−253.

[28] Niu, X.; Li, X.; Pan, J.; He, Y.; Qiu, F.; Yan, Y. *RSC Adv.* **2016**, 6, 84893−84905.

[29] Park, S.; Boo, H.; Chung, T. D. *Anal. Chim. Acta* **2006**, 556, 46−57.

[30] Strakosas, X.; Selberg, J.; Pansodtee, P.; Yonas, N.; Manapongpun, P.; Teodorescu, M.; Rolandi, M. *Sci. Rep.* **2019**, 9, 10844.

[31] Zhai, D.; Liu, B.; Shi, Y.; Pan, L.; Wang, Y.; Li, W.; Zhang, R.; Yu, G. *ACS Nano* **2013**, 7, 3540− 3546.

[32] Bai, Y.; Yang, W.; Sun, Y.; Sun, C. *Sens. Actuators B Chem* **2008**, 134, 471−476.

[33] Kong, T.; Chen, Y.; Ye, Y.; Zhang, K.; Wang, Z.; Wang, X. *Sens. Actuators, B* **2009**, 138, 344−350.

[34] Zhang, X.; Wang, G.; Gu, A.; Wei, Y.; Fang, B. *Chem. Commun.* **2008**, 45, 5945−5947.

[35] Huang, J.; Dong, Z.; Li, Y.; Li, J.; Tang, W.; Yang, H.; Wang, J.; Bao, Y.; Jin, J.; Li, R. *Mater. Res. Bull.* **2013**, 48, 4544−4547.

[36] Wu, S.; Liu, G.; Li, P.; Liu, H.; Xu, H. *Biosens. Bioelectron.* **2012**, 38, 289−294.

[37] Lin, T. W.; Liu, C. J.; Dai, C. S. *Appl. Catal., B* **2014**, 154−155, 213−220.

[38] Vinoth, S.; Rajaitha, P. M.; Venkadesh, A.; Devi, K. S.; Radhakrishnan, S.; Pandikumar, A. *Nanoscale Adv.* **2020**, 2, 4242−4250.

[39] Kannan, P. K.; Rout, C. S. *Chem. - Eur. J.* 2015, 21, 9355−9359.

[40] Choi, T.; Kim, S. H.; Lee, C. W.; Kim, H.; Choi, S.-K.; Kim, S.- H.; Kim, E.; Park, J.; Kim, H. *Biosens. Bioelectron.* **2015**, 63, 325− 330.

[41] Raza, M. H.; Movlaee, K.; Wu, Y.; El-Refaei, S. M.; Karg, M.; Leonardi, S. G.; Neri, G.; Pinna, N. *ChemElectroChem* **2019**, 6, 383−392.

[42] Yang, P.; Tong, X.; Wang, G.; Gao, Z.; Guo, X.; Qin, Y. *ACS Appl. Mater. Interfaces* **2015**, 7, 4772−4777.

[43] Wa, Q.; Xiong, W.; Zhao, R.; He, Z.; Chen, Y.; Wang, X. *ACS Appl. Nano Mater.* **2019**, 2, 4427−4434.

[44] Alsén, N. Röntgenographische Untersuchung der Kristallstrukturen von Magnetkies, Breithauptit, Pentlandit, Millerit und verwandten Verbindungen. *Geol. Foeren. Stockholm Foerh.* **1925**, 47, 19−72.

[45] Kullerud, G.; Yund, R. A. *J. Petrol.* **1962**, 3, 126−175.

[46] Wang, J. H.; Cheng, Z.; Brédas, J. L.; Liu, M. *J. Chem. Phys.* **2007**, 127, 214705.

[47] Bishop, D.; Thomas, P.; Ray, A. *Mater. Res. Bull.* **1998**, 33, 1303−1306.

[48] Knobel, G.; Calimag-Williams, K.; Campiglia, A. D. *Analyst* **2012**, 137, 5639−5647.

[49] Toghill, K. E.; Compton, R. G. *Int. J. Electrochem.* **2010**, 5, 1246−1301.

[50] Li, H.; Zhao, R.; Zhu, J.; Guo, Z.; Xiong, W.; Wang, X. *Chem. Mater.* **2020**, 32, 8885−8894.

[51] Chou, S. W.; Lin, J. Y. *J. Electrochem. Soc.* **2013**, 160, D178− D182.

Part III: Carbon-doped Gallium Nitride

Chapter 9

Study of Carbon-doped GaN via Solid–Gas Reaction Route and Its Defect Related Luminescence

Summary

Carbon-doped gallium nitride (GaN) is a very exciting material for the applications of optoelectronic devices, and the findings related to its defects offer insights regarding possible transitions based on the nature of the defects. Carbon-doped GaN has been synthesized by a simple solid-gas reaction method. An isolated C_N defect state is observed by spectroscopic tools along with the C_N–O_N complex formation.

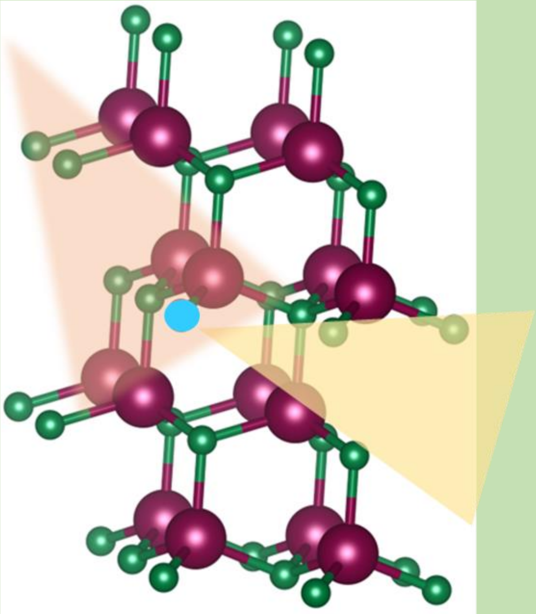

A transition band at ≈3.05 eV in the fundamental absorption band and carbon-related yellow luminescence (YL) were observed in the C-doped samples. Blue luminescence (BL) related to an oxygen was quenched on carbon doping. The origin of this defect-related YL in C-doped GaN is attributed to the carbon-defect C_N (−1 charged) level transitions confirmed by absorption energy, photoluminescence (PL) peak position, and zero-phonon line.

Paper based on this work has appeared in *ACS Appl. Electron. Mater.* **2022**, 4, 3147–3153.

9.1. Introduction

The development of power semiconductor devices has benefitted immensely from the development of gallium nitride (GaN) over the past ten years. Due to the special characteristics of GaN, diodes and transistors manufactured from this material perform better than their Si counterparts and are anticipated to find several uses in the next-generation power converters. **Figure 1** shows the usage of n-type and highly resistive semi-insulating nitride materials, which is necessary for the production of GaN-based devices such as field-effect transistors (FETs) and high electron mobility transistors (HEMTs)[1].

The most common techniques for producing high-quality GaN are metalorganic chemical vapor deposition (MOCVD), hydride vapor phase epitaxy (HVPE), and ammonothermal processes[2]. A low-level impurity of oxygen as donor and carbon[3] or iron[4] as acceptor can be used for introducing semi-insulating behavior in GaN. The synthesis of high-quality semi-insulating GaN has been thoroughly explored using HVPE[5] and MOCVD[6]. A deep acceptor configurated C is responsible for a highly resistive state in N substitution (C_N) and compensation of oxygen as well [7].

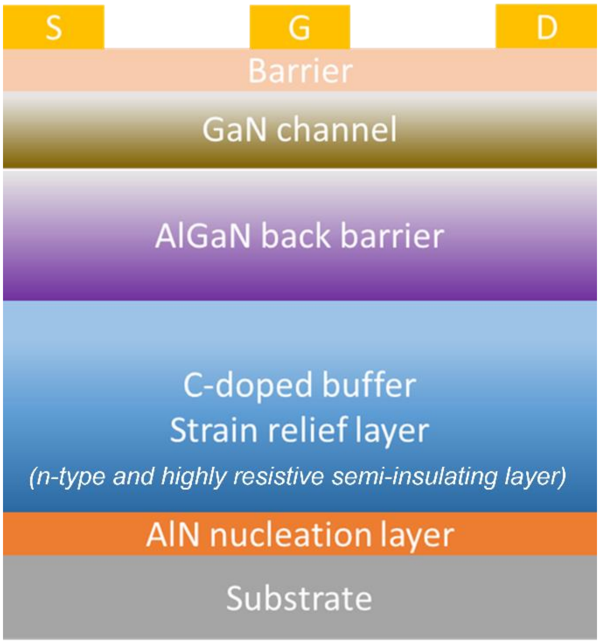

Figure 1: *Representation of conventional high electron mobility transistor's structure fabricated with the usage of carbon doped gallium nitride.*

Doping of carbon creates defect states C_N or $C_N{-}O_N$ complex, which introduces an optical transition referred to yellow luminescence (YL) at ≈2.1−2.2 eV (shown in **Figure 2)**. Although numerous theoretical and experimental methods have been tried over the years to comprehend the characteristics of these defect states, their various energies, and the associated emissions;[7] an experimental characterization of YL is still needed. A study on substrate-free C-doped GaN is of interest for vibrational spectroscopic characterizations as a Reststrahlen-related band exhibition of the substrate obstructs localized vibrational modes (LVMs) of a carbon dopant in GaN[8−12].

It has already been demonstrated that aliovalent anion substitution in the bulk materials modifies the band structure and electrical characteristics of oxides and sulfides like TiO_2, ZnO, CdO, and CdS, making these materials suitable for catalysis applications[13]. Anionic substitution by a simple solid-state synthesis, O by N and F in TiO_2 (e.g., TiNF),[14,15] ZnO (e.g., Zn_2NF),[16] and CdO (e.g., Cd_2NF)[17] and sulfur (S) by phosphorus (P) and chlorine (Cl) in CdS (e.g., Cd_2PCl)[18] gives rise to novel properties. It would be interesting to use this technique for the GaN in the presence of an O impurity because anionic substitution or doping modifies the electrical structure and optical characteristics of the materials.

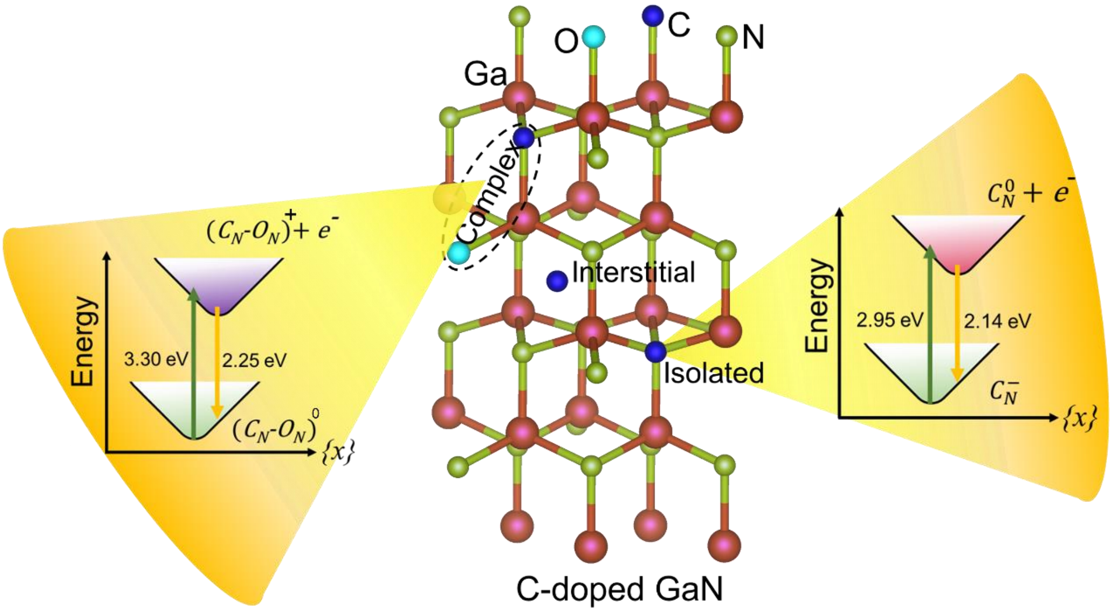

Figure 2: *Representation of photoluminescence causes by carbon doping in the gallium nitride.*

9.2. Scope of present investigation

In the present work, we describe the solid-gas reaction method we used to synthesis carbon-doped GaN. We used Ga_2O_3 as the gallium source, ammonia gas as the nitrogen source, and CH_4 as the carbon source. In order to validate C-doping in GaN, we conducted a spectroscopic investigation (FT-IR, Raman spectroscopy, and XPS). We looked at the local vibration modes (LVM), bonding structure, and elemental composition. Defect related luminescence properties were thoroughly studied.

9.3. Experimental

(i) Solid-gas phase reaction route of C-doped GaN:

Undoped gallium nitride (GaN) and C-doped ($GaN:C_N$) samples have been synthesized by a solid–gas phase reaction route shown in the schematic (**Figure 3a**). In a typical synthesis, 300 mg of Ga_2O_3 powder (Sigma-Aldrich, 99.99%) in an alumina boat, was inserted into a tube furnace (single heating zone) and heated to 1000 °C in the presence of NH_3 gas (2 mL/min) for 4 h. To dope carbon, methane (CH_4, Chemix, 99.999%) was used as another reactive gas (2 mL/min) in addition to NH_3 (2 mL/min). GaN samples with different carbon doping ($GaN:C_N$-(i), $GaN:C_N$- (ii), and $GaN:C_N$) were achieved by varying the reaction time of CH_4 gas.

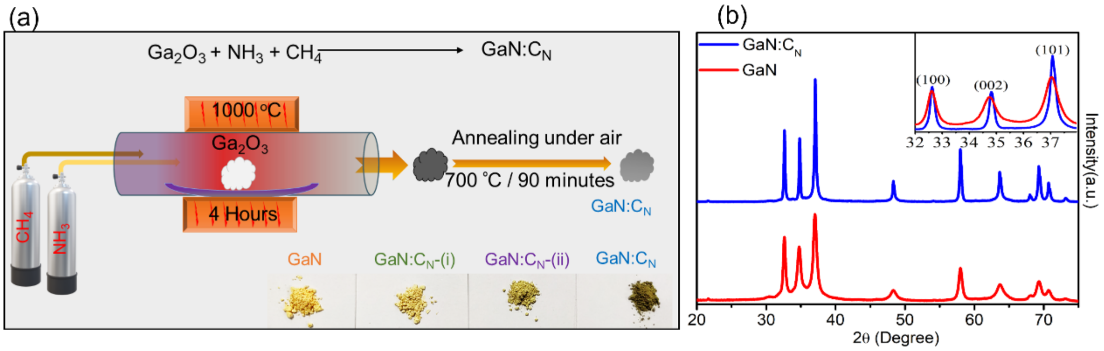

Figure 3: *(a) Representation of solid–gas synthesis route for c-doped GaN. (b) X-ray diffraction patterns of GaN and $GaN:C_N$ samples.*

The CH_4 duration for lower C-doped samples $GaN:C_N$-(i) and $GaN:C_N$-(ii) was kept at 2 and 3 h, respectively. CH_4 was passed for 4 h to obtain the highest doped sample GaN:C_N. A comparison spectroscopic study was mainly performed on undoped GaN and the highest C-doped GaN (GaN:C_N). All samples prepared in the presence of CH_4 appeared dark black because of the surface coating/ adsorption of carbon, and hence, to remove the surface-coated/ adsorbed carbon, samples were annealed at 700 °C for 90 min in the air.

(ii) Characterizations:

X-ray diffraction (XRD) patterns have been recorded by a Rigaku SmartLab SE diffractometer using Cu K_α (λ= 1.54059 Å) radiation. The average crystallites' sizes (d) of the samples were determined by the Scherrer formula, ($d = k\lambda/B\cos\theta$, where k is a constant (i.e., 0.9), λ is the wavelength of the Cu K_α radiation (i.e., 1.54056 Å), θ is the Bragg angle, and B is the full width at half-maximum (FWHM) of the diffraction peak). Fourier Transform Infrared Spectroscopy, Bruker IFS 66v/S spectrometer in ATR mode, and Raman spectroscopy are used to analyse vibrational modes (Jobin Yvon LabRam HR spectrometer with 514 nm Ar laser). The diffuse reflectance spectroscopy (DRS) mode of a PerkinElmer Lambda 750 UV–vis spectrometer and the FLS1000 Edinburgh instruments photoluminescence spectrometer, both of which utilise front-face geometry to prevent self-absorption, were used to conduct the optical measurements. From the reflectance (R) data obtained by DRS mode, absorption data were calculated using the Kubelka–Munk function: $F(R_\infty) = (1 - R_\infty)^2 /(2R_\infty)$, where α, S, and R_∞ correspond to absorption, scattering coefficient, and reflectance, respectively. A Quanta 3D field emission scanning electron microscope has been used to analyse the morphology of materials (FESEM). XPS was obtained utilising an Al K_α monochromator as the X-ray source and a 2 kV Ar^+ ion sputter depth profile with a Thermo Scientific KAlpha spectrometer. A Shirley-type background function and an optimised mixture of the Lorentzian and Gaussian functions were used to fit the XPS spectra.

9.4. Results and Discussion

We have been able to synthesize C-doped samples of GaN with various contents of carbon by a solid–gas reaction route (**Figure 3a**). A notable color change was observed from white-yellow to gray on increasing the carbon content in doped GaN:C_N (**Figure 3a**). XRD patterns of the GaN and GaN:C_N (**Figure 3b**) suggest that GaN retains the wurtzite structure on carbon doping. The average crystallite size of the samples was determined by the Scherrer formula ($d = k\lambda/B\cos\theta$). From FWHM (inset of **Figure 3b**), d is found to be higher (≈57.30 nm) for GaN:C_N than the undoped GaN (≈22.63 nm). The same was also observed in FESEM micrographs presented in **Figure 4** as well, wherein undoped GaN exhibits rod/wire-like morphology whereas GaN:C_N shows a hexagonal morphology, with a much bigger crystallite size in the range of a few micrometers. An attached hexagonal morphology with each other was also observed because of the attachment of facets having similar surface energies along with one of the three axes of the unit cell.

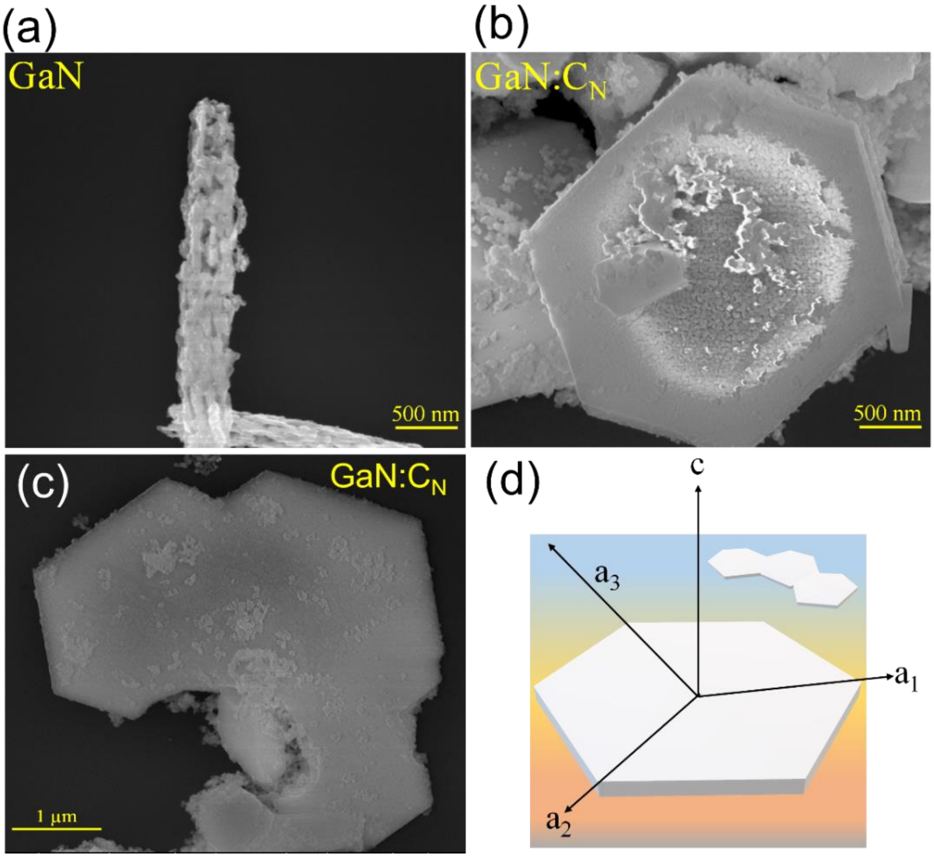

Figure 4: *FESEM images of (a) GaN, (b,c) GaN:C_N and (d) schematic presentation of the formation of hexagonal morphology.*

To verify the carbon doping, and avoid the effect of surface carbon, XPS spectra of 3d peak of Ga and 1s peak of N have been collected (charged corrected to standard 1s at 284.6 eV peak of adventitious carbon). Deconvoluted Ga 3d spectra of undoped GaN and doped GaN:C_N with different concentrations is shown in **Figure 5a**.

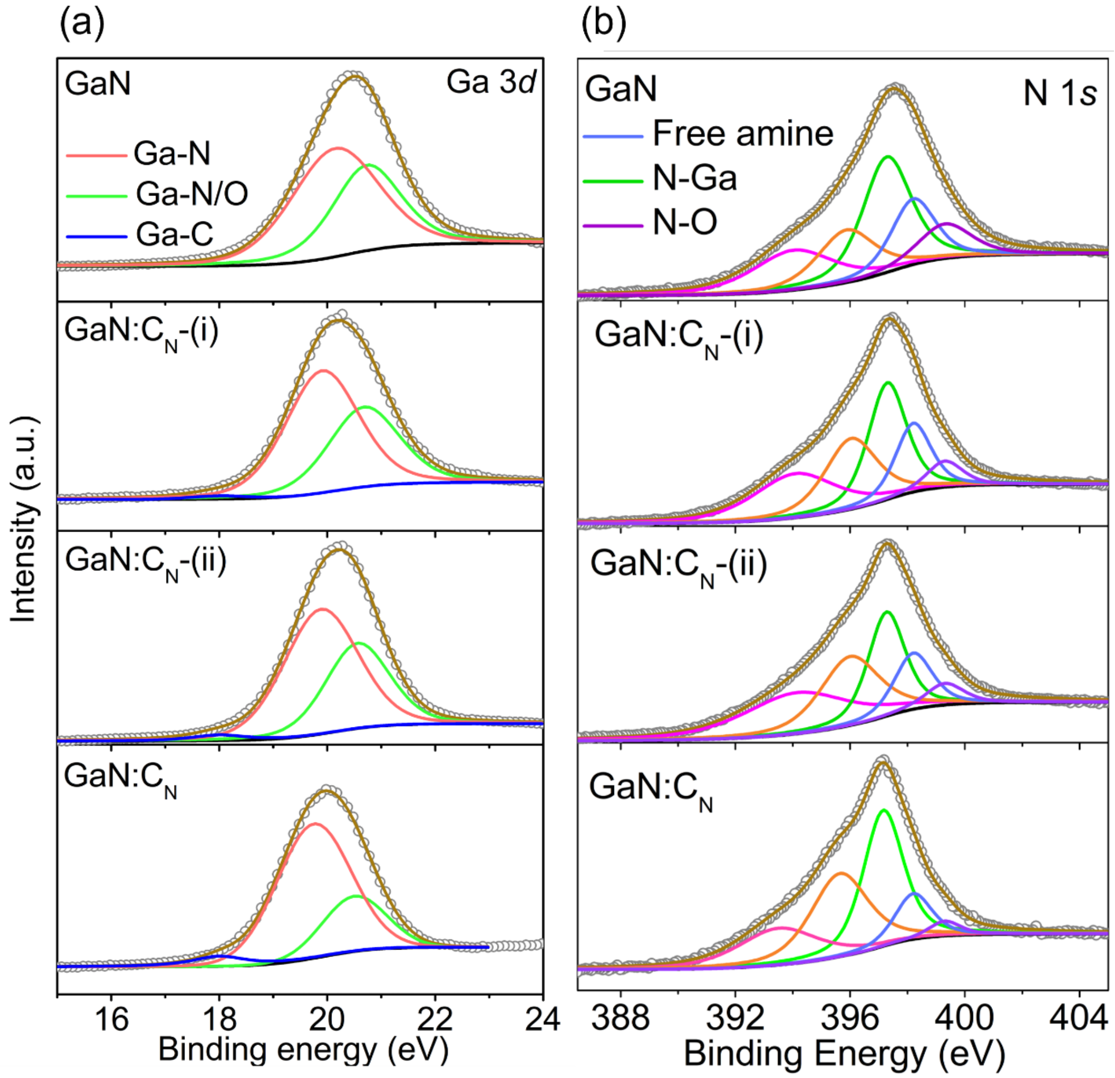

Figure 5: *XPS spectra of (a) Ga3d and (b) N 1s of GaN and GaN:C_N samples.*

An asymmetrical behavior of the Ga 3d spectra toward the lower binding energy is observed, and the spectra can be deconvoluted into three peaks at 18.2, 19.8, and 20.5 eV. Peaks with a low binding energy at 18.2 eV are assigned to the Ga−C bond, and peaks with high binding energy at 19.8 and 20.5 eV are assigned to the Ga−N and Ga− N/O bonds, respectively[19,20]. N 1s spectra are deconvoluted into five peaks at 394.0, 395.9, 397.4, 398.3, and 399.4 eV. Two components at

394.0 and 395.9 eV are assigned to Auger Ga bond contribution[21,22]. Three subpeaks located at 397.4, 398.3, and 399.4 eV are assigned to N−Ga, free amines, and N−O bonds, respectively[19,20]. Ga−N, Ga−N/O, and Ga−C bond % are calculated by peak areas of deconvoluted XPS spectra of Ga 3d, and N−O bond percentages are calculated by peak areas of deconvoluted XPS spectra of N 1s (**Table1**).

Table 1: Ga-N, Ga-N/O, Ga-C and N-O bonds percentage of GaN and carbon doped GaN, calculated by peak areas of deconvoluted XPS spectra of Ga 3d and N 1s.

Sample	Synthesis condition (at 1000°C)	Ga-N (%)	Ga-N/O (%)	Ga-C (%)	N-O (%)
GaN	$Ga_2O_3 + NH_3$	59.8	40.2	--	11.1
GaN:C_N-(i)	$Ga_2O_3 + NH_3 + CH_4$ (2h)	60.2	38.8	1.0	6.1
GaN:C_N-(ii)	$Ga_2O_3 + NH_3 + CH_4$ (3h)	60.5	36.9	2.6	5.4
GaN:C_N	$Ga_2O_3 + NH_3 + CH_4$ (4h)	69.6	25.4	5	3.4

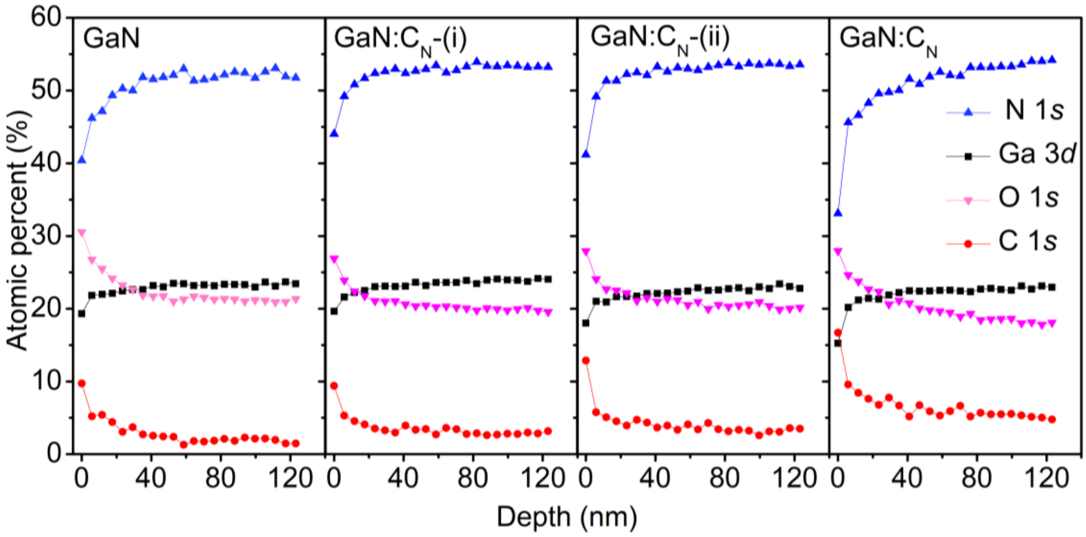

***Figure 6:** Depth distributions of Ga, N, O, C of GaN and GaN:C_N samples measured by XPS.*

Ga−C and Ga−N bonds increased by 0% to 5% and 59.8% to 69.6%, respectively, on increasing the CH_4 gas duration in the reaction, whereas Ga−O/N and N−O bonds decrease from 40.2% to 25.4% and 11.1% to 3.4%, respectively. These considerable changes in the bond percentages depict that C doping help to reduce the oxide content in the GaN. **Figure 6** presents the processed sputter depth profile of undoped and C-doped GaN for determining the contents of Ga, N, C, O, and average stoichiometry. Up to a few nanometers, a high concentration of C and O is observed because of surface oxides and carbon layers, and those were almost sputtered away with 160 s of etch time. Contents of Ga, N, C, and O, and the corresponding average stoichiometry calculated by sputter depth profile are shown in **Table 2**. On increasing the C content from ≈0 to 5%, O content decreases by 22.7 to 17.8%, further confirming the oxygen compensation by C doping.

Table 2: Contents of Ga, N, C and O and corresponding average stoichiometry calculated by sputter depth profile of undoped and C doped GaN samples.

Sample	Ga (%)	N (%)	O (%)	C (%)	Average Stoichiometry
GaN	23.7	53.4	22.7	0.9	$Ga_{0.24}N_{0.53}O_{0.23}$
GaN:C_N-(i)	23.8	53.3	20.6	2.4	$Ga_{0.24}N_{0.53}O_{0.21}C_{0.02}$
GaN:C_N-(ii)	23.7	53.1	19.8	3.4	$Ga_{0.24}N_{0.53}O_{0.20}C_{0.03}$
GaN:C_N	23.6	53.4	17.8	4.9	$Ga_{0.24}N_{0.53}O_{0.18}C_{0.05}$

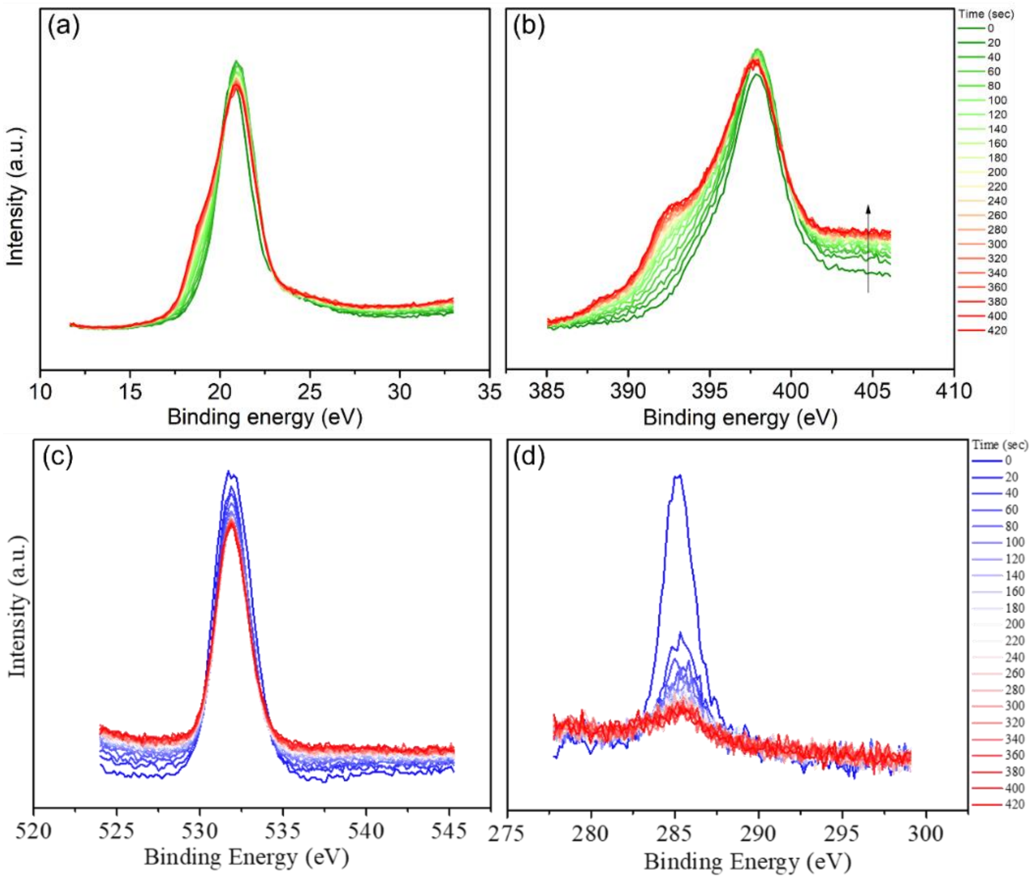

Figure 7: *Core level XPS spectra of (a)Ga 3d, (b)N 1s, (c)O 1s and (d)C1s with respect to sputtering time of GaN and GaN:C_N samples.*

The Ga and N elemental content is found to be ≈23% and 53%, respectively. Even though the results show that the samples are nitrogen rich, it should be noticed that the concentration of N is overestimated because of the substantial contribution of Auger Ga peaks contributions,[21,22] which overlap with the N 1s peak shown in **Figure 5b**. The doping of C and overestimation of N can be further confirmed by sputtering time-dependent study of core-level spectra of Ga 3d and N 1s (**Figure 7**). On increasing the sputtering time, the asymmetricity was observed toward a lower energy of ≈18.1 eV in Ga 3d and ≈394 eV in N 1s (**Figure 7a,b**). A decrease in surface C and O was also observed with the increase in the sputtering time (**Figure 7c,d**).

Vibrational modes of undoped GaN and doped GaN have been investigated by Raman spectra (**Figure 8a,c**), and the different modes were assigned on the basis of theoretical and experimental reports by Wu *et al.* and Ito *et al*[8,11]. Besides E_2(high) and A_1(LO) modes, a new vibrational mode is observed in heavily C doped GaN:C_N at ~765 cm^{-1} (ω_1). This can be further resolved in four modes located at 765(C_N^-,ν_1), 777 cm^{-1} (C_N^-,ν_2), 781 cm^{-1} (C_N^-,ν_3), and ≈803 cm^{-1} ($C_N^- - O_N^0$, ν) (**Figure 8a**).

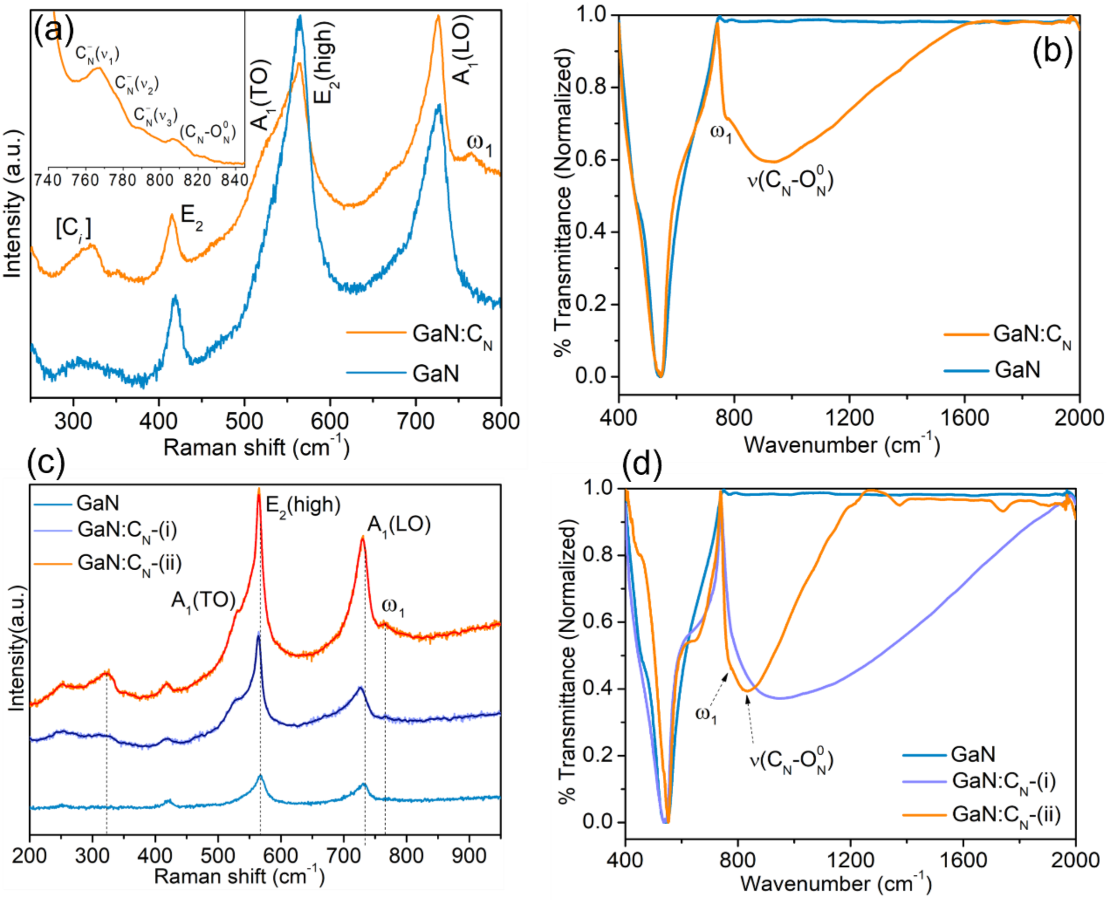

***Figure 8**: (a,c) Raman spectra and (b,d) IR spectra of GaN and GaN:C_N samples.*

A Raman mode observed at 420 cm^{-1} can be attributed to the overtones of transverse acoustic phonons[23]. As the content of C increases, there is a corresponding increase of ω_1 intensity, indicating LVM is related to the doping of C in GaN **Figure 8c**. The intensity of C_N^-,(ν_1) mode is higher than $C_N - O_N^0$ (ν) in Raman spectra where C is present in isolated N with a −1 charge state. Thus, the formation of C_N^- might be preferred over the C_N−O_N complex. The appearance of A_1(TO) mode in doped GaN:C_N with increasing C content indicates the break of symmetry, which is absent in pure GaN. A mode around 320 cm^{-1}, which can be because of the interstitial incorporation of carbon (C_i) suggested in theoretical calculations[24]. The frequencies of LVMs of doped GaN:C_N in the Raman spectra agree well with the FTIR spectra.

The peak in the IR spectra ≈765 cm^{-1} matches with C_N^- (ν_1) of Raman band and confirms the C doping in the form of C_N (**Figure 8b**). A broad peak at ~805 cm^{-1} ($C_N - O_N^0$ (ν)), which is also observed in Raman spectra on increasing the C-content (**Figure 8b,d**), might be because of the theoretically predicted LVM of C_N−O_N complex formation[8]. The formation of this complex might be much less, as predicted by Christenson et al.,[25] with the ratio of [C_N−O_N]/ [C_N] being an order of magnitude smaller than 1 at the growth temperature of 1300 K, which is near our sample preparation temperature. Moreover, C_N and O_N are the next-nearest neighbours, and the binding energy of those complexes is expected to be comparatively low. The Tauc plot of GaN and GaN:C_N reveal a decrease in a fundamental band position on increasing the carbon content (**Figure 9**).

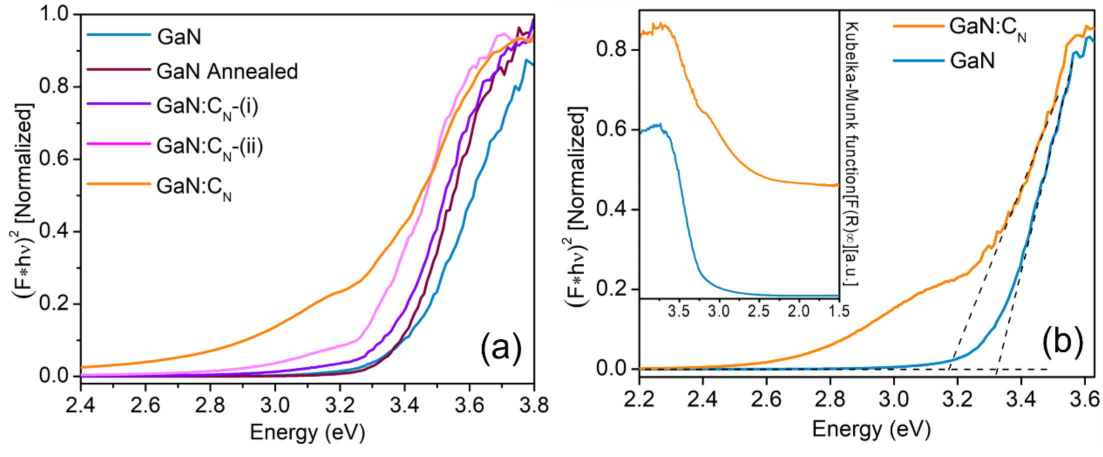

***Figure 9**: Tauc plots of GaN with (a) different cabon content and (b) highest doped sample.*

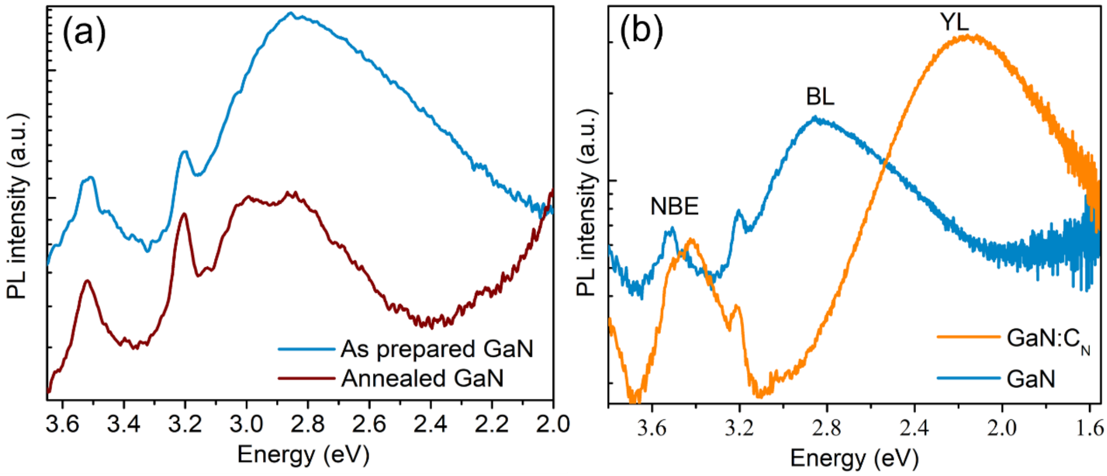

***Figure 10**: Photoluminescence spectra of GaN along with (a) annealed sample and (b) GaN:C_N sample.*

A new shoulder appears in front of the absorption band in highly doped GaN:C_N (**Figure 9a**). The Kubelka–Munk function (F_∞) versus energy plot confirms a transition near to ≈3.05 eV from the expected carbon defect level to the conduction band apart from the fundamental valence band to conduction band transition (inset of **Figure 9b**).

The room-temperature PL spectra of undoped GaN and doped GaN:C_N are presented in **Figure 10**. Near-band edge (NBE) emission is observed with a maximum of 3.51 eV in GaN **(Figure 10a)**. In addition to NBE, an asymmetric broad luminescence at 2.85 eV is observed, which is assigned to the blue luminescence (BL) emission because of the transition from the substitutional O_N donor level. This transition is predicted from 0.25 eV above the conduction-band edge to the V_{Ga}-O_N complex[26,27]. The PL band at ≈3.20 eV is due to recombination of donor-acceptor pair (DAP) with the origin from unidentified shallow acceptors, exciton bound to structural defects including stacking faults and surface-related defects[27,28]. In carbon-doped GaN:C_N, BL is completely quenched, and another defect-related yellow luminescence (YL) is observed with a maximum at 2.15 eV, with zero phonon line (ZPL) at 2.75 eV **(Figure 10b)**. A redshift in NBE with an energy of 3.42 eV along with a shoulder at the same energy of 3.51 eV, suggests the substitutional O_N donor compensation by carbon. Annealed undoped GaN does not show any shift in NBE, or complete quenching in BL and the appearance of YL (**Figures 9a** and **10a**).

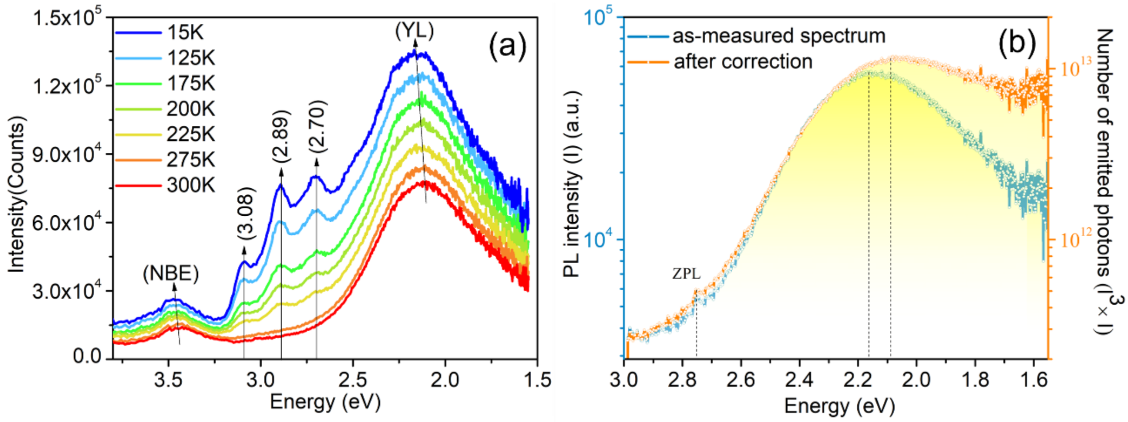

Figure 11: *(a) Temperature dependent and (b) corrected PL spectra of GaN:C_N.*

Thus, it is to be taken as confirmation of the strong evidence of C-doping in the GaN:C_N A temperature-dependent optical measurements' study was also performed to know the nature of NBE and YL at a lower temperature. **Figure 11a** shows the presence of Y_i lines[28] and the absence of carbon-related blue (BL_C) luminescence[7] at ≈2.9 eV on lowering the temperature. The maximum of the YL band lies in the range of 2.11−2.16 eV. NBE becomes more intense, sharper, and blue-shifted as temperature decreases. The broader behavior of NBE at high temperature is due to dissociation of bound excitons because of thermal effects, and it is well explained in the literature[29,30]. The intensity correction suggested by Reshchikov *et al.*[31] was done by multiplying λ_3 with obtained PL intensity to get the number of emitted photons as a function of photon energy to show the correct intensity (**Figure 11b**). The corrected PL spectrum depicts a significant change in lower energies' photon shape only, and the YL band maximum lies at ≈2.10 eV.

A detailed mechanism of such optical transitions, related absorption, and emission energies values have been adopted from the literature to compare with our obtained results shown in **Figure 12**. **Figure 12a** reveals the configuration coordinate diagram of defect-related photophysical processes; photoexcitation (PA), de-excitation (PL) from the ground state to the excited state, and the difference between the bandgap energy and the transition energy denoted by ZPL. Q represents the atomic configuration along with the Franck−Condon approximation. Energy loss is d_{FC}^{g} in the process of relaxation from the equilibrium excited state to the ground state. Nonequilibrium electron−hole pairs generation is represented by G and the recombination process of free carriers is denoted by R under a photoexcitation shown in **Figure 12c,d.**

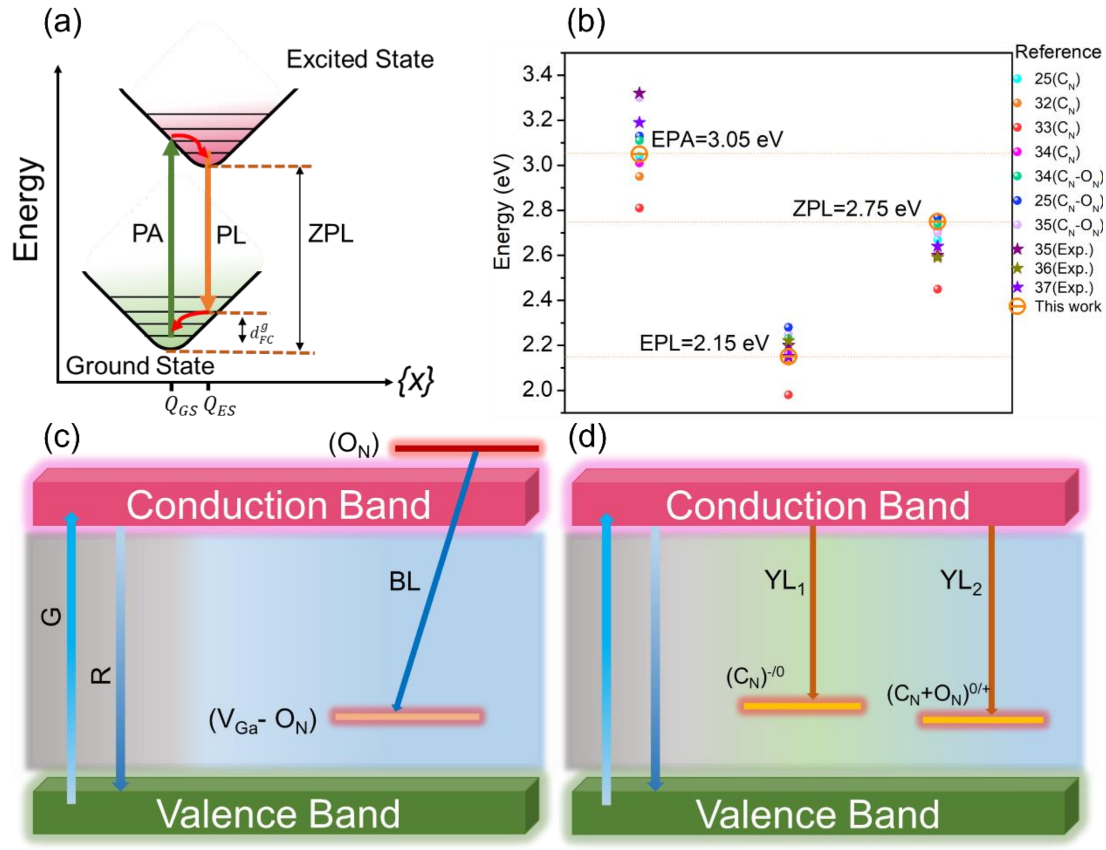

Figure 12: *Diagrams based on reported literature of (a) configuration coordinate and (b) theoretical and experimental energies of photoabsorption (EPA) photoluminescence (EPL) and zero phonon line (ZPL) with comparison of this work. (c,d) Band diagrams along with relevant excitation and recombination processes of defect-related GaN.*

The lower-energy conduction band states are occupied (Moss-Burstein effect)[27] because of oxygen doping in GaN, and electronic transition in higher energy is expected. therefore, a higher absorption edge at 3.51 eV is observed (**Figure 9a**). BL observed in undoped GaN can be explained by the band diagram presented in **Figure 12c** and the proposed transition by Yang *et al*[26]. This BL at ≈ 2.8 eV band is the result of a transition from the doped oxygen (O_N) level at 0.25 eV above the conduction band to the V_{Ga}−O_N complex acceptor at 0.8 eV above the valence-band edge (**Figure 12c**)[26]. Since the oxygen substituted on the N serves as the positively charged donor, and the carbon substituted on N serves as the negatively charged acceptor, they can form the possible C_N–O_N complex which might result in the quenching of the BL. The origin YL band at ≈2.15 eV was argued by carbon doping with the two assignments suggested based on first-principles calculations and experimental studies (**Figure 12d**) in the previous literature. The YL_1 band is attributed to the C_N defect (−1 charged ground state and 0 charged excited state),[25,32–34] and alternatively, the YL_2 band can be caused by the C_N–O_N complex (0 charged ground state and + charged excited state)[25,34,35]. To identify the defect level experimentally, EPA from absorption spectra, EPL and ZPL from emission spectra, and transition energy of defect level ($\Delta E = E_g$-ZPL) have been calculated. The EPA, EPL, and ZPL energies of the defect are found to be 3.05, 2.15, and 2.75 eV, respectively (from **Figures 9, 10 and 11**). ΔE calculated by NBE (≈3.51 eV) is found to be 0.76 eV. These energy values are in good agreement with previously reported theoretical and experimental isolated C_N defect levels (**Figure 12b**)[25,32–37]. Thus, the yellow luminescence observed in our sample is to be attributed to the presence of isolated C_N defect level.

9.5. Conclusions

We conclude by illustrating the solid-gas reaction route to synthesize C-doped GaN and explained the spectroscopic evidence of local vibrational modes due to C-doping. In the absorption spectrum, a transition band is observed at ≈3.05 eV due to carbon doping. Experimental values of vibrational modes indicate the formation of isolated acceptor C_N defect and the possibility of the C_N-O_N complex. A blue luminescence was observed related to oxygen-defect at ≈2.8 eV which is quenched on carbon doping. A carbon defect-related yellow luminescence at ≈2.15 eV is observed, which is responsible for the −1 charged C_N^- level transitions in C-doped GaN. The level related to this C_N defect formation by carbon doping is confirmed by the PL peak position, zero phonon line, and energy of absorption. The current work will help in the investigation of doping levels in nitride materials.

9.6. References

[1] Ehrentraut, D.; Meissner, E.; Bockowski, M. *Technology of gallium nitride crystal growth*; Springer Science & Business Media: **2010**; Vol. 133, pp 3−27.

[2] Mori, Y.; Imade, M.; Maruyama, M.; Yoshimura, M.; Yamane, H.; Kawamura, F.; Kawamura, T. *Handbook of crystal growth Bulk Crystal Growth: Basic Techniques, and Growth Mechanisms and Dynamics*, 2nd ed.; Rudolph, P., Ed.; Elsevier, Amsterdam: **2015**.

[3] Koller, C.; Lymperakis, L.; Pogany, D.; Pobegen, G.; Ostermaier, C. *J. Appl. Phys.* **2021**, 130 (18), 185702.

[4] Vaudo, R. P.; Xu, X.; Salant, A.; Malcarne, J.; Brandes, G. R. *Phys. Status Solidi A* **2003**, 200 (1), 18−21.

[5] Iwinska, M.; Piotrzkowski, R.; Litwin-Staszewska, E.; Sochacki, T.; Amilusik, M.; Fijalkowski, M.; Lucznik, B.; Bockowski, M. *Appl. Phys. Express* **2017**, 10 (1), 011003.

[6] Heikman, S.; Keller, S.; DenBaars, S. P.; Mishra, U. K. *Appl. Phys. Lett.* **2002**, 81 (3), 439−441.

[7] Zimmermann, F.; Beyer, J.; Röder, C.; Beyer, F. C.; Richter, E.; Irmscher, K.; Heitmann, J. *Phys. Status Solidi A* **2021**, 218, 2100235.

[8] Wu, S.; Yang, X.; Zhang, H.; Shi, L.; Zhang, Q.; Shang, Q.; Qi, Z.; Xu, Y.; Zhang, J.; Tang, N.; *et al. Phys. Rev. Lett.* **2018**, 121 (14), 145505.

[9] Yang, J.; Brown, G. J.; Dutta, M.; Stroscio, M. A. *J. Appl. Phys.* **2005**, 98 (4), 043517.

[10] Ibáñez, J.; Hernández, S.; Alarcón-Lladó, E.; Cuscó, R.; Artus,´ L.; Novikov, S. V.; Foxon, C. T.; Calleja, E. *J. Appl. Phys.* **2008**, 104 (3), 033544.

[11] Ito, S.; Kobayashi, H.; Araki, K.; Suzuki, K.; Sawaki, N.; Yamashita, K.; Honda, Y.; Amano, H. *J. Cryst. Growth* **2015**, 414, 56−61.

[12] Cerqueira, M. F.; Vieira, L. G.; Alves, A.; Correia, R.; Huber, M.; Andreev, A.; Bonanni, A.; Vasilevskiy, M. I. *J. Phys. D: Appl. Phys.* **2017**, 50 (36), 365103.

[13] Roy, A.; Rao, C. N. R. *APL Mater.* **2019**, 7 (9), 090901.

[14] Ayyub, M. M.; Prasad, S.; Lingampalli, S. R.; Manjunath, K.; Waghmare, U. V.; Rao, C. N. R. *ChemPhysChem* **2018**, 19 (24), 3410−3417.

[15] Kumar, N.; Maitra, U.; Hegde, V. I.; Waghmare, U. V.; Sundaresan, A.; Rao, C. N. R. *Inorg. Chem*. **2013**, 52 (18), 10512−10519.

[16] Lingampalli, S. R.; Manjunath, K.; Shenoy, S.; Waghmare, U. V.; Rao, C. N. R. *J. Am. Chem. Soc.* **2016**, 138 (26), 8228−8234.

[17] Manjunath, K.; Prasad, S.; Waghmare, U. V.; Rao, C. N. R. *Dalton Trans.* **2018**, 47 (28), 9303− 9309.

[18] Roy, A.; Shenoy, U. S.; Manjunath, K.; Vishnoi, P.; Waghmare, U. V.; Rao, C. N. R. *J. Phys. Chem. C* **2016**, 120 (28), 15063−15069.

[19] Wang, Z.; Huang, B.; Yu, L.; Dai, Y.; Wang, P.; Qin, X.; Zhang, X.; Wei, J.; Zhan, J.; Jing, X.; *et al. J. Am. Chem. Soc.* **2008**, 130 (48), 16366−16373.

[20] Yu, L.; Wang, Z.; Guo, M.; Liu, D.; Dai, Y.; Huang, B. *Chem. Phys. Lett.* **2010**, 487 (4), 251−255.

[21] Alevli, M.; Haider, A.; Kizir, S.; Leghari, S. A.; Biyikli, N. *J. Vac. Sci. Technol. A* **2016**, 34 (1), 01A137.

[22] Banerjee, S.; Onnink, A. J.; Dutta, S.; Aarnink, A. A. I.; Gravesteijn, D. J.; Kovalgin, A. Y. *J. Phys. Chem. C* **2018**, 122 (51), 29567−29576.

[23] Siegle, H.; Kaczmarczyk, G.; Filippidis, L.; Litvinchuk, A. P.; Hoffmann, A.; Thomsen, C. *Phys. Rev. B* **1997**, 55 (11), 7000−7004.

[24] Lyons, J. L.; Glaser, E. R.; Zvanut, M. E.; Paudel, S.; Iwinska, M.; Sochacki, T.; Bockowski, M. *Phys. Rev. B* **2021**, 104 (7), 075201.

[25] Christenson, S. G.; Xie, W.; Sun, Y. Y.; Zhang, S. B. *J. Appl. Phys.* **2015**, 118 (13), 135708.

[26] Yang, H.-C.; Lin, T.-Y.; Chen, Y. F. *Phys. Rev. B* **2000**, 62 (19), 12593.

[27] Kumar, M.; Poulose, A. C.; Nakajima, Y.; Sakthikumar, D.; Kumar, V.; Singh, R. *Phys. E: Low-Dimens. Syst. Nanostructures* **2018**, 104, 187−191.

[28] Reshchikov, M. A.; Morkoc, H. *J. Appl. Phys.* **2005**, 97 (6), 061301.

[29] Zhang, R.; Kuech, T. F. *Appl. Phys. Lett.* **1998**, 72 (13), 1611−1613.

[30] Shan, W.; Schmidt, T. J.; Yang, X. H.; Hwang, S. J.; Song, J. J.; Goldenberg, B. *Appl. Phys. Lett.* **1995**, 66 (8), 985−987.

[31] Reshchikov, M. A. *J. Appl. Phys.* **2021**, 129 (12), 121101.

[32] Lyons, J. L.; Janotti, A.; Van de Walle, C. G. *Appl. Phys. Lett.* **2010**, 97 (15), 152108.

[33] Reshchikov, M. A.; Demchenko, D. O.; Usikov, A.; Helava, H.; Makarov, Y. *Phys. Rev. B* **2014**, 90 (23), 235203.

[34] Zhang, H. S.; Shi, L.; Yang, X. B.; Zhao, Y. J.; Xu, K.; Wang, L. W. *Adv. Opt. Mater.* **2017**, 5 (21), 1700404.

[35] Demchenko, D. O.; Diallo, I. C.; Reshchikov, M. A. *Phys. Rev. Lett.* **2013**, 110 (8), 087404.

[36] Reshchikov, M. A.; McNamara, J. D.; Zhang, F.; Monavarian, M.; Usikov, A.; Helava, H.; Makarov, Y.; Morkoc, H. *Phys. Rev. B* **2016**, 94 (3), 035201.

[37] Ogino, T.; Aoki, M. *Jpn. J. Appl. Phys.* **1980**, 19 (12), 2395.